A Continuum Constitutive Model for the Mechanical Behavior of Woven Fabrics Including Slip and Failure

by
Michael J. King

B.S. Mechanical Engineering
Northeastern University, 2001
S.M. Mechanical Engineering
Massachusetts Institute of Technology, 2003

Submitted to the Department of Mechanical Engineering
in partial fulfillment of the requirements for the degree of

Doctor of Philosophy

at the

MASSACHUSETTS INSTITUTE OF TECHNOLOGY

June, 2006

Author .....
Department of Mechanical Engineering
May 22, 2006

Certified by .....
Simona Socrate
d'Arbeloff Assistant Professor of Mechanical Engineering
Thesis Supervisor

Accepted by .....
Lallit Anand
Professor of Mechanical Engineering
Chairman, Department Committee on Graduate Students

A Continuum Constitutive Model for the Mechanical Behavior of Woven Fabrics Including Slip and Failure

by
Michael J. King

Submitted to the Department of Mechanical Engineering
on May 20, 2006, in partial fulfillment of the
requirements for the degree of
Doctor of Philosophy

Abstract

Woven fabrics are used in many applications, including ballistic armors and fabric-reinforced composites. Advances in small-scale technologies are enabling new applications including fabrics with embedded electronics, active yarn materials, or micro-fluidics. In order to facilitate the design and improvement of such applications, we propose a modeling approach that relates the macroscopic response of the fabric to the behavior of the underlying yarns and weave. The resulting continuum model is more computationally efficient than a discrete model that represents every yarn or fiber explicitly. Because it is physically based on the fabric mesostructure, the model can be used to predict the behavior of novel fabric designs. It can be easily tailored to a wide variety of different applications through the choice of suitable, physically motivated constitutive behaviors for the components that make up the assumed underlying mesostructure.

We first describe a model suitable for slip-free planar deformations of a plain weave Kevlar® fabric in response to in-plane loads. We next extend this model to three dimensional behaviors through the development of an anisotropic shell implementation that includes the resistance of the fabric to bending and twist. The model predictions are validated against a number of experimental investigations.

Yarn friction and yarn pullout experiments are used to study the phenomenon of yarn slip and to characterize the frictional forces that oppose it. We propose a novel approach for capturing slip in a continuum fabric model, where a single deformation mapping describes the motion of the weave crossover points, and velocity fields describe the relative motion of the yarns past these crossover points. This approach allows the same modeling methodology that was developed for the slip-free case to be used in the presence of yarn slip. The resulting theory is non-local—the characteristic unit cell representing the weave mesostructure evolves with the gradients of the slip velocities, and the slip velocities are driven in turn by the gradients of yarn tensions. Consequently, implementing the slip formulation into a commercial finite element code presents significant challenges. Different implementation methods are discussed, and the model is validated by conducting analyses of load conditions where slip can be experimentally observed.

Thesis Supervisor: Simona Socrate
Title: d'Arbeloff Assistant Professor of Mechanical Engineering

Acknowledgements

Wow, this thesis is finally done. And I certainly couldn't have done it alone. A lot of people were there for me throughout my graduate experience, and without their help this thesis would never have been completed.

I want to especially thank my advisor, Professor Simona Socrate. I knew I wanted to work with her from the first time I met her. Her guidance and intellectual insights were invaluable, but her sense of humor and tolerance for my...er...creative wordsmithing, were equally important. Not to mention that she gave me some wonderful opportunities, including sending me to some great conferences. Simona, thanks for being everything I could want in an advisor.

I also received a great deal of guidance and other forms of assistance from the professors who served on my committee. Professor Ned Thomas helped me to keep in touch with the applications of my research, and helped cut through the bureaucracy at the ISN. Professor Raul Radovitzky gave invaluable help with certain mathematical and computational concepts, and provided some great opportunities for me. And Professor David Parks was always willing to spend a few minutes, or a few hours, talking with me about the deeper implications of my research, or some new and exciting concept or algorithm that might be relevant, or just about anything else I needed. Thank you all.

Other people also gave me important guidance. James Singletary from DuPont provided us with all of our Kevlar samples, and helped educate us about the vagaries of textile mechanics in general and Kevlar specifically. Phil Cunniff from the U.S. Army Soldier Systems Center at Natick taught me a great deal about ballistic impacts and fabric armors. And Tom Godfrey, also from the Soldier Systems Center, shared valuable information about his own fabric-related research with us and proved to be a great collaborator and good friend. MIT Professors Mary Boyce, Klaus-Jurgen Bathe, and Nicolas Hadjiconstantinou also helped me when I struggled with this research, for which I am very grateful.

My good friend and collaborator Petch Jearanaisilawong not only developed experimental methods and performed a great deal of the early experimental work upon which this thesis is built, but he also good naturedly put up with my constant badgering because I never seemed to be able to remember where I had written down what he had already told me before about this experiment or that data point. And he never tired of training and re-training me and the students that worked for me to use the experimental equipment. Petch, thanks a lot. You're a great co-author, a great fellow researcher, a great traveling partner, and, to top it all off, a great cook. And I'm proud that I know how to spell your name.

Thanks to Pierre Perdiguier, a visiting student from Ecolé des Mines, who performed the experimental work on biaxially stressed fabrics with slit-like damage. Pierre, you were only here a short time, but your help was invaluable and you were great to have around.

Also thanks to the undergraduates who worked for me, Emily Pfeiffer and Christina Chestnut. You were diligent and hard working, and the experimental work you did was integral to our slip formulation. Christina, the pneumatic fixture you designed is an excellent tool. Congratulations on designing such an effective apparatus.

I want to thank Ray Hardin and Una Sheehan for all the administrative support and equally important words of encouragement and cheery dispositions they provided over

the years. I'd also like to thank Joanne Maxwell and Marco Carega at the ISN, along with Catherine Byrne and Josh Freedman, who helped me solve any and all administrative, financial, and bureaucratic problems that arose in connection with the ISN.

All the graduate students that have labored here at MIT alongside me have been a wonderful source of support. In addition to Petch and Pierre, my other lab mates, Anastassia Paskaleva, Kristin Myers, Asha Balakrishnan, Jamie Kofoid, Tim Johnson, and Bruce Wu were always there to help kill a little time, keep life interesting, commiserate about grad student life, and remind me about events with free food. Sorry for the messy desk and the thermostat wars. I want to thank Nici Ames for all her help with the department computers and software, and Nuo Sheng, Brendan Harley, Yin Yuan, and Yujie Wei for helping me get through my Quals, and also thank Yujie for helping me get through my first semester here at MIT as a T.A. Also, I'd like to thank Michele Aghassi, Susan Martonosi, and all the folk in the ORC for making me feel as welcome in their department as I felt in my own.

Professor Lallit Anand first encouraged me to come to MIT, and gave me the opportunity to T.A. a course, which proved to not only be a valuable experience but also gave me a chance to find an advisor and a thesis topic that was perfect for me. Thank you. I'd also like to thank my professors at Northeastern who prepared me so well and who encouraged me to consider graduate school at MIT in the first place, especially Professors John Rossettos, Hamid Hashemi, and Hameed Metghalchi, who challenged me to strive for excellence.

I had a great support network friends outside of MIT as well. My old college roommates Andy Gilbertson, James Sabino, and Brian Petro-Roy, and my other friends Catherine Leamy, Michael Peloso, and Brian Zenowich have stayed fast and true friends even though the demands of research barely let me see them any more. My vocal band Integration by Parts has been a great diversion that helped me get through the most stressful of times, and I especially want to thank my very dear friend Liz Bonawitz for being a good friend both in a performing group and also at MIT.

I wouldn't be where I am today without all the great advice, support, and love I've received from my family, especially my parents Robert and Margaret, and my sisters Laura and Alice. I also want to acknowledge the influence of my grandfather, Edward Bobalek, who first inspired me to look towards the sciences and to think about getting a PhD.

I save my final thanks for my wonderful fiancée, Carol Meyers. Carol, MIT brought us together, and we have been there for each other for five years now. I couldn't have done it without you. I hope that our graduation marks the beginning of many more great times to come.

This research was supported by, or supported in part by, the U.S. Army through the Institute for Soldier Nanotechnologies, under Contract DAAD-19-02-D-0002 with the U.S. Army Research Office. The content does not necessarily reflect the position of the Government, and no official endorsement should be inferred

Contents

Table of Figures

Chapter 1
Introduction

1.1 Motivation

Woven fabrics are used in a wide variety of applications. The most common use for fabrics is apparel. However, fabrics are also used in a wide variety of engineering applications by various other industries. For example, fabrics are used to make air bags and seat belts in the automotive industry. Both the military and the sporting goods industry employ fabrics to make harnesses, parachutes, tents, and other fabric structures. Fabric awnings and roofs are often used in architectural applications. Two fabric applications that are of particular interest are ballistic armors used to make bulletproof vests and woven composites used by the automotive and aircraft industries to make lightweight, failure-resistant structural members.

All of these applications can be improved by using effective fabric modeling techniques to optimize their designs, so there is already a significant incentive to develop robust and accurate fabric models. However, in addition to these existing fabric applications, emerging small scale technologies are enabling the development of advanced fabric systems. For example, DuPont Inc. recently developed a method of introducing 12 μm micro-channels into 50 μm diameter polymer fibers, shown in Figure 1-1. By spinning these fibers into yarns and weaving them into a fabric, microfluidics technology could be introduced directly into woven fabrics. Such technology could be used to create clothing with cooling or heating capabilities. Other examples of new fabric technologies that have been proposed include fabrics used for military applications, with interwoven electronics devices that could be used as part of a soldier's communication system, or a network of biosensors used to monitor the soldier's medical condition, woven directly into his or her uniform. Still other examples include the use of active polymers in fabrics, that can change their stiffness or length in response to electrical or chemical stimuli. Such technology would enable fabric armor panels or other fabric structures that could become rigid at the touch of a button, or artificial muscle patches incorporated into a worker's clothes that would augment their mechanical strength.

Development of novel technologies like these requires versatile modeling techniques that can be adapted to accurately represent a wide variety of fabric behaviors, since the specific behaviors that are important in any given new technology are largely unknown when the technology is

designed. The modeling technique must be able to accurately predict the response of a fabric without the need for extensive testing of fabric samples, since it is often desirable to know how a given fabric technology that is based on unproven small-scale innovations will behave, before it is practical to manufacture sufficient quantities for testing. It is therefore not sufficient to develop phenomenological fabric models that are fit to specific behaviors by adjusting a large number of arbitrary parameters to match extensive experimental results. Rather, physically motivated fabric models are required that can be used to predict the fabric response based on measured or proposed constitutive parameters of the yarns and the weave structure, and that can be tailored to a wide variety of different fabric applications that employ innovative small scale technologies.

1.2 Fabric Deformation Mechanisms

Fabrics are a challenging material to model, especially when treated as a continuum. They are highly anisotropic—a fabric has a preferred material direction aligned with each yarn family. In general, the behavior of a fabric in one direction is coupled to the behavior in the other in a nonlinear manner. Even under uniaxial loading conditions, the response of a fabric is often highly nonlinear due to geometric effects of the weave and to nonlinearities in the material response of the component yarns. In addition, most applications involving fabrics involve finite (large) rotations and deformations. Fabric deformation mechanisms may include both elastic effects (e.g. stretching of the yarns) and inelastic effects (e.g. slip of yarns resisted by friction). Consequently, we must develop an inelastic, anisotropic, nonlinear continuum model suitable for large deformations and finite strains in order to represent a fabric.

Various deformation mechanisms control the mechanical response of a fabric. First, like the fibers of a composite, the yarns of a fabric are capable of stretching, which is one mechanism by which the fabric can accommodate strain parallel to a yarn family. Because the yarn stiffnesses are often relatively large, deformations accommodated by yarn stretch tend to have significantly larger associated stiffnesses than deformations accommodated by other mechanisms, so yarn stretch is generally important only when strains and loads are large. Other deformation mechanisms dominate when loads are small. Unlike the fibers of a composite, the yarns of a fabric are not straight in the unloaded configuration; because the yarns are interwoven they undulate up and down through the weave. This undulation is referred to as *crimp*. Consequently, small and moderate strains parallel to a yarn family can be accommodated by straightening the yarns of that family, with little yarn stretching. This behavior is referred to as *uncrimping*.

Uncrimping is resisted primarily by the bending resistance of the yarns, and generally requires much smaller loads than yarn stretching, provided that it is permitted by the boundary conditions.

Of course, when one family straightens or uncrimps, the other yarn family must undergo an increase in crimp in order to satisfy the geometrical constraints imposed by the fact that the two families are interwoven. This process is known as *crimp interchange* and is illustrated in Figure 1-2. It is the primary mechanism by which load is transferred from one yarn family to the other. As the other family increases its crimp, the fabric must either contract along that yarn family, if boundary conditions do not prevent such contraction, or the yarns of that family must stretch and the tension carried by those yarns will increase. The crimp interchange phenomenon is similar to a Poisson effect, although it is nonlinear, so the effective Poisson's ratio evolves as the fabric is deformed. This mechanism represents an important difference between fabrics and other anisotropic materials, such as long fiber composites, because it permits the two families of reinforcing structures to interact in a nonlinear manner. In a long fiber composite, the different fiber families do not interact with each other in this manner, and load is not transferred form one family to the other.

The yarn families in a fabric interact in other ways as well. Because the yarns are interwoven, certain modes of deformation will cause the yarns to jam against one another. When this occurs, the yarn cross sections are subjected to transverse loads and are compressed, and the macroscopic mechanical response becomes increasingly stiff. We refer to this phenomenon as *locking* (not to be confused with the numeric locking exhibited by certain finite element formulations), although it is sometimes also called *jamming*. This phenomenon is shown schematically in Figure 1-3. It is most evident when the fabric is subjected to large shear deformations. A fabric can be sheared only so far before the yarns jam and the shear response becomes dramatically stiffer. However, in tightly woven fabrics the locking phenomenon can also occur in response to uniaxial deformation along a yarn family. As the fabric contracts due to crimp interchange effects, the yarn cross sections can begin to jam against one another. Some fabrics are so tightly woven that the yarn cross sections are subjected to a state of transverse compression even when the fabric is macroscopically unloaded. In this case, the compressive stresses acting on the yarn cross sections are balanced by small tensile forces in the yarns, and the net macroscopic stress in the fabric is zero. We refer to such a fabric as *pre-locked*.

Fabrics accommodate in-plane shear deformation by relative rotation of the yarn families at the crossover points, which is sometimes called *trellising*. This mechanism can have both an elastic component and a dissipative component. Of course, at large rotation angles, locking effects will provide additional resistance to shear deformation. Note that shear deformation that

results from yarn rotation is not pure shear or simple shear as defined in the classical sense, and is not volume conservative. As the yarns rotate past one another in the fabric plane, the fabric area decreases because negligible extension takes place along the yarn families while the angle between the families decreases. The volume decrease corresponds to the elimination of the voids between yarns or, once locking has commenced, the compaction of the yarn cross sections. Deforming a fabric in a classically defined pure shearing mode would involve extension along the yarn families and would have a significantly stiffer associated response.

Under certain conditions, yarns can slip past one another and slide through the weave. This is a non-local phenomenon—slip of a yarn at a given crossover point is driven by the gradient of tension across that point, and slip at one location affects the mechanical behavior of the fabric at other locations along the yarn. Slip plays an important role in many situations, including the forming of fabric composites, the resistance to impact of a fabric armor system, and the propagation of damage in biaxially stressed fabrics, e.g. in inflated fabric structures and parachutes.

All these deformation mechanisms—yarn stretch, uncrimping, crimp interchange, locking, trellising, and yarn slip—determine the mechanical response of a fabric. Although some other materials (e.g. long-fiber composites with two orthogonal fiber families) may exhibit similar characteristics to fabrics in certain deformation modes, no other material combines all these mechanisms, and consequently the behavior of fabrics is unique. While not all of these mechanisms may be relevant to every application, our models must be able to capture any of them in order to be sufficiently versatile.

1.3 Background in Fabric Modeling

Fabrics have existed for a substantial amount of time, and many different methods for modeling them have been proposed by researchers from a variety of different industries. Even the meaning of the term "model" differs among researchers. To some, "modeling" means proposing a detailed idealization of the geometry of the weave mesostructure, or developing analytical or computational methods for determining the response of this idealized mesostructure to homogeneous deformation conditions—e.g. to uniaxial or biaxial extension along the yarn family directions. To others, "modeling" means the development of continuum constitutive theories that can be implemented into a finite element framework. An exhaustive list of all fabric modeling efforts is beyond the scope of this work. In this section, we identify several common modeling

approaches, describe the capabilities and disadvantages of each approach, and cite selected examples of researchers who have employed these methods.

One of the simplest approaches used to model fabrics is to homogenize the behavior of the underlying mesostructure and approximate the fabric as an anisotropic continuum. In the framework of a continuum formulation, a woven fabric can be treated as an anisotropic planar continuum with two preferred material directions. Homogenized formulations for fabrics or fabric composite structures have been proposed by a number of different researchers. These include Steigmann [1992] and Baseau [2003], who have developed continuum formulations for "filamentary networks" appropriate for non-reinforced fabrics, Reese [2003], who considers an elastoplastic anisotropic continuum formulation, Xue *et al.* [2003] and Shockey *et al.* ([1999] – [2002]), who describe continuum models for woven composites, Tabiei and Ivanov [2002] who develop a continuum model for analyzing ballistic impacts on woven fabrics, and Raun and Chou [1995] and Gommers *et al.* [1996] who use continuum models for knitted composites.

Homogenized continuum models of this type are more computationally efficient than models that represent every yarn discretely, and they are easy to integrate with other continuum material models when analyzing multi-component systems, such as an armor system with multiple layers. However, the identification of appropriate homogenized material parameters can be a formidable challenge. Different researchers have approached this challenge in different manners. For example, Xue *et al.* determine material properties through empirical testing, while Shockey *et al.* rely both on empirical testing and on detailed finite element modeling. Reese employs mixed element modeling approach of the fabric mesostructure to determine appropriate constitutive properties for a continuum model. Tabiei and Ivanov employ a homogenization method to develop properties that reflect the behavior of a representative fabric unit cell. A common problem with many of these approaches is that fabric responses tend to be nonlinear, and the appropriate homogenized properties may evolve as the fabric deforms. In order to capture this evolution and the resulting nonlinearities, complex relations describing the evolution of the homogenized parameters may be necessary, and the homogenized parameters must be evaluated at different states of deformation in order to quantify these relations. Another problem is that many of these homogenized continuum models are incapable of accounting for all of the fabric mechanisms described in the preceding section, especially mechanisms that stem from the interactions between the yarn families, such as crimp interchange, resistance to trellising, and locking. The omission of potentially important mechanisms makes these models unsuitable for the general analysis of novel fabric systems.

An alternative to representing the fabric as a homogeneous anisotropic continuum is to develop a detailed analytical representation of interwoven yarns that comprise the fabric mesostructure. A large number of such analytical models have been proposed to quantify the structure and behavior of the fabric mesostructure. Such mesostructurally-based analytical models typically are comprised of a set of assumptions about the yarn geometries and a set of mathematical relations that predict the mechanical response of the fabric and its component yarns in specific homogeneous modes of deformation. For example, a model could be formulated to predict the load-extension behavior of a fabric under uniaxial or biaxial tension along the yarn family directions. These mesostructural models are sometimes used to quantify homogenized material properties for use in continuum models of the type described above. Hearle, Grosberg, and Backer [1969] describe a number of classical analytical fabric models. One of the most widely adopted of these, a model proposed by Peirce [1937] and shown in Figure 1-4, provides a mathematical framework for relating the parameters that describe the geometrical configuration of a plain weave fabric with circular yarns.

A number of researchers have employed modified forms of Peirce's geometry to account for yarns with non-circular deformable cross sections. Warren [1992] uses such a modified geometry to predict the response to uniaxial and biaxial response of a woven Kevlar® fabric by treating the yarns as elastica, so that yarn extension and bending effects are coupled. Sagar and his colleagues (Sagar *et al.* [2003] and Sagar and Potluri [2004]) employ a similar modified form of this geometry and use the principle of stationary potential energy to determine the fabric configuration and deformation in response to applied loads. However, all such analytical models are only valid in the specific loading modes for which they have been developed; for example, both Warren's and Sagar's models assume that the yarn families remain orthogonal and hence neither of these models allows shear deformation. Extension of these models to more general load cases is challenging due to the complexity of their geometry.

Other researchers have proposed simpler analytical representations of the mesostructure in order to achieve greater mathematical simplicity or computational efficiency. In a series of three classical articles, Kawabata *et al.* [1973] propose analytical models for the biaxial, uniaxial, and shear deformation behaviors of fabrics based on the much simpler truss geometry shown in Figure 1-5. Other researchers have subsequently employed similar geometries to develop improved analytical models, including Realff *et al.* [1997] who modify Kawabata's uniaxial model to include more complex behaviors such as yarn flattening and consolidation. Kato *et al.* [1999] propose an analytical model based on an alternative truss geometry for predicting the constitutive behavior of a coated fabric composite. This geometry is similar to that proposed by

Kawabata but with additional spars to capture the effect of the coatings and create a unit cell capable of resisting shear deformation. A detailed summary of several other analytical fabric models is given by Realff [1992].

Analytical models of the fabric mesostructure can be incorporated into anisotropic continuum formulations to yield multi-scale models that track the fabric mesostructure as the continuum deforms, thereby combining the benefits of continuum modeling with the capabilities of mesostructural models to follow the evolution of the fabric mesostructure in a single modeling step. We described a such a general multi-scale continuum model in King [2003] and in King *et al.* [2005] that could be tailored to a wide variety of different applications. Other researchers have also proposed similar approaches, although many of these models have more restrictive assumptions. For example, Nadler *et al.* [2006] recently proposed a similar multi-scale modeling approach, which uses the sophisticated elastica geometry described by Warren to represent the fabric mesostructure and hence accurately captures the yarn bending, crimp interchange and yarn stretching mechanisms, but Nadler's model does not include resistance to shear deformation or locking. Boisse and his colleagues (Boisse *et al.* [1997] and Boisse *et al.* [2001]) have developed a simple finite element for simulating the response of plain weave fabric composites during forming processes. The yarn directions evolve as the elements deform, and the fabric response is based on Kawabata's analytical truss model of the weave geometry, thereby capturing yarn stretch and crimp interchange effects along evolving material directions. However, Boisse's formulation requires that the element edges be aligned with the yarn family directions, and hence arbitrary meshes cannot be used. Rattensperger *et al.* [2003] take a similar approach for modeling fabric-reinforced hydraulic hoses, with an assumed fabric lattice geometry similar to that used by Kato, and use a conventional finite element formulation with rebar reinforcements to capture the effects of the reinforcing fabric. However, neither Boisse's nor Rattensperger's models include yarn bending effects, and, like Nadler's model, they also omit locking and resistance of the fabric to shear. On the other hand, Tanov and Brueggert [2003] present a mesostructurally based continuum model that includes shear and locking resistance through diagonal spar elements within the assumed unit cell network. However, a diagonally oriented spar is a less realistic way of capturing the shear or locking resistance in fabrics than that described in King ([2003] and [2005]), and also Tanov's model does not include the crimp interchange mechanism.

For small fabric systems, an effective alternative to continuum modeling is to directly model every yarn in the fabric discretely. For example, the fabric geometry can be recreated exactly using a finite element model, with yarns modeled as homogeneous solids, as is shown in Figure 1-6. This method is used by Ng *et al.* [1998], Boisse *et al.* [2001], and Shockey *et al.* ([1999]-

[2002]) among others. This method has the advantage of capturing all yarn interactions and providing a detailed description of all mechanisms of fabric deformation. However, its very large computational requirements limit it to relatively small systems. This approach is not suitable to the analysis of large or multi-component systems, and is generally used only to gain insight into the mechanics of fabric deformation at the mesostructural level or to estimate homogenized properties for simpler continuum models. Furthermore, the constitutive behavior of the individual yarns can be a source of model uncertainty, as the yarns themselves in many fabrics are not homogeneous but rather are composed of individual fibers. Describing this complex morphology accurately may require even more detailed sub-modeling. In order to achieve greater computational efficiency, discrete models are sometimes constructed from a mix of more efficient structural finite elements (such as trusses, beams, and membranes) which directly model the fabric mesostructure. A wide variety of researchers have employed this mixed element approach, including Reese [2003], MacGlockton *et al.* [2003], who model 3D textile composites, and Cherouat and Billoet [2001], who model pre-impregnated woven composites. While such approaches reduce the computational cost of discrete modeling, there still remain many situations where it is more appropriate or convenient to model the fabric as a continuum.

Some researchers with very specific modeling objectives have developed alternative techniques that do not rely on finite element techniques, especially for ballistic analyses. The most widely used model for predicting the ballistic response of fabrics was developed by Roylance *et al.* [1973] (and has since been refined, e.g. in Roylance [1995]) and consists of a planar array of point masses located at the fabric crossover points to capture the inertia of the fabric, connected by trusses to capture the yarn compliances. Strain waves from a ballistic impact are determined by solving the dynamic force balance at each point mass and propagating the solution forward through time. Similar models with extensions and improvements have been proposed by a number of researchers, including Shim *et al.* [1995] and Termonia [2004], and have been shown to be effective at predicting the ballistic performance of certain classes of woven fabrics. However, models of this type capture only the selected aspects of the behavior of fabrics that are most commonly used in ballistic armors, and therefore are not suitable for more general analyses. An example of a completely different approach that is specialized to a specific application is the model proposed by Breen *et al.* [1994], which is composed of interacting particles and which is specialized to predict the low stress behavior, especially the draping behavior, of woven fabrics. While often very effective at predicting specific behaviors for specific fabrics, these modeling approaches are not sufficiently general to aid in the development of advanced fabric systems based on small-scale technologies.

In this work we discuss the extension of the modeling approach presented in King [2003] and King *et al.* [2005] to three dimensional deformations, and present a method for including slip and failure. Only some of the models mentioned above account for out-of-plane loads and deformations. Those that model every yarn explicitly (e.g. those described by Ng *et al.* [1998] and Shockey *et al.* [2001]) can obviously capture three-dimensional deformations. Some of the models that do not use traditional finite elements (e.g. the interacting particle model described in Breen *et al.* [1994], the ballistic impact model developed by Roylance *et al.* [1973] and by Shim *et al.* [1995], or the analytical model described by Sagar and Potluri [2004]) are also capable of capturing out-of-plane deformations. Most continuum fabric finite element models that include out-of-plane deformations (e.g. those described by Boisse *et al.* [1997], Cherouat and Billouet [2001], Shockey *et al.* [2001], and Tanov and Brueggert [2003]) treat fabrics as membranes with negligible bending and twisting stiffness, although bending and twisting effects may be important in some applications.

Yarn slip is relatively easy to account for in non-continuum models; e.g. a discrete model that models every yarn like that of Shockey *et al.*[2001] or a dynamic wave propagation model like that of Termonia [2004]. Capturing yarn slip in a continuum model is significantly more challenging, as is discussed in Chapter 5, and very little literature concerns continuum fabric models that include slip. Nadler and Steigmann [2003] have proposed a continuum model that uses two different deformation mappings to separately describe the motion of the two yarn families. Slip is calculated from the difference between the two mappings. However, this model does not directly track the locations of the crossover points and omits several important mechanisms that stem from interactions at the crossover points, such as locking.

1.4 Overview of Thesis

Chapter 2 reviews the basic multi-scale modeling approach presented in King [2003] and King *et al.* [2005], and describes how this approach is used to develop a planar, slip-free continuum fabric model for a Kevlar® fabric commonly used in military body armor. Specialization of the approach to the particular fabric, development of the model, and details regarding implementation of the model into the commercial finite element code ABAQUS are described. The model is validated by comparing the predictions of the model to experimental observations of the fabric behavior in response to various simple and complex load conditions.

Chapter 3 describes how the modeling approach is extended to three dimensions through a shell implementation that is capable of capturing resistance to bending and twist. A description of

anisotropic shell behavior is given, since fabrics are highly anisotropic. Next, the assumptions used to develop the shell implementation are described; the most significant is that the membrane response of the shell can be determined using the planar model described in Chapter 2. Experimental and numerical studies used to characterize the bending and twist behavior of the Kevlar® yarns and fabric are detailed. The shell model, like the planar model, is validated by comparing its predictions with experimental observations.

Chapter 4 through Chapter 7 are all concerned with extending the model to include the effects of yarn slip, which is extremely challenging to do in a continuum framework. Chapter 4 describes a series of yarn-to-yarn friction and yarn pullout experiments performed to understand and quantitatively characterize the frictional forces that resist yarn slip. Because of the complexity of the yarn slip phenomenon, a simplified analytical model is developed that allows a hypothesized constitutive law describing yarn slip in a fabric to be related to the observed experimental results.

Chapter 5 describes the difficulties of capturing slip in a continuum framework, and presents a novel approach for doing so. This approach has several advantages over more traditional approaches, such as that proposed by Nadler and Steigmann [2003], the most significant of which is that the same modeling technique described in Chapter 2 can be employed with only modest modifications. The kinematics describing yarn slip, the forces that drive yarn slip, and the appropriate form for a constitutive law relating the two are described. We demonstrate that slip is a non-local phenomenon, hence the theory we use to capture it involves gradients of yarn tensions and slip velocities.

Chapter 6 addresses the challenges that arise when the non-local slip theory described in Chapter 5 is implemented into a finite element framework. First, a simple constitutive law of the form given in Chapter 5 is developed that is consistent with the experimental studies conducted in Chapter 4. Next, various methods of implementing the non-local slip theory are explored, and their various advantages and shortcomings are described. Appropriate boundary conditions on quantities that control slip are developed. Chapter 7 presents several analyses that are used to test and validate the slip implementation. Finally, Chapter 8 gives recommendations for further research into these topics.

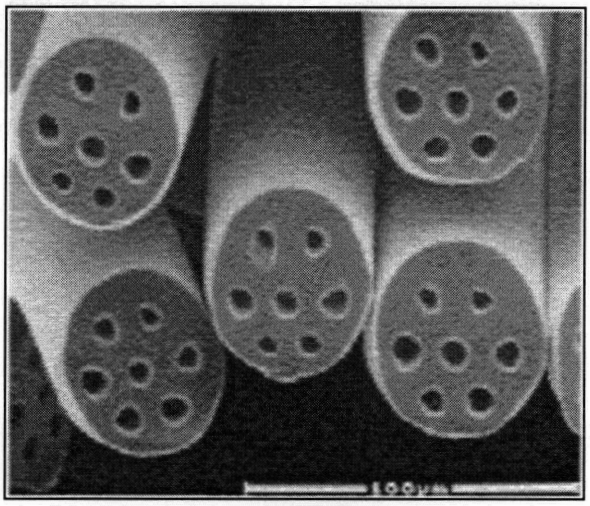

Figure 1-1 Microchannels in polymer fibers manufactured by DuPont, Inc.

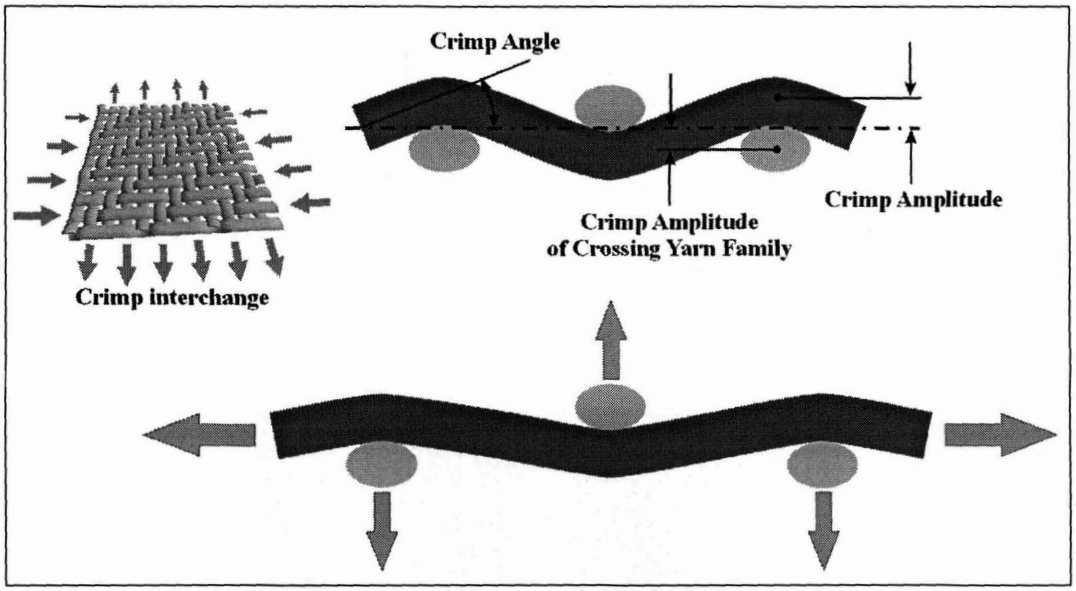

Figure 1-2 Crimp interchange mechanism

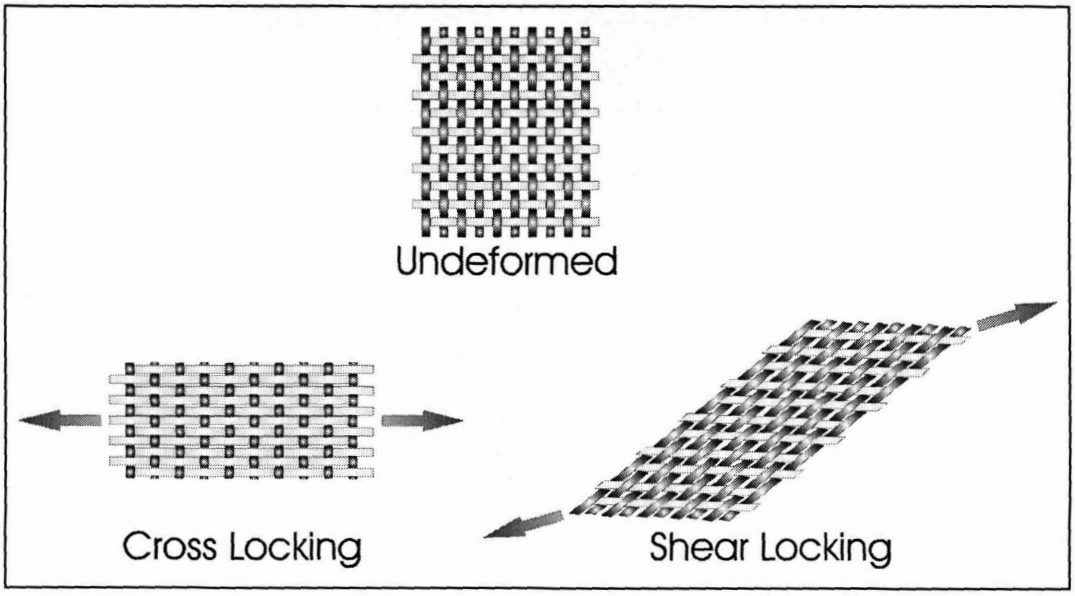

Figure 1-3 Different modes of fabric locking, or jamming

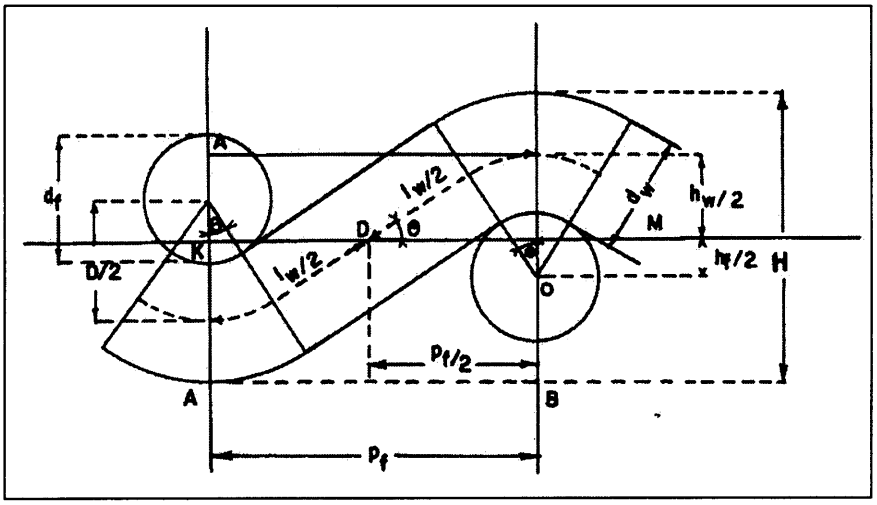

Figure 1-4 Analytical model of fabric mesostructure proposed by Peirce [1937]

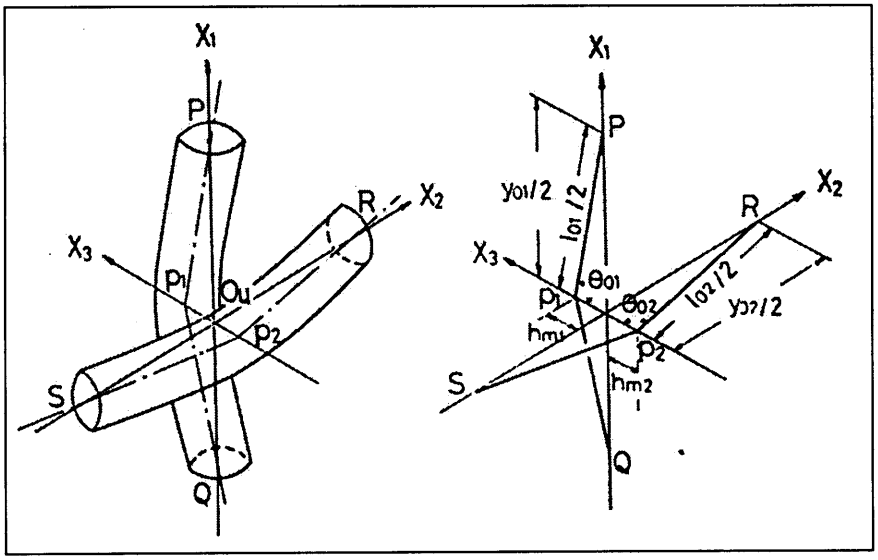

Figure 1-5 Truss geometry proposed by Kawabata *et al* [1973]

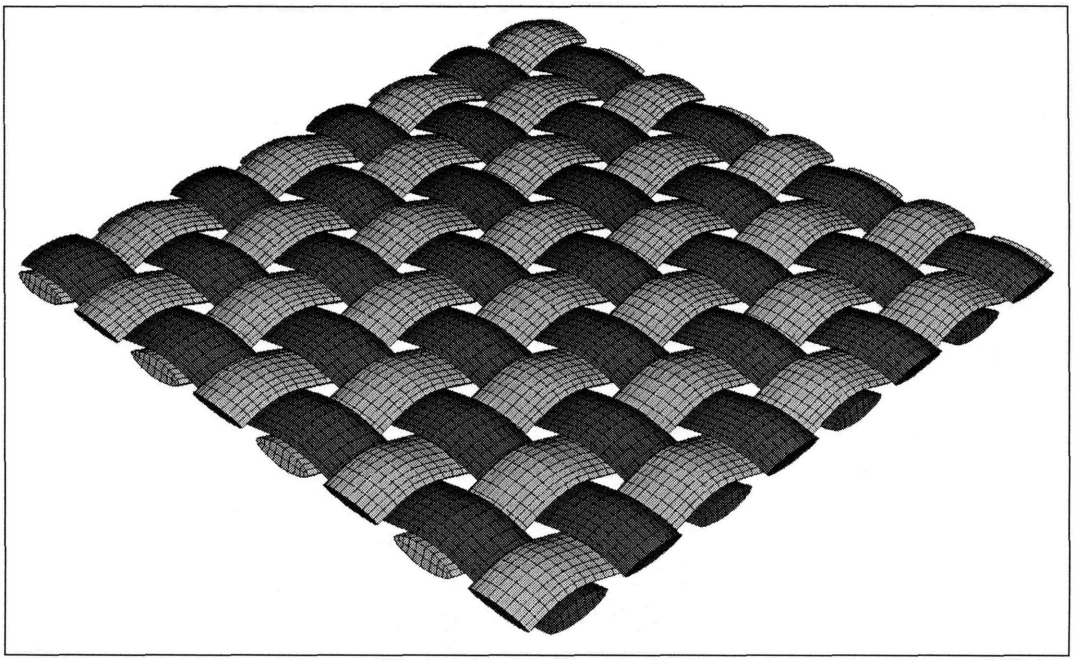

Figure 1-6 Detailed finite element model that represents every yarn discretely

Chapter 2
Slip-Free Planar Model

2.1 Scope of Model and Assumptions

Many of the fabric deformation mechanisms that are of interest, such as crimp interchange and locking, relate to the membrane response of the fabric. Therefore, the initial model developed was a two-dimensional planar model capable of capturing the in-plane response of the fabric to in-plane macroscopic loads. In other words, the initial model assumes that the midsurface of the fabric is initially planar and remains planar throughout deformation, and that all applied loads lie in the plane of the midsurface. The lack of transverse loads means that the through-thickness stresses must be zero on the fabric surfaces. Because the through thickness response of the fabric is so weakly coupled to the in-plane behavior, the through-thickness strains are assumed to be negligible and thickness is assumed to remain constant. Under these conditions, plane stress and plane strain conditions are equivalent, so for simplicity we take the fabric thickness to have a constant unit value. The development of a fabric shell implementation to capture three dimensional behaviors is discussed in Chapter 3.

In the slip-free model it is assumed that that yarns do not slip through the weave, although they are permitted to rotate relative to one another where they cross. In other words, the yarns act as if they are pinned together at the crossover points. The initial model also assumes that the yarns do not break and that no other modes of failure occur. These assumptions are valid in a wide variety of applications and over a wide range of loads, but there are of course some applications and some load ranges where slip and failure comprise a significant part of the fabric response. Expansion of a fabric continuum model to include slip and failure is a challenging undertaking, and is discussed in Chapter 5 through Chapter 7.

The modeling approach that we propose can be easily tailored to particular applications through the inclusion of relevant deformation mechanisms and the omission of mechanisms that do not play a significant role. In this initial model, we include only the mechanisms that are relevant to the experimental responses against which we validate our model. These mechanisms include crimp interchange, locking effects, yarn stretch, yarn bending resistance, and both elastic and dissipative resistance to relative yarn rotation during the trellising process that accommodates in-plane shear. We omit "wrapping" effects that stem from changes in curvature of the yarns

which occur at large shear angles, and other effects that relate to geometric nonlinearities that develop at large shear angles. We develop a representative geometry and associated constitutive laws that are as simple as possible in order to optimize computational efficiency.

2.2 Mechanics of an Anisotropic Planar Continuum

The fabric is represented as a two-dimensional anisotropic continuum where the yarns are not modeled explicitly; rather, the woven fabric is treated as a homogenized anisotropic material, as shown in Figure 2-1. In order for this continuum approximation to be meaningful, the characteristic length scale for the boundary value problem that is analyzed using this approach must be sufficiently large compared to the length scale of the fabric mesostructure, i.e. the distance between crossover points. We review the continuum mechanics that are necessary to describe the mechanical behavior of a two-dimensional anisotropic continuum.

The macroscopic state of deformation is described using the deformation gradient **F**, which is a tensor that describes the gradient of deformation with respect to reference configuration spatial coordinates. The components of **F** in a Cartesian coordinate systems are obtained as:

$$F_{jk}(t) = \frac{dx_j(t)}{dX_k}, \tag{2.1}$$

where $x_j(t)$ is the j-coordinate of a material point at time t, and X_j is the j-coordinate of that point in the reference configuration. Because we consider a two-dimensional continuum, $j,k \in \{1,2\}$. The deformation gradient has the useful property that it describes the transformation of material lines with deformation: a vector ${}^0\mathbf{a}$ that describes a material line in the reference configuration is transformed by deformation into a vector **a** according to:

$$\mathbf{a} = \mathbf{F}\ {}^0\mathbf{a}. \tag{2.2}$$

The deformed length a of this vector is given by:

$$a = \sqrt{\mathbf{a}\cdot\mathbf{a}} = \sqrt{\left(\mathbf{F}\ {}^0\mathbf{a}\right)\cdot\left(\mathbf{F}\ {}^0\mathbf{a}\right)} = \sqrt{{}^0\mathbf{a}\cdot\left(\mathbf{F}^{\mathrm{T}}\mathbf{F}\right){}^0\mathbf{a}}. \tag{2.3}$$

In this manner, the deformation gradient allows stretch and strain along a material line to be determined.

The angle θ between two intersecting material lines **a** and **b** can also be determined from the deformation gradient by taking the dot product of the two vectors in the deformed configuration:

$$\mathbf{a}\cdot\mathbf{b} = \left(\mathbf{F}\ {}^0\mathbf{a}\right)\cdot\left(\mathbf{F}\ {}^0\mathbf{b}\right) = ab\cos\theta. \tag{2.4}$$

This angle relates to the relative rotation of the two material lines and hence to the shear strain at the point where they intersect.

A commonly used stress measure is the Cauchy stress $\boldsymbol{\sigma}$. If a small surface with area dS within the deformed body is defined by a vector $\mathbf{n}dS$, where $\mathbf{n}$ is the unit normal to the surface, and the Cauchy stress in the body at that point is $\boldsymbol{\sigma}$, the traction force vector $\mathbf{t}$ that results from $\boldsymbol{\sigma}$ acting on dS is given by:

$$\mathbf{t} = \boldsymbol{\sigma}\mathbf{n}dS\,. \tag{2.5}$$

This stress measure that must be determined from the applied deformation history in order to define a continuum constitutive model.

An anisotropic material can be described using unit material vectors $\mathbf{g}$ that are oriented parallel to the material directions. In the case of a fabric, the material directions are the directions parallel to the yarn families within the fabric plane. We describe these directions using vectors $\mathbf{g}_1$ and $\mathbf{g}_2$, which give the in-plane orientations of the warp and weft yarn families respectively. Because these vectors are material lines, they transform according to Equation (2.2). Since their reference orientations are known, we can track the evolving anisotropy of the fabric with in-plane deformation.

One important requirement of any continuum constitutive law is that it must be "material frame indifferent", meaning that the functional relationship between stress and deformation must not depend on the frame of reference chosen by the observer. For an isotropic material, it can be shown that this requirement is satisfied as long as the stress depends only on histories of invariants of the stretch tensor $\mathbf{C} = \mathbf{F}^{\mathrm{T}}\mathbf{F}$:

$$\begin{aligned} \sigma &= \hat{\sigma}(I_1, I_2, I_3) \\ I_1 &\equiv \mathrm{tr}(\mathbf{C}) \\ I_2 &\equiv \mathrm{tr}(\mathbf{C})^2 - \mathrm{tr}(\mathbf{C}^2) \\ I_3 &\equiv \det(\mathbf{C}) \end{aligned}\,. \tag{2.6}$$

Equation (2.6) the invariants of $\mathbf{C}$ that are most commonly employed. Spencer [1971] shows that, for an anisotropic material with two preferred material directions (such as a fabric), material frame indifference will be satisfied in the hyperelastic limit (e.g. no slip) as long as the stress depends only on the invariants of $\mathbf{C}$ given in Equation (2.6) and on certain "pseudo" invariants of $\mathbf{C}$ and the reference configuration vectors ${}^0\mathbf{g}_1$ and ${}^0\mathbf{g}_2$ that are of the form given below:

$$\begin{aligned} I &= {}^0\mathbf{g}_i \cdot \mathbf{C}^n \; {}^0\mathbf{g}_j \\ n &\in \{0,1,2\} \end{aligned}\,. \tag{2.7}$$

Therefore, the constitutive law that determines stress $\boldsymbol{\sigma}$ from the deformation gradient $\mathbf{F}$ must employ only the invariants of the forms given in Equations (2.6) and (2.7).

2.3 Overview of Modeling Approach

Our objective is to relate the Cauchy stress σ to the macroscopic deformation gradient $\mathbf{F}$ in a manner that accurately reflects the behavior of the underlying fabric mesostructure (the yarns and the weave), and at the same time determine how the mesostructural configuration evolves and what meso-level forces (e.g. yarn tensions, contact forces between yarns, etc) develop in response to the macroscopically applied deformation. This is accomplished through a five step process:

1). Select a geometry that adequately represents the fabric mesostructure and define a characteristic unit cell. This geometry will not be explicitly represented in the continuum model, but rather provides a means of characterizing the mesostructural configuration using a set of state variables that can be stored at different locations within the continuum.

2). Determine physically motivated component constitutive relations that relate the deformations of the components of the mesostructure to the meso-level forces that evolve. For example, the yarns might behave in a linear elastic manner when stretched, so the yarn tension carried by a yarn truss in the unit cell geometry would be linearly related to the extension of that truss.

3). Establish a method for determining the geometric configuration of the fabric mesostructure from the macroscopic deformation gradient. At any given point in the continuum model the macroscopic deformation gradient is known. The evolved configuration of the fabric unit cell must be related to this macroscopic deformation gradient. This can be accomplished by enforcing equilibrium within the unit cell at the meso-level.

4). Calculate meso-level forces. Once the mesostructural configuration corresponding to a given macroscopic deformation measure has been determined, the meso-level forces that develop in the components of the unit call can be calculated from the component constitutive relations.

5). Finally, transform these meso-level forces into continuum stresses at the macroscopic scale. Although the meso-level forces are themselves of interest (e.g. to predict failures such as yarn breakages or crushing of embedded components by locking forces), a complete continuum model requires that continuum stresses be calculated from the macroscopic deformation gradient. Meso-level forces can be converted into equivalent continuum stresses by finding the stress tensor that generates tractions on

the unit cell boundaries that equal the net effect of the meso-level forces on those boundaries.

This approach is sufficiently general to permit the development of models appropriate for a wide variety of applications. The geometry and constitutive relations chosen in the first two steps control which mechanisms a model can capture and how accurately the model will capture those mechanisms. More sophisticated geometries and more complex, physically realistic constitutive laws will yield more accurate fabric models, at the cost of increased computational cost. Hence these choices can be used to tailor the model to specific applications where particular mechanisms may be of greater or lesser importance.

2.4 Unit Cell Geometry

The initial model is intended to simulate a plain weave ballistic Kevlar® fabric manufactured by DuPont, Inc., designated as fabric style S706. The model is validated against experiments performed on this fabric. The geometry of the weave mesostructure of the particular Kevlar® fabric to be modeled is shown in Figure 2-2. This image was created by embedding unloaded fabric samples in epoxy, sectioning the samples, and photographing them under an optical microscope. These images show that the yarn cross sections have an approximately oval shape and that the weave geometry differs for the two yarn families (the weft yarn families have greater initial crimp amplitudes). Unfortunately, quantitative measurements of the weave geometric parameters cannot be obtained from such images, because the precise location and orientation of the sectioning plane is unknown. However, most of the relevant geometric parameters (yarn spacing, crimp amplitude, fabric thickness, yarn length per unit cell, crimp angle, yarn family orientations) can be determined through macroscopic measurements (see King [2003] for more details). Other parameters, such as the major radii of the yarns, can be estimated from images such as these in conjunction with other macroscopic and microscopic measurements.

We represent this weave mesostructure using a truss geometry similar to that proposed by Kawabata [1973], shown in Figure 2-3. The yarns are represented as a network of trusses connected by pin-joints at their crossover points. These trusses do not lie in the plane of the fabric but are interwoven to capture crimp interchange. They have axial compliance to allow for yarn stretch but are infinitely stiff in bending. The effects of yarn bending are modeled as being concentrated at the crossover points, where the trusses are hinged and bending is resisted by rotational "bending springs". Interactions between yarns at the crossover points are captured by vertical "crossover springs" connecting the truss hinges. The crossover springs have two modes

of deformation. They are capable of extending and contracting to simulate the effects of cross-sectional deformation, which allows the yarns to change their crimp amplitude while remaining in contact. The crossover spring elements also offer elastic and inelastic resistance to relative in-plane rotation of the yarn families—the mechanisms by which fabrics accommodate in-plane shear. Similar truss networks has been used by a number of different authors, such as Ben Boubaker *et al.* [2002], to represent fabric mesostructural geometries.

This geometric representation is somewhat simplistic. Its chief limitation is that it models the yarns as straight with sharp corners at the crossover points, whereas the yarns actually wrap around the crossing yarns with a smooth radius of curvature. This geometry consequently permits configurations that are incompatible because of interpenetrations between the yarns, and cannot capture complex behaviors that are controlled by yarn wrapping effects. However, the effects of wrapping become significant only in very tight weaves with solid yarns, or at very large shear angles. For the specific Kevlar® fabric and load cases considered here, where the yarns are composed of multiple fibers and the shear angles are typically small to moderate, wrapping effects do not impact the fabric response significantly. The proposed geometric description therefore is adequate for capturing the relevant behaviors and is more computationally efficient than more sophisticated geometric descriptions. This modeling approach can be extended to other applications by selecting more suitable geometric descriptions capable of capturing behaviors relevant to those applications.

Kevlar® fabrics exhibit locking behavior, where yarns of one family jam against yarns of the other family either due to large shear deformations or to crimp interchange. When the yarns jam, their cross sections deform. The model geometry does not track changes in the size or shape of the yarn cross sections; however, locking effects are accounted for by introducing truss elements that are oriented normal to the yarns, shown in Figure 2-4. The forces carried by these locking trusses simulate the contact forces between the yarns and resist increasing deformations when locking conditions are met.

The configuration of the weave mesostructure is described by the parameters shown in Figure 2-3 and Figure 2-4:

- the quarter-wavelengths p_i (half the spacing between yarns),
- the yarn length per quarter-wavelength, hereafter referred to simply as "yarn lengths" L_i (half the yarn length between adjacent crossover points),
- the crimp angles β_i,
- the crimp amplitudes A_i,
- the locking truss lengths d_i,

- the angles α_i that the locking trusses make with the fabric plane, and
- the in-plane included angle between the yarn families θ.

We have adopted the convention that the subscript "i" designates the yarn family—1 for the warp yarns and 2 for the weft yarns. Several of these parameters are related through geometric constraints, so that of the thirteen parameters listed, only five are independent. For example, amplitude and crimp angle can be related to wavelength and yarn length through the following expressions:

$$A_i = \sqrt{L_i^2 - p_i^2}\ . \tag{2.8}$$

$$\cos\beta_i = \frac{p_i}{L_i}. \tag{2.9}$$

The locking parameters d_i and α_i can be related to the L_i and p_i through significantly more complex relationships:

$$d_i = \sqrt{p_i^2 \sin^2\theta + A_j^2 \xi_j^2} \quad \text{for } (i,j) \in \{1,2\},\ i \neq j, \tag{2.10}$$

$$\alpha_i = \tan^{-1}\left(\frac{A_j \xi_j}{p_i \sin\theta}\right), \tag{2.11}$$

with

$$\xi_j \equiv \left|1 - \frac{|p_i \cos\theta|}{p_j}\right| \quad \text{for } |p_i \cos\theta| \leq 2p_j. \tag{2.12}$$

No summation is implied by repeated indices. For more details, refer to King [2003]. The configuration of the weave mesostructure can therefore be completely determined from just the two wavelengths p_i, the two yarn lengths L_i, and the yarn angle θ. It should be noted that this selection of five independent parameters is not unique; for example, the two crimp amplitudes A_i could be used as independent parameters instead of the yarn lengths L_i. The most convenient set of independent parameters should be selected.

The reference configuration values of these geometric parameters for Kevlar® S706 are given in Table 2-1.

2.5 Component Constitutive Relations

Constitutive relations relate the forces that develop in the components of the unit cell to changes in the mesostructural configuration that are brought about by macroscopically imposed deformation. A constitutive relation is required for possible mode of deformation of the unit cell

components: eight are necessary for the geometry described in the preceding section. Two describe the response to extension of the yarn trusses. Two describe the response of the rotational bending springs at the crossover points. Two describe the responses of the contact spring. And two describe the response of the locking trusses to compression.

Once uncrimped, Kevlar® yarns generally exhibit linear elastic behavior up to failure. Therefore, the model uses linear elastic relations to describe yarn extension from an initial length ${}^0L_i$ to a deformed length L_i:

$$T_i = k_i\left(L_i - {}^0L_i\right), \tag{2.13}$$

where T_i is the tensile force in the trusses representing the yarns of the i^{th} family and k_i is the stiffness of the yarn segments in the unit cell (which may depend on the yarn family). Some sources (e.g. Shim *et al.* [2001]) suggest that Kevlar® may display rate dependent behavior at large strain rates (greater than 100 s^{-1}). While we do not consider rate dependence of the yarn extension, it could be readily included in the model by changing this constitutive relation. The yarn axial stiffnesses k_i can be determined from tension tests performed on single yarns. Figure 2-5 shows the results of tests on single weft yarns removed from Kevlar® S706, performed using a Zwick tensile tester model BTC-FR010TH.A50. These tests were conducted under quasi-static loading conditions with a strain rate of $0.01s^{-1}$. Because the yarns used in this test had been removed from a woven fabric sample, they were initially crimped rather than straight in the unloaded configuration. Consequently, the load-extension response shows an initially compliant regime as the yarns straighten, followed by a linear elastic response up to a failure load of approximately 90 N. Warp yarns behaved in a similar manner but with a shorter compliant response due to less initial crimp, and a larger average breaking load of approximately 105 N, probably due to the fact that these yarns are damaged less during the weaving process. The axial stiffness of the yarns is calculated from the slope of the linear portion of these curves and is reported in Table 2-1.

Although the yarn bending stiffnesses are relatively small, under loading conditions where crimp interchange can occur yarn bending is the dominant mechanism that resists deformation, until locking forces begin to develop or until the yarns completely straighten. Therefore, yarn bending resistance must be included in order to guarantee a nonzero stiffness at small strains. For the selected geometry, bending is modeled as concentrated at the hinges between yarn trusses at the crossover points. Bending resistance is imparted through rotational springs at these points and is assumed to be linear elastic, with the bending moment M_{bi} exerted on the yarns at the crossover points proportional to the change in the crimp angle β_i:

$$M_{bi} = k_{bi}\left(\beta_i - {}^0\beta_i\right). \tag{2.14}$$

If necessary, the unloaded crimp angle ${}^0\beta_i$ can be adjusted to account for different amounts of permanent set in the yarns. A reasonable estimate of the bending stiffnesses k_{bi} can be determined by manipulating the load-extension data from the single yarn tests shown in Figure 2-5. In the uncrimping (low load) regime, the load-extension data can be converted into moment-crimp angle data provided the initial yarn crimp is known (it can be measured by examining the yarns under a microscope). This allows the moment acting at the crimp peaks to be expressed as a function of the crimp angle, and the slope of this resulting curve corresponds to k_{bi}. In Chapter 3 we discuss more accurate methods for characterizing the yarn bending stiffnesses, which indicate effective rotational spring stiffnesses that are reasonably close to those measured using this method. The measured stiffnesses reported in Table 2-1 are so small that they have a negligible effect on the response of the fabric once the yarns begin to stretch, but they are sufficiently large to impart nonzero stiffness to the model in the low-stress regime.

Relations describing interactions between yarns at the crossover points are generally difficult both to measure and to model at the macroscopic level, since they involve interactions between yarn fibers at a very small scale. In general, the deformations of the yarn cross sections depend nonlinearly on the contacting force between yarns and possibly on other parameters, such as the relative diameters and angles of the crossing yarns and the tensions carried by the yarns. The model adopts a significant simplification: the through-thickness compression of the yarns due to cross sectional deformations at the crossover points is captured by a nonlinear crossover spring that separates the crossing yarn trusses. This spring simulates soft contact conditions, with negligible stiffness in tension and an initially compliant compressive response that becomes increasingly stiff as the distance between yarn centers decreases. An exponential relation with two material parameters K_I and a has been chosen to capture this behavior:

$$F_I = K_I\left(e^{aI} - 1\right). \tag{2.15}$$

Here I is the interference that would exist between the cross sections of the crossing yarns if they remained undeformed. It is defined to be the sum of the initial crimp amplitudes (one half of the fabric thickness) minus the sum of the current crimp amplitudes.

This interference relation is fairly simplistic. A number of researchers, such as Chen *et al.* [2001], Realff [1992], and Realff *et al.* [1997], have shown that yarn interactions at the crossover points are more accurately described by far more complex relations. They have proposed models to capture these interactions that include additional dependencies such as yarn tension or that represent the interactions through distributed pressures rather than point loads. More sophisticated

relations would allow more accurate predictions of changes to the fabric thickness and of the fabric response to transverse pressure loads. However, the effects of these more sophisticated relations on the in-plane response of Kevlar® S706 to in-plane loads are expected to be small.

We attempted to measure the parameters K_I and a using a "sandwich compression test", shown schematically in Figure 2-6. It was believed that through thickness compression would approximately reproduce the cross sectional deformations that occur when the yarns compress against one another at the crossover points. Unfortunately, the material properties measured in this manner are excessively compliant compared to the other measured stiffnesses, which causes the model to predict that the yarn cross sections will almost completely pass through one another rather than cause crimp interchange to occur. We hypothesize that the excessive compliance measured in this test is due to many modes of deformation other than cross sectional compaction at the crossover points that allow the fabric to accommodate the macroscopically applied transverse compression. Additionally, the yarns may be more resistant to cross sectional compaction when under tension than they are in this test. In order to obtain a physically realistic response, it was necessary to scale the values of K_I and a. The values selected for the scaled properties are given in Table 2-1. Because actual displacements associated with cross sectional compaction are small, the model is relatively insensitive to these parameters, as long as they are sufficiently large to cause crimp interchange to occur.

The remaining component constitutive relations all control how the fabric responds to in-plane shear deformation (although the relations that describe locking also can affect in-plane deformations that do not involve shear in a tightly woven fabric). In-plane shear is accommodated in fabrics by relative rotation of the yarn families at the crossover points, sometimes known as "trellising". A large number of works concerning the experimentally measured shear response of woven materials appear in literature: for example, the works of Mohammed *et al.* [2000] and Peng *et al.* [2004]. Fabrics typically can exhibit three regimes of shear behavior, shown in Figure 2-7. Loads build rapidly through a stiff elastic regime, which is followed by a far more compliant regime in which the yarns rotate significantly relative to one another. During much of this regime, the resisting forces increase only slightly if at all, and the majority of the energy that is used to deform the fabric is dissipated through frictional effects. If the load is removed, only a small amount of deformation is elastically recovered. As the relative yarn rotation angle becomes large, the response becomes increasingly stiff and more energy is stored elastically. This is due primarily to locking or wrapping effects. Finally, the locking forces and corresponding stresses become very large, and some other mode of deformation (such as unraveling of the weave or out-of-plane wrinkling) occurs.

We have identified two mechanisms that accommodate trellising, shown schematically in Figure 2-8. Some of the total, macroscopically observed shear angle γ is accommodated by S-shaped bending of the yarns between crossover points; we expect this mechanism to be resisted elastically and designate this component of the total yarn rotation angle to be γ_e. The rest of the rotation angle must be accommodated by relative rotation of the yarns at the crossover points themselves, which is resisted primarily by friction and therefore is a dissipative mechanism; we designate this component of the yarn rotation angle to be γ_f. The total rotation angle will be the sum of these angles:

$$\gamma = \gamma_e + \gamma_f . \tag{2.16}$$

Changes in these angles are driven by the same applied moment M, which describes the total resistance of the fabric to trellising in the absence of locking. As shear angles become large, locking will provide additional resistance. In order to cause shear deformation, the total macroscopically applied load must be sufficient to overcome both the locking resistance to shear deformation and the effective resistance of these two mechanisms that accommodate trellising, as shown in Figure 2-9.

Before the static frictional resistance to rotation has been overcome, no relative rotation at the crossover points can occur and all changes in rotation angle must be accommodated by the s-bending between the crossover points. At small shear angles, resistance from locking is generally negligible. Therefore, the initially stiff elastic regime in the experimentally observed shear behavior is dominated by the S-bending effect. Experiments indicate that the shear response over this small elastic region is approximately linear:

$$M = K_s \gamma_e . \tag{2.17}$$

The elastic stiffness K_s is generally so large enough that the moment M increases rapidly and quickly exceeds static frictional resistance to yarn rotation at the crossover points, and hence the dissipative rotation initiates at very small shear angles (on the order of 10^{-2} rad). We represent the resistance to dissipative rotation with a rate-dependent power law, with $\dot{\gamma}_0$ giving the reference dissipative rotation rate at some reference moment M_0, and an exponent b capturing the rate sensitivity of the dissipative shear behavior:

$$\dot{\gamma}_f = \dot{\gamma}_0 \left(\frac{|M|}{M_0} \right)^b \operatorname{sign}(M). \tag{2.18}$$

Once the static frictional resistance has been overcome, a constant rotation rate can be supported by a constant applied moment M, and hence the rotation angle due to "S"-bending γ_e will also

remain constant. This accounts for the flat portion of the shear response in the middle regime. As shear angles become large, locking forces will begin to increase, which accounts for the ultimate stiffening of the shear response. The parameters in these expressions may exhibit dependencies on the fabric state (e.g., frictional resistance to rotation may be greater when the contact forces between yarns are higher). For simplicity, they are treated as constant material properties, although further dependencies could be included if necessary.

At large shear angles, the locking response dominates. When the fabric locks, the yarns jam against each other and their cross sections are forced deform in order to avoid interfering with one another. Hence locking involves cross sectional compaction. However, the ovalized yarns in Kevlar® S706 typically deform along their longer cross sectional axis (parallel to the fabric plane) during locking, as opposed to the shorter axis (through the fabric thickness). Consequently, the locking response is more compliant than the through-thickness compaction response discussed above. A power law relation is used to describe the compressive force F_L that develops in the locking trusses when their length has been shortened by an amount I_L:

$$F_L = \begin{cases} 0 & I_L \le 0 \\ K_d (I_L)^c & 0 < I_L \end{cases}, \tag{2.19}$$

with $I_L = d_0 - d$, where d is the length of the locking truss and d_0, the length of the truss when locking first starts to occur, depends on the initial geometry of the yarn cross sections and the weave. The locking trusses have no stiffness in tension. The coefficient K_d and the exponent c are two material parameters that, together with d_0, determine the locking behavior. Like some other relations used in this model, this relation is somewhat simplistic, but it has proved effective for the particular fabric and load cases that we have examined.

The material parameters associated with trellising and locking are among the most difficult to determine, since they involve complex interactions between yarns that are essentially bundles of fibers, compressing against one another and rotating past one another in irregular geometries. Although detailed finite element modeling of individual fibers might provide an accurate means of determining these parameters, they can also be determined by examining the shear response of the fabric.

The shear response of the fabric is measured using a "shear-frame" apparatus similar to that described by McGuinness *et al.* [1997] and others (e.g., Mohammed et al. [2000] and Peng *et al.* [2004]). The shear frame is a rhomboidal fixture with hinged corners, shown in Figure 2-10, that grips a square or cruciform specimen of fabric with its yarns aligned parallel to the frame sides. Our specimens were 29.0 cm square. Diagonally opposite corners of the shear frame are pulled apart using the Zwick tensile tester. This subjects the fabric to a state of nearly pure yarn rotation,

with negligible extension along the yarn directions, until the onset of out-of-plane wrinkling at large shear angles. Cruciform samples exhibit less wrinkling.

Most of these tests were conducted at an axial displacement rate of 30mm/min, which corresponds to an initial yarn rotation rate of approximately 2.83×10^{-3} rad/s. All of the shear-related properties and locking properties were determined at this rate (except for the rate sensitivity exponent in Equation (2.18), which required tests at a variety of different rates).

The results of these tests are shown in Figure 2-11. Because the different resistance mechanisms dominate different portions of the response, the material parameters could be readily determined. The elastic stiffness associated with "S"-bending, K_s, relates to the initial slope of the response curve. The reference rotation rate $\dot{\gamma}_0$ and reference moment M_0 relate to the rotation rate imposed in the test and the load at which the response flattens, respectively. The rate sensitivity exponent b relates to how much this load varies when the test is conducted at different rates. The yarn major radii R_i, which control the initial length of the locking trusses d_0, relate to the amount of shear that occurs before the response starts to significantly stiffen due to locking, and the locking truss constitutive parameters K_d and c relate to the stiffening rate and non-linearity of the response at large shear angles. Geometric complexities prevent these parameters from being directly extracted from the response curves. By simulating the shear frame tests using the model and varying each property in turn, the appropriate portion of the predicted response can be fitted to the experimental data and the locking and yarn rotation properties can be determined. The fitted properties are given in Table 2-1.

2.6 Relating Continuum Deformation to Mesostructural Evolution

The geometric and constitutive relations characterize the behavior of the fabric mesostructure, but in a continuum model the mesostructural behavior must be related to the behavior of the macroscopic continuum. A means of determining the weave mesostructural configuration from the state of deformation of the macroscopic continuum is required. For the selected geometry, five independent parameters are required to characterize the fabric configuration at a given location. A convenient set consists of the quarter wavelengths p_i and the angle between yarn families θ (which describe the amount of stretch and shear, respectively, that the unit cell has undergone), and the yarn lengths L_i (which relate to stretch of the yarns and the change in their crimp). More complicated geometries, especially those used to represent different weave patterns (e.g. twill or satin weaves) would require more independent parameters.

At the continuum level, the yarn families can be described by vectors that are aligned with the yarns and that connect adjacent crossover points. These vectors will have magnitudes equal to $2p_i$, twice quarter wavelengths, and describe the dimensions of the unit cell measured along the yarn family directions, as is shown in Figure 2-3. The angle between these vectors is θ, the angle between the yarn families. Under the assumption that no yarn slip occurs, the crossover points deform in an affine manner with the continuum and hence these vectors are material lines and transform with the deformation gradient according to Equation (2.2). Three parameters—the quarter wavelengths p_i and the angle θ between the yarn families—can therefore determined directly from the deformation gradient:

$$p_i = \sqrt{\mathbf{F}^0\mathbf{p}_i \cdot \mathbf{F}^0\mathbf{p}_i} = {}^0p_i\sqrt{{}^0\mathbf{g}_i \cdot \left(\mathbf{F}^T\mathbf{F}\right)^0\mathbf{g}_i}\,. \tag{2.20}$$

$$\cos\theta = \frac{\mathbf{p}_1 \cdot \mathbf{p}_2}{p_1 p_2} = \frac{\mathbf{F}^0\mathbf{p}_1 \cdot \mathbf{F}^0\mathbf{p}_2}{p_1 p_2} = \frac{{}^0p_1\,{}^0p_2\,{}^0\mathbf{g}_1 \cdot \left(\mathbf{F}^T\mathbf{F}\right)^0\mathbf{g}_2}{p_1 p_2}\,. \tag{2.21}$$

Note that the p_i and θ depend only on pseudo-invariants of $\mathbf{C} = \mathbf{F}^T\mathbf{F}$, ${}^0\mathbf{g}_1$, and ${}^0\mathbf{g}_2$ that are of the form given in Equation (2.7). Therefore, the relation between the macroscopic deformation gradient and the evolution of the weave mesostructure that forms the basis of the constitutive law will satisfy material frame indifference.

The deformation gradient does not directly determine the other independent parameters required to characterize the fabric configuration. With only the wavelengths p_i and yarn angle θ fixed, an infinite number of configurations are possible with varying yarn lengths L_i of the two families, as is shown in Figure 2-12. In a quasi-static case, the mesostructure will adopt the configuration that satisfies through-thickness equilibrium, where the through-thickness forces exerted by one yarn family equals the through-thickness force exerted by the other yarn family. For this model, the equilibrium configuration can be found by using energy-based arguments.

As the two free parameters are varied, the yarns undergo different degrees of stretch and crimp, and the locking trusses and contact spring are compressed by different degrees. Hence, the remaining parameters control the balance between the elastic energy stored in the unit cell through yarn extension, yarn bending, and locking in each of the two families, and the elastic energy stored in the crossover spring. Every possible configuration will correspond to a particular level of total elastic energy stored within the unit cell. For a given state of macroscopic deformation, the fabric will assume the configuration with the smallest stored elastic energy, subject to the constraint that the configuration must satisfy the requirements imposed by the macroscopic deformation gradient—i.e. the configuration must have the appropriate values of p_1, p_2 and θ. This minimum energy configuration will satisfy through-thickness equilibrium.

In this model there are only two free parameters, L_1 and L_2, and the elastic energy stored in the unit cell for a given macroscopically imposed deformation gradient $\mathbf{F}$ can be visualized as a function of these parameters, as shown in Figure 2-13. We refer to this function as a "conditional energy function" because it depends on the deformation gradient. The values of the free parameters L_1 and L_2 that minimize this energy function while the parameters fixed by the deformation gradient are held constant will describe the equilibrium configuration that the mesostructure will adopt. In most cases, numerical techniques are necessary to minimize the conditional energy function, as a closed form for the state of minimum energy does not exist. Refer to King [2003] for a more detailed description of this energy minimization method.

More complicated representative geometries (e.g. geometries used to represent other weave patterns, such as twill and satin weaves) may have a larger number of free parameters. At this time we have not considered in detail any geometry other than that shown in Figure 2-3.

One final comment must be made with regard to dissipative deformation mechanisms and rate-dependent effects. In this model, different possible configurations corresponding to various values of the free parameters L_i can all be instantaneously adopted through purely elastic deformation mechanisms, and so the only constraint on these configurations is that they must be consistent with the applied macroscopic deformation gradient. However, in more sophisticated models, different configurations may be accommodated through rate-dependent dissipative deformation mechanisms. Examples of such models include those with elastic-viscoplastic yarns where the tension depends not only on their extension but also on the extension rate, or with visco-elastic yarn cross section behavior that leads to energy dissipation during the locking process, described in Appendix A. In these cases, there is an additional constraint on the configurations that the mesostructure may adopt—the configuration must be reached by an evolution path that satisfies the appropriate equations of state. Finding the mesostructural configuration that satisfies equilibrium in such situations is more challenging.

2.7 Relating Meso-level Forces to Macroscopic Stress

Once the mesostructural configuration that corresponds to a given deformation gradient has been determined, the internal forces carried by the unit cell components, including yarn tensions, yarn bending moments, moments between yarns at the crossover point, and contact forces at the crossover point and from locking, can be calculated from the component constitutive relations. In many cases, these forces may themselves be of interest, especially for predicting the onset of failure. For example, embedded components in advanced fabric systems may be crushed by

excessive contact forces. Or, the yarn tensions may be used to predict what level of macroscopic load will cause the yarns to break. However, in order to completely describe the constitutive behavior of the fabric continuum, these internal forces must be transformed into equivalent macroscopic continuum stresses.

For traditional hyperelastic material models that have a well defined strain energy density function ϕ that depends only on invariants of $\mathbf{C}$ and pseudo-invariants of $\mathbf{C}$ and ${}^0\mathbf{g}_i$, the Cauchy stress σ at the continuum level can be calculated from by differentiating the strain energy density function with respect to the stretch tensor $\mathbf{C}$:

$$\mathbf{S} = 2\frac{\partial \phi}{\partial \mathbf{C}} = 2\sum_k \frac{\partial \phi}{\partial I_k}\frac{\partial I_k}{\partial \mathbf{C}}. \qquad (2.22)$$
$$\boldsymbol{\sigma} = J^{-1}\mathbf{F}\mathbf{S}\mathbf{F}^{\mathrm{T}}$$

Here I_k are the invariants and pseudo-invariants, $\mathbf{F}$ is the deformation gradient, and J is the determinant of $\mathbf{F}$. Note that ϕ is the traditional strain energy density function, not the conditional energy function discussed in the previous section. The strain energy density at any deformation gradient $\mathbf{F}$ corresponds to the minimum value of the conditional energy function per unit reference volume, minimized over all admissible configurations consistent with $\mathbf{F}$. For a very simple fabric model where ϕ can be calculated exactly as a function of $\mathbf{F}$, this approach can be used to calculate the stress. For example, consider a simplified fabric-like model with no crimp interchange, locking, or dissipative yarn rotation, zero crimp in both yarn families, and linear elastic relations relating yarn extension to force F carried by the yarns, and relating relative yarn rotation to moment M between yarn families. The relative component constitutive relations in this case are:

$$F_i = k_i\left(p_i - {}^0p_i\right), \qquad (2.23)$$

$$M = K_s\left({}^0\theta - \theta\right), \qquad (2.24)$$

where k_i are the stiffnesses associated with each yarn segment in the unit cell, and K_s is the elastic shear stiffness (clockwise rotation of the 2-direction yarn family relative to the 1-yarn family is defined as positive). Since p_1, p_2, and θ depend only on $\mathbf{F}$, the mesostructural configuration of this simplified fabric depends only on $\mathbf{F}$ and hence has an energy density function ϕ that can be expressed in closed form:

$$\phi = \frac{1}{8\,{}^0p_1\,{}^0p_2}\left\{k_1\left(p_1 - {}^0p_1\right)^2 + k_2\left(p_2 - {}^0p_2\right)^2 + K_s\left({}^0\theta - \theta\right)^2\right\}. \qquad (2.25)$$

When p_1, p_2, and θ are expressed in terms of invariants of the form given in Equation (2.7)

according to Equations (2.20) and (2.21), Equation (2.22) can be used to calculate $\boldsymbol{\sigma}$ exactly. It can be shown that the Cauchy stress in this case is:

$$\begin{aligned}\boldsymbol{\sigma} = &\frac{1}{2p_2 \sin\theta}\left(F_1 - \frac{M\cos\theta}{2p_1 \sin\theta}\right)(\mathbf{g}_1 \otimes \mathbf{g}_1) \\ &+ \frac{1}{2p_1 \sin\theta}\left(F_2 - \frac{M\cos\theta}{2p_2 \sin\theta}\right)(\mathbf{g}_2 \otimes \mathbf{g}_2) \\ &+ \frac{M}{4p_1 p_2 \sin^2\theta}(\mathbf{g}_1 \otimes \mathbf{g}_2 + \mathbf{g}_2 \otimes \mathbf{g}_1)\end{aligned} \quad . \tag{2.26}$$

Each term corresponds to the effects of one of the three meso-level forces F_1, F_2, and M acting on the unit cell faces, as is shown in Figure 2-14. Each yarn force F_i acts along a yarn direction $\mathbf{g}_i$. The distance between yarns measured in a direction normal to $\mathbf{g}_i$ is $2p_j \sin\theta$, where $j \neq i$, so the force is divided by this quantity to give force per unit width. Unit thickness is assumed. The moment M exerts a traction $F_{Mi} = M/2p_i$ on each of the four unit cell faces, but these tractions act normal to the directions $\mathbf{g}_i$. In order to be expressed in terms of $\mathbf{g}_i \otimes \mathbf{g}_j$ tensor products, these forces from the moments must be resolved along directions parallel to $\mathbf{g}_1$ and $\mathbf{g}_2$, which requires additional $\sin\theta$ and $\cos\theta$ factors. We note that when this stress tensor is applied to any of the unit cell faces intersected by the i^{th} yarn family using Equation (2.5), the resulting traction exactly equals the net effect of F_i and F_{Mi} acting on that face.

Unfortunately, this approach cannot be used in cases where the strain energy function cannot be expressed in a closed analytical form. This is the case for the proposed model because the mesostructural configuration, and hence the energy stored per unit volume, is not directly determined by the deformation gradient—the additional free parameters L_i must be determined numerically, as described in King [2003]. Instead, the continuum stress can be determined from the meso-level forces using equilibrium arguments. The macroscopic Cauchy stress $\boldsymbol{\sigma}$ that is equivalent to a set of meso-level forces must exert a traction on a unit cell face that equals the net effect of the meso-level forces acting on that face. Therefore, the Cauchy stress must always have the general form:

$$\boldsymbol{\sigma} = N_1(\mathbf{g}_1 \otimes \mathbf{g}_1) + N_2(\mathbf{g}_2 \otimes \mathbf{g}_2) + S_{12}(\mathbf{g}_1 \otimes \mathbf{g}_2 + \mathbf{g}_2 \otimes \mathbf{g}_1). \tag{2.27}$$

Here N_1 and N_2 are the total meso-level forces per unit width and thickness that operate along the yarn directions (parallel to the fabric midsurface), and S_{12} is the total shear force (per unit width and thickness) acting on the unit cell faces (also parallel to the fabric midsurface) that counteracts any moment between the yarn families. It can be proved that as long as the unit cell components

are in local equilibrium, the stress tensor will be symmetric, and that the out-of-plane components of the meso-level forces will cancel.

For the actual fabric model, we must use this equilibrium approach to determine the stress. The stress tensor is determined according to the following procedure:

1. Determine all load-bearing mesostructural components that intersect the boundaries of the unit cell.
2. Determine the tractions that these components exert on the unit cell faces, including the effects of any moments that are carried by the components.
3. Project these tractions onto a plane parallel to the midsurface of the fabric. The out-of-plane components will cancel.
4. Resolve the projected tractions along the $\mathbf{g}_1$ and $\mathbf{g}_2$ vectors.
5. Divide the resolved forces by the appropriate projected areas to obtain stresses. Express the results in the tensorial form given in Equation (2.27).

Note that this process could have been used to obtain the stress tensor for the simplified model; it yields the same expression given in Equation (2.26) that was calculated from Equation (2.22). The stress tensor for the actual Kevlar® S706 fabric model is more complex; it has contributions from yarn tensions T_i, yarn bending moments M_{bi}, the locking forces F_{Li}, and the moment between the yarn families M:

$$\begin{aligned}\boldsymbol{\sigma} = &\frac{1}{2p_2\sin\theta}\left(\begin{array}{l} T_1\cos\beta_1 - \dfrac{M_{b1}\sin\beta_1}{L_1} - \dfrac{M\cos\theta}{2p_1\sin\theta} - \dfrac{F_{L1}p_1}{d_1} \\ -F_{L2}\left(\dfrac{{p_2}^2\cos^2\theta}{p_1 d_2} + \dfrac{p_2\sin\alpha_2|\cos\theta|\sin\beta_1}{L_1}\right)\end{array}\right)(\mathbf{g}_1\otimes\mathbf{g}_1) \\ &+\frac{1}{2p_1\sin\theta}\left(\begin{array}{l} T_2\cos\beta_2 - \dfrac{M_{b2}\sin\beta_2}{L_2} - \dfrac{M\cos\theta}{2p_2\sin\theta} - \dfrac{F_{L2}p_2}{d_2} \\ -F_{L1}\left(\dfrac{{p_1}^2\cos^2\theta}{p_2 d_1} + \dfrac{p_1\sin\alpha_1|\cos\theta|\sin\beta_2}{L_2}\right)\end{array}\right)(\mathbf{g}_2\otimes\mathbf{g}_2)\cdot \\ &+\left(\frac{M}{4p_1p_2\sin^2\theta} + \frac{F_{L1}p_1\cos\theta}{2p_2d_1\sin\theta} + \frac{F_{L2}p_2\cos\theta}{2p_1d_2\sin\theta}\right)(\mathbf{g}_1\otimes\mathbf{g}_2 + \mathbf{g}_2\otimes\mathbf{g}_1)\end{aligned} \tag{2.28}$$

The stress expression does not involve the force that compresses the crossover spring, since this spring does not intersect the unit cell faces In addition to the force parameters, the stress expression also contains geometrical parameters that describe the current configuration of the unit cell.

2.8 Implementation and Numerical Issues

The Kevlar® S706 fabric model was implemented into ABAQUS/Standard, a commercially available implicit finite element code, through a user-defined material "UMAT" subroutine. ABAQUS solves nonlinear problems by using a Newton-Rhapson iteration scheme to find the equilibrium solution at the end of each time increment. For each integration point in the finite element mesh, the UMAT is called and is supplied with the deformation gradients $\mathbf{F}(t)$ and $\mathbf{F}(t + \Delta t)$ at the beginning and the end of the time increment respectively, and also the values of all state variables at the beginning of the increment. The UMAT must calculate the Cauchy stress σ at the end of the time increment, and also the updated values of the state variables at the end of the increment (which are used to track and output the evolving configuration of the unit cell). The Newton-Rhapson scheme also requires the material Jacobian $d\sigma/d\mathbf{E}_t$ to be calculated, which gives the variations of the stress σ that result from variations of the incremental strain $\mathbf{E}_t$. ABAQUS uses a small strain measure for the incremental strain:

$$\mathbf{E}_t = \frac{1}{2}\left(\mathbf{F}_t + \mathbf{F}_t^T\right) - \mathbf{1}, \tag{2.29}$$

where the incremental deformation gradient $\mathbf{F}_t$ describes the change in deformation at the end of the time increment (at time $t + \Delta t$) relative to the state of deformation at the beginning of the time increment (at time t):

$$\mathbf{F}(t + \Delta t) = \mathbf{F}_t \mathbf{F}(t). \tag{2.30}$$

This model was limited to in-plane, quasi-static analyses only. Issues related to the numerical implementation of the model are briefly discussed in this section.

The minimization of the conditional energy function that relates the deformation gradient to the fabric mesostructural configuration must be performed numerically because no closed form exists for the conditional energy function due to the complexity of the model geometry. Various numerical minimization schemes were investigated. For a detailed description of these techniques, refer to King [2003] and to Press *et al.* [1992]. Of these techniques, the downhill simplex technique was found to be the most effective for the current model, partly because it does not require derivatives of the conditional energy function. For different unit cell geometries, other numerical minimization techniques might prove more effective.

Steigmann [1992], Baseau [2003], and others have shown that an un-reinforced elastic network, like the Kevlar® S706 fabric model, is mathematically guaranteed to be stable only as long as the network is in tension. Even when the fabric continuum is constrained to remain planar, the fabric geometry chosen for the current model is unstable and capable of buckling

when placed in compression. For the unit cell geometry considered, two modes of buckling are possible: the yarn trusses can bend at the crossover points and rotate out of the fabric plane, increasing their crimp (subsequently referred to as "yarn buckling"); or they can rotate about axes perpendicular to the fabric plane, causing a shearing motion of the fabric (subsequently referred to as "shear buckling"). These buckling modes are shown in Figure 2-15, and can lead to instabilities that prevent convergence during a nonlinear quasi-static analysis using an implicit finite element code, since quasi-static implicit codes do not include the stabilizing effects of inertia.

A related shortcoming of the continuum fabric model is that it does not explicitly represent the internal material structure, so inertial effects associated with the rotational motions of mesostructural components are not accounted for in the mass matrix used in dynamic analyses. The continuum model tracks the inertia associated with motions of the centers of mass of the yarns, but not the inertia associated with rotation of the yarn trusses. Hence the continuum mass matrix will underestimate the intertia of the fabric.

These issues can be both addressed by the explicit addition of inertial resistance to yarn rotation at the meso-level. The changes in orientation of the yarn trusses over a given time increment in can be divided by the length of that time increment to determine average rotational velocities, and the change in velocity can be divided by the same time increment to approximate average rotational accelerations. These accelerations are then multiplied by the rotational inertias of the yarn segments about appropriate axes to yield reaction moments, which can then be converted into effective forces at the unit cell faces and included in the stress along with the quasi-statically determined meso-level forces. This procedure stabilizes the buckling modes in quasi-static implicit analyses and accounts for the additional rotational inertia of the yarn segments in dynamic analyses.

It should be noted that in a quasi-static case, inertial effects are not included and this inertial stabilization technique therefore becomes a purely numerical technique for imparting stability. The magnitude of the stabilizing forces depends both on the size of the time increment employed by the Newton-Rhapson scheme and the inertias used to calculate the stabilizing forces. In some cases, very small time increments may be necessary to achieve sufficient stabilization for obtaining convergence. In these cases, the rotational inertias of the yarn segments can be scaled in order to increase the stabilizing forces and permit larger time steps, as long as the stabilizing loads do not become so large that they approach the magnitude of the actual meso-level forces, since inertial effects should be negligible in a quasi-static analysis. For the Kevlar® S706 fabric model that we considered, use of the actual rotation inertia of the yarn segments was sufficient to

stabilize the model, and resulted in stabilizing loads that were several orders of magnitude smaller than the meso-level forces for reasonably sized time steps.

One final numerical issue that arises is that the fabric constitutive model exhibits a behavior similar to the numeric "locking" that is traditionally observed when fully integrated displacement-based finite elements are used to model incrompressible or nearly incompressible materials. This numeric locking should not to be confused with the physical phenomenon that we refer to as "fabric locking" that occurs because interwoven cross sections jam against one another. Like nearly-incompressible material models that lock, the fabric model exhibits oscillating stress (and yarn tension) contours and variable element stiffnesses that depend on the element formulations when certain boundary conditions are applied. The stress oscillations do not vanish as the mesh is refined. For fabrics, this behavior does not arise from incompressibility—fabrics are compressible, undergoing large volume changes during shear and crimp interchange—but rather from inextensibility of the yarns. Just as a nearly incompressible material is much stiffer in response to volumetric changes than it is in response to isochoric deformation, the fabric is much stiffer in response to deformations that involve stretching of the yarns than it is in response to deformations that do not (e.g. during crimp interchange, etc.). We have devoted significant effort towards understanding this phenomenon, but have not yet been successful in developing an element formulation that eliminates it. The problem is especially noticeable when the fabric is subjected to non-uniform strains that can be accommodated by trellising or crimp interchange. Fortunately, even in this worst case, the errors in the stresses (and the tensions) calculated at the integration points are acceptably small, and as actual tensions and stresses become large, the errors become negligible. Refer to Appendix C for a detailed discussion of this phenomenon and of different techniques that we have investigated for eliminating it.

2.9 Validation – Uniaxial Strip Tests

In order to test and validate this initial model, we considered three sets of quasi-static experiments on samples of Kevlar® S706. Each set of experiments involved more complex boundary conditions. In each set of experiments, our goal was to establish whether the fabric model was capable of predicting the appropriate macroscopic loading and deformation response, and whether the fabric model correctly captured the evolution of the fabric mesostructure and the growth of meso-scale level forces that would cause failure.

In the first set of experiments, rectangular strips of fabric were cut parallel to one of the two yarn family directions and loaded using a Zwick uniaxial tensile tester at a nominal axial strain

rate of 0.01 s^{-1}. A photograph of such a test is shown in the inset of Figure 2-16. For these tests, the load-direction yarns at each edge of the strips were removed over a width of 0.64 cm in order to control the exact number of yarns per specimen and to eliminate effects due to yarn slip and fraying at the free edges, leaving an effective specimen size of 2.54 cm by 25.4 cm with exactly 34 loaded yarns. This large aspect ratio was chosen to minimize end effects at the grips. Each of these tests was simulated in ABAQUS/Standard using the geometric parameters and constitutive properties determined as described above and summarized in Table 2-1. The models were uniformly meshed with approximately square elements of sufficient density determined through a mesh refinement study. Eight-node plane strain reduced integration elements, designated CPE8R elements within ABAQUS, were employed. Because yarn tensions were large, the numerical locking problem described in Appendix C did not affect the results.

The models successfully predicted the macroscopic deformations and loads and the growth of meso-level forces that lead to failure in this case. In the experiments, the fabric strips undergo uniform lateral contraction in response to the imposed axial strain (except near the grips, where the clamping effects prevent lateral contraction). This behavior was well captured by the model. For the warp direction tests, the model predicts that at 4% nominal axial strain, the fabric strip will have undergone a 4.5% transverse contraction due to crimp interchange, compared to a 4.0% average contraction observed in the experiments. For the weft-direction tests, the model predicts a 5.8% contraction at 4% nominal axial strain, compared to a 5.9% average contraction observed in experiments. Greater contraction occurs in the weft-direction tests because the weft yarns have a greater degree of initial crimp and consequently crimp interchange dominates a larger portion of the response in the weft-direction test.

The model predictions of the macroscopic load response were very accurate as well. Figure 2-17 and Figure 2-18 show the experimental load-strain curves for the warp and weft direction tests, along with the corresponding model predictions. Note that load has been normalized to average load per yarn; this does not imply that the load carried by all the yarns is the same. The total loads on the samples can be computed by multiplying the loads shown in these figures by the number of yarns per sample (thirty-four). The model accurately predicts the correct mechanical response using only the properties determined independently from the tests described above; no curve fitting was performed.

The last requirement for the model is the capability to predict the growth of meso-level loads when the continuum is subjected to macroscopic loading. This is especially important for predicting the onset of failure. In the uniaxial strip tests, failure occurs when the yarns begin to break, which is governed by the tensile load carried by the yarns. Figure 2-16 shows the model

predictions for the warp yarn loads in the warp-direction tensile test at 4% nominal axial strain. The model indicates that the outermost yarns carry the greatest loads and are expected to fail first, with yarn failures propagating inwards. This is consistent with the behavior observed during experiments, as shown in Figure 2-19. Of course, the model predicts that the largest yarn loads will occur at the grips due to the clamping effects there. In the experiments, the strips did indeed often fail at the grips, but not always. Slippage in the grips, which is not included in the model, sometimes alleviated the loads at grips and failure instead occurred at intermediate locations along the strip. Because the average yarn strengths can be estimated from the single yarn tests, the model can be used to predict the macroscopic loads at which the yarn failure will initiate in the loaded fabric strip, even though the model does not capture failure directly. Figure 2-17 and Figure 2-18 show the model predictions of the load at which the yarns will begin to fail, which are in very good agreement with the experimental data.

2.10 Validation – Bias-Extension Tests

The model was in good agreement with experiments in the very simple case of uniaxial extension, so we next considered a more complex loading case, commonly referred to as a "bias-extension test". In this test, a rectangular fabric strip is cut so that the loading direction is oriented at 45° to the yarn directions. Such tests are described by various authors, e.g Peng and Cao [2005]. In order to avoid gripping yarns at both ends, it is generally recommended that the strips have an aspect ratio of approximately 3:1 or greater. Our samples measured 3.49 cm by 9.50 cm.

Relatively complex deformation patterns manifest during a bias extension test. Yarns in the central portion of the strip undergo a state of almost pure yarn rotation as they attempt to align with the loading direction—this portion of the strip undergoes a large and relatively uniform lateral contraction. Clamping effects at the ends prevent lateral contraction, which results in a triangular region at each end of the strip that undergoes almost no deformation at all. These triangular regions are bounded by narrow bands characterized by large tensions and jamming forces and increasing shear strains. These deformation contours are illustrated in Figure 2-21. Lines have been drawn on the samples parallel to the yarn directions and in a rectangular grid pattern to show the deformations clearly and facilitate comparison to the model predictions. As was the case for the uniaxial tests, the model predicts these deformation patterns very well, as is evident in Figure 2-21. The model predictions shown in this figure are not scaled to match the

photos of the experiments—the lateral contraction predicted by the simulation and the lateral contraction observed in the experiment are in good agreement.

The macroscopic load response in a bias-extension test is dominated by the shear and locking properties of the fabric. Unfortunately, bias-extension tests are generally poorly suited for quantitative comparisons of load responses due to their variability. The extremely low resistance to shear deformation of the fabric before it locks, combined with the sensitivity of the test to small variations in the bias angle and the sample orientation, introduces a great deal of inconsistency into the experimental measurements. For example, in one set of nine tests, the extension at failure varied between 24 and 32 mm and the failure load varied between 1000 and 1300 N. In Figure 2-22 we display experimental load-displacement curves that were within one standard deviation from the average. Model predictions, obtained using the properties in Table 2-1, are also shown in Figure 2-22. The model predicts the average bias-extension response accurately with regard to both the strain at which stiffening begins to occur and the stiffened slope. At very large strains, where the stresses greatly exceed the stresses that develop in the shear frame tests, the model response is too stiff compared to the experimental response. This may be an effect of the inherent limitations of this initial model, which is capable of capturing only failure-free in-plane deformation. The fabric in the bias-extension tests exhibits both wrinkling and unraveling of the weave at large strains, which lead to a more compliant response. The deviation may also be a result of the simplistic geometry used to represent locking. The truss-based locking geometry captures the locking effect relatively accurately at small to moderate shear angles, but becomes far less accurate at large shear angles.

In the bias extension tests, the strips fail when gradients in the locking forces become so great that they cause the weave to begin to unravel at the edges, as is shown in Figure 2-23. The unraveling occurs along diagonal bands that flank the low-deformation triangles at each end of the strip and that continue across the sample. The fabric is eventually pulled apart along these bands. While the initial model can not capture the unraveling, which involves yarn slip, it can predict the distribution of locking forces up to the onset of failure. Locking force contours predicted by the model are shown in Figure 2-24. The model predicts bands of large locking forces bounding the low-deformation triangles at the ends and continuing across the sample. Such bands are also evident in the experiments by examining how tightly compacted the weave becomes in these regions. The gradients of these locking forces, were they to drive yarn slip, would cause the weave to unravel in the manner observed in Figure 2-23. Hence we are able to use the model's capability of tracking meso-level loads to predict macroscopic failure in this case as well as the simple case of uniaxial extension.

2.11 Validation – Slit-Damage Tests

We considered one final case to validate this initial model. In some applications, fabrics are subjected to biaxial loads and their resistance to propagation of damage is of interest. Examples of such applications include inflatable fabric structures and parachutes. Godfrey and Rossettos ([1998] and [1999]) have studied damage propagation in biaxially stressed fabrics using a "slit-damage" test. In this test, shown schematically in Figure 2-25, a cruciform-shaped fabric specimen is cut so that the yarn families are oriented parallel to the cruciform arms. In the center of the specimen, a number of adjacent yarns are cut to create a slit. The specimen is then loaded biaxially. The first uncut yarn at the end of the slit is subjected to a very large tension, much larger than the nominal tension across the specimen width. This concentration of tension is similar to a stress concentration that manifests at the tip of a sharp crack, and depends on the size of the slit. Godfrey and Rossettos have shown that in a fabric which does not permit significant yarn slip, this tension concentration will become large and a self-propegating tear will result in a sudden, catastrophic failure of the sample, similar to a brittle fracture in a cracked material that is resistant to plastic deformation. However, if yarn slip can occur, it tends to reduce the tension concentration and prevent a catastrophic failure, just as plasticity in a ductile material reduces the stress concentration at a crack tip and prevents brittle fracture. Godfrey and Rossettos identified two modes of slip around the slit, shown in Figure 2-26. A visually obvious mode of slip involves the cut yarns slipping through the weave away from the slit. In the presence of biaxial stresses, these yarns drag the horizontal crossing yarns along with them. However, this creates a second mode of slip, as the crossing yarns are forced to slip past the uncut vertical yarns at the end of the slit. It is this mode of slip that relieves the tension concentration in the yarns at the end of the slit.

Godfrey and Rossettos arrived at these conclusions using a combination of experiments and simple analytical models. We wanted to reproduce their results using our more versatile finite element model. We recreated their experiments and observed the same phenomena and same modes of slip around the slit. We then simulated the experiment using the model and analyzed the predicted tension contours, shown in Figure 2-26. Our model predicts physically realistic tension fields: tensions in the cut vertical yarns are low near the slit, but tensions in the uncut vertical yarns at the end of the slit are very large, which in the absence of slip would lead to self-propagating tearing. This is consistent with the rapid damage propagation in fabrics that do not permit significant slip that was observed by Godfrey and Rossettos, and with the tension predictions of their simple model..

Although this model does not include yarn slip, it can be used to predict where and how slip will begin to occur. Yarn slip in a fabric must be necessarily accompanied by gradients in tension along a yarn, because if a yarn is slipping past a crossover point, it must be resisted by certain forces at that crossover point. Under steady-state conditions, tension in the slipping yarn must be greater on one side of the crossover point than the other to offset these resisting forces, which implies a step increase in tension along a slipping yarn at each crossover point. In a continuum approximation, step changes in tension at points along the yarn correspond to a gradient in tension along the yarn. For more details regarding slip in fabrics, refer to Chapter 4 through Chapter 7.

We examined the gradients in the tension in the vertical yarns, shown in Figure 2-26. There are two regions of large tension gradients near the slit. The tensions in the cut yarns increase as distance from the slit increases, which implies that these yarns will tend to slip away from the slit, which is readily observed in experiments. However, the model also predicts that tensions decrease in the un-cut yarns at the end of the slit as distance from the slit increases, which implies slip in the opposite direction. These yarns will tend to slip towards the slit, or, equivalently, the crossing yarns will tend to slip along these yarns away from the slit. This is the second slip mode that Godfrey and Rossettos observed and predicted would alleviate the tension concentration. Although this model cannot capture the slip process, it does predict the two modes of slip that Godfrey and Rossettos observed and predicted using their simple analytical model.

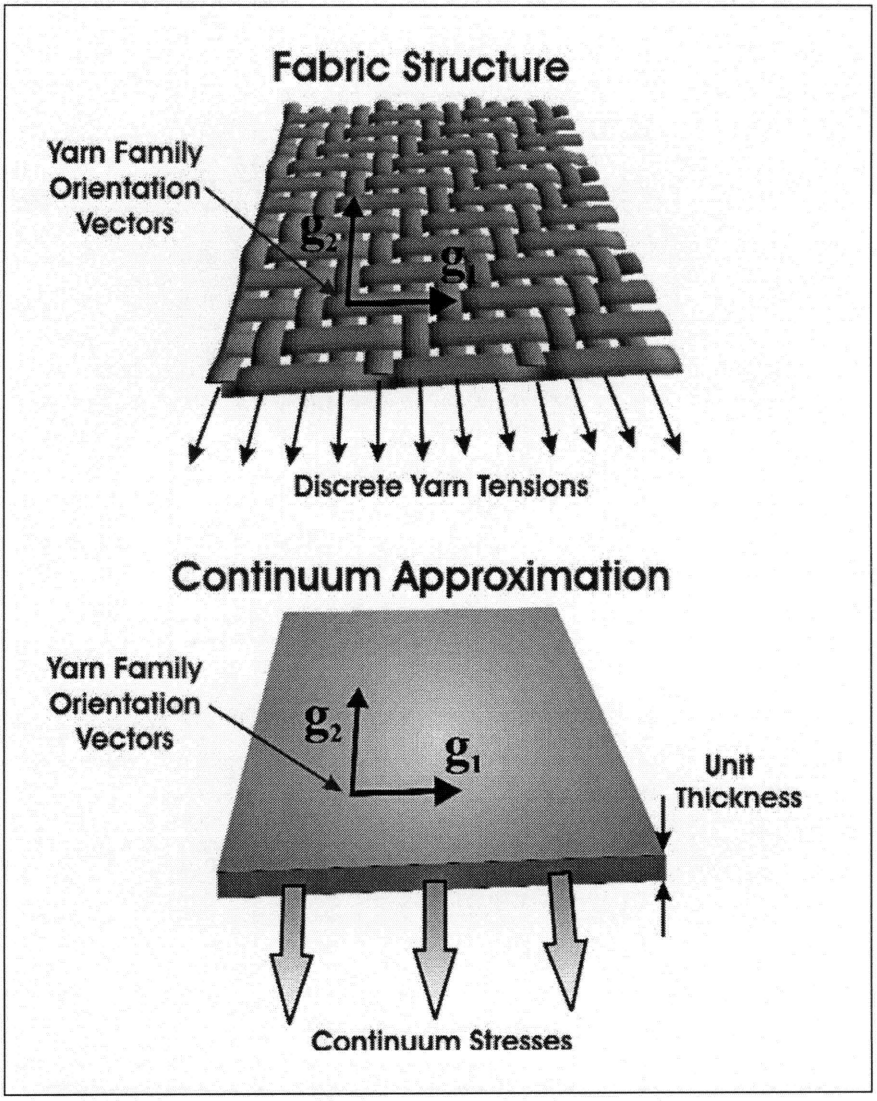

Figure 2-1 Approximating a fabric as an anisotropic continuum

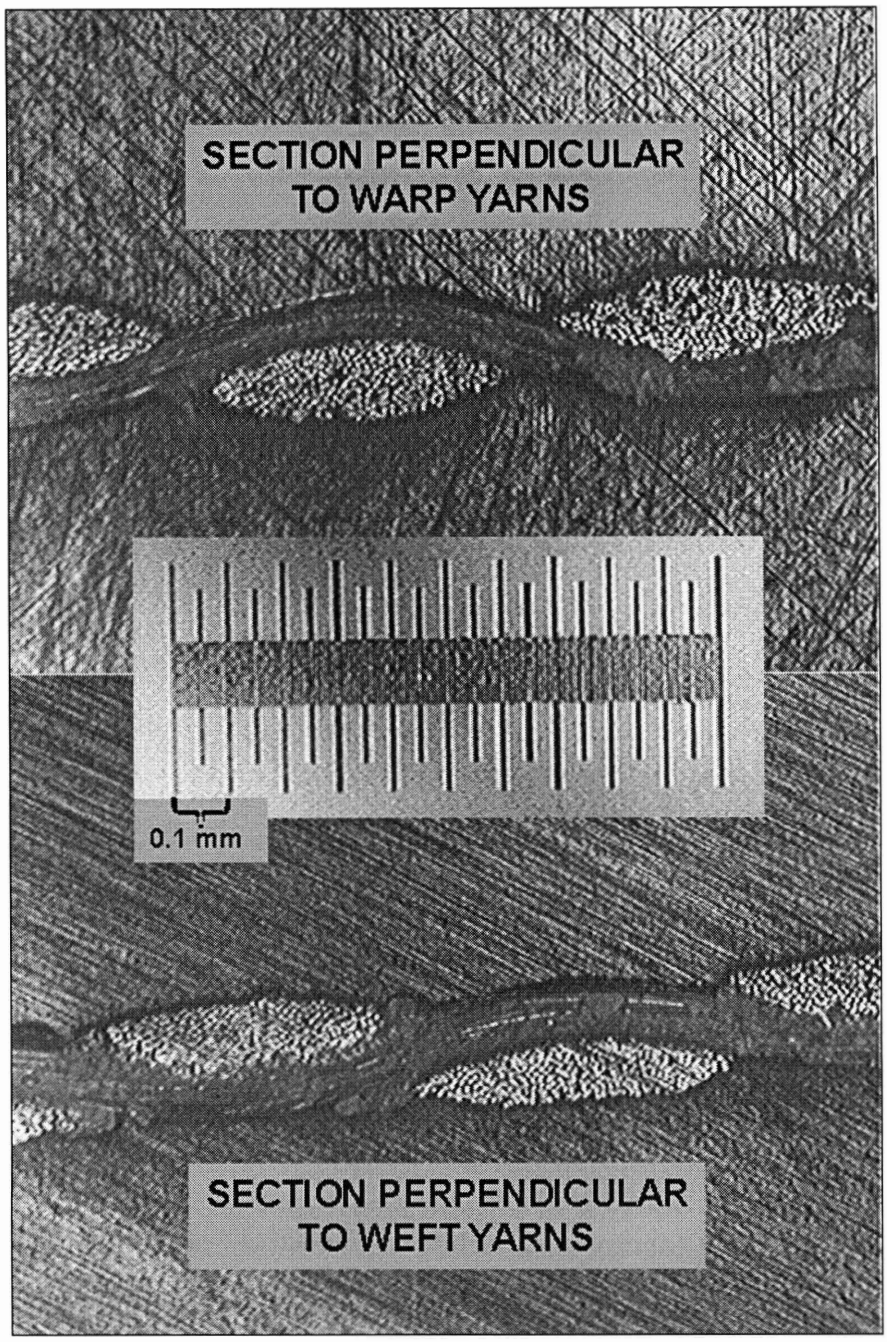

Figure 2-2 Micrographs of Kevlar® S706 weave mesostructure

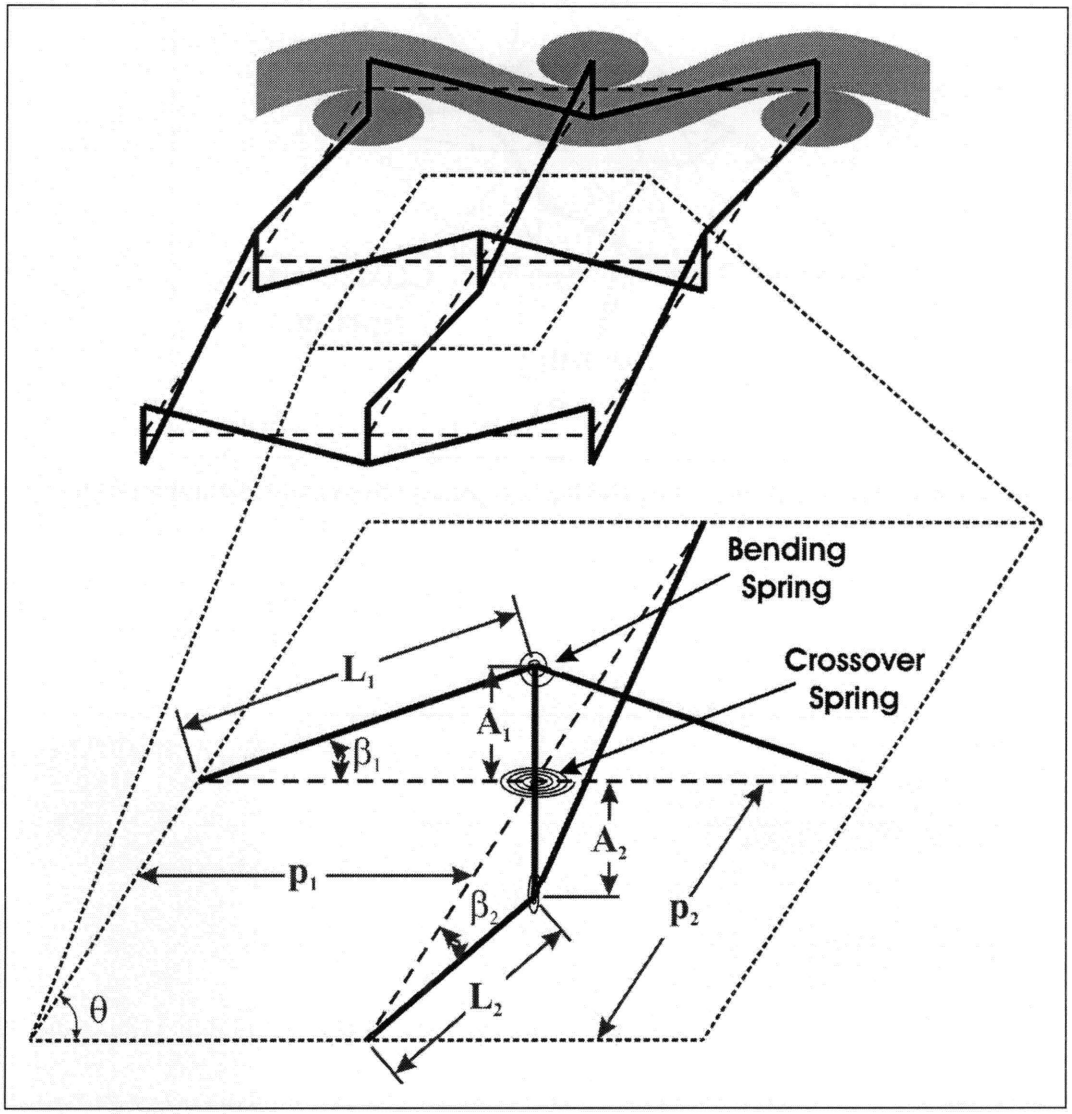

Figure 2-3 Representative mesostructural geometry used for Kevlar® S706 model (locking trusses not shown)

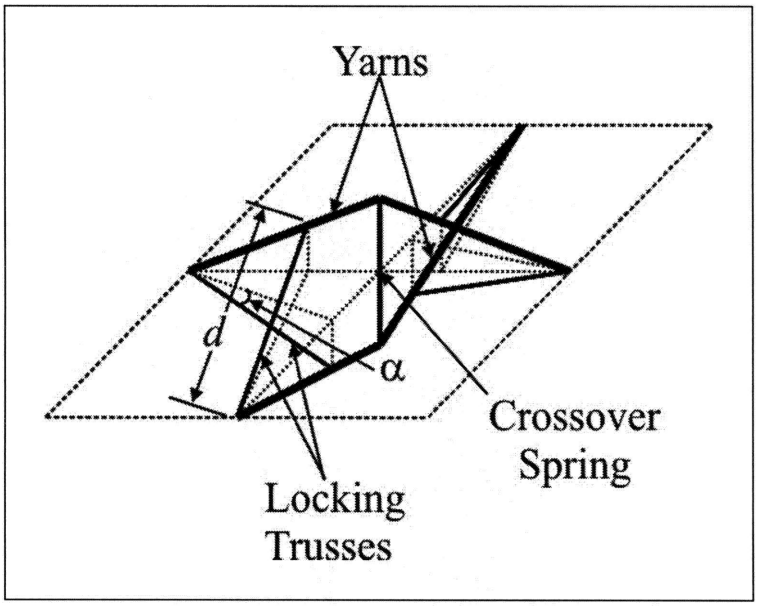

Figure 2-4 Trusses used to capture locking in representative mesostructural geometry

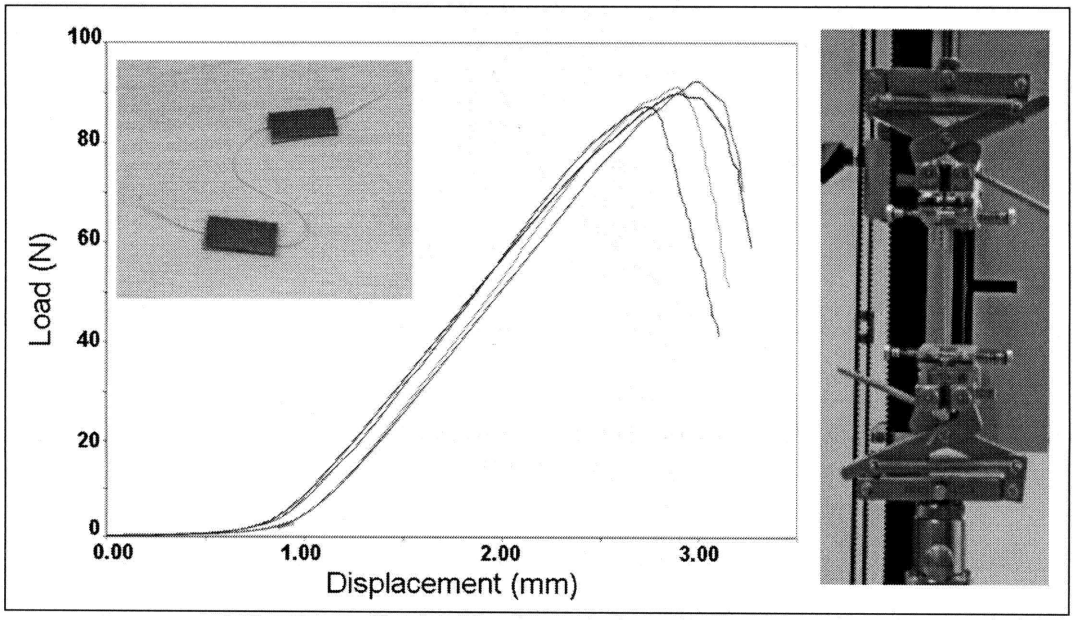

Figure 2-5 Single yarn tensile test (sample, results, and apparatus)

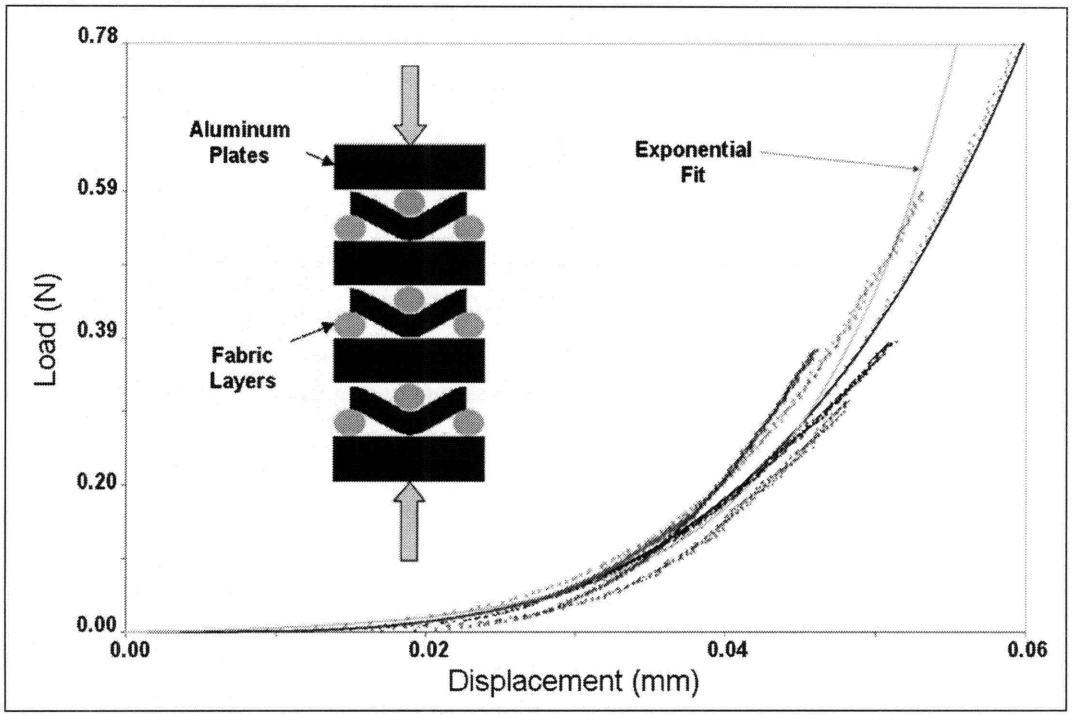

Figure 2-6 Sandwich compression test schematic and results

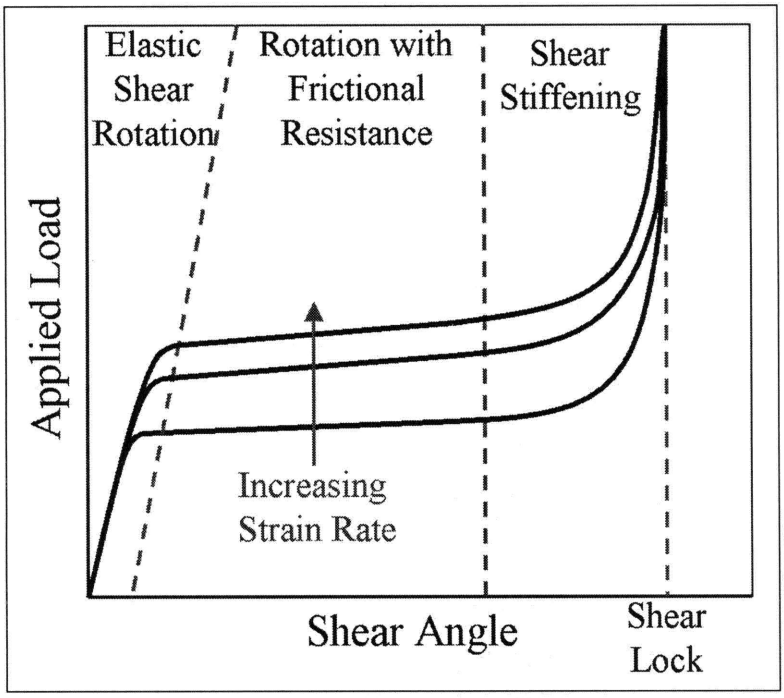

Figure 2-7 Different regimes of the typical response of a fabric to in-plane shear

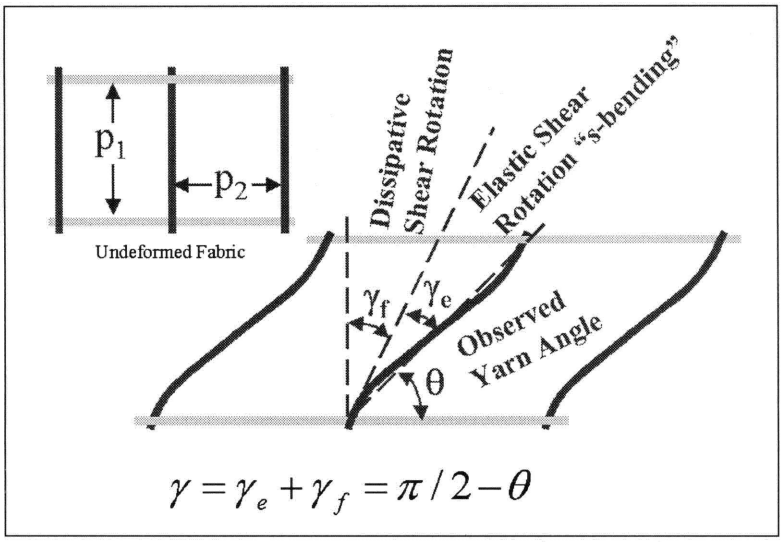

Figure 2-8 Decomposition of relative yarn rotation angle

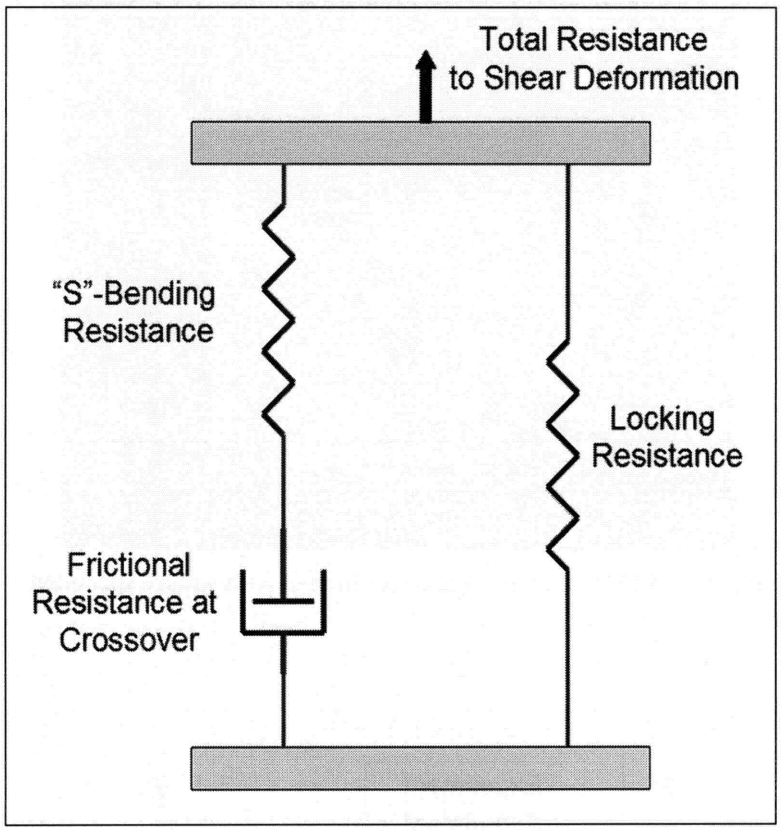

Figure 2-9 Schematic of different resistances to shear deformation

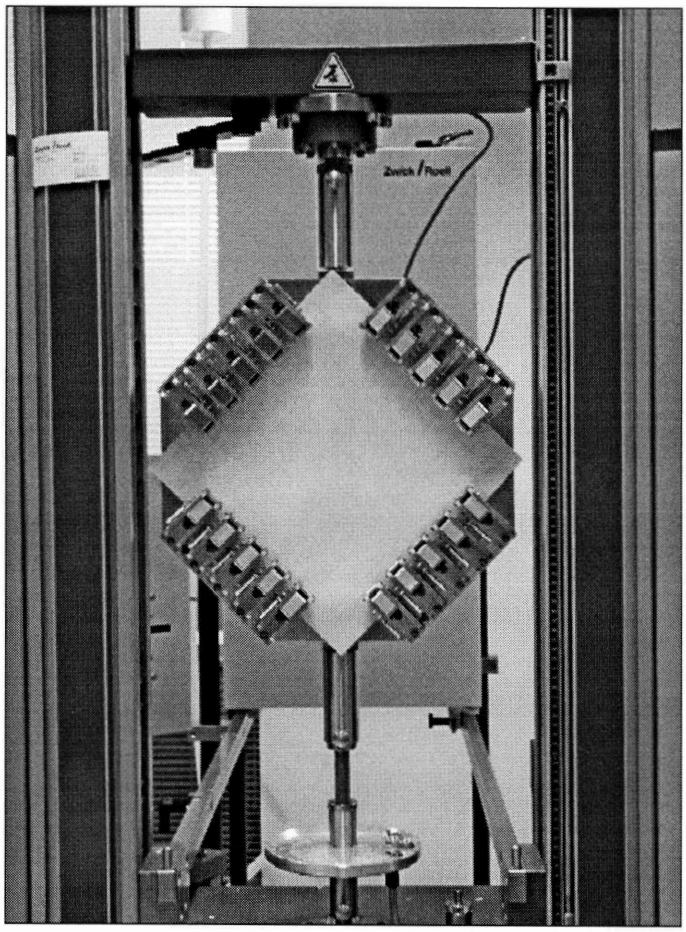

Figure 2-10 Shear frame apparatus loaded with square specimen

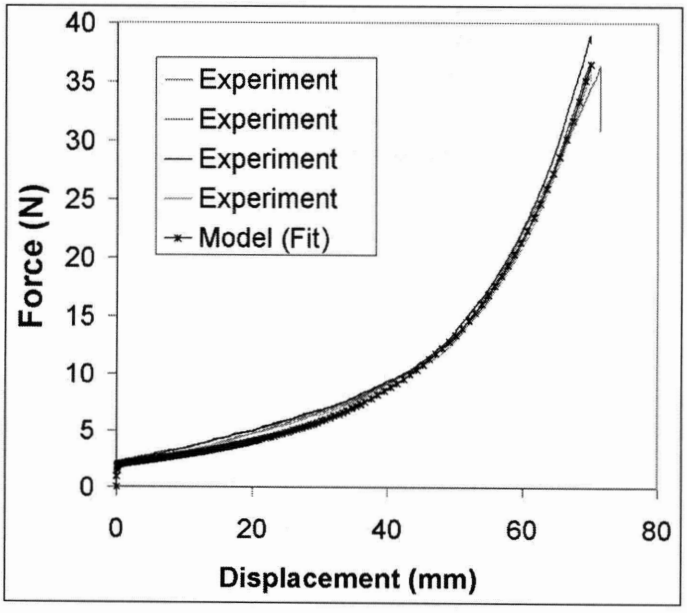

Figure 2-11 Experimentally measured shear response of fabric, with fitted model prediction

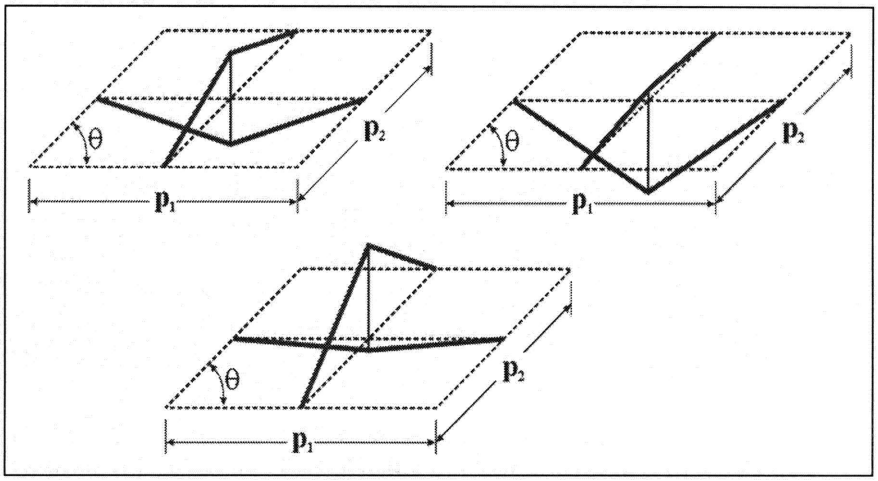

Figure 2-12 Different mesostructure configurations possible for the same p_1, p_2, and θ

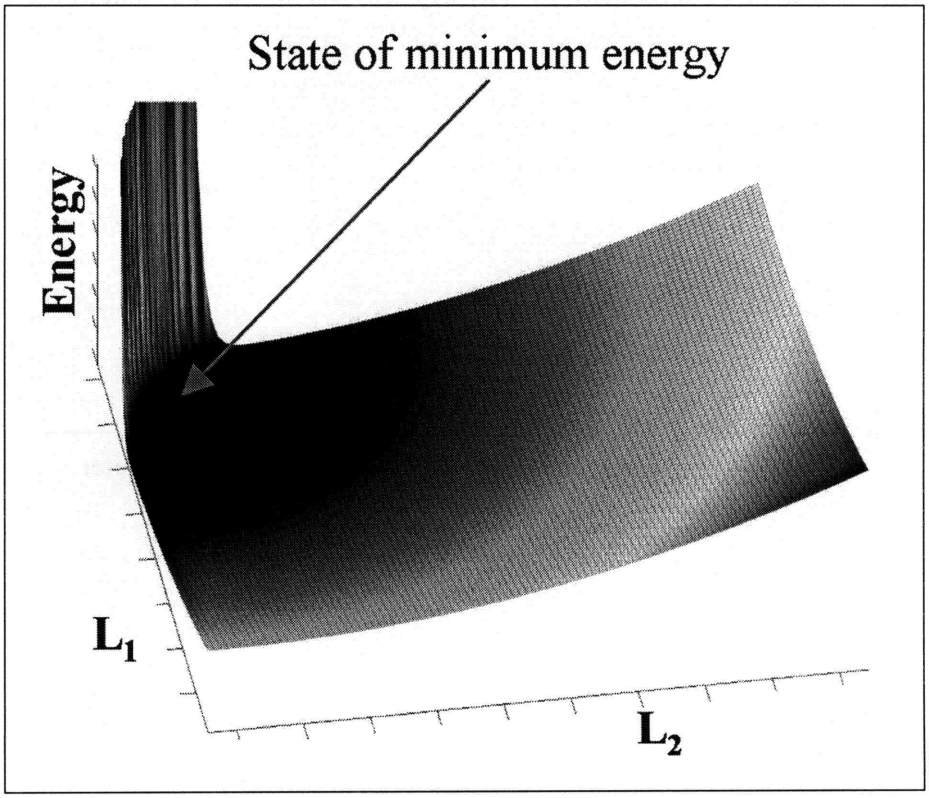

Figure 2-13 Energy stored in unit cell as a function of L_1 and L_2 for a particular deformation gradient

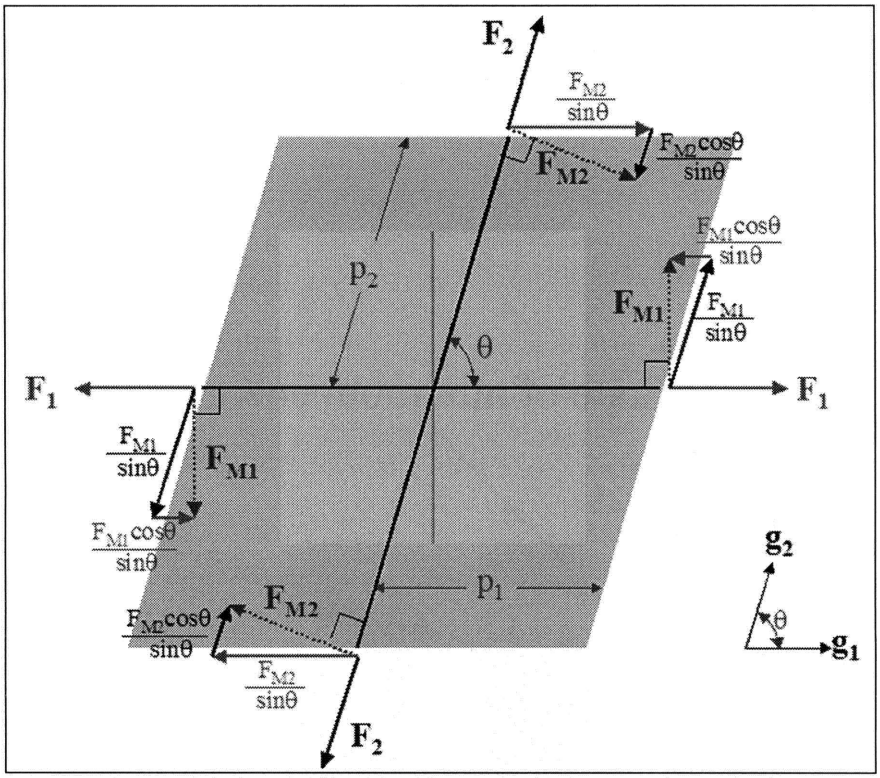

Figure 2-14 Tractions from meso-level forces acting on unit cell faces

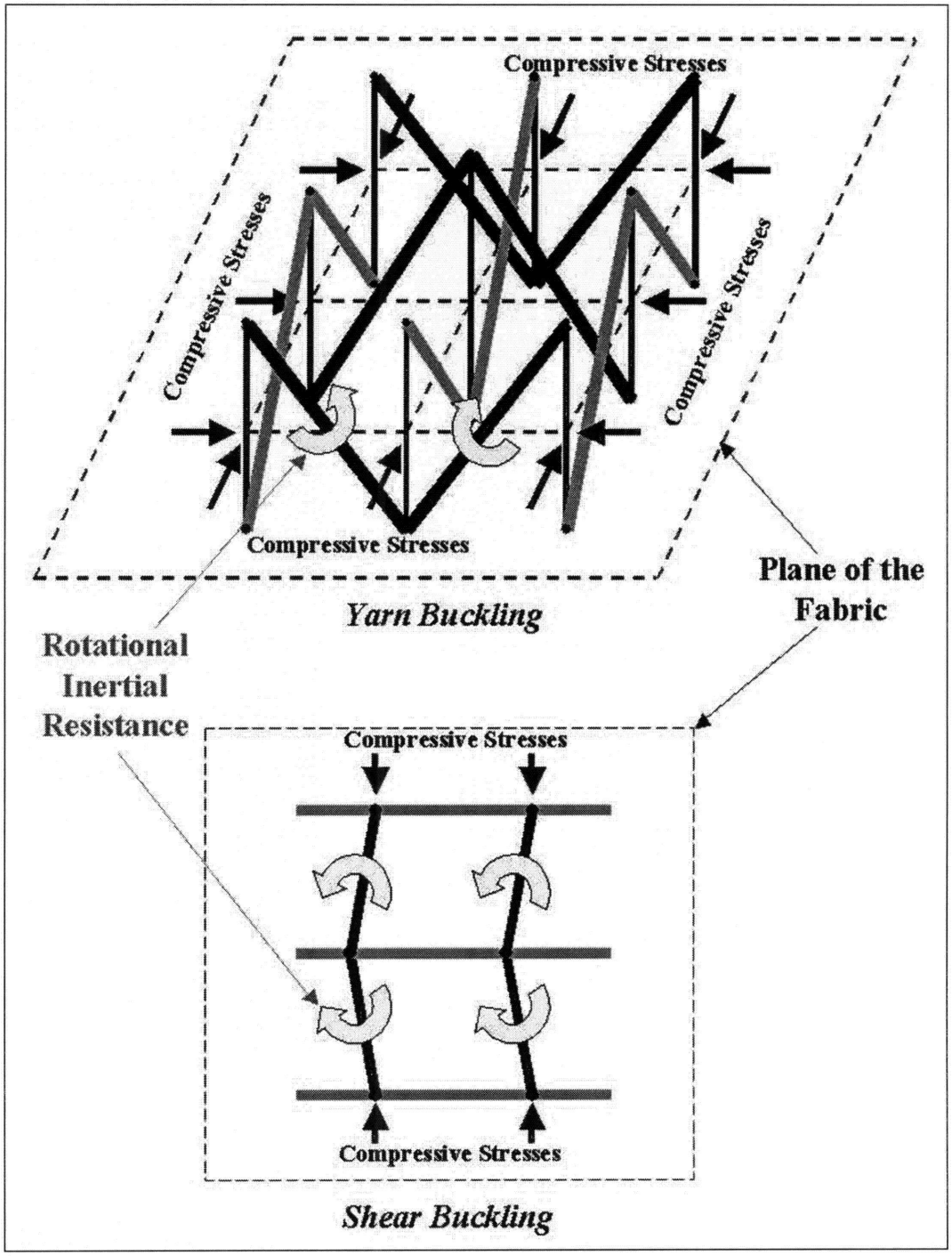

Figure 2-15 Possible buckling modes of the unit cell geometry when compression

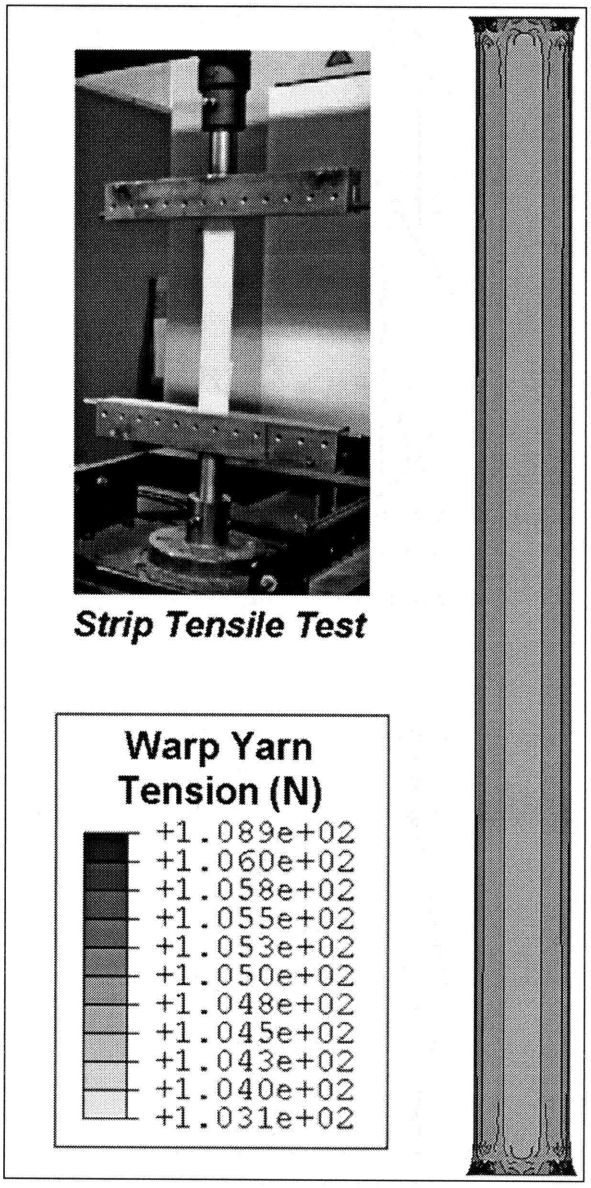

Figure 2-16 Tension contours in fabric strip subjected to uniaxial tension; (inset) photograph of uniaxial fabric strip test

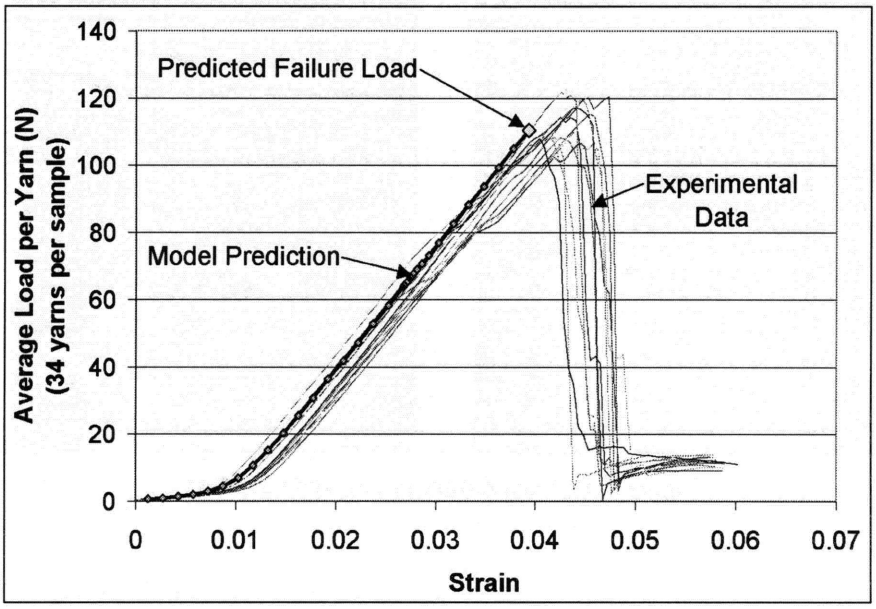

Figure 2-17 Load-strain response in warp-direction uniaxial fabric strip tests, with model prediction

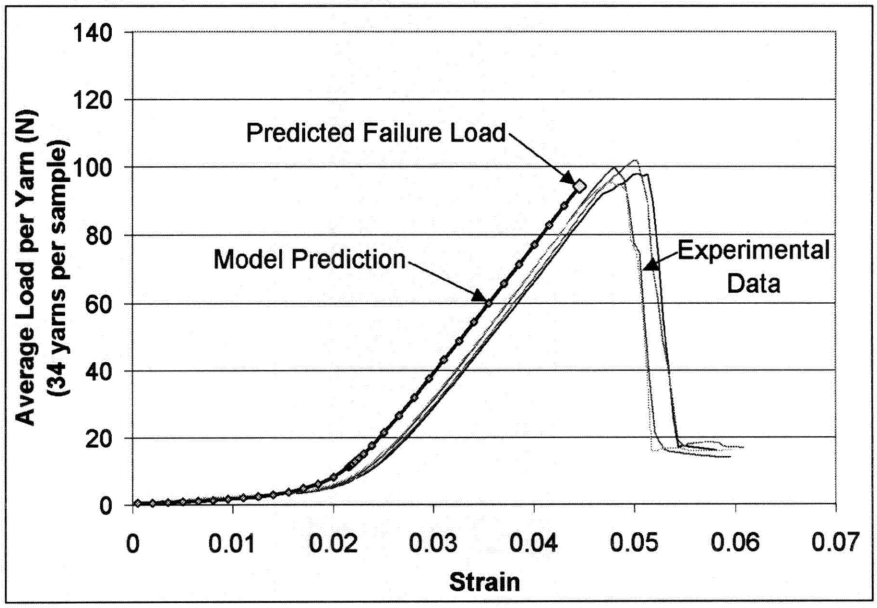

Figure 2-18 Load-strain response in weft-direction uniaxial fabric strip tests, with model prediction

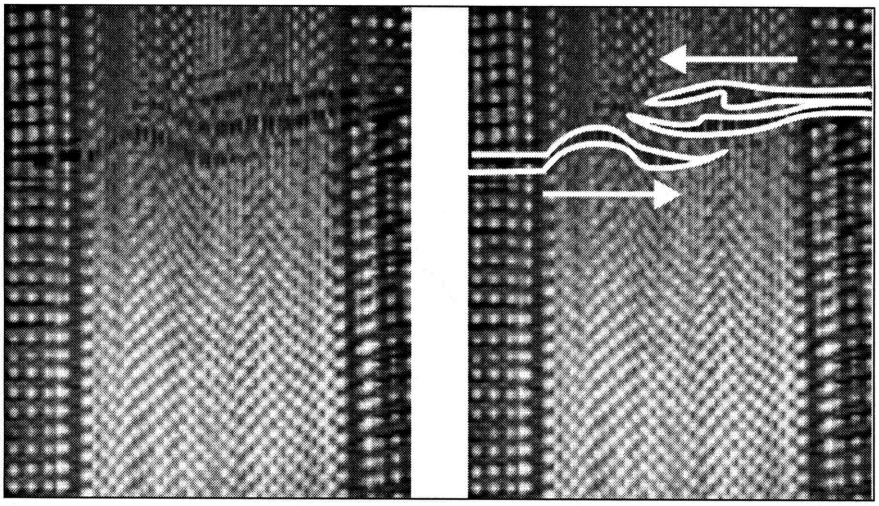

Figure 2-19 Yarn failure in uniaxial strip test

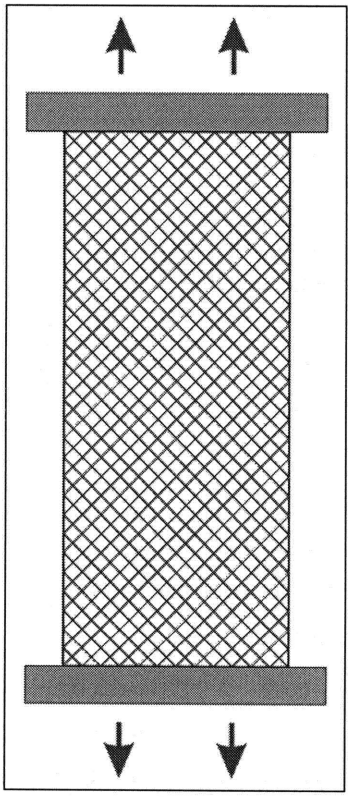

Figure 2-20 Schematic of bias-extension test

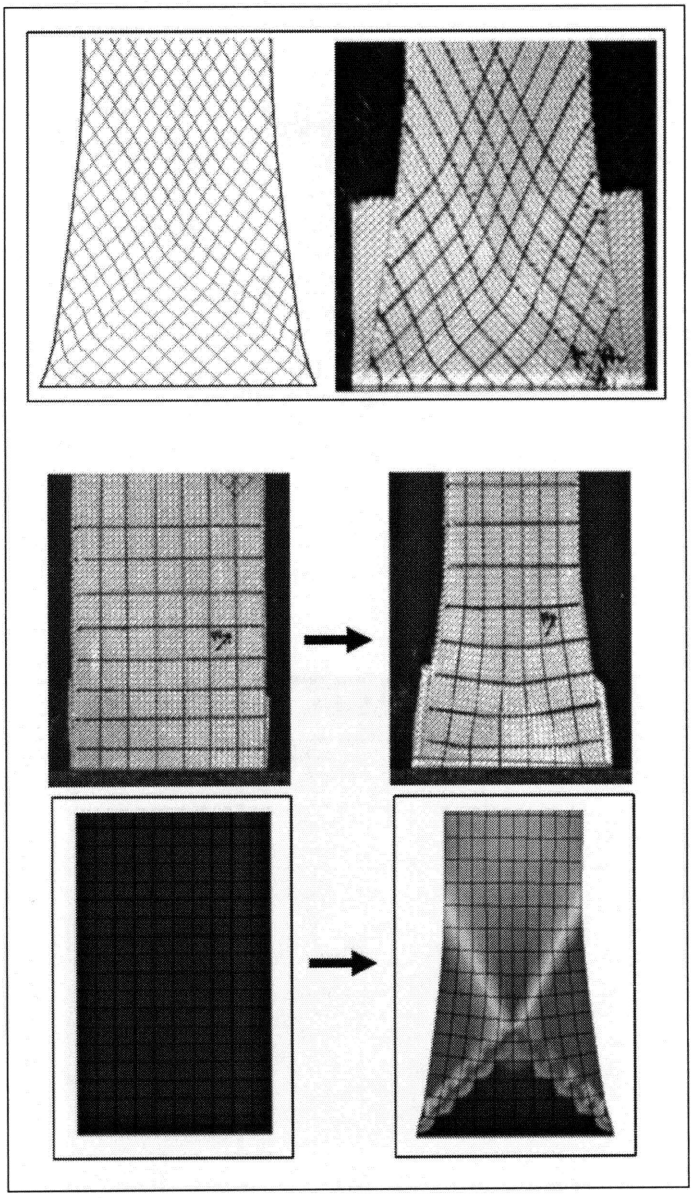

Figure 2-21 (Top) Predicted and observed yarn orientations near the end of a bias-extension sample (lines are parallel to yarn families); (Middle and Bottom) Observed and predicted deformations (with shear-strain contours) near the end of a bias-extension sample

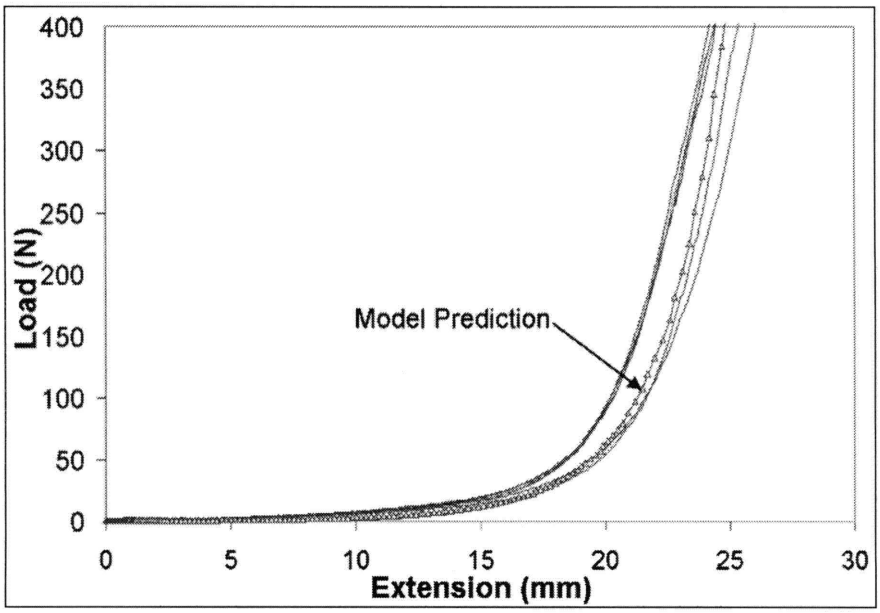

Figure 2-22 Some load responses measured in bias-extension tests, with model prediction

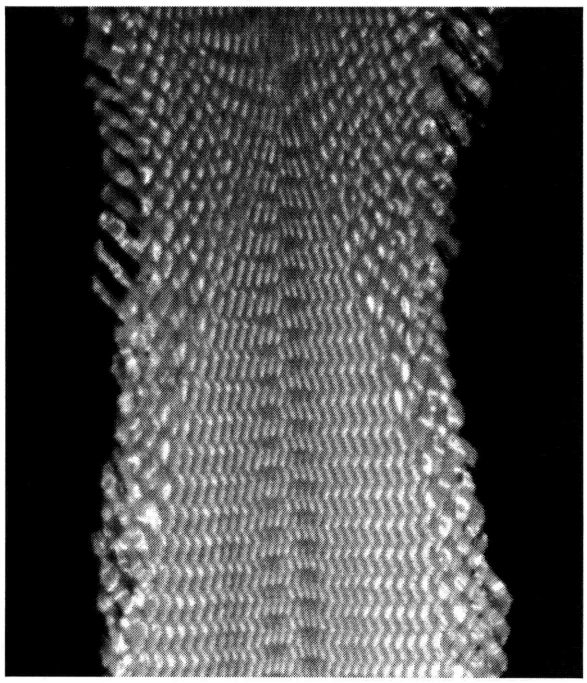

Figure 2-23 Failure in bias extension due to weave unraveling from locking effects

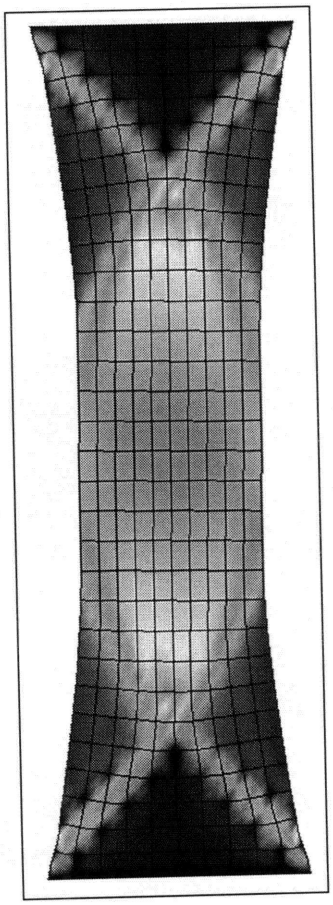

Figure 2-24 Predicted locking force contours in bias-extension

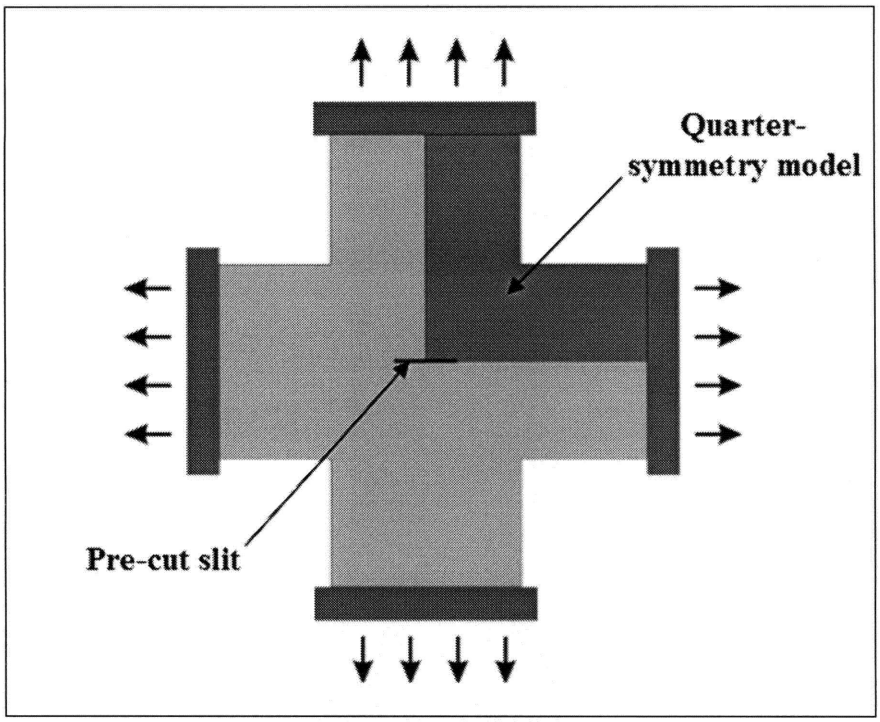

Figure 2-25 Schematic of slit-damage test

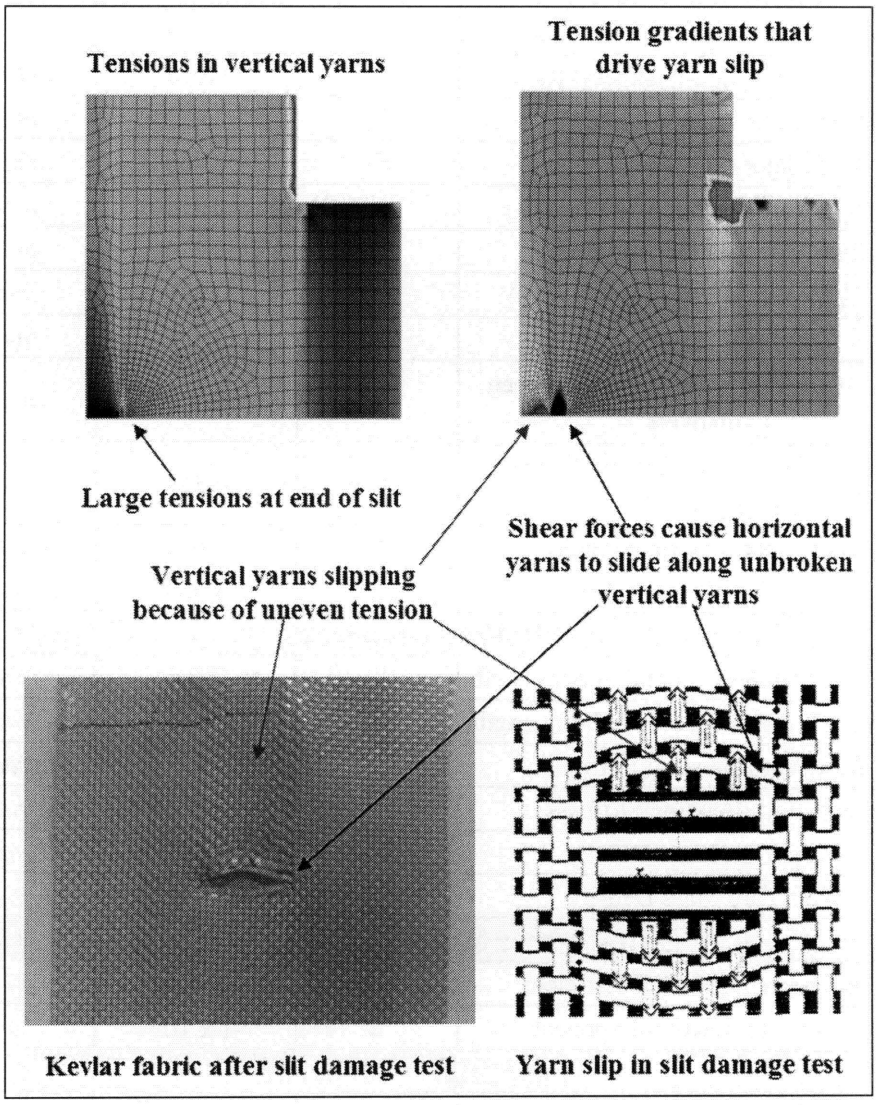

Figure 2-26 Mechanisms that affect damage propagation in slit-damage test; (Top left) Model prediction of tensions in vertical yarns (Top right) Gradients in tension in vertical yarns; (Bottom left) Photograph of slit after application of sub-critical loads; (Bottom right) Schematic showing two modes of slip around slit (Godfrey and Rossettos, [1998] and [1999])

Table 2-1 Measured Properties of Kevlar® S706 used in planar model

Property	Symbol	Value	Unit
Geometric Properties			
Fabric Thickness [a]	-	*0.300*	*mm*
Warp Minor (through-thickness) Radius	r_1	0.075	*mm*
Weft Minor (through-thickness) Radius	r_2	0.075	*mm*
Warp Major (in-plane) Radius	R_1	0.400	*mm*
Weft Major (in-plane) Radius	R_2	0.400	*mm*
Initial Warp Quarter Wavelength	${}^0p_1$	0.374	*mm*
Initial Weft Quarter Wavelength	${}^0p_2$	0.374	*mm*
Initial Warp Amplitude [a]	${}^0A_1$	*0.060*	*mm*
Initial Weft Amplitude [a]	${}^0A_2$	*0.090*	*mm*
Initial Warp Half Yarn Length Between Crossovers	${}^0L_1$	0.378	*mm*
Initial Weft Half Yarn Length Between Crossovers [a]	${}^0L_2$	*0.384*	*mm*
Warp Relaxed Crimp Angle	${}^0\beta_1$	1.412	*radians*
Weft Relaxed Crimp Angle	${}^0\beta_2$	1.334	*radians*
Single Yarn Properties			
Warp Yarn Stiffness Per Half Yarn Length	k_1	3764	*N/m*
Weft Yarn Stiffness Per Half Yarn Length	k_2	3948	*N/m*
Warp Yarn Bending Stiffness	k_{b1}	0.00124	*Nm/radian*
Weft Yarn Bending Stiffness	k_{b2}	0.00073	*Nm/radian*
Warp Yarn Mass Density	ρ_1	1441	kg/m^3
Weft Yarn Mass Density	ρ_2	1441	kg/m^3
Interference Stiffness Properties			
Interference Relation Coefficient	K_I	0.00309	*N*
Interference Relation Exponent	a	1×10^6	*1/m*
Locking Stiffness Properties			
Locking Stiffness	K_d	1.36×10^{13}	N/m^c
Locking Exponent	c	3.70	-
Yarn Rotation (Shear) Properties			
Elastic Rotational Stiffness	K_s	0.0131	*Nm/radian*
Reference Dissipative Rotation Rate	$(d\gamma/dt)_0$	0.00284	*radians/s*
Reference Dissipative Rotation Moment	M_0	3.2×10^{-6}	*Nm*
Dissipative Rotation Rate Sensitivity	b	4.0	-

[a] *Dependent on other parameters or not required by model*

Chapter 3
Out of Plane Deformation

3.1 Mechanics of Anisotropic Continuum Shells

In some applications, the out of plane response of a fabric is of interest. Examples include the forming of composites with fabric reinforcement, the penetration of a fabric armor system by a ballistic projectile, and the bending of apparel as it is worn. As described in Section 1.3, most existing continuum fabric models capture three-dimensional behaviors by treating the fabric as a membrane, with negligible bending and twist stiffness. While the planar model described in Chapter 2 can be readily implemented into a membrane formulation, in some applications the bending and twist stiffness of the fabric may have a non-negligible effect on the deformations that occur. We therefore extend the planar continuum model described in Chapter 2 to a three-dimensional shell implementation to permit the analysis of out-of-plane fabric deformations, including transverse penetration and fabric wrinkling that occurs at large shear deformations (a common phenomenon in fabric composite forming operations). As in the case of the planar model, we specialize our model to plain weave Kevlar® fabric, manufactured by DuPont Inc. Two Kevlar® fabrics were considered: style S706, which is a very tightly woven fabric; and style S726, which has larger yarns and is more loosely woven.

For an in-depth description of the development of a shell implementation, refer to Bathe [2003]. In any shell formulation, the shell response is characterized by a set of generalized forces that must be related to the different modes of shell deformation. We first identify these modes of deformation and the corresponding generalized forces. Following classic methodologies (e.g. as described in Belytschko *et al.* [2000]) to describe the kinematics of a shell, we define the midsurface of the shell as a reference surface and then choose a suitable theory of shell kinematics. Most fabrics are relatively thin and insensitive to transverse shear effects; consequently, it would be appropriate to use the classical Kirchhoff-Love shell theory, which assumes that material lines that are initially straight and normal to the midsurface remain straight and normal. However, some commercially available finite element codes (e.g. ABAQUS) offer only extremely limited Kirchhoff-Love shell element formulations. Consequently, we consider the more general Mindlin-Reissner theory, which assumes that material lines that are initially straight and normal to the midsurface remain straight, but not necessarily normal; such shells

allow transverse shear. By using the appropriately small fabric thickness, and by choosing relatively stiff transverse shear behaviors, our shell elements will exhibit negligible transverse shear strains and will approach the Kirchhoff-Love limit. Using Mindlin-Reissner shells has the additional benefit that the shell implementation could also be used (with some modification) for woven fabric composites, where transverse shear effects may be important to the material response.

To describe the shell kinematics, we define a curvilinear coordinate system (ξ_1, ξ_2, ξ_3) with the ξ_1 and ξ_2 directions tangent to the shell midsurface and ξ_3 normal to the midsurface at every point. The ξ_1 and ξ_2 coordinates parametrize the midsurface, which lies at $\xi_3 = 0$. The location of any material point X in the reference configuration is given by (X_1, X_2, X_3), where (X_1, X_2, 0) gives the location of point $\hat{X}$, which lies at the projection of X onto the midsurface, and X_3 gives the perpendicular distance between X and the midsurface. In the deformed configuration, point $\hat{X}$ will occupy location $\hat{x}$, located at (x_1, x_2, 0). The position of point X (which now occupies location x) relative to location $\hat{x}$ can be described by a vector ζ. Because Mindlin-Reissner theory permits transverse shear, this vector ζ will not necessarily be normal to the reference surface.

A Mindlin-Reissner shell has nine modes of deformation. Three involve membrane deformations of the midsurface—membrane stretch along the ξ_1 and ξ_2 directions and membrane shear. These membrane deformations can be described using a two-dimensional membrane deformation gradient $\mathbf{F}^m$, which has components:

$$F^m{}_{\alpha\beta} = \frac{\partial x_\alpha}{\partial X_\beta}, \tag{3.1}$$

where $\alpha, \beta = \{1,2\}$. Consider a point that lies on the fabric midsurface and a plane tangent to the midsurface at that point. The orientation of a midsurface material line passing through the point can be described by a vector $\mathbf{a}$ that lies in the tangent plane and hence only has components in the ξ_1 and ξ_2 directions. The vector $\mathbf{a}$ has length a equal to the length of the material line and is oriented parallel to the projection of the material line onto the tangent plane. In the reference configuration, we refer to this vector as ${}^0\mathbf{a}$. Provided this reference vector ${}^0\mathbf{a}$ is known, the corresponding vector in the deformed configuration will be mapped according to:

$$\mathbf{a} = \mathbf{F}^m \, {}^0\mathbf{a}. \tag{3.2}$$

The length of the material line in the deformed configuration, and consequently the membrane stretch in the direction of the material line, can be calculated as:

$$a = \sqrt{{}^0\mathbf{a} \cdot \left(\mathbf{F}^{m\mathrm{T}}\mathbf{F}^m\right){}^0\mathbf{a}}\,. \tag{3.3}$$

The in-plane angle between two material lines $\mathbf{a}_1$ and $\mathbf{a}_2$ can be determined by dotting them together:

$$\mathbf{a}_1 \cdot \mathbf{a}_2 = a_1 a_2 \cos\theta\,, \tag{3.4a}$$

$$\Rightarrow \cos\theta = \frac{\mathbf{a}_1 \cdot \mathbf{a}_2}{a_1 a_2} = \frac{{}^0\mathbf{a}_1 \cdot \left(\mathbf{F}^{m\mathrm{T}}\mathbf{F}^m\right){}^0\mathbf{a}_2}{\sqrt{{}^0\mathbf{a}_1 \cdot \left(\mathbf{F}^{m\mathrm{T}}\mathbf{F}^m\right){}^0\mathbf{a}_1}\sqrt{{}^0\mathbf{a}_2 \cdot \left(\mathbf{F}^{m\mathrm{T}}\mathbf{F}^m\right){}^0\mathbf{a}_2}}\,. \tag{3.4b}$$

By comparing this angle to the angle between ${}^0\mathbf{a}_1$ and ${}^0\mathbf{a}_2$, the amount of membrane shear can be determined.

The shell has two modes of transverse shear, which can be characterized by two scalar strain values ε_{T1} and ε_{T2}. Consider two planes that each contain the normal to the deformed midsurface and a material line along one of the two directions ξ_1 or ξ_2; the scalars ε_{T1} and ε_{T2} describe the angles that the respective projections of vector ζ onto these planes make with the deformed midsurface normal. We expect these strains to be small. There is also a mode of through-thickness deformation, which can be described by a scalar giving the through thickness stretch λ_t:

$$\lambda_t = \frac{|\varsigma|}{X_3}\,. \tag{3.5}$$

Finally, because the midsurface is not flat, we must consider three additional modes of deformation that describe the bending curvature along the ξ_1 and ξ_2 directions and the twisting curvature of the midsurface at any given state of deformation. This is typically done using a symmetric bending tensor **B**, which is defined in the following manner. Given any material line contained in the midsurface, described by vector **a** as defined above, the bending tensor **B** is the rank two symmetric tensor that gives:

$$\kappa_a = \frac{1}{a^2}\mathbf{a} \cdot \mathbf{B}\mathbf{a}\,, \tag{3.6}$$

where κ_a is the curvature (the inverse of the radius of curvature) of the material line in space. This tensor is sometimes called the "second fundamental form". Assuming it is known, the bending curvatures κ_1 and κ_2 along directions ξ_1 and ξ_2 can be calculated from Equation (3.6).

The final mode of deformation is twist, which is defined as follows. Consider vectors parallel to the ξ_1 and ξ_2 directions tangent to the midsurface at a point (ξ_1, ξ_2). These vectors define a tangent plane P at point (ξ_1, ξ_2). As variations in position along the directions ξ_α are considered, the vectors parallel to the ξ_1 and ξ_2 directions may change their orientations with respect to P by

angles γ_1 and γ_2, respectively. Twist $\varphi_{\alpha\beta}$, can be defined as the change in orientation γ_α of material lines parallel to the ξ_α direction with respect to changes in ξ_β:

$$\varphi_{\alpha\beta} = \frac{\delta\gamma_\alpha}{\delta\xi_\beta}. \tag{3.7}$$

In other words, it is the change in orientation of material lines in the midsurface parallel to one direction per unit distance traveled in the other direction. A shape exhibiting a state we refer to as "pure twist" (where $\kappa_1 = \kappa_2 = 0$ and $\varphi_{12} \neq 0$) is shown in Figure 3-1. It can be shown that $\varphi_{12} = \varphi_{21}$, and that this value can be calculated from the bending tensor in the following manner:

$$\varphi_{12} = (\mathbf{a}_1 \cdot \mathbf{B}\mathbf{a}_2 + \mathbf{a}_2 \cdot \mathbf{B}\mathbf{a}_1), \tag{3.8}$$

where $\mathbf{a}_1$ and $\mathbf{a}_2$ are aligned with the ξ_1 and ξ_2 directions, respectively.

We have described how a Mindlin-Reissner shell has nine different modes of deformation—two "membrane" stretching modes, a "membrane" shearing mode, a mode involving changes to the shell thickness, two transverse shearing modes, two out-of-plane bending modes, and one out-of-plane twisting mode. We next characterize nine generalized forces that correspond to these nine deformation measures.

Because the fabric is an anisotropic material, the membrane stresses can be expressed using tensors defined using the yarn orientations, as discussed in Chapter 2. If we redefine the vectors $\mathbf{g}_1$ and $\mathbf{g}_2$ to be unit vectors in the tangent plane to the midsurface at a given point, parallel to the projections of material lines along the yarn families, then the membrane stresses can still be expressed in the form given by Equation (2.27), substituting the membrane stress $\boldsymbol{\sigma}^m$ for $\boldsymbol{\sigma}$. The three generalized forces N_1, N_2, and S_{12} correspond to the three modes of membrane deformation.

The out-of-plane bending and twisting moments (per unit width), which correspond to the bending and twisting modes of deformation, can be expressed in a similar tensorial form:

$$\mathbf{M} = M_1(\mathbf{g}_1 \otimes \mathbf{g}_1) + M_2(\mathbf{g}_2 \otimes \mathbf{g}_2) + T_{12}(\mathbf{g}_1 \otimes \mathbf{g}_2 + \mathbf{g}_2 \otimes \mathbf{g}_1), \tag{3.9}$$

where M_1 and M_2 give the moments (per unit width) associated with bending the shell about the tangent axes perpendicular to the $\mathbf{g}_1$ and $\mathbf{g}_2$ directions respectively, and the term T_{12} reflects the moment (per unit width) resisting twist deformation between the two families, as defined above. Physically, the $\alpha\beta$-components of the $\mathbf{M}$ tensor in a two dimensional Cartesian coordinate system on the tangent plane give the magnitude of the moment (per unit width) acting about a tangent axis perpendicular to the α-direction, on a face perpendicular to the β-direction. This quantity represents a bending moment when $\alpha=\beta$ and a twisting moment otherwise. The bending moment M transmitted by the shell about an arbitrary tangent axis $\mathbf{b}$ is calculated as $M = |\mathbf{M}\mathbf{b}|$. This

moment has contributions from both the bending resistance of each yarn family and the twisting resistance between the yarn families.

The generalized forces corresponding to transverse shear and through-thickness stretch can be expressed by the quantities σ_{T1}, σ_{T2}, and σ_N, which give the transverse shear stresses along the ξ_1 and ξ_2 directions and the through-thickness stress respectively.

In order to describe the general response of an anisotropic shell, it is necessary to relate $\mathbf{M}$, $\boldsymbol{\sigma}^m$, the transverse shear stresses σ_{T1} and σ_{T2}, and the out-of-plane normal stress σ_N to the kinematic quantities $\mathbf{F}^m$, $\mathbf{B}$, the transverse shear strains ε_{T1} and ε_{T2}, and the through-thickness stretch λ_t.

In commercial finite element codes, these relationships are often derived by integrating the material response through the shell thickness. This approach is appropriate as long as the structure being represented by the shell is actually continuous and homogeneous through its thickness, or composed of multiple layers that are continuous and homogeneous. However, a fabric is not composed of layers of homogeneous media but rather is a very complex spatial structure that we are only approximating as a continuum shell. Therefore, these relationships cannot be calculated by integrating the material response through the shell thickness. Instead, it is necessary to establish appropriate constitutive relations either by deriving them from knowledge of the fabric structure or by experimentally measuring the response of fabric samples to simple modes of deformation. Because fabrics are an anisotropic material, these relations will depend on material directions—the orientations of the yarn families $\mathbf{g}_i$ within the plane of the fabric—that may evolve during the deformation process.

3.2 Limiting Assumptions

In order to relate the generalized shell forces to the shell deformations, we introduce a number of simplifying assumptions. First, we assume that the membrane response (the relationship between $\boldsymbol{\sigma}^m$ and $\mathbf{F}^m$) can be described by the planar fabric model described in Chapter 2, and that this relationship is not affected by out-of-plane deformations and loads. This implies that the membrane response described by the planar model for a fabric with a flat midsurface remains valid as the fabric is deformed out-of-plane and the midplane becomes curved. In other words, we neglect coupling effects that cause the membrane response to change as the fabric deforms out-of-plane. (Note that this assumption does not imply the converse; the anisotropic out-of-plane bending response will have a strong dependence on the current state of membrane strain, since membrane strain can change the orientations of the yarn families). The error associated with

this assumption should be small provided that the curvatures do not become excessively large; that is, as long as the radii of curvature ρ remain significantly larger than the yarn spacing $2p$ and the fabric thickness t, as shown in Figure 3-2. We expect this error to be especially small for loosely woven fabrics. More tightly woven fabrics might exhibit coupling between out-of-plane deformations and the membrane response as curvatures become large, since large curvatures could affect the manner in which the yarns jam against one another.

We choose not to define the shell thickness to be equal to the local fabric thickness, which varies in space due to the undulation of the yarns in the weave, but rather to have an initially uniform characteristic value t (which we take to be equal to the sum of the yarn thicknesses). In the cases we have examined, changes in fabric thickness tend to be small and are of little interest, so for simplicity we assume that this characteristic thickness remains constant, and we assume that through-thickness stresses have no effects on the other out-of-plane behaviors or on the membrane response. In cases where the through-thickness behavior is of interest, it can be readily measured using transverse compression tests of the sort described in Chapter 2 and related to the compaction of the crossover spring in the unit cell geometry shown in Figure 2-3.

As discussed in the preceding section, we expect transverse shear strains to remain small because fabrics are typically very thin compared to their other dimensions. Therefore, we assume that transverse shear is uncoupled from the other shell behaviors and relate transverse shear strains to transverse shear stresses assuming linear elastic behaviors, with very large stiffnesses.

Under these limiting assumptions, $\boldsymbol{\sigma}^m$ can be calculated from $\mathbf{F}^m$ by using the planar continuum fabric model. The through-thickness and transverse shear responses are controlled by simple relationships and are uncoupled from other modes of deformation. The final necessary components of the shell behavior are the relationships describing bending and twist.

3.3 Experimental Investigation of Bending

The bending of fabrics, especially fabrics woven from multi-fiber yarns, is a relatively complex phenomenon, even under the assumptions that curvatures are small enough so that linear elastic material laws and small-strain large-rotation theory can be used. Interfiber sliding and yarn friction effects create nonlinearities in the bending response of a multifiber yarn, as discussed by Grosberg [1966], even when the yarn is initially straight. The presence of initial curvatures of the yarns due to "set" induced by the weaving process introduces additional nonlinearities, as described by Sagar and Potluri [2004]. Hence we expect the moments about

tangent axes perpendicular to the yarn directions M_1 and M_2 to depend on curvatures of the yarn families κ_1 and κ_2 respectively in a nonlinear manner.

To determine M_1 and M_2, we must determine the moment-curvature relation per yarn associated with bending a fabric sample about a tangent axis orthogonal to a given yarn family. This relation is not the same as the relation associated with a single yarn isolated from the fabric; a woven fabric is stiffer (per yarn) than a single yarn due to various effects. For example, crossing yarns may provide some additional resistance to fabric curvature. Furthermore, the response of multi-fiber yarns is controlled by inter-fiber frictional effects and hence depends on the transverse forces on the yarns, which are greater in a fabric (also discussed by Grosberg [1966]). In addition to merely measuring or deriving a bending relation to be implemented in the shell model, it is important to understand the phenomena that control the bending response and to account for any deviations between the measured response and the values that can be predicted analytically. This will provide insight on how modifications to the fabric material or architecture will affect the fabric bending behavior and aid in the design of fabric technologies.

We first consider the bending response associated with a single yarn. In many fabrics, including the plain weave Kevlar® fabrics with which we are specifically concerned, the yarns are composed of a large number of untwisted circular fibers. The yarns have a fixed cross-sectional area (dependent on the number of fibers per yarn) but a variable cross-sectional shape, which is frequently approximated as ellipsoidal or lenticular. Kevlar® interfaces have a fairly low friction coefficient, which means that frictional forces between fibers in a yarn are typically small, especially when transverse forces on the yarn are also small. Although the bending response can be nonlinear and can include dissipative effects, we can determine upper and lower analytical bounds for the maximum and minimum bending stiffnesses associated with a single a yarn by considering bounding cases for which the response is linear elastic. The lower bound is calculated by assuming that the fibers which compose the yarn are all bent to the same radius of curvature, that the curvature is sufficiently small so that the individual fiber bending response can be described by small-strain, large-rotation theory with a linear elastic material law, and that the fibers do not interact (inter-fiber frictional forces are negligible). In this case the minimum bending stiffness of a single yarn (expressed as an effective value of the quantity (EI)) is the sum of the bending stiffnesses of its individual fibers:

$$(EI)_{\min} = n\frac{E\pi r_f^{\,4}}{4}, \tag{3.10}$$

where E is the modulus of the Kevlar®, r_f is the radius of the individual fibers, and n is the number of fibers per yarn. This quantity has units of [N-m^2]. The upper bound is calculated using

the same assumptions except that in this case we assume that the fibers cannot slip relative to one another (infinite friction) and hence the yarns act as if they were a homogeneous structure with the same cross-sectional shape (assumed to be ellipsoidal) that they have when woven in the fabric:

$$(EI)_{\max} = \frac{E\pi Rr^3}{4}, \tag{3.11}$$

where R and r are the major and minor radii of the yarns ellipsoidal cross sections respectively. Refer to Table 3-1 for the values of these bounds for the Kevlar® yarns under consideration.

The actual bending response of the single yarns was measured using two methods. In one method, tensile tests were performed on single yarns pulled from the fabric, as shown in Figure 2-5. The yarn response exhibits two regimes—a low-stiffness regime where the yarns straighten or "uncrimp", and a high-stiffness regime where the yarns stretch. The high stiffness regime shows that the Kevlar® yarns under consideration exhibit a linear elastic response up to their breaking strain. By employing knowledge of the initial crimped shape of the unloaded yarn, the low-stiffness portion of the force-displacement curves can be transformed into moment-crimp angle curves, and the bending response can be roughly estimated. This method was used to estimate the response of the bending springs in the unit cell for the planar model in Chapter 2. Only the responses (for both families) of the Kevlar® style S706 yarns were characterized using this method.

We developed a more direct method of determining the bending response of a single yarn. Samples were prepared by cutting rectangular specimens of fabric approximately 2.5 cm by 5 cm. These specimens have a known number of yarns N crossing their shorter dimension. Most of the yarns of the other family were removed, leaving only a narrow strip of woven fabric to hold the sample together. A sample of this type is shown in Figure 3-3. The parallel single yarns were then placed in an elongated three-point bending test apparatus (shown in Figure 3-4) and the bending response of the yarns was directly measured. The fabric thickness was approximately two orders of magnitude smaller than the test span and the vertical displacement of the center probe was limited to ranges where the curvature of the sample was smaller than the curvature of the probe, meaning that the contact area between the center probe and the yarns remained small relative to the test span. Consequently, we were able to use beam theory to calculate the effective bending stiffness per yarn of the sample:

$$(EI)_{eff} = \frac{1}{N}\frac{FL^3}{48d}, \tag{3.12}$$

where F is the measured force, L is the test span, and d is the displacement of the center probe. This test was performed on yarns from both families of both the Kevlar® styles S706 and S726.

The bending stiffness (per yarn) of the woven fabric was measured by cutting rectangular samples and testing them in the same elongated three-point bending, with the yarns of interest oriented perpendicular to the fixture's longer dimension. The samples were similar to those used to measure the stiffness of the individual yarns, except that the crossing yarns were not removed. Both Kevlar® styles S706 and S726 were tested in this manner.

Interestingly, the measured moment-curvature response of both the single yarns and the woven fabric for both Kevlar® styles was linear up to relatively large curvatures, though we do concede that our experiments to date are not exhaustive, and that there may be nonlinearities that manifest at larger curvatures or under different loading conditions. It is also possible that the nonlinearities described by other researchers are negligibly small for the plain weave Kevlar® fabrics that we consider.

Because the measured response is linear, we characterize the bending response with a single bending stiffness $(EI)_{eff}$. The measured stiffnesses for both the single yarns and the woven fabric samples are presented in Table 3-1. The single yarn stiffnesses measured by the two different methods are comparable for both the yarn families of the S706 fabric, although the data from the elongated 3-point bending tests was considered to be more reliable because it relies less on idealizations of the geometry. The single yarn stiffnesses for the S726 samples were measured using only the elongated 3-point bending test. For single yarns taken from both fabrics, the warp yarns were somewhat stiffer in bending than the weft yarns. One possible explanation for this is that the weft yarns are damaged during the weaving process; another is that the yarns of the two families have slightly different cross sectional shapes due to the geometry of the weave.

The measured values for the single yarn bending stiffnesses all lay between the analytically estimated bounds. One bound assumes frictionless behavior between yarn fibers, while the other assumes infinite friction. Grosberg [1966] has shown that the actual behavior, which corresponds to finite friction, should lie between the bounds, which is consistent with our experiments. In all cases, the measured stiffnesses of the single yarns were much closer to the lower bound, which implies that in single yarns isolated from a fabric, the frictional forces between the fibers are relatively small and the fibers tend to slide past one another when the yarn bends.

As expected, the fabric exhibited a stiffer bending response per yarn than the unwoven yarns did. For the S706 fabric, the per-yarn stiffness was approximately 2.2-2.3 times greater than the

stiffness of the unwoven yarns for both the warp and the weft yarn families. The S726 fabric also exhibited in increase in stiffness over the single-yarn stiffness; the increase in this case was between 1.9 and 2.1 times. However, the measured per-yarn bending stiffness values still fall between the analytically calculated lower and upper bounds.

As mentioned above, there are several possible reasons for the increase in bending stiffness when the yarns are woven into a fabric. Some of the increase in stiffness may be due to the presence of the crossing yarns. However, since these yarns consist of bundles of fibers aligned parallel to the bending axis, the additional bending stiffness from these yarns is likely small. A more probable explanation is that the transverse compressive forces on the yarns are greater when they are woven into a fabric. Consequently, the frictional forces between fibers are greater. Greater frictional forces result in greater interactions between the fibers, and the yarns behave more like solid beams and less like bundles of fibers. Therefore, their stiffness should increase, as Grosberg shows. This effect would be greater for a tightly woven fabric, which could explain why the tightly woven S706 exhibits a slightly greater increase in stiffness per yarn than the more loosely woven S726.

While we understand why the fabric has a larger bending stiffness per yarn than a group of individual yarns, the exact bending stiffness of the fabric is difficult to predict without using extremely detailed models of the interacting fibers. However, the bending stiffness can be analytically bounded, and because the mechanisms that control the bending stiffness are understood, relative changes to the bending stiffness resulting from changes to the yarn design can be predicted. For example, a coating applied to the yarns would increase inter-fiber interactions and the fabric's bending stiffness would increase, approaching the upper bound. If the fabric were wetted with a lubricant or woven more loosely, inter-fiber interactions would decrease, and consequently the fabric's bending stiffness would also decrease, approaching the lower bound.

Because the experiments indicate that the yarn moment-curvature relation remains approximately linear even at moderately large curvatures for the fabrics that we consider, we use this linear relation in our current shell implementation:

$$M_i = k_{Bi}\kappa_i = k_{Bi}\left(\mathbf{g}_i \cdot \mathbf{B}\mathbf{g}_i\right). \tag{3.13}$$

Here κ_i is the curvature of the fabric in the direction of the *i-th* yarn family, calculated using Equation (3.6), and k_{Bi} is the bending stiffness per unit width associated with the *i-th* yarn family given in Table 3-1. If a more complex relation is necessary to describe a given fabric, this relation can be readily modified.

3.4 Experimental and Numerical Investigations of Twist

Twist is the other mode of out-of-plane deformation that must be accounted for, but twist in woven fabrics is a very complex phenomenon. In order to better understand the kinematics of twist, we first consider several bounding cases of simple prototypical structures subjected to a state of pure twist. The first is the case of a continuous plate subjected to the pure twisting mode pictured in Figure 3-1. A continuous plate accommodates pure twist by developing gradients of in-plane shear strain that vary through the plate thickness. Shear strains are positive on one face and negative on the other. Twist is somewhat analogous to bending: bending of a plate is accommodated by in-plane normal strain gradients, while twist is accommodated by in-plane shear gradients. The twist stiffness of a plate is dependent on the shear modulus of the material; the bending stiffness of a plate is dependent on the Young's modulus.

The other bounding case is a material formed from two continuously distributed orthogonal families of non-interacting fibers with no supporting matrix. A sparsely woven fabric with circular, frictionless yarns that do not significantly interact might be approximated by this model. When these fibers are aligned with orthogonal directions ξ_1 and ξ_2, this structure has no resistance to twist as defined in Equation (3.7). Twist is accommodated by linear gradients of the out-of-plane fiber angles. Since the fibers do not interact, they are not subject to any local twisting about their own axes, and since this state of pure twist results in zero bending curvatures along the fiber directions, the fibers are not subject to any bending either. The structure accommodates twist with purely rigid body motions of the component fibers and hence has zero twist stiffness.

An intermediate case is that of a network of interwoven beams that are clamped together at their crossover points. A sparsely woven fabric in which the yarns do not rotate relative to one another at the crossover points (e.g. due to friction or to non-circular cross sectional shapes) would be approximated by this case. In this structure, twist is accommodated by linear gradients of the out-of-plane rotation angles of the beams as in the preceding case, but because the beams cannot rotate relative to one another at the crossover points, there must be a longitudinal gradient of the rotation of the beam cross sections along the beams' axes. The beams are therefore locally twisted about their longitudinal axes. The twist stiffness of the structure depends on the torsional stiffness (and hence on the shear stiffness) of the beams.

In order to understand the twist behavior of a fabric and to determine which of these prototypical cases best approximate the fabrics that we are considering, we constructed detailed finite element models of the fabric structure, shown in Figure 3-5. Both models represented flattened yarns woven in an initially orthogonal plain weave. The more densely woven model represents the Kevlar® S706 weave geometry. The more sparsely woven model has a similar

weave geometry except that the yarn cross sections are 50% smaller, which effectively eliminated all locking effects. Consequently, we were able to study the mechanisms that control twist in both densely and sparsely woven fabrics. The models use linear elastic transversely isotropic material models to simulate the yarns, since the yarns are much stiffer axially than in the transverse or shear directions. This material model is characterized by four moduli that correspond to the yarn stiffness in response to axial loading, transverse loading, longitudinal shear loading, and transverse shear loading, as shown in Figure 3-6. A "hard contact" algorithm is used to prevent interpenetration of the yarns, and tangential sliding is modeled using simple Coulomb friction. Contacting surfaces are permitted to separate after contact. Since the goal of these models is to obtain a qualitative understanding of the phenomena that govern twist at the structural level, we did not directly measure all the yarn properties or the friction coefficients. Estimated properties were sufficient for a qualitative understanding.

In order to study the mechanisms that resist twist deformation, we analyzed the stress fields that developed in the yarns and the elastic strain energy stored in the models (as predicted by the finite element code) when they are subjected to a state of pure twist. We also varied the elastic properties in order to determine which aspects of the yarn behavior impact the fabric's twisting mechanisms most significantly.

For the sparse fabric model, twist is accommodated by longitudinal gradients of cross sectional rotation of the yarns, as in the third prototypical case discussed above. Twist is accompanied by the buildup of axial stresses and longitudinal shear stresses. These stresses are shown schematically in Figure 3-7. The axial stresses indicated bending about an angled cross sectional axis, which is a mode other than torsion by which a beam-like structure with a non-circular cross section can accommodate a longitudinal gradient of cross sectional rotation. The shear stresses correspond to torsion about the yarn longitudinal axis, which is a more obvious mode of accommodating longitudinal gradients of cross sectional rotation. The energy stored within the sparse weave structure increases monotonically with twist angle, as shown in Figure 3-8, which is consistent with the observed monotonic increases in the stresses. Increasing the axial modulus or the longitudinal shear modulus of the yarns resulted in a significant increase in the stiffness of the structure since these moduli increase the bending and longitudinal twist stiffnesses respectively, while increasing the transverse modulus or the transverse shear modulus had little effect on the response. We conclude that a sparse fabric is closest to the intermediate prototypical case discussed above. Twist is accommodated by torsion and bending of the yarns, and any mechanism that increases the torsional or bending stiffness of the yarns will correspondingly increase the stiffness of the fabric twist response. Because the bending and

torsional stiffnesses of the individual multi-fiber yarns are relatively low, the twist stiffness of a sparse fabric will be fairly small.

The dense weave exhibits different behaviors. Because the weave is dense, the fabric is in a "locked" state in the untwisted configuration, meaning that there are compressive forces acting on the yarn cross sections even when the fabric is macroscopically unloaded. Accordingly, the model predicts compressive transverse stresses in the yarns in the untwisted configuration. As the twist is applied, these compressive transverse stresses actually decrease because the twisted configuration imposes less compaction upon the yarns and the compressed cross sections are allowed to relax. Because the yarns are under greater constraints in the dense weave, the bending and twisting modes of the individual yarns that were observed in the sparse weave are not possible. Instead, the only significant stresses that developed with the application of twist deformation were longitudinal shear stresses acting in the plane of the fabric. These stresses were positive on one face of the fabric and negative on the other, varying through the fabric thickness. A dense fabric therefore reacts to twist in a similar manner to the first prototypical case discussed above (a homogenous plate), where twist is accommodated by through-thickness gradients of in-plane shear strain.

As shown in Figure 3-8, the energy stored in a dense fabric is much higher that that associated with a sparse weave for equal twist angles, and does not increase monotonically with twist angle. The strain energy is initially nonzero (due to the initial state of yarn compression from locking). It initially decreases with twist, as the transverse from locking stresses relax, before the longitudinal shear stresses that result from the twisting deformation have increased significantly. The strain energy reaches a minimum and then increases when the loss in locking energy is exceeded by the increase in twisting energy. Variation of the elastic properties illustrates these trends. Increasing the transverse modulus shifts the minimum in the strain energy response curve to the right, since there is more compressive locking energy to be released, but the positively sloped portion of the curve exhibits the same stiffness (since this part of the curve reflects a stage when no additional transverse compression is relaxing). On the other hand, increasing the longitudinal shear modulus both shifts the minimum to the left, since the twisting energy accumulates faster, and increases the ultimate twist stiffness of the fabric. A minimum in the strain energy at a non-zero twist angle is also consistent with observations of the macroscopic behavior of the fabric. A small, flat sample of fabric tends to snap to a twisted "saddle" shape when perturbed. We conclude that the twist response of a densely woven fabric is controlled by two competing mechanisms—the relief of compressive stresses from locking and the build up of longitudinal shear stresses in response to twist. Initially the locking response dominates, which

means that a dense fabric is actually in an unstable configuration when flat and will tend to snap to a slightly twisted configuration. At larger twist angles, the resistance of the yarns to longitudinal shear dominates the twist response.

As was the case for bending, the twist stiffness of the fabric is very difficult to predict analytically. However, once the twist response has been measured, the effects on this response of changes to the yarn or weave structure can be predicted since the underlying controlling phenomena are understood.

We investigated two methods for measuring the twist behavior. First, we experimented with a "twist harness test" pictured in the lower inset in Figure 3-9. A harness consisting of a loop of thread is secured to each pair of opposite corners of a small fabric sample (approximately 2.5 cm x 2.5 cm), and a tensile tester applies load in opposite directions, creating a state of nearly pure twist. The second method uses a custom-built test apparatus shown in Figure 3-9. A fabric strip is clamped between a pair of grips. One grip slides and is tensioned by a dead weight that applies a small, constant tensile load to the sample while permitting axial stretching. The other is attached to a shaft with a cable wound around it; tension on the cable rotates the shaft with a moment proportional to the shaft diameter, while a counterweight applies a twisting load in the opposite direction. Because the mode of deformation created by this apparatus is not pure twist (as evidenced by the irregular deformed shape visible in Figure 3-9), the twist properties must be found by fitting the prediction of the shell model to the measured data.

The two methods for measuring the twist properties yield comparable results for the ultimate twist stiffness. However, the harness test results were difficult to reproduce consistently—slight variations in the initial configuration of the fabric sample caused significant variation in the measured results. The results of the twist tests performed on Kevlar® S706 using the twist apparatus are shown in Figure 3-10. This fabric has a dense weave, so we expect to see an instability at a twist angle of zero—small positive twist angles should result in a negative moment as the fabric snaps to a slightly twisted configuration. However, as can be seen from Figure 3-10, the forces associated with the instability and corresponding snap through are either negligibly small compared to the twisting forces that develop at even relatively small twist angles, or are counteracted by frictional effects and hence are not evident in the measured response. Instead, we see two regimes in the response—the fabric first provides negligible resistance to twist, and then (as the twist angle exceeds the angle that presumably corresponds to the energy minimum) the resisting moment begins increasing, approximately linearly. Since numerical implementation of the twist instability and any counteracting frictional forces would be challenging and computationally expensive, and would affect only a very small region of the twist response, we

do not include them in the material response that we implement into the shell model. Instead, we implement a bilinear twist response:

$$T_{12} = f_{bilinear}(\varphi_{12}) = f_{bilinear}(\mathbf{g_1} \cdot \mathbf{Bg_2} + \mathbf{g_2} \cdot \mathbf{Bg_1}); \tag{3.14}$$

with

$$f_{bilinear}(\varphi) = \begin{cases} k_0\varphi & |\varphi| \le \varphi_c \\ \left(k_T(|\varphi| - \varphi_c) + k_0\varphi_c\right)sign(\varphi) & |\varphi| > \varphi_c \end{cases}. \tag{3.15}$$

Here φ_c is the "critical" twist angle that corresponds to the point where the resisting moment begins to increase linearly (which is presumably close to the point of minimum strain energy), k_T is the stiffness associated with twist after the fabric has been twisted beyond φ_c, and $k_0 << k_T$ is a small positive number that imparts numerical stability at twist angles smaller than φ_c. This bilinear model allows a good fit of the experimental data shown in Figure 3-10 up to relatively large twist values (greater than 10 rad/m).

Note that when the appropriate twist properties given in Figure 3-10 are used, the shell model predicts the correct deformed shape for the specimen in the twist test apparatus, as shown in the upper inset in Figure 3-9. It is energetically more favorable for the sample subjected to twisting rotation at its ends to form triangular facets that accommodate the rotation through bands of localized twist and bending instead of through uniform twist deformation. This pattern was observed in the experiment and is well predicted by the shell model.

3.5 Implementation and Validation

The fabric shell constitutive relations discussed above were implemented into a pre-existing shell formulation in the implicit finite element code ABAQUS/Standard. We experimented with both "S4" and "S4R" shell elements, which are four node doubly curved elements with six degrees of freedom per node (three displacements and three rotations, although the so called "drilling" degrees of freedom—the rotations about the midsurface normal—have no associated stiffness in this implementation). The S4 elements are fully integrated while the S4R elements employ a reduced integration scheme (and hence hourglass control). Both are suitable for "thick shell theory" (i.e. they include transverse strains and through-thickness effects, although they approach the Kirchhoff limit as their thickness becomes small), and can be used for cases with finite membrane strains and large rotations. The two element types gave nearly identical results when membrane forces were large. When membrane forces were small, the fully integrated elements exhibited the same numeric locking-like behavior discussed in Chapter 2 and Appendix

C, and the reduced integration elements required hourglass stiffness to avoid the problem of spurious modes. However, for the load cases considered the locking errors were small and with the addition of hourglass stiffness the two element types performed comparably. We therefore used the S4R reduced integration elements for the bulk of our analyses due to their greater computational efficiency. The shell behavior was defined using a user-defined general shell section "UGENS" subroutine, which directly calculates the shell response characterized by σ^m, $\mathbf{M}$, σ_{T1}, σ_{T2}, and σ_t from $\mathbf{F}^m$, $\mathbf{B}$, ε_{T1}, ε_{T2}, and λ_t, along with any relevant state variables. The material constants were taken from Table 2-1, Table 3-1, and Figure 3-10.

We performed various experiments on complex out-of-plane behaviors of the fabric, and then simulated these experiments using the shell implementation to verify that the model correctly captured the observed fabric response. These experiments included bias-extension tests, shear frame tests (both of which are described in Chapter 2), and low-speed transverse indentation tests. All tests were performed using the Kevlar® fabric style S706.

In the bias-extension test, a rectangular strip of fabric at least with a length to width ratio of at least 3:1 is cut and loaded so that the yarn families are oriented at 45° to the loading direction. Its deformation is characterized by lateral contraction in the central region of the strip as the yarns rotate to align with the load. Once the jamming forces between the yarn families become large, the fabric buckles and develops a central wrinkle running along the length of the sample. The shell model predicted these deformation patterns well, as shown in Figure 3-11, provided that small out-of-plane perturbations of the initial strip configuration were applied to the model to initiate the buckling. These perturbations were approximately three orders of magnitude smaller than the dimensions of the strip. The specific post-buckled shape displays a limited dependence on the initial out-of-plane perturbation and on the level of mesh refinement, but the essential features of the buckled configuration remain realistic and consistent with the experiments.

As described in Chapter 2, bias extension tests do not generate consistent, repeatable load-extension data, since small variations in the orientation and the initial deformation state of the samples can significantly affect the measured responses. Figure 3-12 shows the experimentally measured bias extension responses that were within one standard deviation of the average. The load-displacement curve predicted by the shell model was consistent with the average experimentally measured response. The response predicted by the shell model is slightly less stiff than the response predicted by the planar model using a comparable mesh. This result is consistent with the fact that the shell model allows the additional wrinkling mode of deformation.

The second type of test that we considered was a shear-frame experiment. In this experiment, shown in Figure 3-13 , a cruciform-shaped sample is clamped into a frame with hinged corners.

Opposite corners are pulled apart, which subjects the fabric to a state of nearly pure yarn rotation with negligible extension along the directions of the yarn families. Consequently, these tests are well suited for measuring the response of the fabric to shear deformation. However, as the shear angle becomes large and jamming starts to dominate the in-plane response of the fabric, the fabric begins to wrinkle or buckle out of plane. The wrinkled shape (i.e. the buckling mode) is not the same in every test; it is very sensitive to defects in the fabric and variations in the manner in which the fabric is clamped within the frame. The magnitude of this effect also depends on the sample size and geometry and the applied shear angle. The test shown in Figure 3-13 shows certain buckled shapes starting to initiate in compression and tension, although the wrinkles here are relatively small in magnitude compared to the sample size.

The shell model captured the physically observed wrinkled shapes, again provided that small out-of-plane perturbations were initially applied to the model. As was the case in the bias-extension test, the specific buckled shape that occurred depended on the initial perturbation and the level of mesh refinement. Figure 3-14 shows examples of various wrinkled shapes exhibited by the fabric shell model when it was used to simulate the shear frame experiment, with deformations scaled for clarity. The lower energy modes, on the left of the figure, were consistent with the shapes actually observed in the experiments (the higher energy modes shown on the right did not physically occur). As in the bias-extension case, the load-displacement responses for the shear frame tests predicted by the shell elements were consistent with experimental measurements and slightly more compliant than those predicted by the planar fabric model.

We also performed and simulated a low-speed transverse indentation tests. A cruciform sample of fabric approximately 15 cm x 15 cm was clamped into a horizontal frame, and a 1 cm diameter probe was pushed 25 mm into the sample. The measured force-displacement curve was significantly less stiff than the predicted curve, presumably due to difficulties in uniformly pre-tensioning the sample. However, the simulation accurately predicted the rounded diamond shape of the z-direction contours shown in Figure 3-15, which occur because the fabric is anisotropic and stiffer along one yarn direction. These contours were made clearer on the actual sample by the addition of a small amount of fluid.

Ideally, we would like to have run more extensive validation cases, including composite forming analyses. However, as an implicit finite element code, ABAQUS/Standard is not well suited for large deformation shell analyses with complex contact conditions, and was unable to analyze such cases even for simple material models. We recommend the implementation of this shell model into an explicit finite element code in order to analyze a wider variety of large-deformation three-dimensional cases.

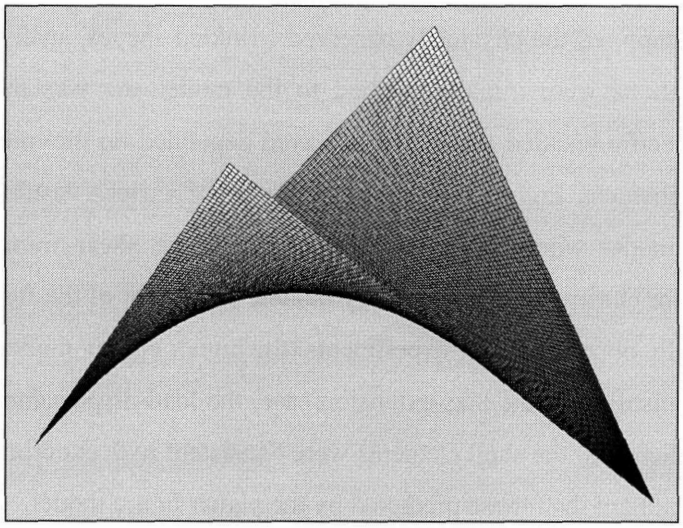

Figure 3-1 Saddle shape associated with pure twist

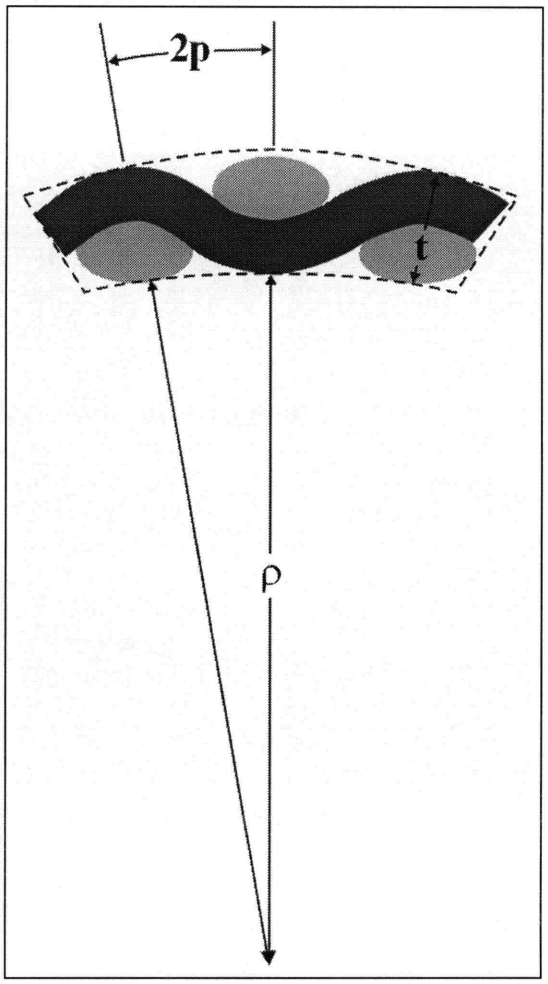

Figure 3-2 Comparison of characteristic fabric dimensions *p* and *t* to radius of curvature

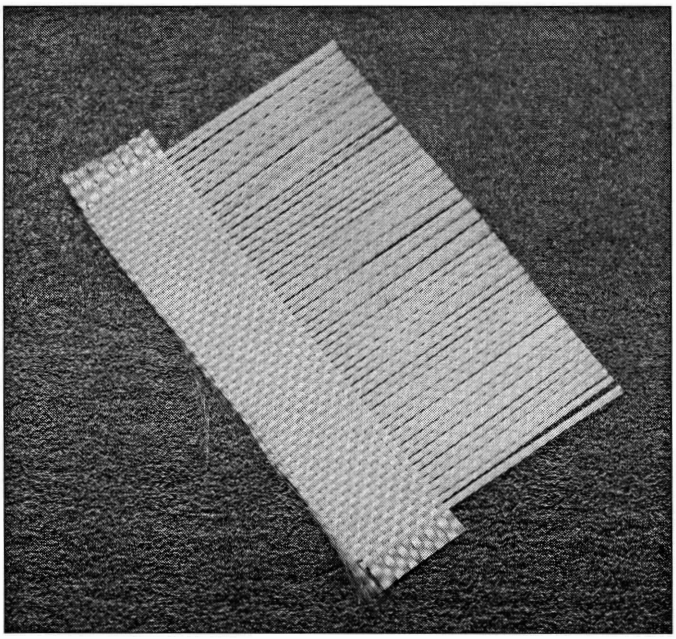

Figure 3-3 Sample used to measure single yarn bending stiffness in three point bend test

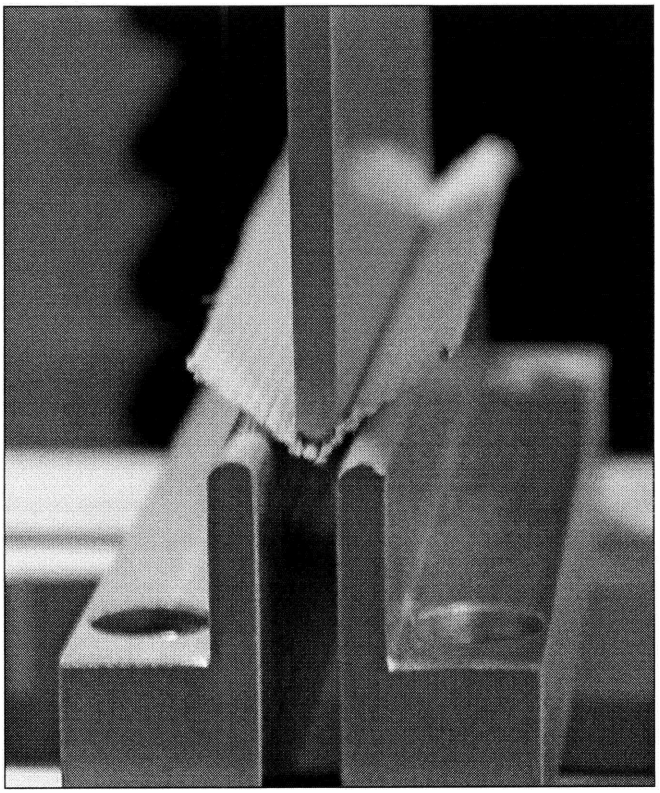

Figure 3-4 Fabric sample in elongated three-point bending apparatus

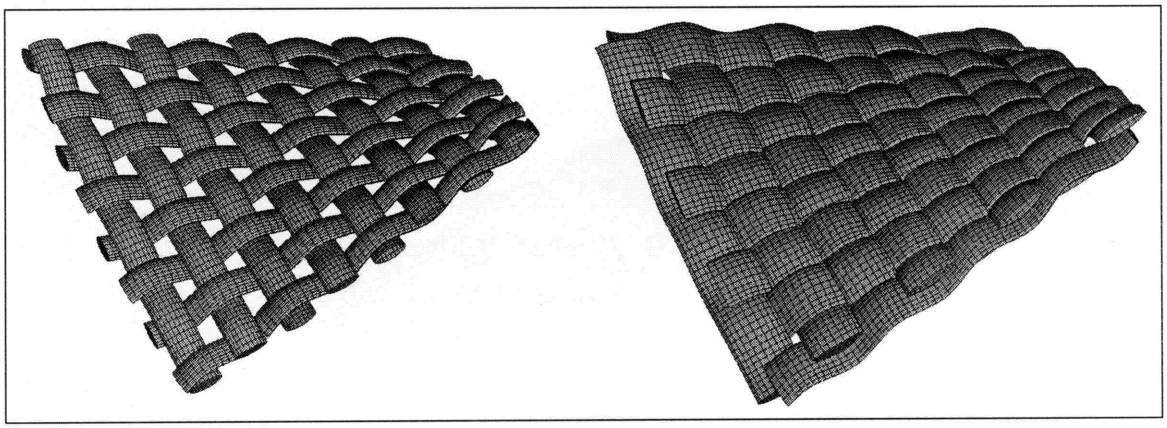

Figure 3-5 Detailed finite element models for analysis of twist in sparse and dense weave fabrics

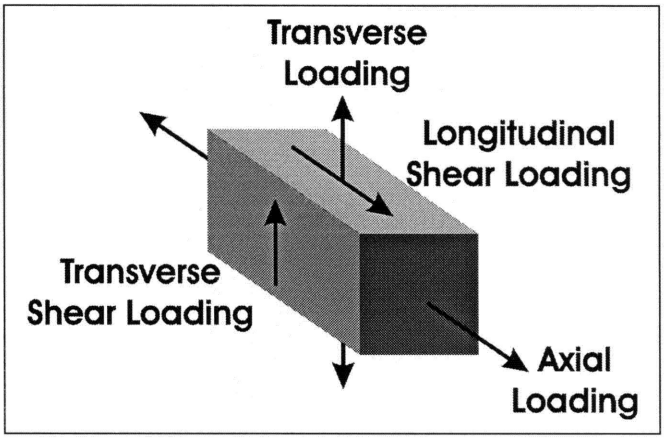

Figure 3-6 Different loading modes on a transversley isotropic material

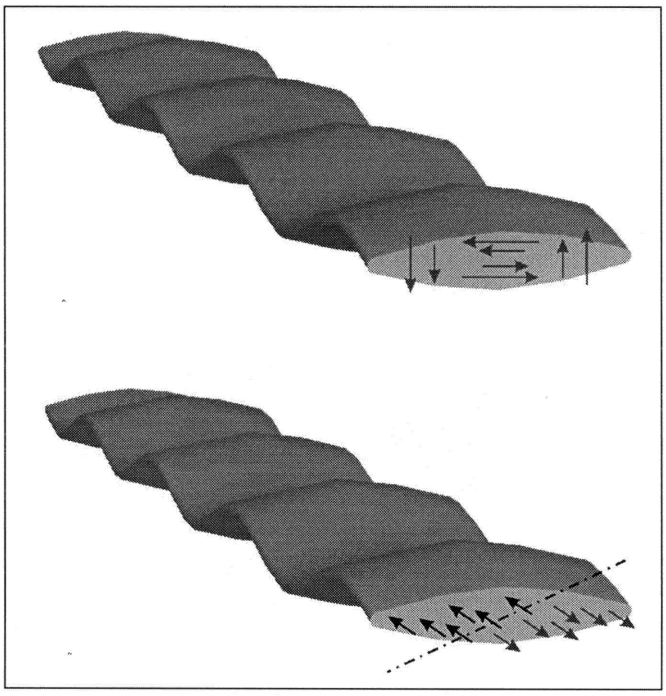

Figure 3-7 (Top) Shear stresses corresponding to twist about longitudinal axes; (Bottom) Axial stresses corresponding to bending about angled cross sectional axis

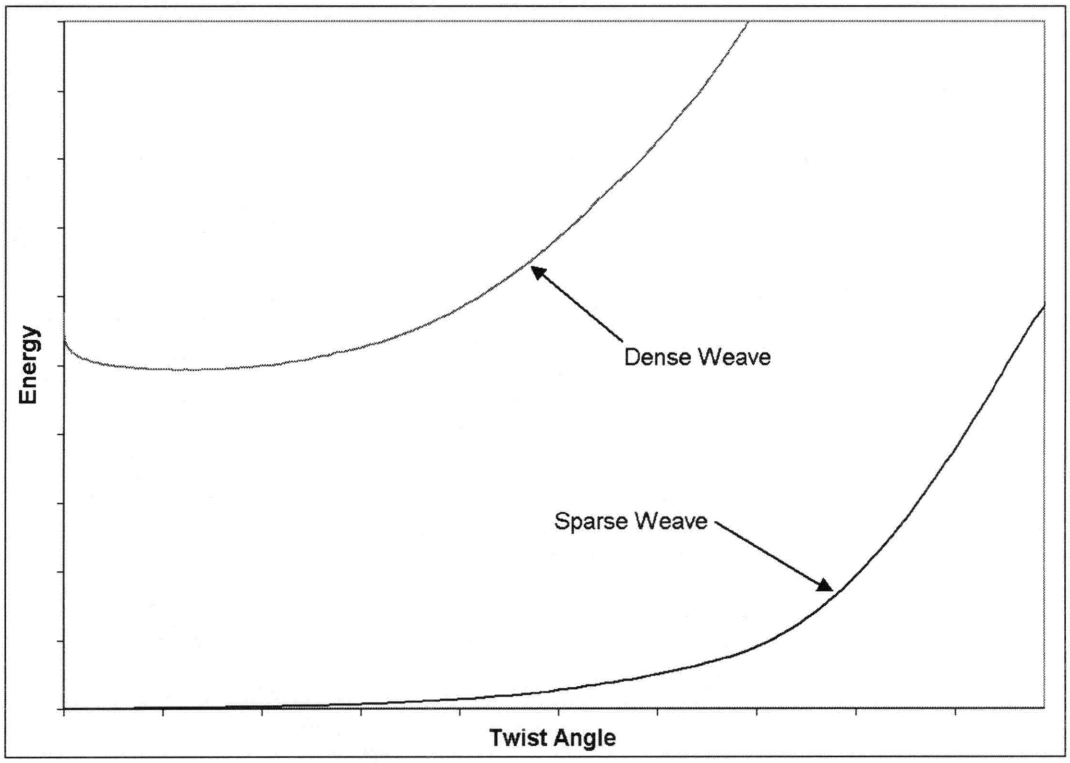

Figure 3-8 Strain energies associated with twist in detailed finite element models

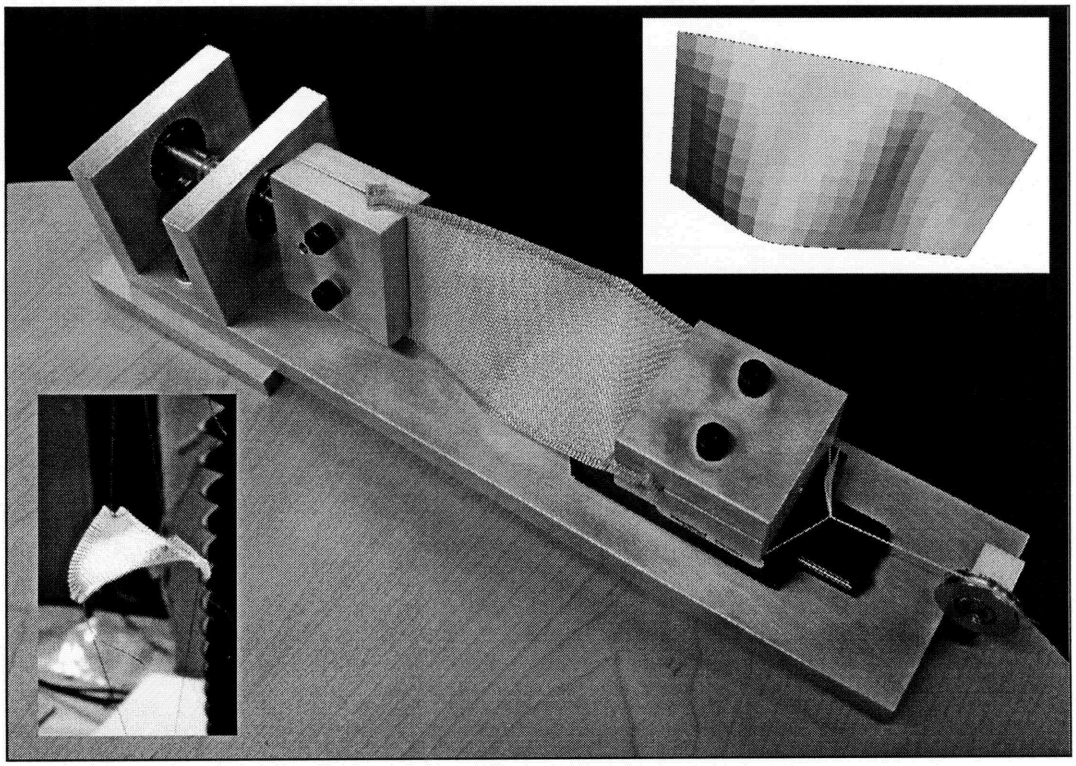

Figure 3-9 Twist test apparatus with corresponding model prediction of twisted shape (upper inset) and an alternative harness twist test method (lower inset)

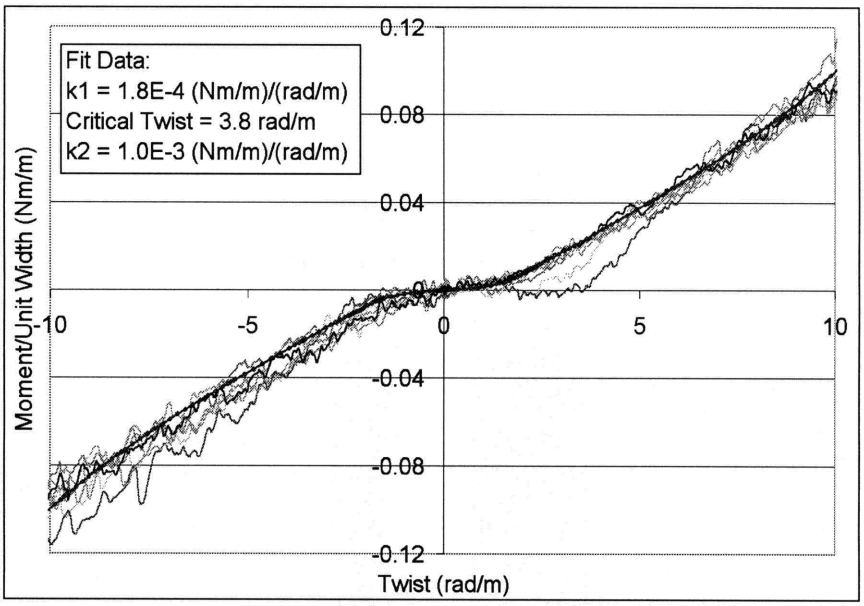

Figure 3-10 Twist test results and fitted model prediction

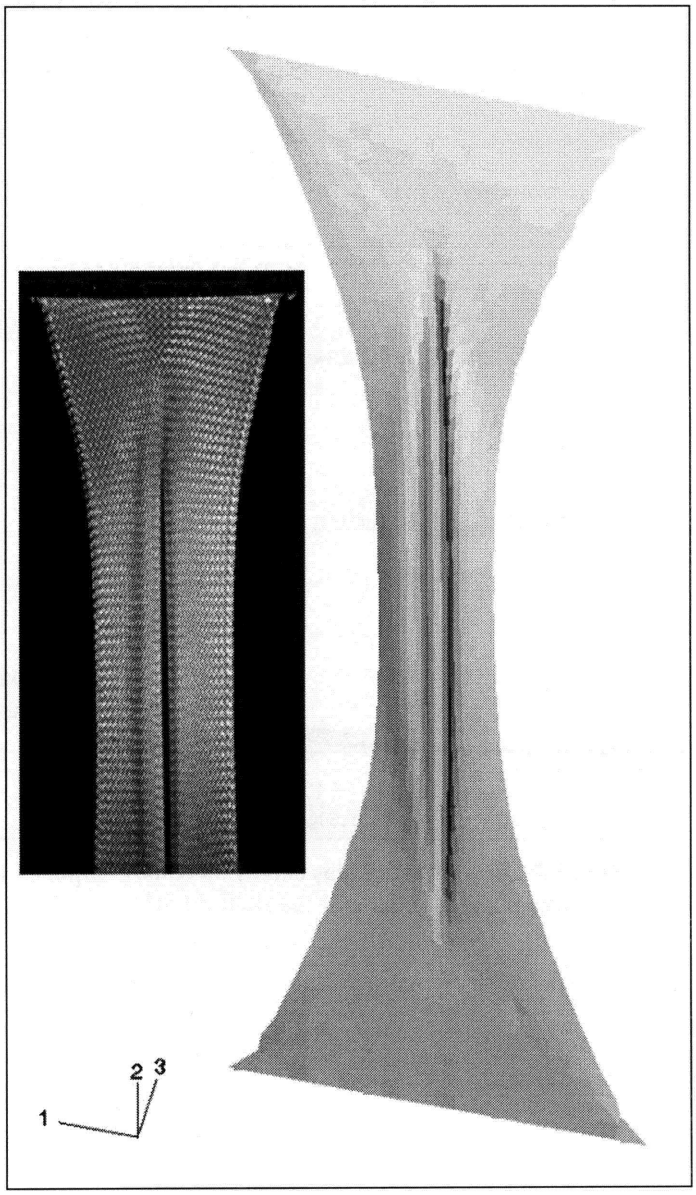

Figure 3-11 Wrinkled shape prediction for bias extension test with actual shape (inset)

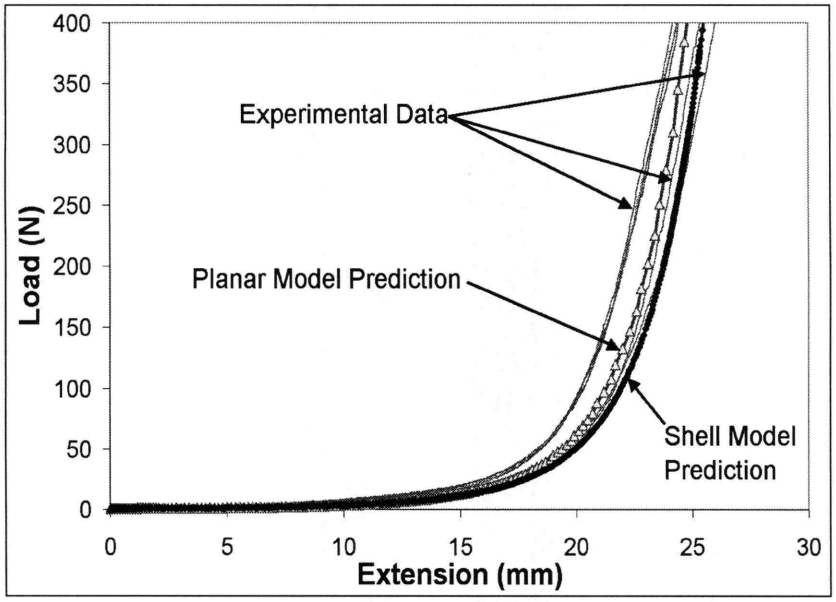

Figure 3-12 Typical load extension curves for the bias extension tests, compared to the predictions of the planar model and the shell model

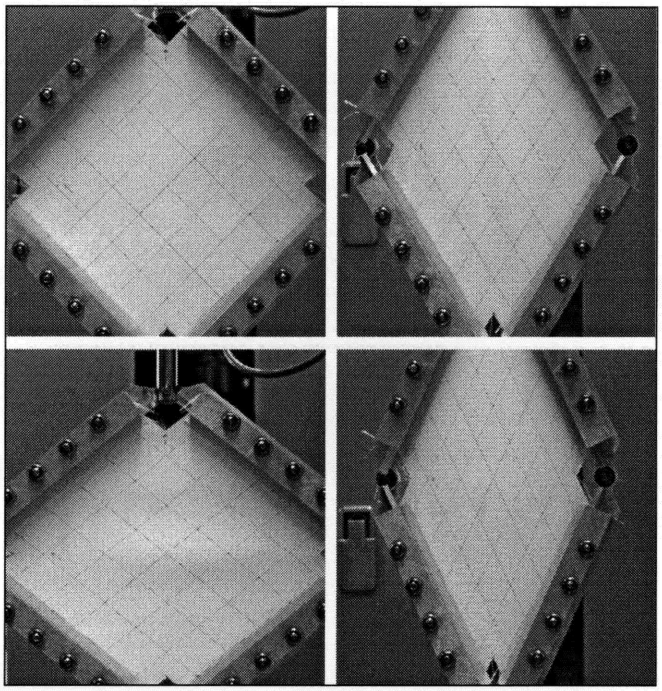

Figure 3-13 Shear frame experiments showing undeformed configuration (top left), deformed shape in compression (bottom left), and in tension (right)

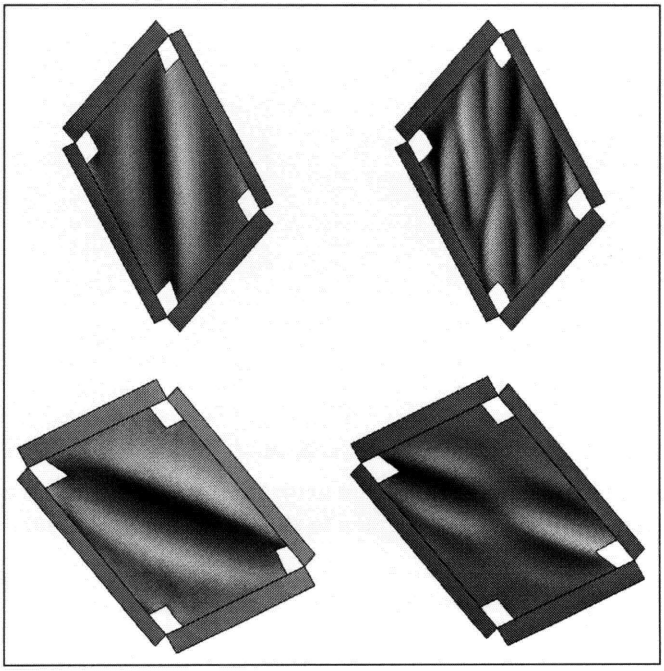

Figure 3-14 Different wrinkled shapes exhibited by the fabric shell model in shear frame experiments during extension (top) and compression (bottom) (deformations scaled for clarity)

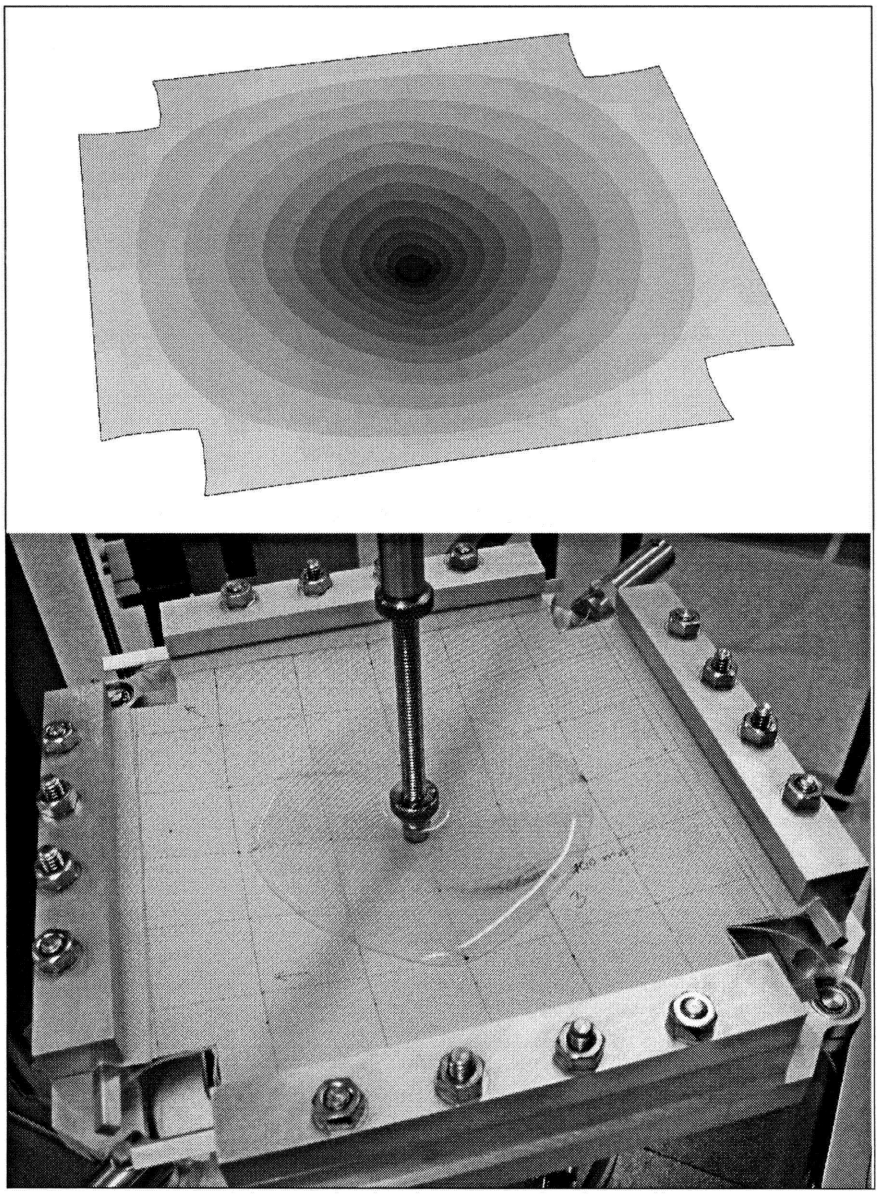

Figure 3-15 Predicted deformation contours and actual deformed shape in transverse indentation test (fluid added to specimen to show z-direction contour)

Table 3-1 Bending Properties of Kevlar Yarns and Fabrics

	Fabric Style S706		Fabric Style S726	
Material	Kevlar® KM2		Kevlar® 129	
Modulus (GPa)	85		98	
Fiber Diameter (μm)	12		12	
Fibers per Yarn	400		560	
Thread Count per cm	13.4		10.2	
Yarn Minor Radius (mm)	0.075		0.075	
Yarn Major Radius (mm)	0.196		0.273	
	Bending Stiffnesses (EI/yarn) Nm^2			
	Warp Yarns	Weft Yarns	Warp Yarns	Weft Yarns
Lower Analytical Bound	3.46×10^{-8}		5.58×10^{-8}	
Unwoven Yarn (from tensile test)	1.56×10^{-7} $\pm 5.94 \times 10^{-8}$	9.30×10^{-8} $\pm 7.69 \times 10^{-9}$	N/A	N/A
Unwoven Yarn (from 3-point bending test)	1.52×10^{-7} $\pm 3.64 \times 10^{-8}$	7.37×10^{-8} $\pm 1.58 \times 10^{-8}$	1.58×10^{-7} $\pm 2.62 \times 10^{-8}$	9.52×10^{-8} $\pm 1.12 \times 10^{-8}$
Fabric (from 3-point bending test)	3.40×10^{-7} $\pm 1.39 \times 10^{-8}$	1.69×10^{-7} $\pm 7.59 \times 10^{-9}$	3.40×10^{-7} $\pm 1.93 \times 10^{-8}$	1.78×10^{-7} $\pm 1.49 \times 10^{-8}$
Upper Analytical Bound	5.53×10^{-6}		8.86×10^{-6}	

Chapter 4
Experimental Investigation of Slip

4.1 Overview of Slip in Fabrics

Yarn slip in fabrics in plays an important role in a variety of applications, especially in studying the impact of a projectile on a woven ballistic armor, as described by Termonia [2004], and in the forming of a fabric composites. Yarn slip also plays a key role in the concentration of yarn tensions near damaged regions in the fabric and in the propagation of damage, as described by Godfrey and Rossettos ([1998] and [1999]). Slip is also the primary mechanism by which failure occurs in the bias-extension test described in Chapter 2—large locking force gradients cause yarns to slip out of the weave at the edges, the weave unravels, and the samples are pulled apart. However, yarn slip in fabrics is very difficult to characterize experimentally. Yarn slip is resisted by frictional interactions both with neighboring yarns and the crossing yarns over and under which the slipping yarns is woven, but these interactions are extremely complex and depend strongly on the configuration of the weave mesostructure.

Various methods have been proposed for studying these frictional interactions. Rebouillat [1998] describes a series of experimental studies of the tribological properties of Kevlar® yarns, especially the yarn-to-yarn frictional coefficients and the fabric surface frictional coefficients at different rates. However, because of the complex geometry of contact areas between yarns in a fabric, the frictional effects that control yarn slip in a fabric are difficult to predict from friction coefficients measured for individual yarns. A number of different researchers, including Pan and Yoon [1993] and Shockey *et al.* [2001], have conducted yarn pullout tests, which are another method of experimentally quantifying frictional effects that control yarn slip. In these tests, one or more yarns are pulled from a fabric sample and information about the frictional resistance to the slip of the pulled yarn can be inferred from the measured pullout response. We have employed both these methods in order to gain a qualitative and quantitative understanding of the frictional forces that resist yarn slip.

4.2 Yarn-to-Yarn Friction Measurement

We first measure the yarn-to-yarn frictional resistance between yarns that have been removed from the fabric, following a protocol recommended by ASTM standards. Contact between the

yarns is achieved by twisting them around one another. The yarns are subjected to very different loading conditions when they are woven into a fabric: the contact areas have different sizes and orientations, the yarn cross sections may be different shapes, and the yarns are subjected to different tensions and transverse compressive forces. Consequently, we cannot quantitatively predict the resistance to slip in a fabric from the coefficients of friction measured in this type of test. However, we can use this test to characterize the qualitative frictional behavior of these yarn materials—i.e. to determine what friction coefficient values are reasonable for these yarn materials, and whether or not frictional effects associated with the yarn materials exhibit rate dependence.

The American Society for Testing and Materials describes a test method for determining the coefficient of friction between two yarns in ASTM D3412-01: *Standard Test Method for Coefficient of Friction, Yarn-to-Yarn*. The apparatus recommended by ASTM is shown schematically in Figure 4-1. A yarn is passed through a sequence of pulleys and twisted around itself to form a yarn helix. As the yarn is pulled through the apparatus at a constant rate, an input tension T_i is applied at one end, and the output tension T_o is measured at the other end. (Rebouillat [1998] uses a slightly different method to measure yarn-to-yarn friction, where yarn is wrapped around a drum and another yarn is pulled over the drum. This method is also described in ASTM D3412-01). According to the ASTM standard, the yarn-to-yarn friction coefficient μ can be calculated from the tension differential as follows:

$$\mu = \frac{\ln \dfrac{T_o - \Delta T/2}{T_i + \Delta T/2}}{2\pi n \alpha}, \tag{4.1}$$

where ΔT is the tension differential measured when the yarn is not twisted about itself. ΔT results from frictional resistance in the pulleys. The parameter n is the number of times the yarn is twisted about itself, and α is the apex angle given by:

$$\alpha = 2\tan^{-1}\left(\frac{H}{V-W}\right), \tag{4.2}$$

where H, V, and W are geometric parameters that relate to the dimensions of the test apparatus shown in Figure 4-1.

We designed and built a modified version of this test apparatus, shown in Figure 4-2, that has the ability to adjust the apex angle α. The upper part of the apparatus is connected to the lower part via a pair of threaded rods that allow for the height V to be varied. Additionally, the spacing between the pulleys $2H$ can be varied by attaching the pulleys in different holes along the apparatus. The input tension T_i is applied by hanging a weight from one end of the yarn. The

fixture is attached to the lower grip on a tensile tester and the yarn is clamped in the upper grip and pulled through the apparatus by the tensile tester crosshead. The tensile tester load cell is used to measure the output tension T_o.

The ASTM equations given above encompass certain simplifying assumptions. We re-derive the equation for the friction coefficient μ in order to identify these assumptions and ensure that they are valid for our modified fixture. We assume that the twisted yarns forms a helix as shown in Figure 4-3, and that the helix is oriented vertically. Note that the tensions T_1 and T_4 acting on the yarns as they enter and exit the helix respectively are not necessarily equal to the input and output tensions T_i and T_o, and that the intermediate tensions T_2 and T_3 are not necessarily equal to each other, because there may be frictional resistance in the pulleys.

A helix is defined by the following set of parametric equations that depend on the total rotation angle θ about the central axis:

$$\begin{aligned} x(\theta) &= R\cos\theta \\ y(\theta) &= R\sin\theta, \\ z(\theta) &= c\theta \end{aligned} \tag{4.3}$$

where R and c describe the radius and the pitch of the helix respectively. At any given point in the helix, the radius of curvature is given by:

$$\rho = \frac{R^2 + c^2}{R}, \tag{4.4}$$

and the arc length associated with a differential change in θ is:

$$d\ell = \sqrt{R^2 + c^2}\, d\theta. \tag{4.5}$$

This differential section $d\ell$ passes through angle $d\phi$, given by:

$$d\phi = \frac{d\ell}{\rho} = \frac{R}{\sqrt{R^2 + c^2}} d\theta. \tag{4.6}$$

The helix parameters R and c can be related to the apex angle α in the following manner. At the point where the yarn first enters the helix, where $\theta = 0$, the slope of the yarn must be continuous, so the following relation must hold:

$$\cot\frac{\alpha}{2} = \left.\frac{dz}{dy}\right|_{\theta=0} = \left.\frac{c\ d\theta}{R\cos\theta\ d\theta}\right|_{\theta=0} = \frac{c}{R}. \tag{4.7}$$

Some algebraic manipulation allows $d\phi$ to be expressed as a function of α and $d\theta$:

$$d\phi = \sin\frac{\alpha}{2} d\theta. \tag{4.8}$$

We now consider a balance of forces on the differential yarn section shown in Figure 4-4. We assume that one end of the section is subjected to tension T, and the other end to tension $T + dT > T$; tension increases in response to shear loads from frictional effects. Frictional effects exert a shear force per unit length $\tau = \mu\sigma$ acting parallel to the contact area, where σ is the force per unit length acting normal to the contact area, and μ is the friction coefficient that we are attempting to measure. Taking $d\phi$ to be small and dT to be negligible compared to T, a balance of forces in the radial direction gives:

$$\begin{aligned} (T + T + dT)\sin\left(\frac{d\phi}{2}\right) &= \sigma d\ell \Rightarrow \\ \sigma &= \frac{T}{\rho} \end{aligned} \qquad (4.9)$$

In the tangential direction, balance of forces gives:

$$\begin{aligned} T + \tau d\ell - (T + dT) &= 0 \Rightarrow \\ \mu\sigma\rho d\phi - dT &= 0 \Rightarrow \\ \frac{dT}{T} &= \mu d\phi = \mu \sin\frac{\alpha}{2} d\theta \end{aligned} \qquad (4.10)$$

For each full twist, the total θ–range through which the yarns pass increases by 2π radians for each side of the helix. If we assume that the pulleys that lie between T_2 and T_3 are frictionless (so that $T_2 = T_3$), and that all the remaining pulley friction ΔT is evenly divided between the pulleys before the helix and the pulleys after the helix (so that $T_4 = T_o - \Delta T/2$ and $T_1 = T_i + \Delta T/2$) , we can integrate Equation (4.10) to find the tension differential that results in the test:

$$\begin{aligned} \int_{T_3}^{T_4}\frac{dT}{T} + \int_{T_1}^{T_2}\frac{dT}{T} &= 2\int_0^{2\pi n}\mu \sin\frac{\alpha}{2} d\theta \Rightarrow \\ \mu &= \frac{\ln\dfrac{T_o - \Delta T/2}{T_i + \Delta T/2}}{4\pi n \sin\dfrac{\alpha}{2}} \end{aligned} \qquad (4.11)$$

For small helix angles α, this equation is identical to Equation (4.1), the equation given in the ASTM standard. However, as we have noted, this equation is valid only as long as the helix is vertical, the pulleys between T_2 and T_3 are frictionless, and α is small. While it is relatively easy to ensure that the helix remains vertical during the test, the other two assumptions may not hold in our modified apparatus.

We therefore modify the ASTM equation to be correct for our apparatus. Since there are two pulleys each between T_i and T_1, between T_2 and T_3, and between T_4 and T_o, we assume that each

pair of pulleys contributes one third of ΔT; therefore, $T_1 = T_i + \Delta T/3$, $T_3 = T_2 + \Delta T/3$, and $T_o = T_4 + \Delta T/3$. It follows from Equation (4.10) that $T_2/T_1 = T_4/T_3$, which allows us to calculate T_2 knowing ΔT, T_i, and T_o:

$$T_2 = \frac{-\Delta T/3 + \sqrt{\Delta T^2/9 + 4\left(T_i + \Delta T/3\right)\left(T_o - \Delta T/3\right)}}{2}, \tag{4.12}$$

and hence calculate μ:

$$\mu = \frac{\ln \dfrac{T_2}{T_i + \Delta T/3}}{2\pi n \sin\dfrac{\alpha}{2}}. \tag{4.13}$$

We conducted a series of tests at different rates, for different numbers of twists n. All tests were conducted with the same V and H values; however, the helix angle α varied because W depends on n. We conducted tests at 10, 100, and 1000 mm/min, with one, two, and three twists (which correspond to n = 0.5, 1.5, and 2.5 respectively, because the first half twist brings the yarns into contact but does not wrap them about one another). No tests were conducted with one twist at 10 mm/min. The results of these tests are summarized in Table 4-1.

The tests with more than one twist gave far noisier and more variable data, presumably because in these tests the yarn fibers tended to become entangled throughout the helix. Interestingly, the friction coefficients calculated for these tests were lower than those corresponding to the single twist tests (n = 0.5), in spite of the fact that the single twist tests had fewer visible fiber entanglements. This may be due to the fact that, with only half a twist, the geometry of the twisted yarns is not really a double helix and hence Equation (4.10) may not be an accurate means for calculating the friction coefficient μ. Since the difference in calculated μ between two twists and three twists is smaller than the difference between one and two twists, the data may be converging as the number of twists increases. The ASTM standard recommends using three twists (n = 2.5) to measure μ.

The three-twist tests indicate a friction coefficient of μ ~ 0.27. This value is consistent with the values reported by Rebouillat [1998]. There appears to be some slight rate dependence of the friction coefficient μ—for example, as the rate is increased from 10 to 1000 mm/min, the coefficient increases from ~0.25 to 0.29 for the cases with three twists. This trend is apparent for all three sets of tests with different numbers of twists. However, the increase is so small relative to the variance of the test results that rate dependence of the friction coefficient cannot be conclusively established. The measured rate dependence is on the order of a 5-10% increase in μ

per order of magnitude increase in slip rate. Although Rebouillat observes little rate dependence of μ over speed ranges of 96 mm/min to 600 mm/min for the particular yarns that he considers, he states that Kevlar® yarns are known to exhibit an increase in the friction coefficient at increasing rates.

4.3 Yarn Pullout Tests

Yarn pullout tests are a more attractive method for investigating the phenomenon of yarn slip in woven fabrics, because they directly cause yarns to slip through a weave. In these tests, a fabric specimen is loaded to some fixed load or displacement in a direction parallel to one of its yarn families, and then a yarn or yarns of the other family are pulled from the weave at a constant rate. Since the macroscopically measured pullout force at any given time depends on the embedded length of the pulled yarn, which is a well defined value, and on the frictional resistance to slip at each crossover point along the embedded length, information about frictional resistance to slip within a fabric at different rates can be determined from such tests.

We have developed two different test methods for performing yarn pullout tests. The first utilizes a biaxial tensile testing machine, shown in Figure 4-5. The biaxial machine can independently apply displacements and measure loads on two different axes. For these tests, rectangular strips of Kevlar style S706 fabric are prepared that are approximately 30 cm long and 12 cm wide, with the yarns that are to be pulled out aligned along the shorter dimension. Crossing yarns (parallel to the long direction) are removed until exactly 85 remain, with a 12.7 mm "tail" on one side of the sample and approximately 5 cm of loose yarn on the other side. As many crossing yarns as possible are used in order to maximize the measured forces during the test; for this particular fabric, samples with more than 85 crossing yarns require pullout forces that can locally exceed the breaking strength of the yarns. The sample is clamped in the biaxial tester with its longer dimension parallel to the machine's x-axis, and with the tail oriented away from the machine's y-axis load cell. The sample is loaded to a target cross load by x-direction displacement, which is then held constant throughout the test. The y-displacements of the x-axis grips are coupled to the moving y-axis grip using a set of linkages, and one or more of the yarns parallel to the machine's y-axis are clamped in the static y-axis grips that are attached to the load cell. Applying y-direction displacement causes the sample to be pulled away from the clamped yarns, and as the yarns are pulled from the fabric the pullout force is measured. Tests can be performed with cross loads varying from initial values of 100 to 500N, at speeds between 5 and 50 mm/min.

This test apparatus suffered from several shortcomings. First, the biaxial machine was designed to test much larger loads (in the range of ~10-100 kN) than those that occur during the pullout test (~0-50 N), so there is significant noise in the measured data. Secondly, the biaxial machine is capable only of displacement control, meaning that the applied displacement in the cross direction is held constant but the applied cross load can vary throughout the test. Because of the crimp-interchange mechanism by which a fabric transfers load from one yarn family to the other, a constant cross displacement causes the applied cross load to increase as the pullout force increases, and the average cross loads over the course of the tests are therefore larger than the nominal cross loads at the start of the test. Ideally, the test should be performed under constant cross load conditions. Finally, the biaxial machine is driven by mechanical screws and is capable of a maximum pull speed of 50 mm/min; ideally, we would like to test at much faster load rates to better investigate rate dependence of the frictional behavior.

We therefore designed a special fixture to address these concerns, shown in Figure 4-6. The fixture attaches to the lower grip of a Zwick uniaxial tensile tester. A sample of the same type described above is clamped between two sliding grips. Pneumatic air cylinders attached to these grips are pressurized to apply a constant cross load, between 90 and 900 N. One of the yarns is then gripped in the tensile tester's upper grip and pulled from the sample, at load rates up to 2000 mm/min. The Zwick supports smaller load cells, and hence this apparatus is capable of measuring the pullout forces much more accurately at a wider range of load rates than the biaxial apparatus, under constant cross load rather than constant displacement conditions.

We performed tests using both methods. The results of these tests are described in Section 4.5. Because of the shortcomings of the biaxial apparatus, we consider the data measured using the pneumatic fixture on the Zwick uniaxial test machine to be the more accurate.

4.4 Analytical Model of Yarn Pullout

Throughout the pullout process, the number of crossover points through which the embedded yarn passes and the force required to pull the yarn through these points are both known. Although some researchers (e.g. Pan and Yoon [1993] or Shockey *et al.* [2001]) suggest that the total resistance to slip will be proportional to the embedded length, the nonlinearity of the force-displacement response exhibited in many cases indicates that this is unfortunately not the case. This nonlinearity was also observed by Shockey *et al.* [2001], who suggest that it results from differences in the static and dynamic friction response of the yarns, or from local relaxation of the fabric around the yarn as it is pulled out. While these effects certainly may contribute to

nonlinearity of the response, they do not fully account for it. Even without these effects the pullout response is nonlinear in most cases due to an effect sometimes called the "capstan effect". The pulled yarn is not straight but is bent over and under a succession of crossing yarns, as shown in Figure 4-7. The conditions along the pulled yarn are not uniform; tension increases from zero at the free end to the total pullout force at the gripped end, while the crimp decreases over the same embedded length. The frictional forces resisting slip depend on contact force between the pulled yarn and the crossing yarns, and hence on the tension and the crimp angle of the pulled yarn. Since both these parameters vary along the yarn, the frictional resistance at the crossover points also varies along the pulled yarn in a complex manner. Therefore, the frictional resistance to slip at a given crossover point cannot be determined simply by dividing the total pullout force by the number of crossover points the pulled yarn passes through.

We have developed an analytical model that predicts the nonlinear yarn pullout response from a set of geometric assumptions and from a hypothesized constitutive law describing the frictional resistance to slip at each crossover point. By fitting the predictions of this model to experimentally measured pullout data, a suitable yarn slip constitutive law can be determined. The model is derived in the following manner. We start by considering the n^{th} crossover point from the free end along the slipping yarn. A simplified representation of the forces acting at this crossover point is shown in Figure 4-8. The slipping yarn is being pulled through this crossover point at a constant velocity v^{slip}. We refer to the direction along the slipping yarn towards which it is moving as "downstream," and the opposite direction as "upstream". The crossover point downstream of point n is point $n+1$. We next assume that, at a given instant in time, the geometrical configuration of the yarns can be represented using a truss-like geometry shown in Figure 4-9, where all the yarn bending is concentrated at the crossover points. This geometry is the similar to the truss geometry used in Chapter 2 to represent the weave mesostructure in the fabric continuum model. Trusses represent both the yarns and also the lines of contact force between yarns.

We define the following parameters for the analytical pullout model. At any given crossover point n, we designate the crimp amplitude of the slipping yarn as A_n, the length of the slipping yarn between crossover point n and point $n+1$ as $2L_n$, the in-plane spacing between the yarns that cross at n and at $n+1$ as $2p_n$, and the angle the slipping yarn makes with the fabric plane immediately downstream of crossover point n as the crimp angle β_n. Similarly, we designate the amplitude of the crossing yarn family at n to be A_{cn}, the crossing yarn length between crossover point n and the neighboring crossover points as $2L_{cn}$, the in-plane spacing between the sliding yarn and its neighbors as $2p_{cn}$, and the angle that the crossing yarn makes with the fabric plane

between the slipping yarn and its neighbors as the crossing crimp angle β_{cn}. Using this geometry, we can express β_{cn} in terms of L_{cn} and A_{cn}:

$$\sin \beta_{cn} = \frac{A_{cn}}{L_{cn}}. \tag{4.14}$$

Because the amplitude of the sliding yarn may vary from one crossover point to the next, the yarn length and crimp angle of the slipping yarn, $2L_n$ and β_n, both depend on the amplitude A_n at point n and the amplitude A_{n+1} at the downstream crossover point, as well as on the in-plane yarn spacing p_n:

$$\tan \beta_n = \frac{(A_n + A_{n+1})}{2p_n}, \tag{4.15}$$

$$(2L_n)^2 = (2p_n)^2 + (A_n + A_{n+1})^2. \tag{4.16}$$

We next define the forces acting at the crossover point. The yarn slipping through the weave is under tension T_n just downstream of crossover point n. Because there are forces f_n^R acting on the yarn that resist slip, the tension in the yarn on the "upstream" side of the crossover point T_{n-1} must be less than the downstream tension T_n in order to satisfy equilibrium under steady-state conditions (no acceleration) and maintain a constant slip velocity. Furthermore, unless the crimp amplitude is zero, the yarns make an angle with the fabric plane, and therefore there also must be a net normal force F_{Nn} acting between the slipping and crossing yarns to counteract the out-of-plane components of the yarn tensions. Note that the net forces f_n^R and F_{Nn} are not actually point loads but rather represent the net effect of the complex pressure and shear stress distributions over all the interfaces between contacting yarns.

In densely woven fabrics like the one shown in Figure 4-8, the "locking" or "jamming" phenomenon described in Section 1.2 occurs. Because the yarns are interwoven, they can jam against one another, compacting their yarn cross sections and increasing the fabric resistance to further deformation. This state can occur even when the fabric is macroscopically unloaded; such a fabric is said to be "pre-locked". Locking can significantly increase the size and change the orientations of the contact surfaces between yarns, and can apply additional contact pressures over these surfaces. Hence locking will affect both F_{Nn} and f_n^R.

We capture locking effects in the manner detailed in Chapter 2, by placing trusses along the lines of contact between the yarn cross sections. The same nonlinear locking force relation that is used in the continuum model is used in this simple analytical model to describe the load in these trusses:

$$F_L = \begin{cases} 0 & d_L \le 0 \\ K_L\left[R_c^e(\alpha, r, R) + r - d_L\right]^a & d_L > 0 \end{cases}, \tag{4.17}$$

where K_L and a are material properties determined from picture-frame shear tests described in Chapter 2. The parameter d_L is the length of the locking truss, and R_c^e and α are parameters that relate to the geometry of the locking truss and the interference between the contacting yarn cross sections (which are assumed to be oval shaped). At a given crossover point n, these parameters are:

$$d_{Ln} = \sqrt{A_{cn}^{\ 2} + p_n^{\ 2}}, \tag{4.18}$$

$$R_{cn}^e = \sqrt{(R\cos\alpha_n)^2 + (r\sin\alpha_n)^2}, \tag{4.19}$$

$$\alpha_n = \tan^{-1}\frac{A_{cn}}{p_n}, \tag{4.20}$$

where r and R are the minor (through-thickness) and major radii of the oval yarn cross sections, respectively. Refer to Chapter 2 for further description of this locking model.

We next introduce a number of simplifying assumptions. First, we assume that the tensions in the crossing yarns T_{cn} are the same at all crossover points along the sliding yarn. Furthermore, we assume that these tensions remain constant throughout the experiment:

$$T_{cn} = \text{constant} \equiv T_c. \tag{4.21}$$

For the pneumatic fixture, which applies a constant load to the crossing yarns, this assumption should be accurate provided that the grips holding the sample are correctly aligned. For the biaxial machine, which applies a constant cross displacement rather than a constant cross load, this assumption will not be strictly true.

Next, we assume that the axial stiffnesses of the yarns are sufficiently large so that the changes in yarn length due to yarn stretching are negligible. Therefore, any extension along a yarn family must occur through the flattening of the crimp in the yarns (a decrease of A and a corresponding increase of p). This assumption is reasonable because the axial stiffnesses of the Kevlar® yarn segments between crossover points are large, on the order of 1 x 10^7 N/m, while the loads in this test are very small compared to this stiffness, less than 50 N. We also assume that, because they are under tension, the yarn cross sections are sufficiently resistant to compaction in the fabric's through-thickness direction that the sum of the crimp amplitudes of the sliding yarn and the crossing yarn (i.e. half the fabric thickness t) at any given crossover point remains constant, regardless of the tensions and crimp angles at that crossover point:

$$A_n + A_{cn} = \text{constant} \equiv \frac{t}{2}. \tag{4.22}$$

This assumption is consistent with experimental observations: while the cross sections do compact and change their shape under load, the total changes in the fabric thickness tend to be small.

Next, we assume no slip occurs in the direction parallel to the crossing yarns. This assumption, when coupled with the negligible yarn stretch assumption, has the important implication that the length of the crossing yarns between crossover points L_{cn} must be the same at every crossover point along the sliding yarn and remains constant throughout the analysis:

$$L_{cn} = \text{constant} \equiv L_c. \tag{4.23}$$

Finally, we assume that the spacing between the crossing yarns $2p_n$ is the same at every crossover point along the sliding yarn and remains constant throughout the analysis:

$$p_n = \text{constant} \equiv p \tag{4.24}$$

In other words, we expect differences in the fabric shear angle along the sliding yarn to be small.

We derive the analytical model by enforcing equilibrium at each crossover point along the yarn. In the direction normal to the fabric plane, equilibrium implies:

$$T_n \sin\beta_n + T_{n-1} \sin\beta_{n-1} + F_n^N = 2T_c \sin\beta_{cn} + F_{cn}^N. \tag{4.25}$$

Here F_n^N and F_{cn}^N are through-thickness forces that arise from effects other than the out-of-plane components of yarn tension. Although these components are generally small compared to the components that stem from yarn tensions, they are important near the free end of the slipping yarn where tensions are small. They originate primarily from yarn bending and locking effects:

$$F_n^N = F_0 + \frac{k_b\left(\beta_n - {}^0\beta\right)}{L_n}\cos\beta_n + \frac{k_b\left(\beta_{n-1} - {}^0\beta\right)}{L_{n-1}}\cos\beta_{n-1}, \tag{4.26}$$

$$F_{cn}^N = F_0 + \frac{2k_{bc}\left(\beta_{cn} - {}^0\beta_c\right)}{L_c}\cos\beta_{cn}. \tag{4.27}$$

Here k_b is the bending stiffness of the yarns, ${}^0\beta$ gives the reference crimp angle corresponding to zero bending moment in the yarn, and F_0 gives the component of the through-thickness force that stems from non-bending effects, such as the out-of-plane component of the locking forces. We expect this term to be much smaller than the other terms thus neglect it. We define F_{Nn} to be the net through-thickness force acting between the yarn families, and define it as the average of the out of plane contributions of each yarn family (which should be equal, according to Equation (4.25)):

$$F_{Nn} \equiv \frac{\left(T_n \sin\beta_n + T_{n-1}\sin\beta_{n-1} + F_n^N\right) + \left(2T_c \sin\beta_{cn} + F_{cn}^N\right)}{2}. \tag{4.28}$$

In-plane equilibrium along the slipping yarn gives:

$$T_n \cos\beta_n = T_{n-1}\cos\beta_{n-1} + f_n^R. \tag{4.29}$$

The resistance to slip f_n^R, which is the net in-plane effect of all forces acting on the sliding yarn, must counteract the change in the in-plane projection of the yarn tension across the crossover point. In general, f_n^R will depend on the specific geometry of the contacting regions and the exact pressure distributions. In our simplified model we express it as a function of the normal force between the yarn families F_{Nn}, the locking force F_{Ln}, and the geometry of the weave as characterized by A, β, L, and p, and the rate of slip v^{slip}. This function is the constitutive law that must be characterized.

If we assume that a given constitutive relation allows f_n^R to be calculated, we can combine it with equilibrium Equations (4.25) and (4.29), the constitutive relations for locking and bending given in Equations (4.17), (4.26), and (4.27), the geometric relations in Equations (4.14), (4.15), and (4.16), and the simplifying assumptions in Equations (4.21), (4.22), (4.23), and (4.24) to generate a system of two equations at each crossover point. These equations depend only on constitutive parameters, known constants, and on T_n and A_n (the downstream tension and amplitude of the slipping yarn) and on the neighboring values T_{n-1}, A_{n-1}, and A_{n+1}, (the upstream tension and the amplitudes of the pulled yarn at the upstream and downstream crossover points, respectively). If we then consider a yarn that passes through N crossover points, with T_n and A_n as two unknown degrees of freedom at each crossover point, we get $2N$ equations that depend on $2N+3$ unknowns. The extra unknowns, A_0, A_{N+1}, and T_0 are boundary values that describe the amplitudes at each end of the sliding yarn and the tension just upstream of the last crossover point.

If suitable boundary conditions are defined, then the number of unknowns is reduced to $2N$ and the system can be solved to determine the tension and geometry at every point along the slipping yarn. However, rather than solve a system of $2N$ nonlinear equations simultaneously, we make one additional simplification. We assume that the changes in crimp along the pulled yarn are gradual, so that the relative change in crimp amplitude between adjacent crossover points is small:

$$\frac{|A_n - A_{n\pm1}|}{|A_n|} << 1 \quad \Rightarrow \quad A_{n\pm1} \approx A_n \tag{4.30}$$

While this assumption holds, Equations (4.15) and (4.16) become:

$$\tan\beta_n \approx \frac{A_n}{p}, \tag{4.31}$$

$$L_n^{\,2} \approx p^2 + A_n^{\,2}. \tag{4.32}$$

For the particular experimental cases that we have examined, this assumption is reasonable. In all cases the maximum change in amplitude between adjacent crossover points is less than 4% the size of the smallest predicted amplitude at any point along the pulled yarn, which corresponds to negligible errors in crimp angle, yarn length, and tension.

The simplification allows the system to be solved recursively, since the equations at a given crossover point no longer depend on the conditions downstream of that crossover point. Provided the upstream tension and amplitude corresponding to the n^{th}-*1* crossover point are known, a system of two equations at the n^{th} crossover point can be used to calculate the downstream tension and amplitude at that crossover point. This procedure can be repeated for each of the N crossover points. The tension downstream of the N^{th} crossover point is the applied tension necessary to pull the yarn from the weave when it passes through N crossover points. By performing this procedure for N = {1,2...} and then converting the different values of N into embedded lengths (by multiplying N by the crossover point spacing $2p$), the force-displacement curve necessary to pull a yarn at a constant velocity from the fabric corresponding to a proposed constitutive law can be determined.

We next define suitable boundary conditions at the free end of the yarn. We assume that before passing through the $n=1$ crossover point, which we define as the first crossover point where equilibrium Equations (4.25) and (4.29) are satisfied, the sliding yarn passes over a yarn at $n=0$, as shown in Figure 4-10. Because the sliding yarn does not pass around the crossing yarn at $n=0$ as it does at all other crossover points, but merely bends against it, we expect a different set of equilibrium conditions be satisfied. The tension upstream of this crossover point will be zero, since the end of the yarn is free, but a small tension T_0 just downstream of this crossover point may exist due to frictional interactions where the yarns contact. Furthermore, the yarn will be bent about the $n=1$ crossover point so that there is some crimp angle just upstream, β_0, and an amplitude A_0 that corresponds to that value of β_0 consistent with Equation (4.15). As long as T_0 is small, the model is relatively insensitive to these boundary conditions, especially if locking effects are non-negligible. Nevertheless, they must be defined realistically.

Since we assume the crossing tension T_c to be non-negligible and since the tensions in the sliding yarn are very small at the $n=0$ crossover point, we assume the crossing yarn will be almost straight, with crimp amplitude A_{c0}=0. We apply the constant thickness assumption,

Equation (4.22), and take A_0 to be approximately $t/2$. We estimate the downstream tension T_0 to be approximately half what it would be at any other crossover point with $T_{n-1} = 0$ and $A_{n-1} = t/2$, since both locking effects and normal forces at this crossover point will be approximately half as large (because the yarn only is bent around on one side of the crossover point). For reasonable constitutive laws with realistic friction coefficients, this gives a $T_0 \sim 0.01$ N, which is consistent with the last non-zero force measured in the pneumatic apparatus pullout tests before the yarn is pulled completely from the weave.

For any given constitutive law relating f_n^R to forces F_{Nn} and F_{Ln}, geometric parameters A, β, L, and p, and slip velocity v^{slip}, the analytical model can be used to predict the yarn pullout force-displacement curve. By comparing this curve to experimentally measured curves corresponding to different applied cross loads and pull speeds, an appropriate constitutive relation can be developed.

4.5 Experimental Results

We conducted a series of yarn-pullout experiments using both the biaxial machine and the pneumatic fixture on the Zwick uniaxial tensile tester. All samples had 85 crossing yarns and 12.7 mm tails. On the biaxial machine, we conducted tests with 100 N, 300 N, and 500 N nominal axial cross loads, although because the machine was displacement controlled, the cross loads increased as load was applied to the pulled yarn and hence the actual average cross loads were somewhat higher. Tests were conducted at pullout rates of 5 mm/min, 27.5 mm/min, and 50 mm/min. On the Zwick machine we conducted tests with constant cross loads of 100 N, 300 N, and 500 N, at rates of 5 mm/min, 50 mm/min, and 500 mm/min.

A typical pullout response from the biaxial machine is shown in Figure 4-11. Because of the load cells on the biaxial machine were designed to measure much larger loads than these, the data from these tests was very noisy; the curve in Figure 4-11 has had this noise filtered out. A typical curve from the Zwick machine is shown in Figure 4-12. The loads shown in this figure are lower than those in Figure 4-11 because this particular test was performed with a smaller cross load. No filtering of the Zwick data was necessary because the load cells on the Zwick machine are more precise. In some of the Zwick experiments, photos were taken of the sample as the yarn was pulled out using a camera that was synchronized with the test machine. Selected photos are also shown in Figure 4-12.

Both sets of experiments show a steep initial increase in load as displacement is applied to the gripped yarn that is to be pulled out. Some of the displacement during this initial load ramp is due

to flattening of the crimp in the pulled yarn as it is loaded, and some is due to shearing of the sample (since the crossover yarns apply frictional resistances normal to their orientation in the unloaded configuration, some shearing is necessary so that they can support these loads). Both phenomena are visible in the photographs in Figure 4-12. Once a critical load is reached, the load abruptly drops as the yarn starts to slip. This drop may indicate that dynamic frictional resistances are smaller than static frictional resistances. A period of relatively constant load follows as the tail is pulled into the sample and the yarn slips through the fabric under steady state conditions—we refer to this constant load as the "steady-state pullout force". As the tail enters the sample, the load begins to drop in a nonlinear manner—we refer to this region of the response as the "pullout region".

Because the load cell on the Zwick machine was more sensitive than that on the biaxial machine, no noise filtration was necessary and it was possible to see oscillatory peaks in the pullout response at the 5 mm/min and 50 mm/min test rates (the machine sampling rate was not sufficient to see these peaks clearly in the 500 mm/min tests). These peaks are not experimental noise. They occur because the yarns have some set to them—an unloaded yarn pulled from the fabric retains some crimp. As these yarns are displaced so that their set undulations become out of phase with the undulations imposed by the weave, bending forces cause the total pullout force to increase. When the phase shift reaches the point where the imposed undulations are exactly opposed to the set undulations (i.e. after the slipping yarn has slipped a distance equal to the spacing of the crossing yarns), the bending forces tend to drive the slipping yarn to the next position which aligns the undulation phase, and the load drops. This continues until the total distance slipped equal twice the crossing yarn spacing, at which point the process starts to repeat. This accounts for the fact that the wavelength of the oscillations in the load-displacement response is, on average, 1.5 mm, almost exactly double the spacing of the crossing yarns. Because the pulled yarn is under larger tension near the gripped end and therefore straighter with less crimp than it is near the free end, the set undulations do not have exactly the same period at all locations along the length of the pulled yarn, which accounts for the double peaks evident near the beginning of the load displacement curve when tensions are largest. These double peaks occur because not all of the set undulations are in phase with the weave-imposed undulations at the same time. These oscillatory peaks allow us to verify the accuracy of the assumption described in Equation (4.24), that the spacing of the crossing yarns remains constant along the pulled yarn throughout the analysis. The data implies that it is not strictly accurate because the wavelength of the oscillations of the load-displacement exhibited a slight but consistent increase from the

beginning to the end of the tests. However, the change in wavelength is less than 5% over the course of any test.

Only 40 to 41 peaks appear on average during the pullout region after the tail has been pulled into the sample. The length of the this region is only 60 to 61 mm on average before the pullout load reaches zero. With a yarn spacing of 0.747 mm, this corresponds to about 80 to 82 crossing yarns, which is consistent with the 40 to 41 observed peaks. However, all samples were prepared with 85 crossing yarns. The reasons for the discrepancy can be discerned from the photographs in Figure 4-12. When the force reaches zero, a small length of the pulled yarn is still embedded in the sample, passing over and under several crossing yarns. These crossing yarns likely impart negligible resistance to slip because the yarns are composed of many small, untwisted fibers. Near the end of the yarn, where tensions are very low, there are no forces that tend to preserve the shape of the yarn cross section or cause the fibers to interact. The fibers are splayed apart, and hence the locking forces on the pulled yarn vanish and the bending stiffness of the pulled yarn drop almost to zero. The drop in bending stiffness of a multi-fiber yarn that results from the removal of transverse forces is discussed in Section 3.3. With negligible locking and bending forces, very little tension builds up in the yarn near the free end. Therefore, even though the yarn passes through 85 crossing yarns, the last few have almost no effect on the response and only about 80 to 82 are effective. Also, in some cases, one or more crossing yarns would separate from the others at the very beginning of the test and slip down along the tensionless yarn tails. Such a yarn is also evident in Figure 4-12. This also reduces the number of effective crossing yarns that the pulled yarn passes through.

We first hypothesized that the frictional resistance to slip, f^R, could be decomposed into a component f_N^R that depends on the normal force at a crossover point F_N, and a component f_L^R that is independent of the normal force and that stems primarily from locking effects:

$$f^R = \hat{f}_N^R(F_N) + f_L^R . \tag{4.33}$$

The first constitutive relation that we explored was one where f_N^R was proportional to the normal force with a rate-dependent constant of proportionality μ_N, and where f_L^R was a constant f_0. The property μ_N was assumed to vary with slip velocity v^{slip} only. Using this relatively simple relation, the analytical model predicted a nonlinear pullout response that can be fit to the experimental data very well, as shown in Figure 4-13. The analytical model does not, of course, predict the oscillations in the response that come from yarn set. Increasing the constant f_0 scales the entire response since it increases the resistance at every crossover point equally, while increasing μ_N changes the degree to which the "capstan effect" causes a nonlinear buildup of tension and hence

changes the nonlinearity of the pullout region. A large f_0 and a small μ_N result in a nearly linear curve; a larger μ_N and a smaller f_0 that predict the same steady state pullout force predict a far more nonlinear drop in the pullout region. The analytically predicted response can be fitted to any experimental response by adjusting these two constitutive parameters so that the analytic model predicts the same steady state pullout force and the same pullout work from the point where the tail enters to sample to the point where the force reaches zero—the area under the pullout curve. This ensures that the correct amount of overall scaling and nonlinearity has been achieved.

These parameters were calculated for every experiment performed on the biaxial machine, which were completed first. The resulting values are shown in Figure 4-14, with f_0 plotted against μ_N. By assuming that μ_N varies linearly with slip rate, a simple rate dependent constitutive law was established:

$$\begin{aligned} f^R &= \left(\tilde{\mu} v^{slip} + \mu_0\right) F_N + f_0 \\ &= \left(21.333\left[\frac{s}{m}\right] v^{slip} + 0.0612\right) F_N + 0.050[N] \end{aligned} \tag{4.34}$$

The parameter f_0 was estimated by averaging the f_0 data from all experiments, while the parameters $\tilde{\mu}$ and μ_0 were determined by averaging the μ_N data at each rate. This one constitutive law was then used to predict the pullout response for a variety of different load cases. These responses are compared to the experimentally measured responses in Figure 4-15. In most cases, the analytical model predicts the experimentally observed pullout curves remarkably well, even with this very simplistic constitutive model.

However, the data implies that a more sophisticated model may be necessary. As is evident in Figure 4-15, the response is overpredicted for some cases with a 100 N nominal cross load. Figure 4-14, which shows all the measured μ_N and f_0 values, also implies shortcomings in the simple constitutive law. On this plot there are negatively sloped isolines that characterize pairs of properties (μ_N, f_0). All property pairs falling on one of these lines will predict the same total steady state pullout force for a given applied cross load, but with different amounts of nonlinearity of the pullout curve. Lines further from the origin correspond to larger steady state pullout forces. Ideally, if this constitutive law was sufficiently descriptive, all the values from experiments conducted at the same rate should occupy a single point—there should only be one common pair of values at any given slip rate. This was not the case. Most of the values corresponding to the 300 N and 500 N nominal cross loads did fall on one isoline, meaning that properties measured from these experiments all predict the same steady state pullout force for a given applied cross load, although they imply different degrees of nonlinearity of the pullout

curve. Since the fitting process is relatively sensitive to the nonlinearity of the curve, scatter along this line is not surprising—small changes in the nonlinearly of the curve can produce large variations in the fitted properties. However, experiments conducted with a 100 N nominal cross load consistently fell on a different isoline, closer to the origin. These tests required a very different set of material properties in order to get a good fit. This is also evident from Figure 4-16. This figure plots the observed steady-state pullout force as a function of applied cross load per crossing yarn, along with the prediction of the analytical model based on the constitutive law given in Equation (4.34). While the prediction fits the measured data relatively well for the cases with 300 N and 500 N nominal applied cross loads, it significantly overestimates the steady state pullout load foe the cases where the nominal applied cross load was 100 N. Since constitutive properties should not vary depending on the loads that are applied, we concluded that a more sophisticated constitutive law was necessary.

We hypothesized that the deficiency in the simple constitutive law related to the resistance that stems from locking, f_L^R. As the cross load is decreased, the fabric is compacted less and locking forces become smaller, and hence we would expect f_L^R to decrease. However, the constitutive law given in Equation (4.34) treats f_L^R as constant, independent of the locking forces. This could explain why the model overpredicts the frictional resistance for the cases where the cross load is only 100 N. Fortunately, the locking force F_L can be calculated from the analytic model, using Equation (4.17). We therefore proposed a more realistic constitutive law that includes the effect of locking force variation where resistance f^R is proportional to both normal contact force F_N and the locking force F_L:

$$f^R = \hat{\mu}_N\left(v^{slip}\right)F_N + 2\hat{\mu}_L\left(v^{slip}\right)F_L. \tag{4.35}$$

This law provides a much better fit of the biaxial data. Not only did the fitted property pairs (μ_N, μ_L) from the biaxial tests fall on the same isoline when plotted against each other, as shown in Figure 4-17, but the analytical prediction of the steady state pullout force as a function of cross load, using averaged μ_N and μ_L data, did not significantly over- or underestimate the experimentally measured results, as shown in Figure 4-18.

4.6 Interpretation of Experimental Results

Using this constitutive model, we analyzed the data from the Zwick tests and determined μ_N and μ_L pairs for each experiment that fit the analytically predicted response to the experimental measurements. The resulting data for both the Zwick and the biaxial experiments are given in Figure 4-19, although the Zwick data is considered to be more accurate. Nearly all the (μ_N, μ_L)

pairs fall on the same isoline, indicating that, with this constitutive model, the analytical model predicts the same steady state pullout forces for nearly all the experiments conducted at the same cross load. Only the cases with the highest displacement rates and smallest cross loads (500 mm/min and 100 N, respectively) have a different steady-state response. These cases indicate a significantly larger value of μ_N and a significantly smaller value of μ_L, and a larger steady state force.

The fitted values are also shown in Figure 4-20 and Figure 4-21, plotted against slip velocity. The component of slip resistance that depends on the normal contact force F_N increases slightly with slip rate. The average value of μ_N measured from the Zwick experiments increases approximately 3% from 0.086 to 0.089 when the rate is increased from 5 to 50 mm/min, and approximately 20% from 0.089 to 0.107 when the rate is increased from 50 to 500 mm/min, although the data measured at this rate was far more variable. This is roughly consistent with the increase in the friction coefficients measured in the yarn-to-yarn frictions tests described in Section 4.2, which increased approximately 4% when the rate was increased from 10 to 100 mm/min, and approximately 10% when the rate was increased from 100 to 1000 mm/min. However, the increase in μ_N at higher rates is somewhat larger than might be expected from the yarn-to-yarn friction tests.

Additionally, the measured values of μ_N are significantly smaller than might be expected from the friction coefficient values μ measured in the yarn-to-yarn friction tests. The coefficient μ_N is not a friction coefficient like μ, which relates a tangential resistance force per unit area to a contact pressure, but rather is a constant of proportionality that relates a net effective resisting force to a net effective through-thickness force which is represented in the analytical model by the crossover spring, as shown in Figure 4-22. In the absence of locking, Equation (4.10) implies that the tension T_2 downstream of any crossover point can be calculated from the upstream tension T_1 according to the following relation:

$$T_2 = T_1 e^{2\mu\beta}, \tag{4.36}$$

because the total angle through which the slipping yarn wraps about the crossing yarn is twice the crimp angle β. Hence, the following relation between μ and μ_N can be derived:

$$\begin{aligned} \mu_N \equiv \frac{f^R}{F_N} &= \frac{(T_2 - T_1)\cos\beta}{(T_2 + T_1)\sin\beta} \\ &= \frac{1}{\tan\beta}\frac{e^{2\mu\beta}-1}{e^{2\mu\beta}+1} = \frac{\tanh(\mu\beta)}{\tan\beta} \end{aligned} \tag{4.37}$$

For β values that are reasonable for this fabric, ranging from 0.0 to about 0.4 radians, this

expression implies that dependence on β is very small (and hence we are justified in treating μ_N as a material property), but μ_N should be only slightly smaller than μ. For $\mu = 0.27$ (as measured in the yarn-to-yarn friction tests), μ_N should be approximately 0.256. Therefore, there must be other effects that cause the measured values μ_N to be so much smaller, on the order of 0.08 ~ 0.10. Locking effects no doubt account for some or all of this discrepancy, because in the presence of locking, the contact pressures over some portion of the contact area are assumed to contribute to the locking force F_L and not the normal force F_N, as is shown in Figure 4-22. Also, locking effects may change the pressure distributions even on contact areas not directly subjected to locking pressures. Another possibility is that, because the yarns cross at nearly right angles in the fabric in the pullout test, as opposed to wrapping around one another in a helical manner, fiber entanglements between yarns or other effects that increase the friction coefficient may play less of a role than in the yarn to yarn friction tests.

The average values of μ_L measured from the Zwick experiments ranged from approximately 1.11 at 5 mm/min to 0.89 at 50 mm/min to 0.65 at 500 mm/min, decreasing approximately logarithmically. The biaxial experiments indicated larger values of μ_L that decrease more rapidly. The values of μ_L are so large because of the idealized geometry assumed in the analytical model to represents the locking phenomenon. As is shown in Figure 4-9 and Figure 4-22, the analytical model represents this effect with a truss inclined to the fabric plane. As is described in Chapter 2, the properties for the locking trusses are determined by fitting the model predictions to the experimentally measured shear response of the fabric, where the primary effect of locking is to apply in-plane forces that resist shear deformation. However, as is evident in Figure 4-22, the actual net locking forces are oriented at a much greater inclination to the fabric plane than the locking trusses are. Therefore, to apply the same effective in-plane forces, the locking trusses must carry loads F_L that are smaller than the actual net locking forces that act in the fabric. Since the model calculates locking resistance f_L^R from the effective locking forces F_L carried by the trusses, which are smaller than the real locking forces, the corresponding coefficient μ_L will be larger than the real friction coefficient. For the geometry of the fabric in question, the in-plane projection of a unit force carried by the locking trusses is on the order of eight times larger than the projection of a unit force oriented normal to the actual locking contact surfaces shown in Figure 4-22, so we expect the μ_L values to be on the order of eight times larger than they would be if they related the real locking forces to f_L^R.

The decrease in μ_L with slip rate is likely related to the fact that the yarn cross sections deform inelastically in response to locking effects. Appendix A describes a series of experiments

where the fabric is subjected to cyclic shear loads. These experiments imply that the yarn cross section become compressed due to locking effects, but that this compression is not immediately recovered upon the removal of load. Instead, the cross sections relax slowly, over seconds or tens of seconds, in a manner that can be described by a visco-elastic relation. This inelasticity is probably due to the fact that the yarns are composed of many untwisted fibers, and the deformation of the yarn cross section is affected by inter-fiber frictional effects. The slow recovery of the cross sections from transverse compaction may account for the decrease in μ_L with slip rate. At low slip velocities, the cross sections have time to relax and apply large locking forces within the weave. As the slip velocity is increased, the cross sections do not have time to relax and are forced into their compressed configuration all along the yarn as it is pulled through the weave. Because the cross sections never have time to relax, locking forces are probably considerably smaller at larger rates. As the rates become very large, μ_L may approach a limiting value because there is a limit to the amount of compression the crossover points undergo.

This phenomenon could also explain why the increase in μ_N is larger at large rates. At large rates, when the cross sections have no time to relax and generate locking forces, the fabric would behave more similarly to a sparsely woven fabric. The contact areas over which locking forces are exerted, shown in Figure 4-22, would be smaller, and hence the dependence of the resistance on the normal forces F_N, characterized by μ_N, would become larger.

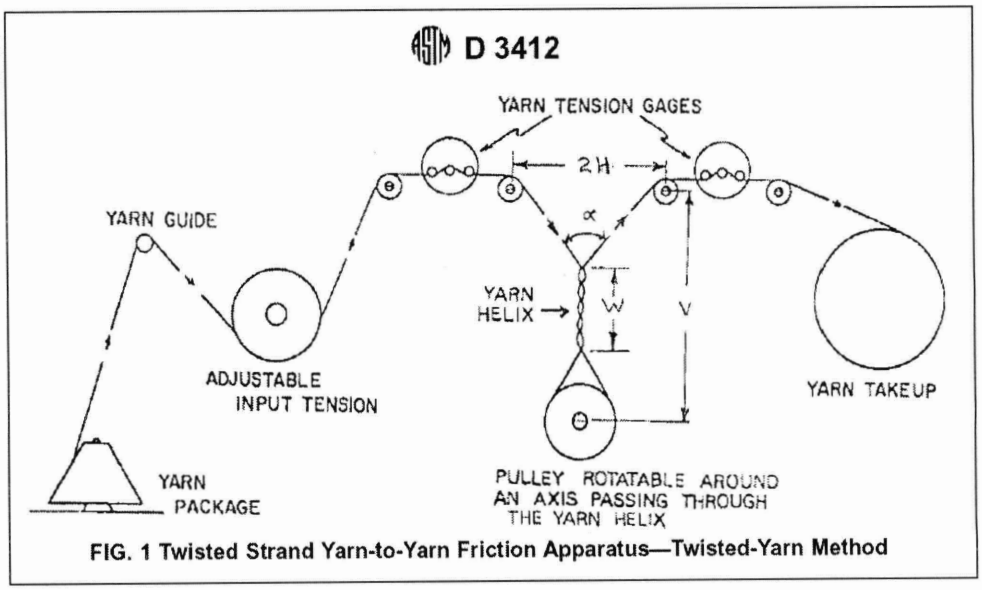

Figure 4-1 Schematic of yarn-to-yarn friction test apparatus from ASTM D3412-01

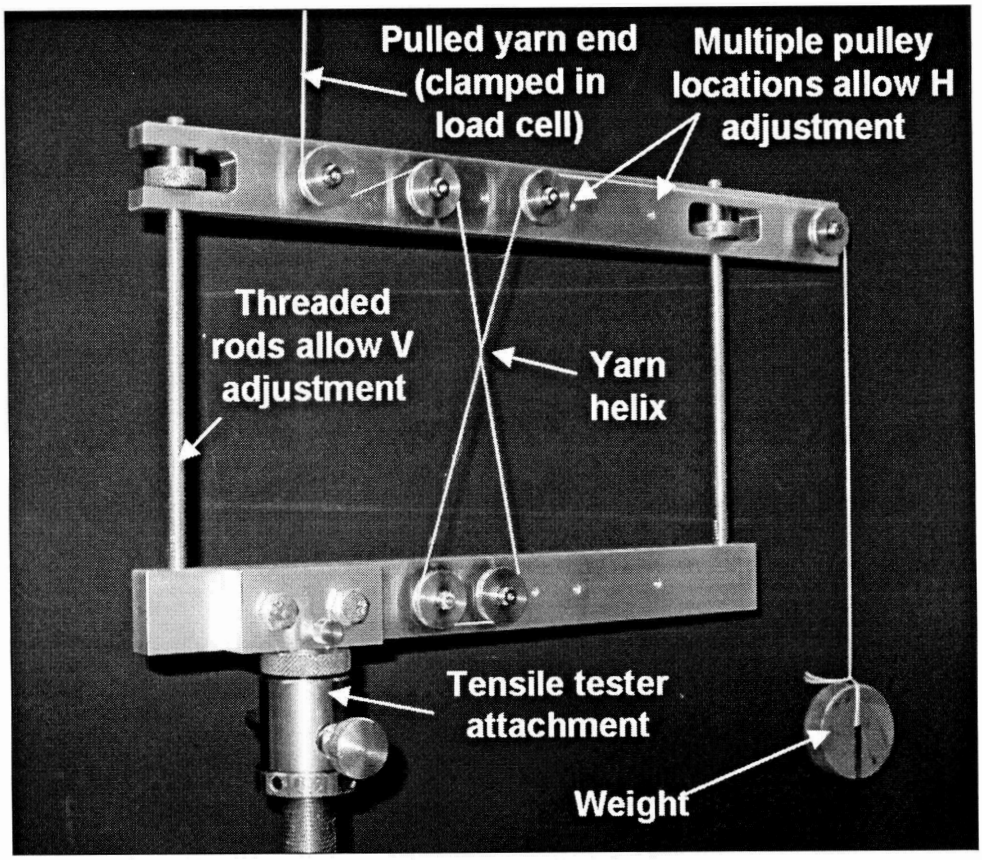

Figure 4-2 Modified yarn-to-yarn friction test apparatus

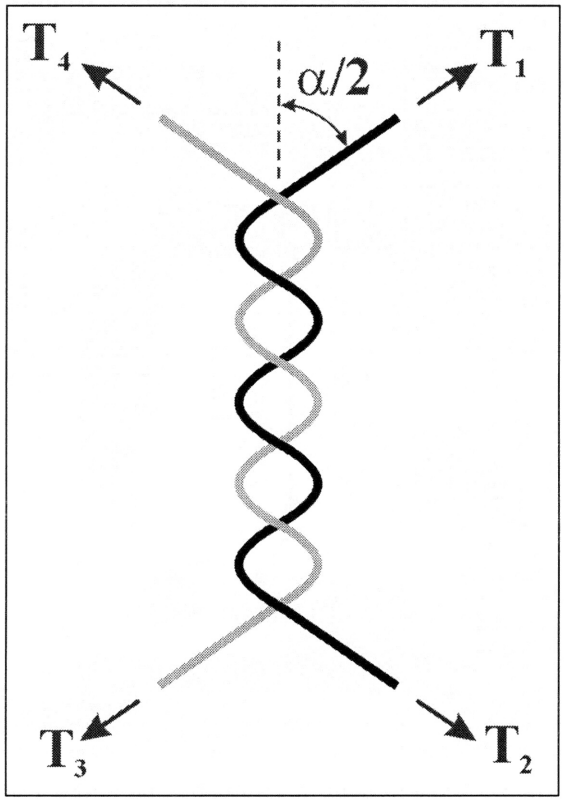

Figure 4-3 Yarn helix in a yarn-to-yarn friction test

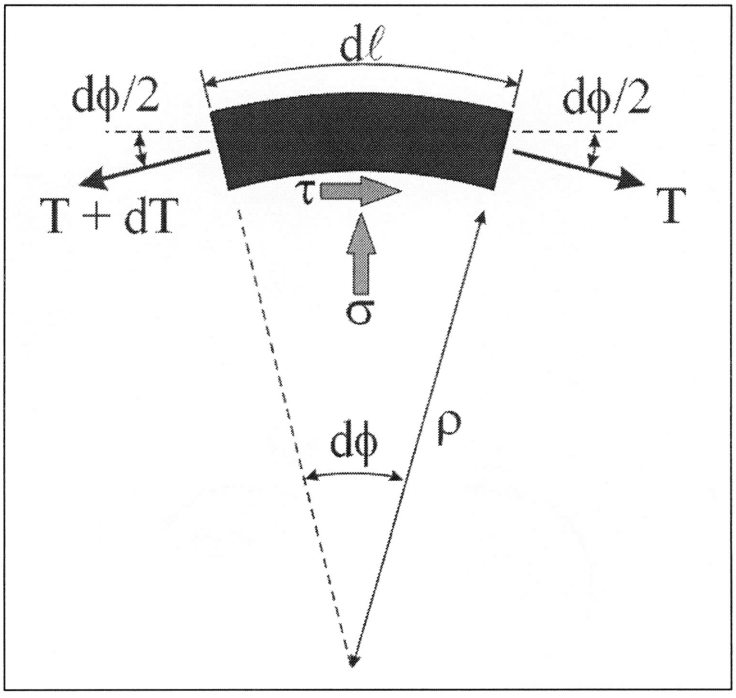

Figure 4-4 Forces on a differential section of a helically wrapped yarn

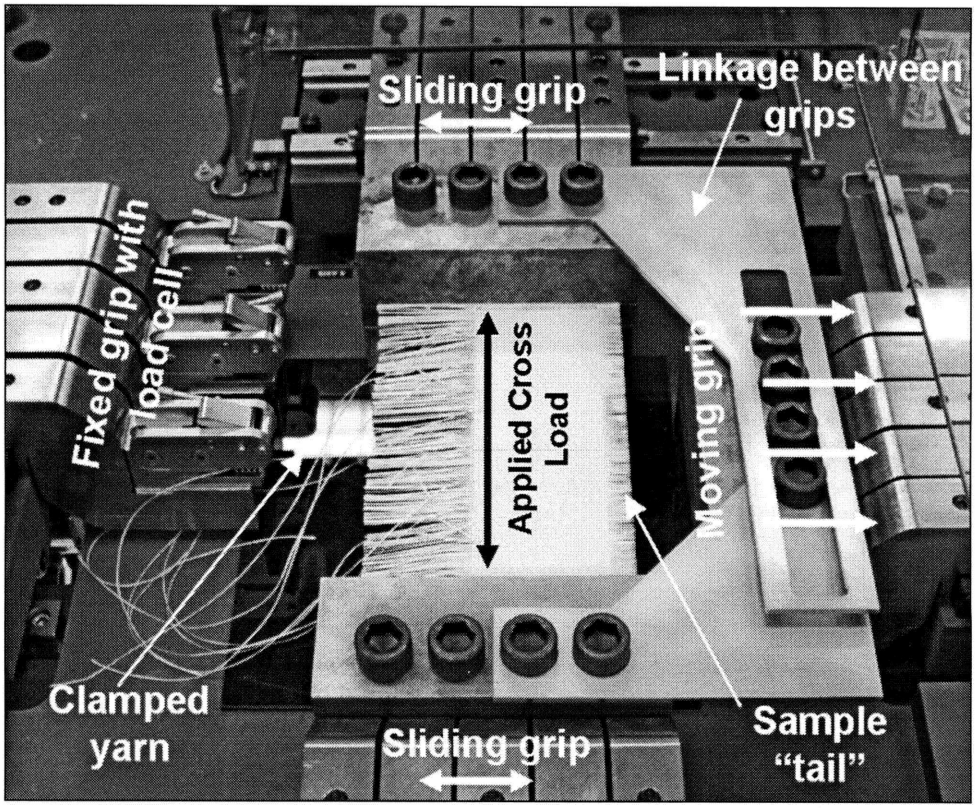

Figure 4-5 Yarn pullout test using biaxial tensile tester

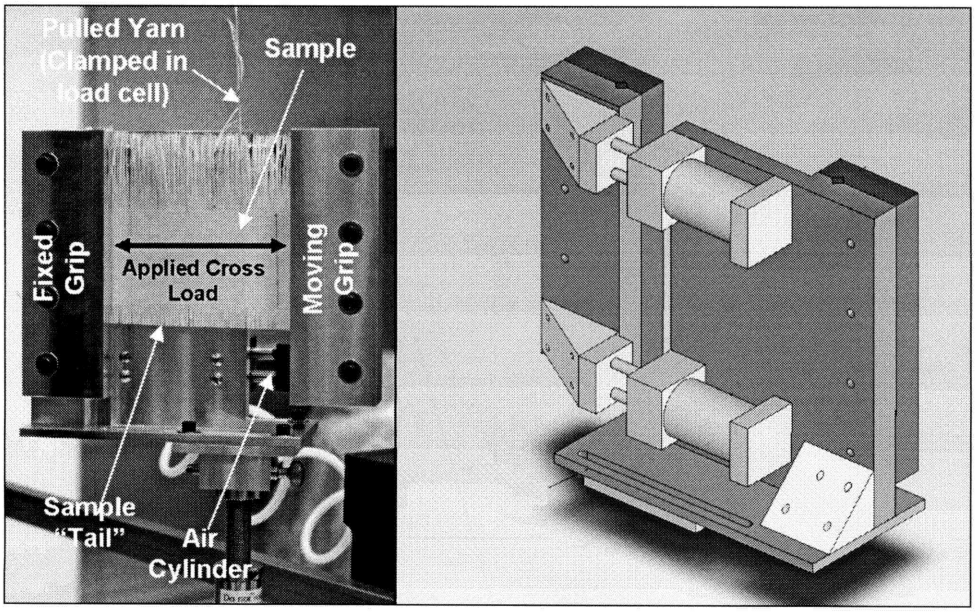

Figure 4-6 Pneumatic fixture for performing yarn pullout test using a uniaxial tensile tester

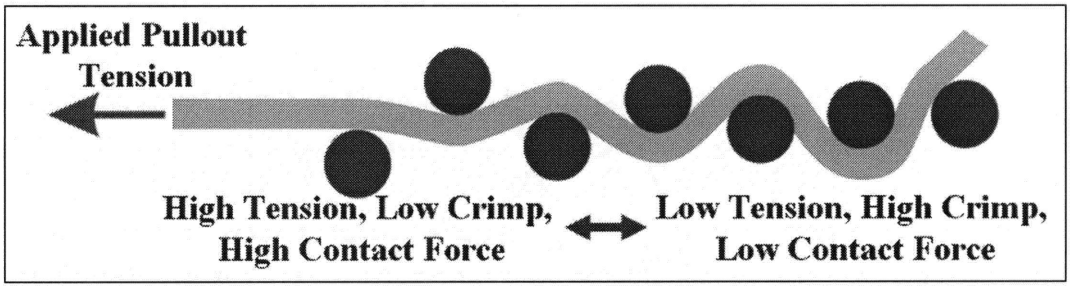

Figure 4-7 Varying conditions along a slipping yarn

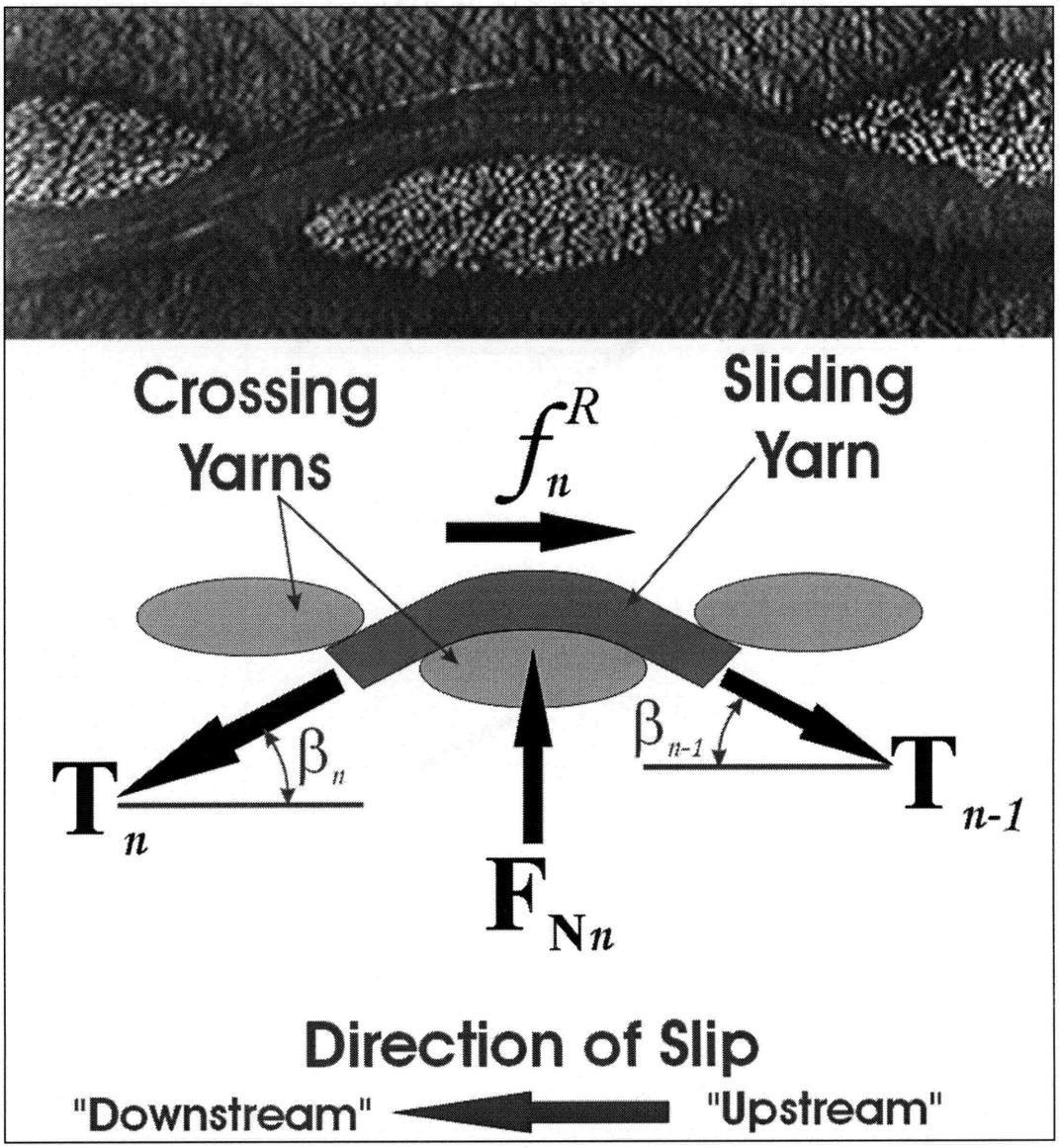

Figure 4-8 Simplified representation of forces acting a yarn crossover point

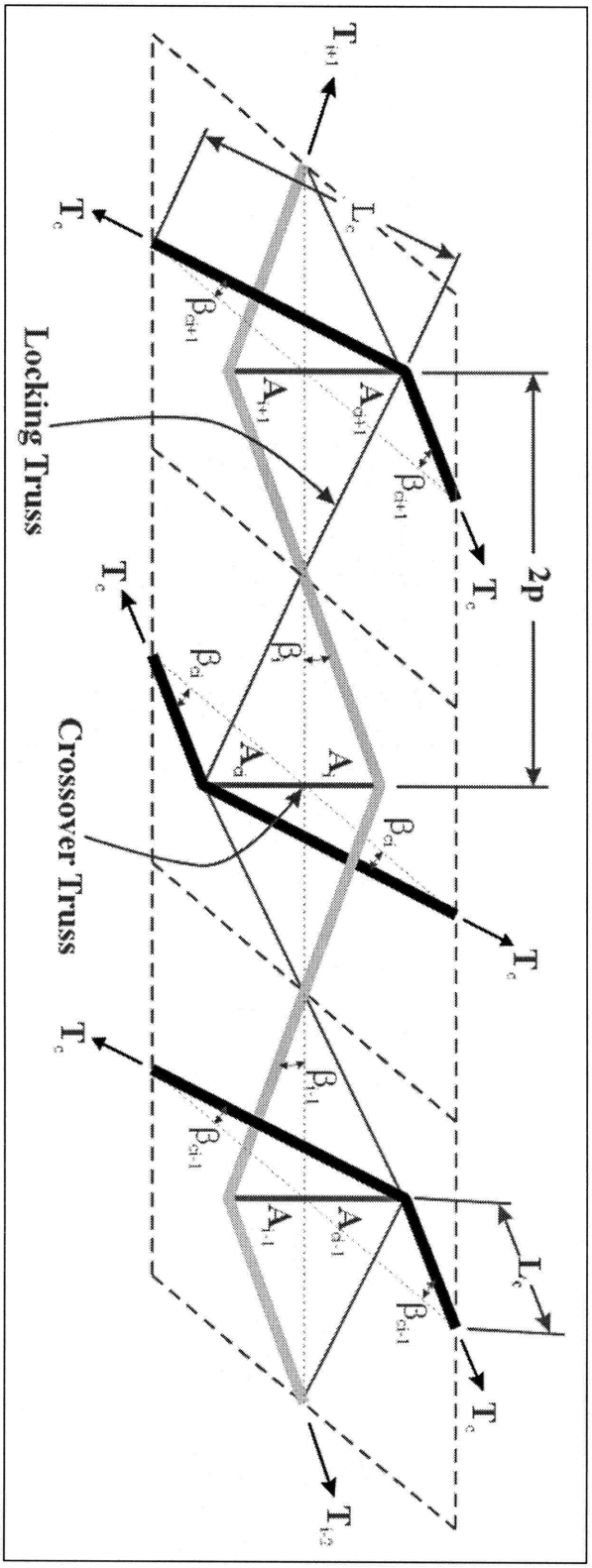

Figure 4-9 Truss geometry for analytical pullout model

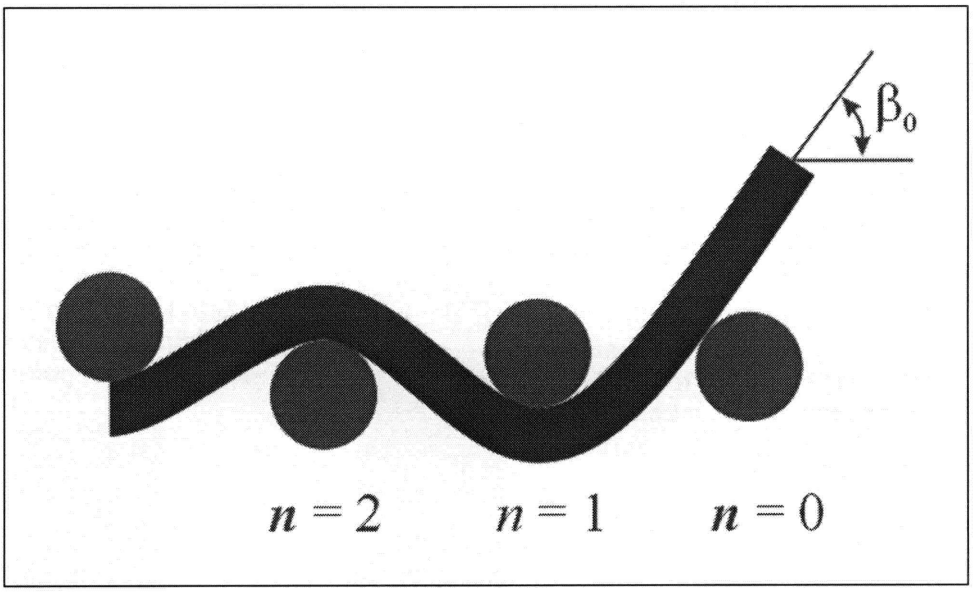

Figure 4-10 Conditions at the free end of a slipping yarn

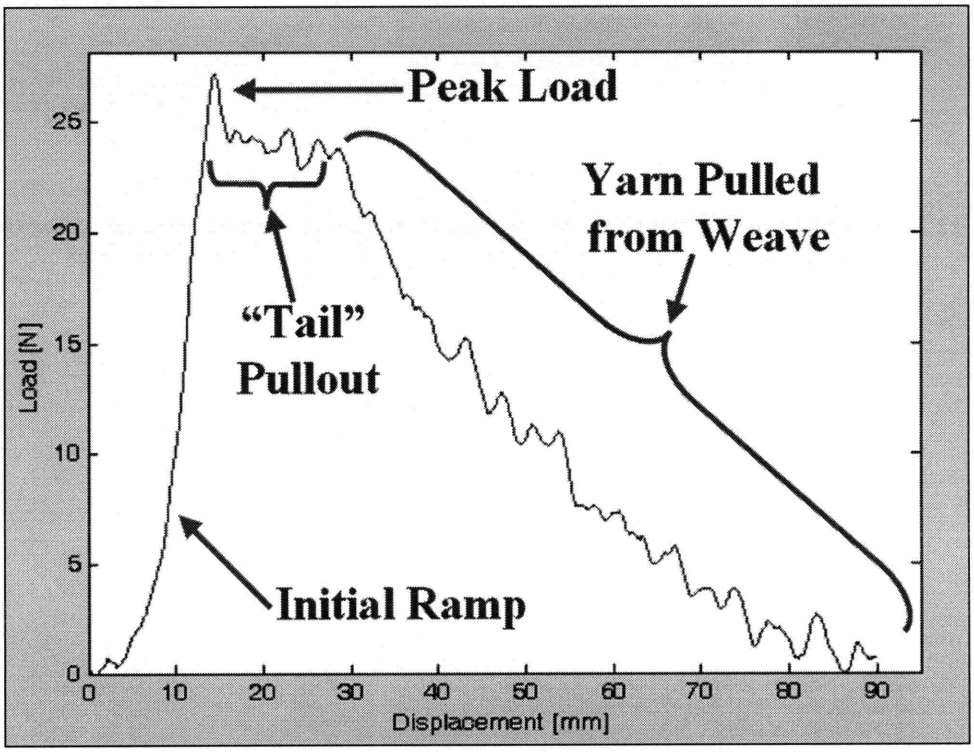

Figure 4-11 Typical force-displacement response during yarn pullout using biaxial machine

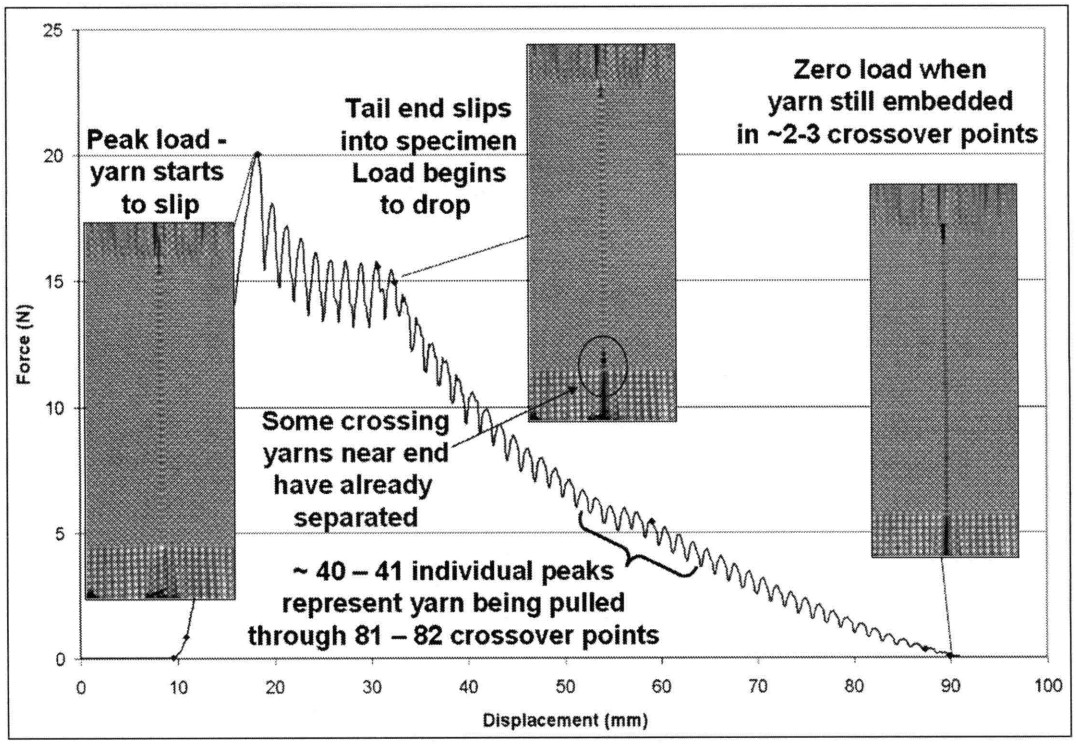

Figure 4-12 Typical force-displacement during yarn pullout measured using pneumatic apparatus on Zwick uniaxial tensile tester, with photographs of sample at different states

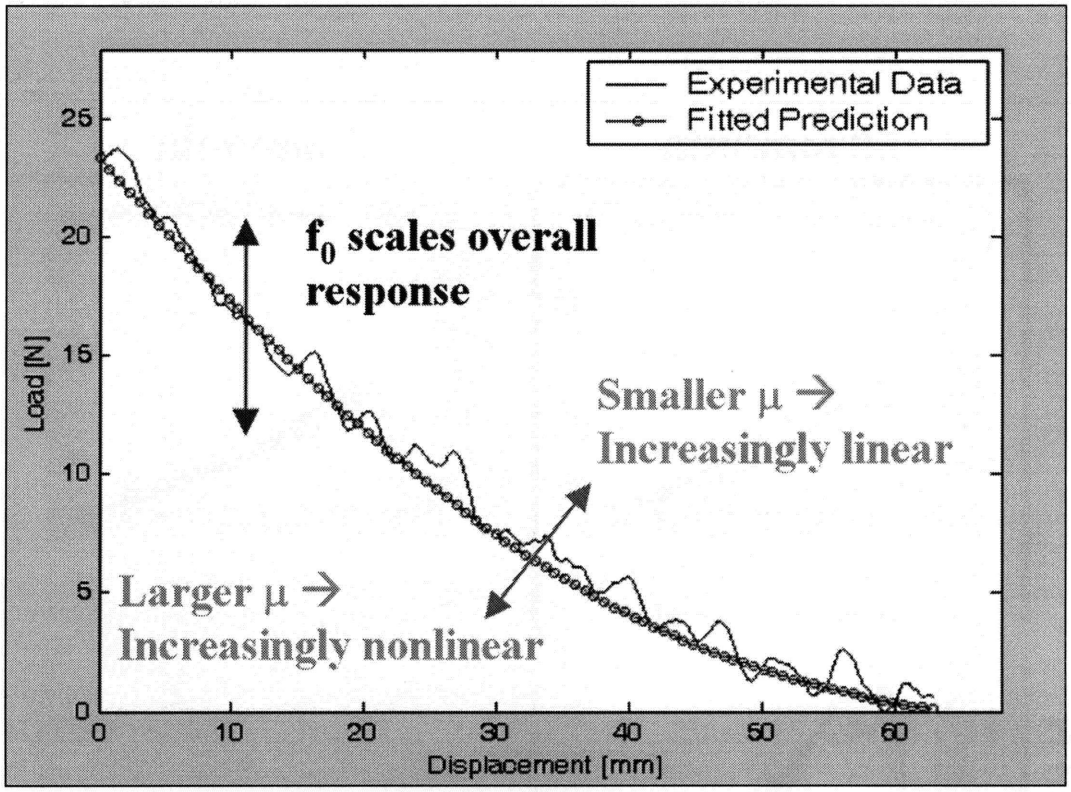

Figure 4-13 Pullout response predicted by initial constitutive law

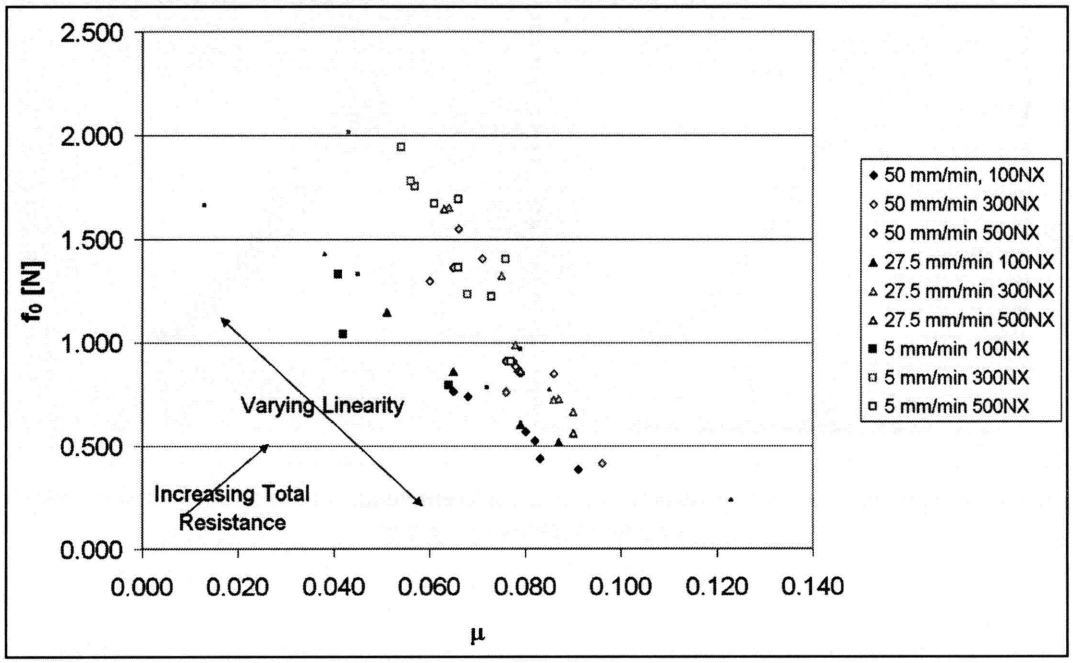

Figure 4-14 Fitted μ_N and f_0 values using initial constitutive law

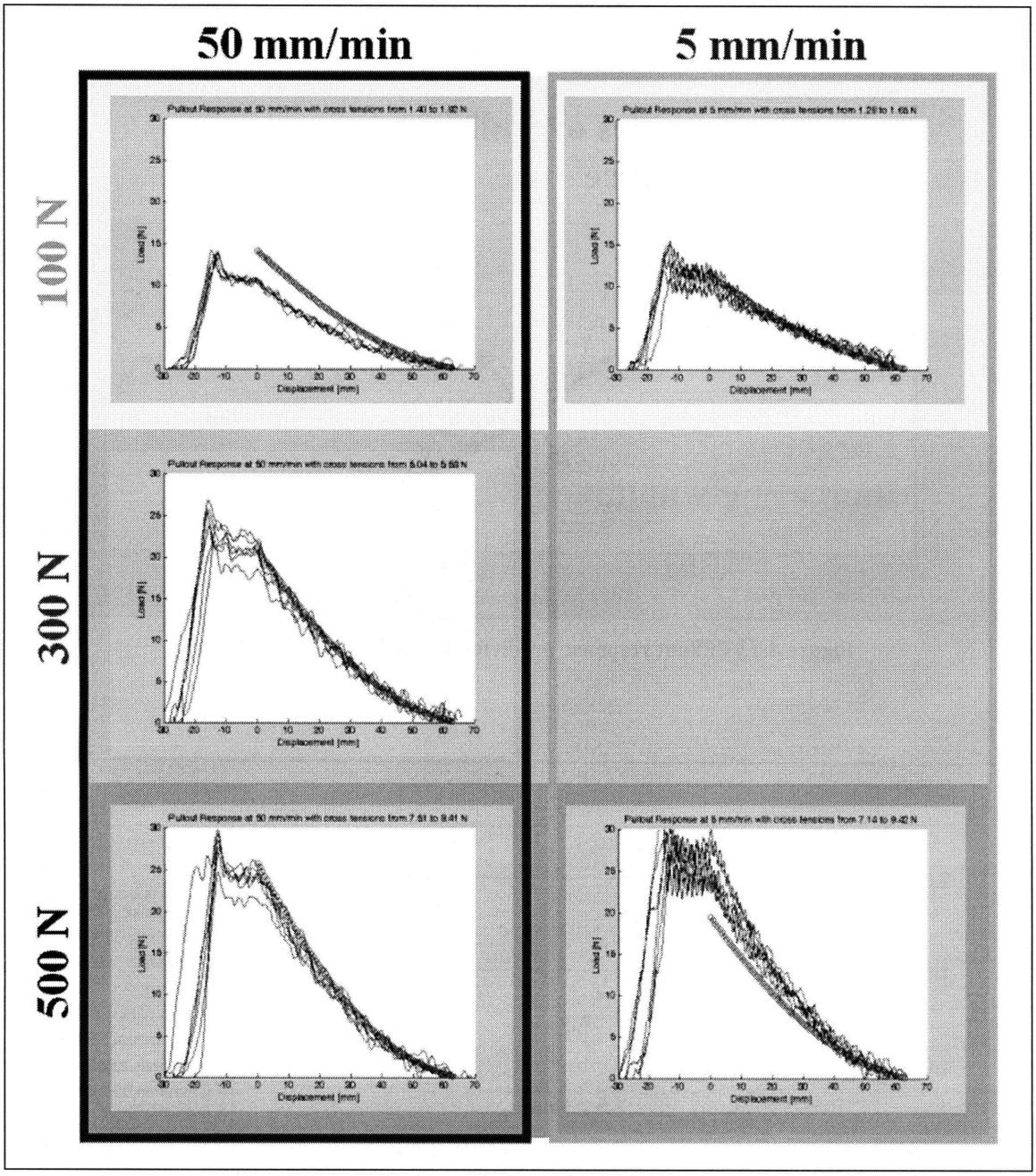

Figure 4-15 Experimental pullout responses under different conditions with analytical predictions using initial constitutive law

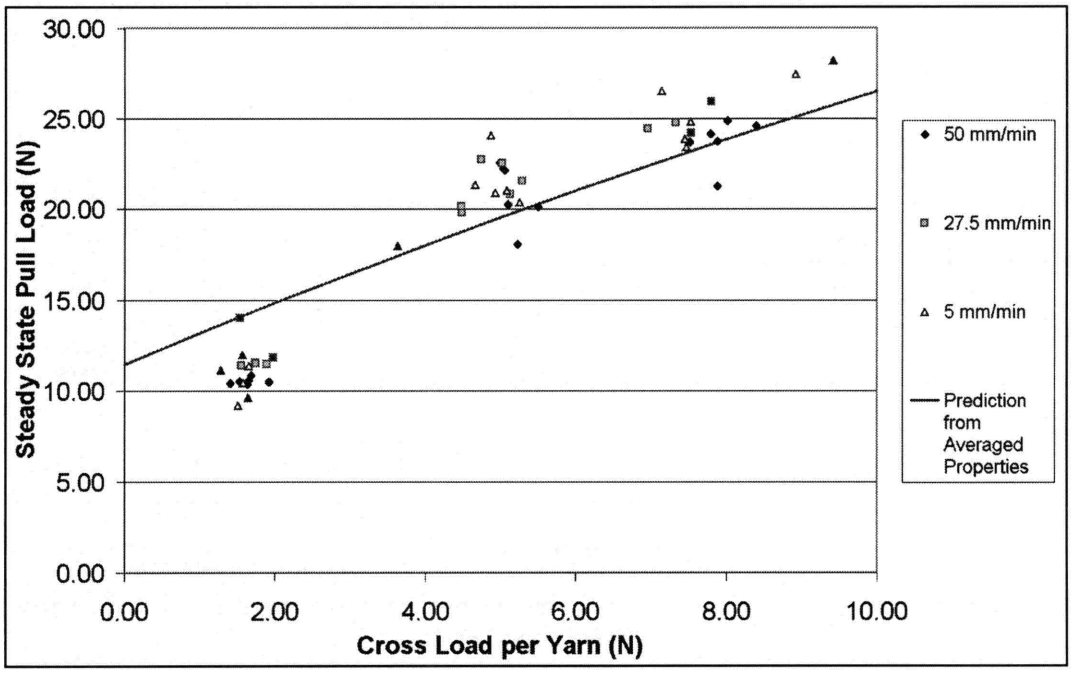

Figure 4-16 Experimentally measured steady state pullout force, with predictions of the initial constitutive law

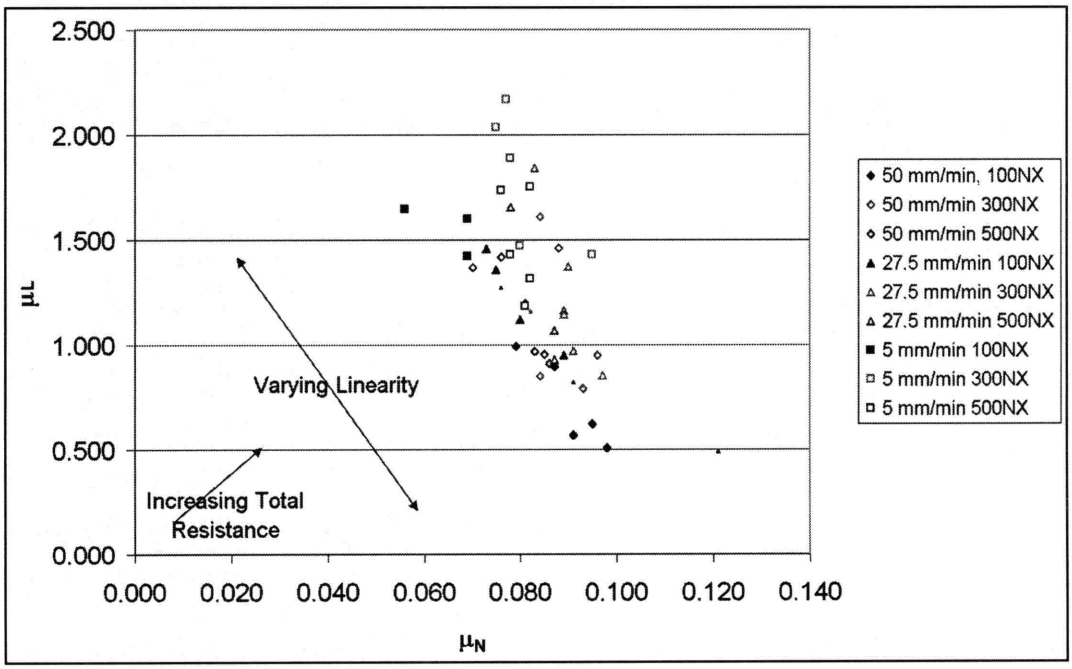

Figure 4-17 Fitted μ_N and μ_L values using revised constitutive law

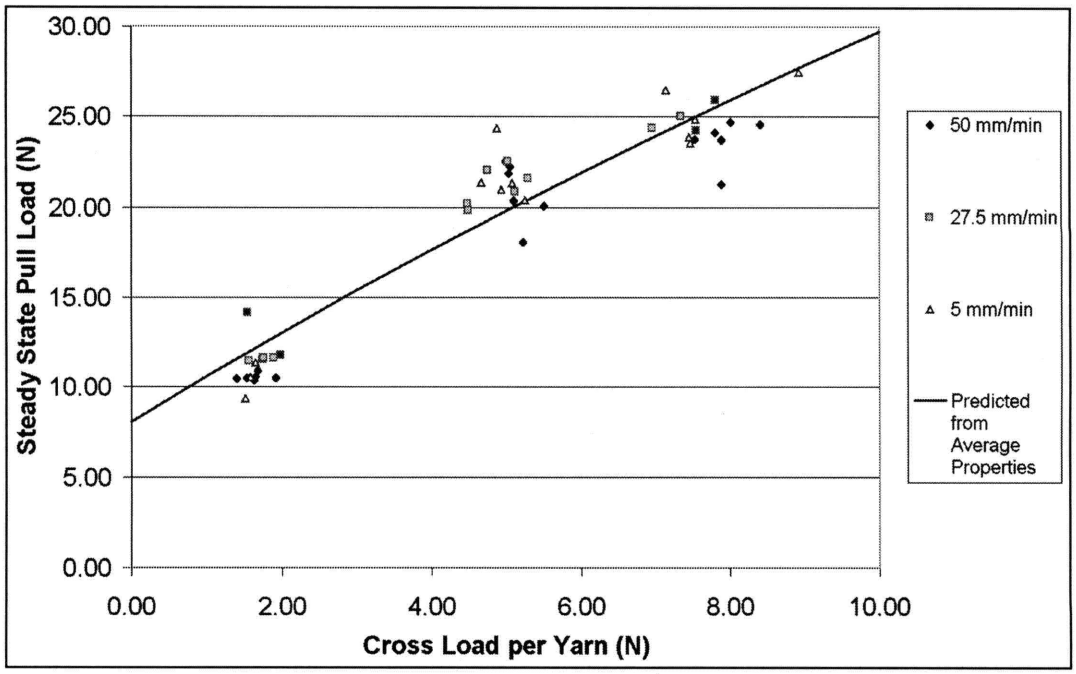

Figure 4-18 Experimentally measured steady state pullout force, with predictions of the revised constitutive law

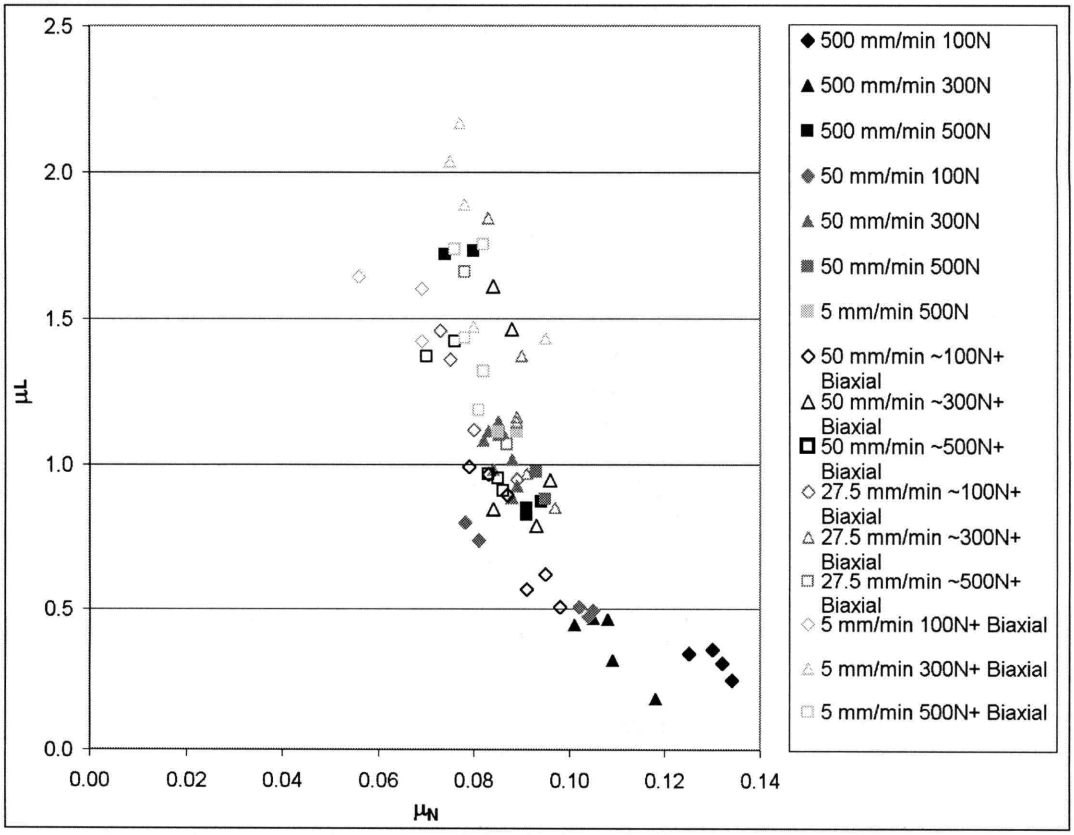

Figure 4-19 Fitted μ_N and μ_L values using revised constitutive law for all tests

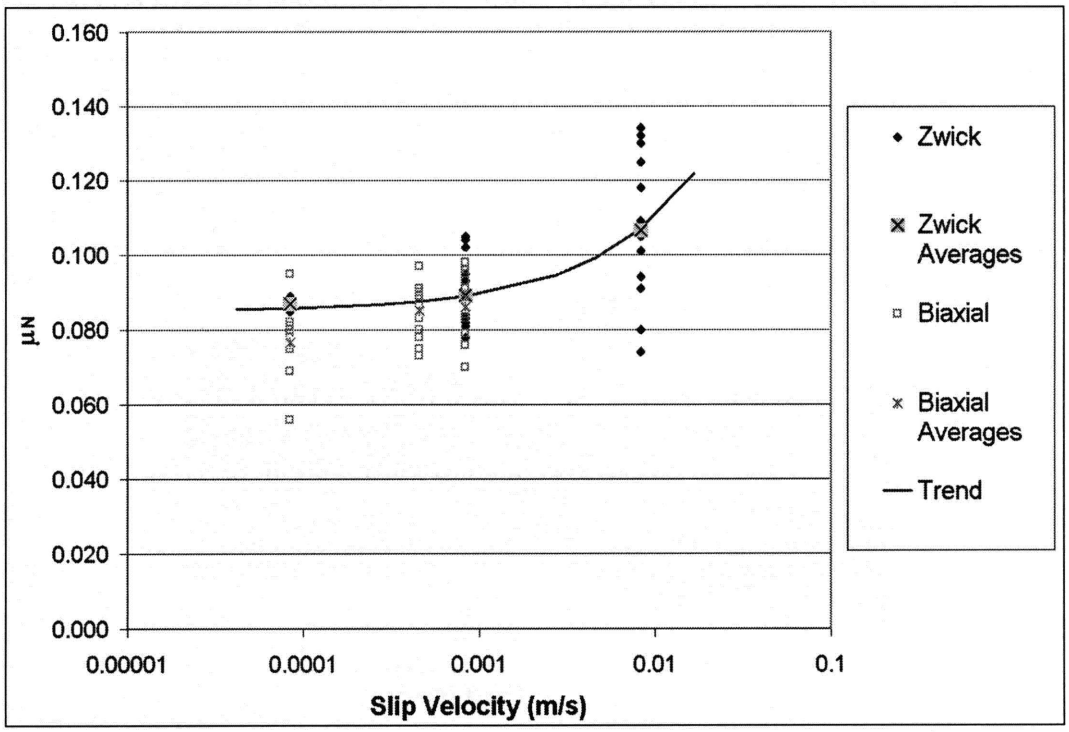

Figure 4-20 Fitted μ_N values using revised constitutive law as a function of v^{slip}

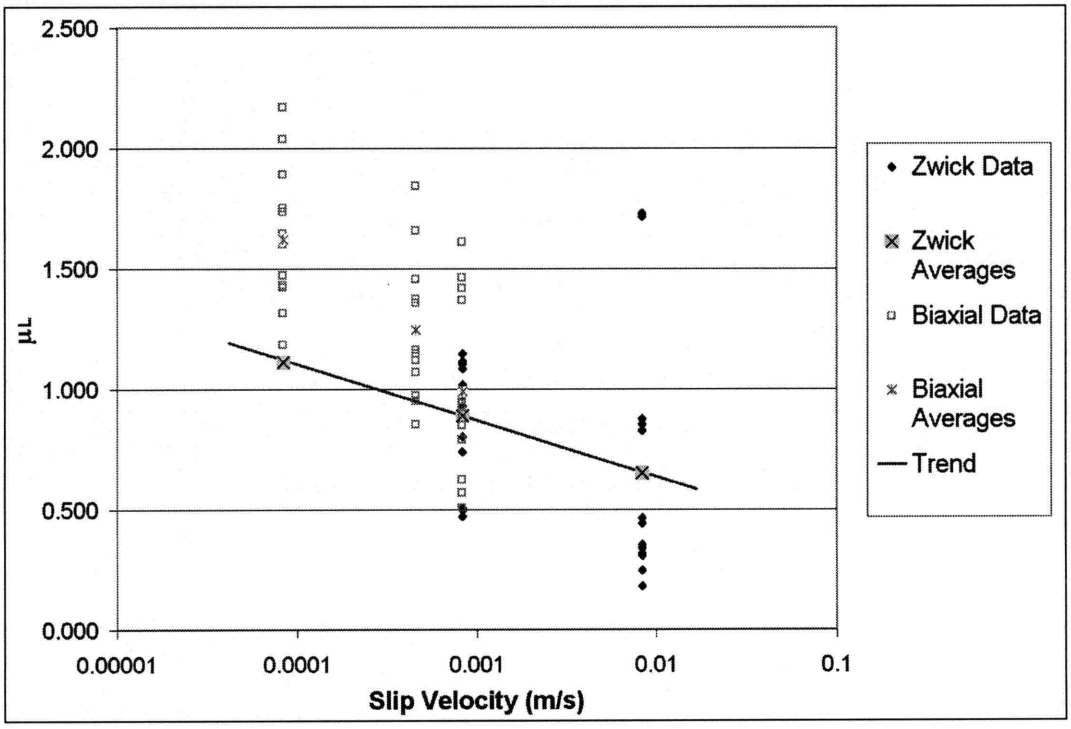

Figure 4-21 Fitted μ_L values using revised constitutive law as a function of v^{slip}

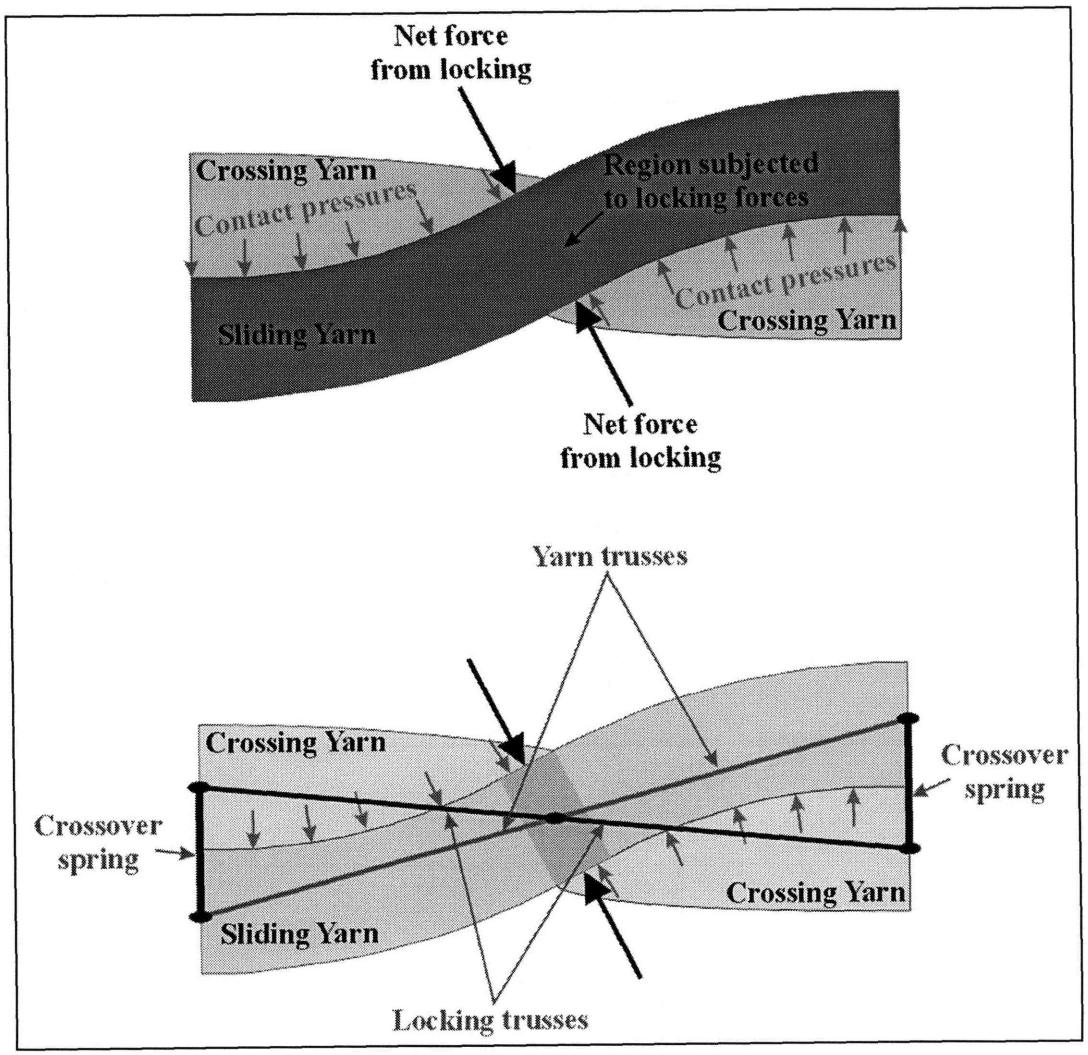

Figure 4-22 Geometry of forces at crossover point

Table 4-1 Results of yarn-to-yarn friction experiments

	Constant Parameters			
	2H (mm):	25.4	V (mm):	137
	Input Tension T_i (N):	0.98		
	Number of Twists			
	0	1/2	1 1/2	2 1/2
W (mm):	N/A	3.5	7.5	11.0
α	N/A	0.190	0.196	0.201
Test Speed (mm/min)	Average Output Tension T_o and *Standard Deviation* (N)			
10	1.04 *0.00*	N/A *N/A*	1.84 *0.12*	2.65 *0.14*
100	1.04 *0.00*	1.31 *0.01*	1.87 *0.02*	2.76 *0.09*
1000	1.04 *0.00*	1.37 *0.02*	2.02 *0.07*	3.02 *0.16*
Test Speed (mm/min)	Calculated Friction Coefficient μ			
10	**N/A**	**N/A**	**0.277**	**0.253**
100	**N/A**	**0.444**	**0.284**	**0.264**
1000	**N/A**	**0.494**	**0.315**	**0.288**

Chapter 5
Continuum Slip Model

5.1 Kinematics of a Continuum Fabric Model with Slip

The kinematics of a continuum representing a fabric that is subject to slip are much more complex than those associated with a slip-free fabric. In a slip-free fabric a single deformation mapping can be used at the continuum scale to describe the motion of both yarn families, because the crossover points of the weave are material points, and both families of yarns move in an affine manner with the weave. However, when slip occurs, a single deformation mapping can no longer be used to describe the motion of yarn material of both families. Since each yarn family can slip relative to the other, points on the two yarn families that occupied the same location in the reference configuration may occupy distinct locations in a deformed configuration. Therefore, two distinct deformation mappings, characterized by deformation gradients $\mathbf{F}_1$ and $\mathbf{F}_2$, are necessary to describe the motion of the two yarn families, as is shown at the top of Figure 5-1. By comparing these deformation gradients, the amount of slip at any given location can be determined. A two-deformation gradient approach of this kind has been proposed by Nadler and Steigmann [2003].

A drawback of this approach is that the locations of the crossover points are not directly followed. The interactions between the two yarn families occur at the crossover points and determine the evolution of the fabric mesostructure and its macroscopic mechanical response. Without directly tracking the crossover points, it is difficult to accurately describe the complex interactions of the two yarn families through mechanisms such as crimp interchange, trellising, locking of the weave, etc. The multi-scale modeling approach described in Chapter 2 cannot be easily modified to account for a description of the fabric deformation with two deformation gradients.

An alternative, more effective approach is shown at the bottom of Figure 5-1. In this approach, we use a single mapping to describe the motion of the crossover points of the weave, rather than the motion of the actual yarn material that composes the fabric. We refer to the gradient of this mapping as the "weave deformation gradient", even though it does not describe the motion of actual material and hence is not actually a "deformation gradient" in the classical sense. The motion of yarn material is described by slip velocity fields that give the velocity of the

material that composes each yarn family relative to the weave crossover points at every location. With this approach, we consider the fabric continuum to represent a "pseudo-material" that is defined by the location of its crossover points rather than the locations of its component yarns. Like the true deformation gradient in the slip-free case, the weave deformation gradient $\mathbf{F}$ allows the relative motion of adjacent crossover points to be calculated, and hence $\mathbf{F}$ determines the in-plane deformation of the fabric unit cell (the stretches of the unit cell along the yarn family directions and the shear angle corresponding to relative in-plane rotation of the yarn families). However, there is one important difference from the slip-free case. In the slip-free case, the amount of yarn material associated with every crossover point remains constant, and hence (in the absence of shear deformation) the unloaded unit cell configuration remains constant and uniform throughout the fabric. In the slip-enabled case, the yarns are allowed to slip past the crossover points and through the weave at different rates, and hence the amount of yarn material of each family that is associated with each crossover point becomes a state variable that evolves at every point as the fabric is deformed. In other words, at every location the unloaded unit cell configuration evolves with deformation and varies from point to point in the weave, as is shown in Figure 5-2.

This approach for describing the kinematics of a slip-enabled fabric has several advantages. It is easy to compare model predictions and experimental measurements since the model directly follows the locations of the crossover points, which are readily observable in experiments. Another advantage is that failure modes such as yarn pullout and weave unraveling can be readily included in the formulation. By tracking the amount of yarn that has slipped past a crossover point at a given location and comparing it with the distance from that yarn's free end in the reference configuration, the onset of weave unraveling can be determined and the unraveled crossover point can be removed from the continuum model. Because the yarns will never re-weave themselves, crossover points will never be created.

The most significant advantage of this approach is that it allows a model to be developed using the same multi-scale modeling approach described in Chapter 2, provided that the response of the fabric to deformation is calculated with respect to the evolved unit cell. In the slip-free model, the deformation gradient $\mathbf{F}$ maps the wavelength vectors $\mathbf{p}_i$ of the yarn families (which give the orientations of the yarn families and the spacing between crossover points, and hence determine stretch and shear of the unit cell) from their reference values to their values in the deformed configuration. The evolution of the weave mesostructure, the meso-scale level forces, and the corresponding macroscopic stresses are then determined from physically motivated relations at the mesoscale. In the slip-enabled formulation, the weave deformation gradient is

used to determine $\mathbf{p}_i$ in the deformed configuration, and the response of the fabric can be calculated in the same manner. The only difference is that the unloaded configuration of the unit cell evolves in the presence of slip and is defined by a set of state variables rather than by material properties. The remainder of this chapter details how this evolution is determined from meso-level forces within the fabric.

5.2 Kinematics of Slip at Mesoscale

We first quantify the unloaded configuration of the unit cell. Any given crossover point can be identified either by its location $\mathbf{X}$ in the reference configuration or by its location $\mathbf{x}(t)$ in the deformed configuration at time t, since the mapping between $\mathbf{X}$ and $\mathbf{x}(t)$ is unique. At time t, adjacent crossover points along a yarn will have an in-plane spacing $2p$ measured along the in-plane projection of the yarn family. However, because of the crimp of the yarns, the length of yarn between the crossover points will have a value of $2L > 2p$. In the deformed configuration, this section of yarn may carry a load. The corresponding unloaded length of that yarn section is 2ℓ, shown in Figure 5-3. We define $\ell_i(\mathbf{X},t)$ to be the unstretched yarn length per quarter wavelength at time t (hereafter referred to as the "unstretched yarn length") that is associated with yarn family i and with the crossover point that was located at $\mathbf{X}$ in the reference configuration. In the slip-free model, the tension in the yarns was given by Equation (2.13) and depended on the difference between the yarn length L_i in the deformed configuration and the length ${}^0L_i$ in the reference configuration. In the presence of slip, the tension for the same linear elastic yarns is given by:

$$T_i = k_i(L_i - \ell_i). \tag{5.1}$$

It depends on the yarn length L_i in the deformed configuration and the unstretched yarn length ℓ_i at that time and location.

This parameter ℓ_i is one of the state variables that describe the unloaded configuration of the unit cell. It will initially have the value of ${}^0L_i$ (assuming that the yarns are unstretched in the reference configuration) but will evolve as the yarns slip. We must develop relations that describe this evolution. Define:

$$\lambda_i(\mathbf{X},t) \equiv \frac{L_i(\mathbf{X},t)}{\ell_i(\mathbf{X},t)} \tag{5.2}$$

to be the stretch of the yarn of family i at a given location and time. We next define two scalar fields $v_1(\mathbf{X},t)$ and $v_2(\mathbf{X},t)$ to be the instantaneous velocities at time t at which un-stretched yarn

material of the warp and weft families respectively are sliding past a crossover point that was located at **X** in the reference configuration. We refer to these velocities as SLIDY (SLIp Displacement of the Yarn) velocities. If a stretched yarn of family i has some macroscopically observable velocity $v_i^{slip}(\mathbf{X},t)$ at time t relative to a crossover point which was located at **X** in the reference configuration, then the SLIDY velocity is given by:

$$v_i(\mathbf{X},t) \equiv \frac{v_i^{slip}(\mathbf{X},t)}{\lambda_i(\mathbf{X},t)}. \tag{5.3}$$

These velocities can alternatively be considered as functions of the location **x** in the deformed configuration:

$$v_i(\mathbf{x}(\mathbf{X},t),t) = v_i(\mathbf{X},t). \tag{5.4}$$

Next consider a section of the weave consisting of n crossover points along a yarn whose associated average wavelength vector is given by $\mathbf{p}_i = p_i\mathbf{g}_i$. (Recall that $\mathbf{g}_i$ is a unit vector parallel to $\mathbf{p}_i$). In the deformed configuration, one end of the weave section lies at $\mathbf{x} - n\mathbf{p}_i$ and the other end at $\mathbf{x} + n\mathbf{p}_i$. In the reference configuration, the average wavelength vector associated with these crossover points is given by ${}^0\mathbf{p}_i = {}^0p_i{}^0\mathbf{g}_i$, and the ends of the same weave section lie at $\mathbf{X} - n^0\mathbf{p}_i$ and $\mathbf{X} + n^0\mathbf{p}_i$. At some time t, this weave section will contain a total unstretched yarn length of $2n\ell_i^{avg}$, where ℓ_i^{avg} is the average unstretched yarn length associated with each crossover point in the weave section. The instantaneous rate of change of the total unstretched yarn length in the section will be:

$$\frac{\partial(2n\ell_i^{avg})}{\partial t} = v_i(\mathbf{x} - n\mathbf{p}_i,t) - v_i(\mathbf{x} + n\mathbf{p}_i,t), \tag{5.5}$$

when v_i is expressed as a function of current locations of the crossover points, or

$$\frac{\partial(2n\ell_i^{avg})}{\partial t} = v_i(\mathbf{X} - n^0\mathbf{p}_i,t) - v_i(\mathbf{X} + n^0\mathbf{p}_i,t), \tag{5.6}$$

when v_i is expressed as a function of reference locations of the crossover points. The SLIDY velocity v_i is defined to be positive when it acts in the same direction as vector $\mathbf{p}_i$.

Since n is constant, the instantaneous rate of change of the average unstretched yarn length associated with each crossover point in this section is:

$$\dot{\ell}_i^{avg} = \frac{v_i(\mathbf{x} - n\mathbf{p}_i,t) - v_i(\mathbf{x} + n\mathbf{p}_i,t)}{2n}. \tag{5.7}$$

The velocities at each crossover point are discrete values. But under the continuum approximation, we assume that the length scale of the problem is sufficiently large so that the

velocities can be approximated as smooth, continuous fields. Under this assumption, as the length of the weave section becomes small, the terms $v(\mathbf{x} - n\mathbf{p},t)$ and $v(\mathbf{x} + n\mathbf{p},t)$ can be approximated as:

$$\begin{aligned} v_i(\mathbf{x}+n\mathbf{p}_i,t) &\approx v_i(\mathbf{x},t)+np_i\left.\frac{\partial v_i}{\partial \xi_i}\right|_{\mathbf{x},t} \\ v_i(\mathbf{x}-n\mathbf{p}_i,t) &\approx v_i(\mathbf{x},t)-np_i\left.\frac{\partial v_i}{\partial \xi_i}\right|_{\mathbf{x},t} \end{aligned} \quad . \tag{5.8}$$

Here we define ξ_i as a coordinate in the deformed configuration measured parallel to $\mathbf{p}_i$ so that:

$$\frac{\partial(\ )}{\partial \xi_i} \equiv \vec{\nabla}(\ )\cdot\mathbf{g}_i\,, \tag{5.9}$$

Substituting Equations (5.8) and (5.9) into Equation (5.7) and assuming that the average unstretched yarn length over a number of crossover points near $\mathbf{x}$ are representative of the individual unstretched yarn length at $\mathbf{x}$ gives the following expression for $\dot{\ell}_i$:

$$\dot{\ell}_i = -p_i\vec{\nabla}(v_i)\cdot\mathbf{g}_i\,. \tag{5.10}$$

In many finite element formulations, it is convenient to express gradients in terms of the reference configuration coordinates. If v is expressed in terms of reference configuration coordinates of the crossover points, we can approximate $v(\mathbf{X} - n^0\mathbf{p},t)$ and $v(\mathbf{X} + n^0\mathbf{p},t)$ as:

$$\begin{aligned} v_i(\mathbf{X}+n^0\mathbf{p}_i,t) &\approx v_i(\mathbf{X},t)+n\ {}^0p_i\left.\frac{\partial v_i}{\partial \zeta_i}\right|_{\mathbf{X},t} \\ v_i(\mathbf{X}-n^0\mathbf{p}_i,t) &\approx v_i(\mathbf{X},t)-n\ {}^0p_i\left.\frac{\partial v_i}{\partial \zeta_i}\right|_{\mathbf{X},t} \end{aligned} \quad . \tag{5.11}$$

We define ζ_i as a coordinate in the reference configuration measured parallel to ${}^0\mathbf{p}_i$ so that:

$$\frac{\partial(\ )}{\partial \zeta_i} \equiv \mathbf{Grad}(\ )\cdot{}^0\mathbf{g}_i\,. \tag{5.12}$$

Equation (5.10) can then be written in the following equivalent form:

$$\begin{aligned} \dot{\ell}_i &= -{}^0p_i\mathbf{Grad}(v_i)\cdot{}^0\mathbf{g}_i \\ &\equiv -{}^0p_i v_i' \end{aligned} \quad . \tag{5.13}$$

Here we define the following operator:

$$(\ )_i' \equiv \mathbf{Grad}(\ )_i\cdot{}^0\mathbf{g}_i\,. \tag{5.14}$$

Assuming that the SLIDY velocity fields $v_i(\mathbf{X},t)$ at a given instant are known, the evolution rate of the unstretched yarn lengths $\dot{\ell}_i$ can be calculated.

5.3 Slip Driving Force

We now characterize the forces that drive slip. As described in Chapter 4, slip can occur under a variety of different conditions in a fabric. For example, if a single yarn is gripped and pulled, or if a yarn under tension breaks, that yarn will slide through the weave due to differences in tension acting on its ends. If the fabric is damaged by adjacent yarn breakages (i.e. "slit-like" damage described in Section 2.11 and pictured in Figure 2-26) and is subjected to biaxial tension, two modes of slip will occur, as is discussed by Godfrey and Rossettos ([1998] and [1999]) and in Section 2.11. The broken yarns will tend to slip out of the weave away from the slit, but they will drag the crossing yarns with them and hence these crossing yarns will slip along the unbroken yarns at the ends of the slit. The first mode of slip occurs due to uneven tensions acting on the broken yarns; the second is due to gradients in shear angles of the crossing yarns that are under tension, which cause transmission of force from neighboring slipping yarns. Inertial effects drive slip in fabrics in a bulletproof vest during a ballistic impact, as discussed by Termonia [2004]. A small number of yarns are impacted by a projectile and are subjected to large displacement rates. However, inertial forces prevent the surrounding yarns from displacing at the same rates, and the impacted yarns slip through the weave.

Still other types of macroscopic loadings can drive slip in other cases. When fabrics are subjected to large loads that are not aligned with the yarn directions, such as in a bias-extension test described in Section 2.10, the yarn families rotate relative to each other and attempt to align with the loads until the locking phenomenon arrests this motion. At this point, increasing loads cause the yarn ends to slip out of the weave at the edges of the fabric, and the fabric starts to unravel, as is shown in Figure 2-23. In this case, slip is caused by gradients in the locking forces, which are very large inside the fabric but necessarily zero at the edges. Another case where fabric slip is observable is during composite forming operations, where dry or impregnated fabrics are formed into various three dimensional shapes by stamping or drawing applications. During these processes, the fabrics are subjected to transverse shear loads as they are dragged across the surfaces of the dies or drawing tools. These transverse shear forces can induce significant amounts of yarn slip within the fabric.

Although slip can be caused by a wide variety of different loading conditions at the macroscopic scale, we must identify a single driving force f at the mesoscale that causes slip to occur. As is described in Chapter 4, when a yarn is slipping past a crossover point, the crossing yarn exerts complex tractions on the slipping yarn. Some component of these tractions provides resistance to slip, which we designate as f^R. We consider f^R to be a positive scalar, with the understanding that it always acts in a direction that opposes slip. We can identify the meso-level

force f that drives slip by considering steady state slip conditions, where slip velocity is constant. Under these conditions, the slip driving force f must equal the slip resistance f^R, so whatever meso-level force counteracts the slip resistance f^R must be slip driving force f.

Consider a single crossover point which a yarn is slipping past under steady state conditions. Just "downstream" of the crossover point (i.e. in the direction which the yarn is slipping) the slipping yarn intersects the fabric plane at some crimp angle β_D and is under some tension T_D, while it intersects the fabric plane at a different crimp angle β_U and is under a different tension T_U just "upstream" of the crossover point. Under steady-state conditions, the difference between the upstream and downstream tensions, projected onto the fabric plane, must exactly counteract the slip resistance f^R in order to satisfy equilibrium:

$$f^R = T_D \cos\beta_D - T_U \cos\beta_U . \tag{5.15}$$

Since it exactly counteracts f^R, the we identify this difference in the projected tension across a crossover point as the slip driving force f:

$$f \equiv T_D \cos\beta_D - T_U \cos\beta_U . \tag{5.16}$$

When the projected tension is greater on one side of a crossover point than on the other, the differential will tend to cause the yarn to slip past that crossover point. While slip is occurring, the resistance to slip f^R supports the projected tension differential. Regardless of the macroscopic conditions that result in slip, at the mesoscale slip always corresponds to projected tension differentials across the crossover points.

In a discrete model where every yarn is modeled individually, the projected tension differential across a crossover point is easily determined. In a continuum model, the length scale is assumed to be sufficiently large that tensions can be approximated by smooth, continuous fields. As shown in Figure 5-4, a series of step changes in projected tension across successive crossover points along a yarn can be represented by a smoothly varying projected tension field. The gradient of the projected tension field at a given crossover point determines magnitude of the projected tension differential at a crossover point. Consider a yarn slipping past a crossover point located at $\mathbf{x}$, with a $\mathbf{p}$ vector describing the quarter-wavelength and orientation of the slipping yarn and pointing in the direction of slip. A point on this yarn halfway between the crossover point and the crossover point immediately downstream lies at $\mathbf{x} + \mathbf{p}$; a point halfway between the crossover point and the crossover point immediately upstream lies at $\mathbf{x} - \mathbf{p}$. Under the continuum assumption of smooth continuous tension fields, the downstream projected tension $T_D\cos\beta_D$, which is evaluated at $\mathbf{x} + \mathbf{p}$, can be approximated as a function the upstream projected tension

$T_U \cos\beta_U$ (which is evaluated at **x** – **p**), the gradient of the projected tension field at **x**, and the distance between the two points *2p*:

$$\begin{aligned} T_D \cos\beta_D &= \left(T\cos\beta\right)\Big|_{\mathbf{x}+\mathbf{p}} \\ &\approx \left(T\cos\beta\right)\Big|_{\mathbf{x}-p} + 2p\frac{\partial}{\partial\xi}\left(T\cos\beta\right) \\ &= \left(T\cos\beta\right)\Big|_{\mathbf{x}-p} + 2p\vec{\nabla}\left(T\cos\beta\right)\cdot\mathbf{g} \\ &= T_U\cos\beta_U + 2p\vec{\nabla}\left(T\cos\beta\right)\cdot\mathbf{g} \end{aligned} \qquad (5.17)$$

Here p, $\mathbf{g}$, T, and β are, respectively, continuum approximations at **x** of the quarter-wavelength, the in-plane yarn orientation vector, the tension, and the crimp angle. The gradient operator $\partial(\ )/\partial\xi$ is defined in the same manner as in Equation (5.9). This equation can be substituted into Equation (5.16) to determine an expression for the driving force f in terms of the continuum tension fields:

$$f \equiv T_n\cos\beta_n - T_{n-1}\cos\beta_{n-1} \approx 2p\vec{\nabla}\left(T\cos\beta\right)\cdot\mathbf{g}\,. \qquad (5.18)$$

The driving force f carries a sign that indicates the direction along the yarn along which the tension is increasing, relative to the vector **g**.

As was the case for evolution of the unstretched yarn length, described in Equation (5.10), the slip driving force depends on a gradient of a quantity projected along a yarn family. However, unlike the equation for the evolution of the unstretched yarn length, the slip driving force equation has a coefficient of *2p* instead of *–p*. The factor of *2* appears because the tension differential is determined across a crossover point, which has an in-plane size of *2p*. In the case of the unstretched yarn length evolution, there are two segments of yarn per crossover point, so the evolution of each occurs across half a crossover point, which has an in-plane size of p. The slip driving force equation has a positive coefficient because increasing tension along a yarn corresponds to a positive driving force according to our sign convention, whereas increasing slip velocity along a yarn corresponds to a net loss of yarn material in any given section and hence a negative evolution rate.

As we did for $\dot{\ell}$, we can re-write the expression for f in terms of reference-configuration gradients. Restoring the yarn family identifiers i (which have thus far been omitted for clarity) gives a final expression for the slip driving force f_i in yarn family i:

$$
\begin{aligned}
f_i &= 2\ {}^0p_i \mathbf{Grad}\left(T_i \cos\beta_i\right) \cdot {}^0\mathbf{g_i} \\
&\equiv 2\ {}^0p_i \left(T_i \cos\beta_i\right)'
\end{aligned}
\tag{5.19}
$$

The gradient along the yarn family operator $(\ )'$ is defined in Equation (5.14). If the tension fields T_i and the yarn crimp angles β_i are known, the forces f_i that drive slip can be calculated.

In the slip-free case, the crossover points provide infinite resistance to slip, and hence they can support arbitrarily large projected tension gradients. As the gradients in the tension fields increase, the driving force f will increase, but the resistance to slip f^R will undergo a corresponding increase and no slip will occur. In the slip enabled case, there will be some maximum resistance that the crossing yarns can exert through static frictional effects. When the tension gradients become large enough so that the driving force f exceeds this maximum static resistance, the yarns will begin to slip at some velocity v^{slip}. It can be shown that, provided slip velocities increase as the driving force increases, slip will tend to reduce gradients in the projected tensions. Consequently, a slip-enabled fabric can support only finite projected tension gradients.

5.4 Slip Constitutive Law

In the preceding sections, we describe how the forces f_i that drive slip can be determined from the gradients in the projected tensions along the yarns, and how the mesostructure around a crossover point evolves (through the evolution of the unstretched yarn lengths ℓ_i) in the presence of gradients of the SLIDY velocities v_i, which can be calculated from the slip velocities of the stretched yarns v_i^{slip}. The final element required by the slip theory is a constitutive law that relates the slip driving forces f_i and the slip velocities v_i^{slip}. In Chapter 4 we describe various experimental investigations that we conducted in order to understand the relationship between the forces f^R that resist slip and the slip velocity v^{slip}. We now present a generalized form for a constitutive law and then specialize it according to the experimentally studied slip resistances.

In some ways, yarn slip in woven fabrics can be considered to be analogous to plasticity in elastic-plastic materials. Elastic-plastic materials deform only elastically until an appropriate loading metric (e.g. a Mises stress) reaches some critical resistance of the material to plastic deformation (e.g. a yield stress), at which point plastic deformation can occur. Slip-enabled fabrics deform in a slip-free manner until the magnitude of the slip driving force exceeds a critical resistance to slip, at which point slip can occur. We define the parameter f^C to be the smallest magnitude of the driving force f at which non-zero slip velocities can occur at a given fabric state.

Before yarns begin to slip, this parameter is equal to the maximum slip resistance that can be exerted by static frictional effects. As long as the magnitude of the driving force f is smaller than f^C at every crossover point, no slip will occur. At some point, the projected tension gradients may become sufficiently large so that the magnitude of f reaches f^C, at which point slip can occur. Note that once slip commences and the slip velocity v^{slip} is nonzero, the value of f^C may change due to differences between dynamic and static frictional effects. f^C may also evolve as the fabric state evolves; for example, if the through thickness force F_N increases, frictional effects would become larger and f^C would likely increase. We can define a "slip overforce function" that is analogous to the yield function in plasticity theory:

$$f^O \equiv |f| - f^C. \tag{5.20}$$

Next, we define a "flow rule" that describes the direction of slip. We expect slip to occur in the direction of the driving force:

$$v^{slip} = |v^{slip}| \operatorname{sign}(f). \tag{5.21}$$

We define v^{slip} to be positive when the yarn is sliding past the crossover point in the direction indicated by **g** and **p**. To verify that v^{slip} and f should have the same sign, imagine a yarn slipping past a crossover point with a positive velocity. Since the resisting force f^R acts in the negative direction, we expect the downstream tension, which lies in the positive direction, to be greater than the upstream tension. Thus tension increases in the positive direction and f, as calculated from Equation (5.19), will have a positive sign.

In general, slip could be governed be either a rate-independent or a rate-dependent constitutive law. In the rate-independent case the overforce can never exceed zero:

$$f^O = |f| - f^C \leq 0. \tag{5.22}$$

When f^O is less than zero, no slip occurs and $|v^{slip}| = 0$. Only when $f^O = 0$ can $|v^{slip}|$ can be nonzero. This allows us to define a consistency condition:

$$|v^{slip}| f^O = 0. \tag{5.23}$$

In this case, as the fabric is macroscopically loaded and the projected tension differentials become large enough to drive slip, exactly enough yarn slip will occur at every moment so that at all times the magnitude of the driving force f at every point is limited to the value of f^C (which depends on the fabric state and which may evolve), regardless of the applied loading rates. The magnitude of the slip velocity $|v^{slip}|$ can be arbitrarily large in order to satisfy this condition. We note that implementation of such a rate-independent constitutive law presents significant challenges, as the implementation of three-dimensional rate-independent plasticity laws do.

However, implementation of slip is further complicated by the fact that the slip theory is non-local: the slip driving forces and the evolution of the of the yarn lengths must be calculated from gradients of yarn tensions and slip velocities, respectively.

Fortunately, the experiments described in Chapter 4 indicate that the resistance to slip depends on the slip rate, and consequently it is more appropriate to develop a rate-dependent slip law. In a rate dependent model, a "viscosity" law relates the magnitude of the slip velocity $|v^{slip}|$ to the magnitude of the slip-driving force $|f|$. In many rate dependent plasticity models, a power law type relation is used to relate the plastic strain rate to the magnitude of the stress that drives plasticity. An analogous power-law type viscosity model for yarn slip in a fabric would have the following general form:

$$\left|v^{slip}\right| = \begin{cases} 0 & |f| \le f^C \\ v_0 \left(\dfrac{|f| - f^C}{f_0 - f^C} \right)^a & |f| > f^C \end{cases}, \tag{5.24}$$

where a describes the rate sensitivity of the expression and v_0 gives the slip velocity magnitude at some reference driving force magnitude f_0. We will show that such a viscosity law fits the experimental measurements described in Chapter 4 well.

The experiments indicate that the essential features of the slip response for the Kevlar® fabric can be captured with a relatively simple law that describes the resistance f^R that opposes steady-state slip at a constant velocity v^{slip}:

$$f^R = \hat{\mu}_N\left(v^{slip}\right)F_N + 2\hat{\mu}_L\left(v^{slip}\right)F_L . \tag{5.25}$$

Here F_N is the through-thickness force exerted by one yarn family on the other at the crossover point, and F_L is the force carried by the locking truss in the idealized unit cell geometry that represents the compressive contact between the cross sections when the fabric jams. The yarn pullout experiments in Chapter 4 give average values of μ_N and μ_L at three different slip velocities v^{slip}, shown in Figure 4-20 and Figure 4-21. The μ_N values increase non-linearly with slip velocity, while the μ_L values decrease with slip velocity.

Decreasing frictional resistance with increasing velocity leads to inherently dynamic effects which cannot be easily captured in the quasi-static implicit framework that we will use to validate the slip model. We therefore neglect the rate dependence of μ_L and treat it as constant. For the same reason, we also neglect the abrupt drop in resistance as the yarns start to slip, which is presumably due to the difference between the static and dynamic frictional resistance.

Because the experiments in Chapter 4 were conducted under steady state conditions, the magnitude of the slip driving force $|f|$ must balance the slip resistance f^R, so we can write the following expression:

$$|f| = \hat{\mu}_N\left(v^{slip}\right)F_N + 2\mu_L F_L . \tag{5.26}$$

If we invert the general power-law viscosity relation given in Equation (5.24) to get $|f|$ as a function of $|v^{slip}|$, we get:

$$|f| = f^C + \left(f_0 - f^C\right)\left(\frac{\left|v^{slip}\right|}{v_0}\right)^{\frac{1}{a}} . \tag{5.27}$$

Comparing this relation with Equation (5.26) implies that, in order for the power-law viscosity relation to be consistent with the experimentally measured constitutive behavior for the slip resistance, μ_N must have the following form:

$$\mu_N = \mu_c + \left(\mu_0 - \mu_c\right)\left(\frac{\left|v^{slip}\right|}{v_0}\right)^{\frac{1}{a}} , \text{ with} \tag{5.28}$$

$$\mu_c \equiv \frac{f^C - 2\mu_L F_L}{F_N} \text{ and } \mu_0 \equiv \frac{f_0 - 2\mu_L F_L}{F_N} .$$

As is shown in Figure 5-5, this form for μ_N fits the experimentally measured data very well, and hence a power-law relation is a reasonable means of approximating the relationship between $|v^{slip}|$ and $|f|$. Substituting this expression into Equation (5.26) and inverting to solve for $|v^{slip}|$ gives a final form for the constitutive relation:

$$\left|v^{slip}\right| = \begin{cases} 0 & |f| \le 2\mu_L F_L + \mu_c F_N \\ v_0\left\{\dfrac{1}{\mu_0 - \mu_c}\left(\dfrac{|f| - 2\mu_L F_L}{F_N} - \mu_c\right)\right\}^a & |f| > 2\mu_L F_L + \mu_c F_N \end{cases} . \tag{5.29}$$

The critical slip resistance f^C depends on both the locking force F_L carried by the locking truss and the contact force F_N carried by the crossover spring in the model:

$$f^C = 2\mu_L F_L + \mu_c F_N . \tag{5.30}$$

The constitutive relation has five material properties that can be determined from the pullout experiments. μ_L is determined directly by averaging all the μ_L values at all slip velocities. The value μ_0 is the value of μ_N at some slip velocity $v^{slip} = v_0$. The value of μ_c is the value of μ_N that corresponds to zero slip velocity; it can be determined by extrapolating the μ_N-v^{slip} data back to

$v^{slip} = 0$. Finally the rate sensitivity a can be determined provided the value of μ_N is known at some velocity $|v^{slip}|$ other than v_0:

$$a = \frac{\ln\left(\frac{|v^{slip}|}{v_0}\right)}{\ln\left(\frac{\mu_N - \mu_c}{\mu_0 - \mu_c}\right)}. \tag{5.31}$$

Data from the biaxial tests and the Zwick tests yield slightly different values for these properties as reported in Table 5-1.

The behavior of the simplified slip constitutive relation is shown in Figure 5-6. For a given value of F_N there is a critical force $f^C = 2\mu_L F_L + \mu_c F_N$ that is independent of slip velocity. When the driving force f is smaller in magnitude than f^C, no slip occurs. Increasing the magnitude of the slip driving force past f^C causes increasingly large slip velocity magnitudes, with the rate of increase determined by the exponent a and the reference force $f_0 = 2\mu_L F_L + \mu_0 F_N$ that results in a corresponding reference velocity v_0.[1]

Even though this simple constitutive relation omits several aspects of the slip response, such as the decrease of μ_L with v^{slip}, it still predicts the pullout behavior measured in Chapter 4 with very good accuracy. Figure 5-7, Figure 5-8, and Figure 5-9 show the pullout responses measured using the Zwick apparatus at 5 mm/min, 50 mm/min, and 500 mm/min respectively at different cross loads, and compare these responses with the predictions of the analytical model using the slip constitutive relation and the material properties from the Zwick tests in Table 5-1. Although the representation of μ_L as constant causes the response to be slightly overpredicted at the fastest rates and the largest cross loads, where locking effects are most important and where the locking friction should drop, the predictions of the pullout responses are generally accurate. This indicates that this simplified slip law is sufficient for validation of the slip theory. In future work more complex and accurate slip constitutive laws may prove to be more effective, especially if a dynamic analysis is performed utilizing an explicit finite element framework.

[1] As F_N is increased, the critical force f^C increases and the rate of increase of slip velocity with f decreases. When there is no through-thickness force, $F_N = 0$ and the only resistance stems from locking effects, which are treated as rate independent. Hence in this case, the response becomes rate independent, with $f^C = 2\mu_L F_L$. Once this resistance is exceeded, $|v^{slip}|$ can be arbitrarily large. To avoid this situation, which can introduce instabilities in an implicit analysis, we enforce a numerical "floor" of 0.01 N on the value of F_N used to calculate $|v^{slip}|$. If the actual value of F_N is smaller than this value, the constitutive law uses this value instead, so the relation always retains some rate dependence.

5.5 Combined Slip Formulation

Combining all the elements of a slip formulation discussed in this chapter results in a non-local slip theory. A single deformation mapping is used to describe the motion of the weave crossover points in space relative to some reference configuration. The gradient **F** of this mapping, referred to as the "weave deformation gradient", can be used to calculate the deformed configuration of the unit cell, including the deformed yarn lengths L_i. The tensions are calculated from the difference between these deformed lengths and the unstretched lengths ℓ_i:

$$T_i = \hat{T}_i\left(L_i - \ell_i\right). \tag{5.32}$$

The initial values of these unstretched yarn lengths are known, but they evolve with deformation. Gradients in the tensions along the yarns result in driving forces f:

$$f_i = 2\,{}^0p_i\left(T_i \cos\beta_i\right)' \tag{5.33}$$

If sufficiently large, these forces drive slip velocities v_i^{slip} according to a constitutive law that depends on the meso-level forces in the fabric:

$$v^{slip} = \left|v^{slip}\right| \operatorname{sign}(f). \tag{5.34}$$

$$\left|v^{slip}\right| = \begin{cases} 0 & |f| \le 2\mu_L F_L + \mu_c F_N \\ v_0\left\{\dfrac{1}{\mu_0 - \mu_c}\left(\dfrac{|f| - 2\mu_L F_L}{F_N} - \mu_c\right)\right\}^a & |f| > 2\mu_L F_L + \mu_c F_N \end{cases}. \tag{5.35}$$

Using the stretches in the yarns λ_i, which can be calculated from L_i and ℓ_i, these slip velocities can be converted to SLIDY velocities v_i that reflect the rate at which unstretched yarn material slips relative to the crossover points:

$$v_i \equiv \frac{v_i^{slip}}{\lambda_i}. \tag{5.36}$$

Finally, gradients of the SLIDY velocities along the yarns cause the unstretched yarn lengths to evolve:

$$\dot{\ell}_i = -{}^0p_i v_i'. \tag{5.37}$$

So the yarn tensions, and hence the stresses, depend on state variables that evolve in the presence of gradients of quantities calculated from gradients of tensions. Implementing this non-local theory into a finite element framework presents significant challenges which are discussed in the next chapter.

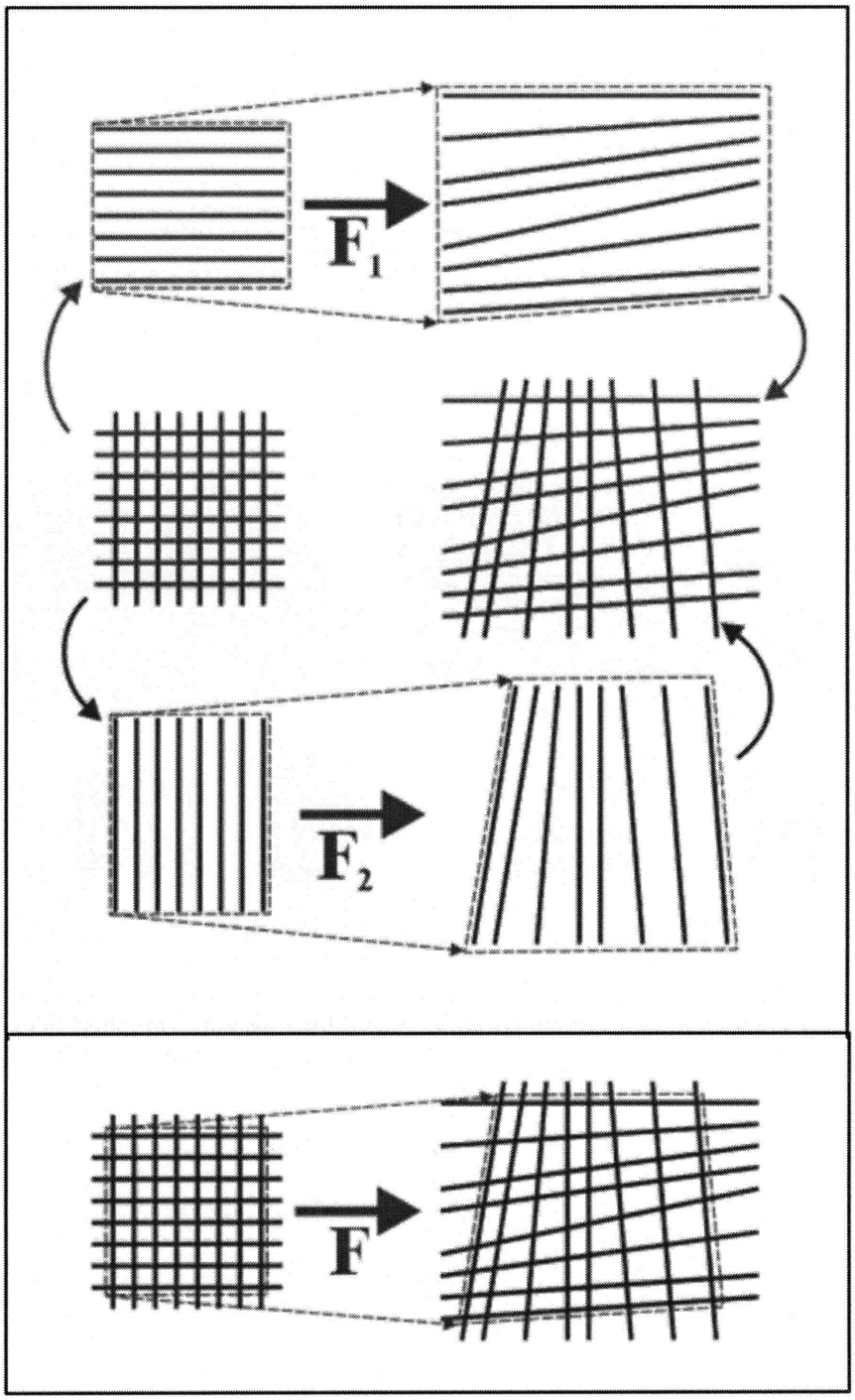

Figure 5-1 Two approaches for describing the kinematics of a fabric in the presence of slip; (Top) Use separate deformation mappings to describe the motion of each yarn family; (Bottom) Use a single deformation mapping to describe the motion of the crossover points

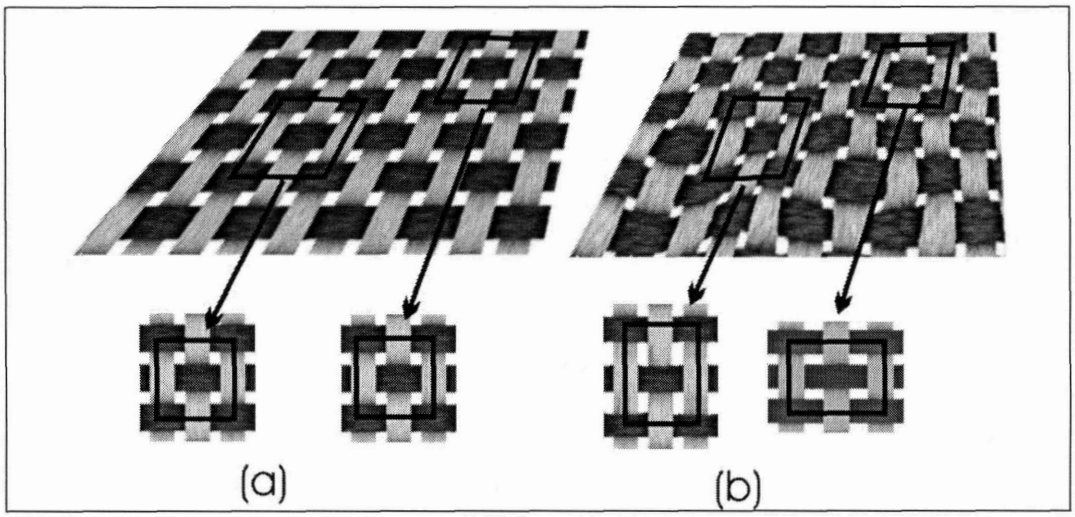

Figure 5-2 Differences between the slip-free and slip-enabled formulation (a) Yarn lengths associated with a crossover point remain constant and uniform throughout fabric (b) Yarn lengths associated with crossover point evolve with slip and vary from point to point

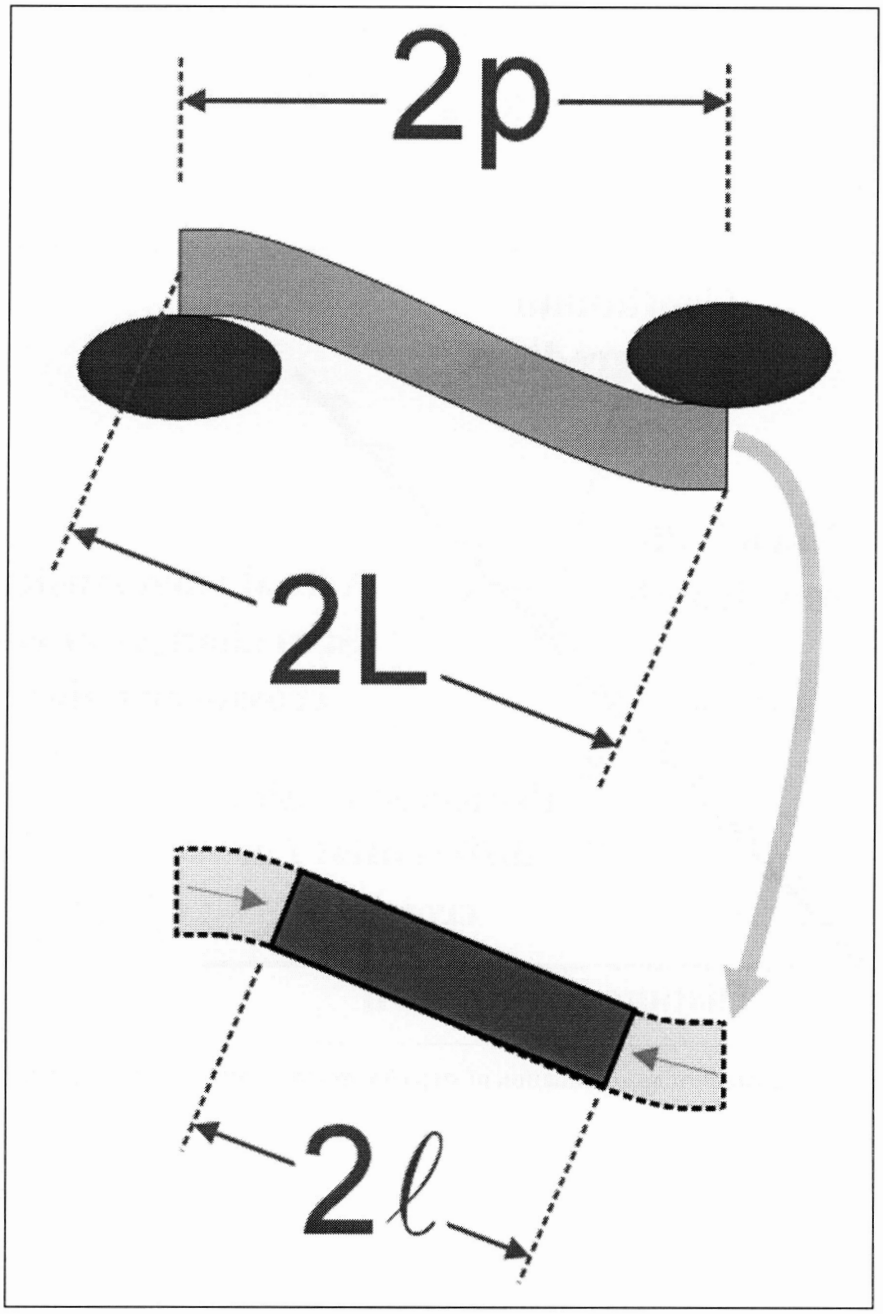

Figure 5-3 Description of the amount of yarn material between adjacent crossover points

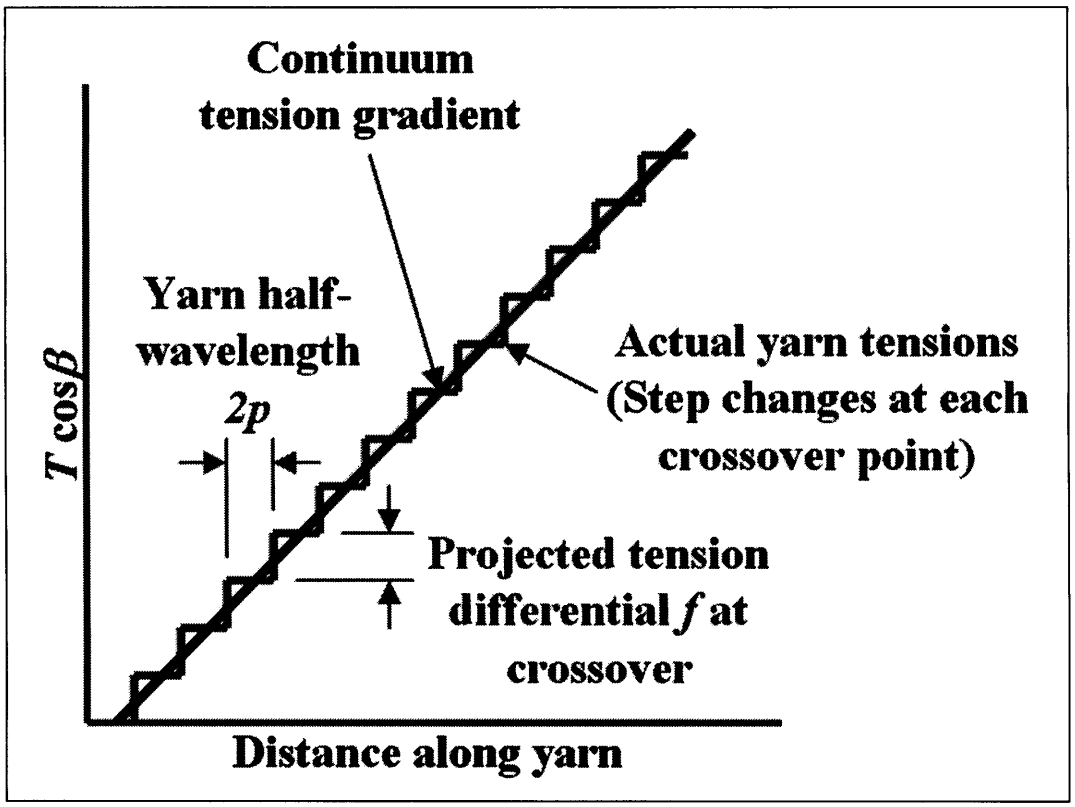

Figure 5-4 Continuum approximation of step changes in tension along a slipping yarn

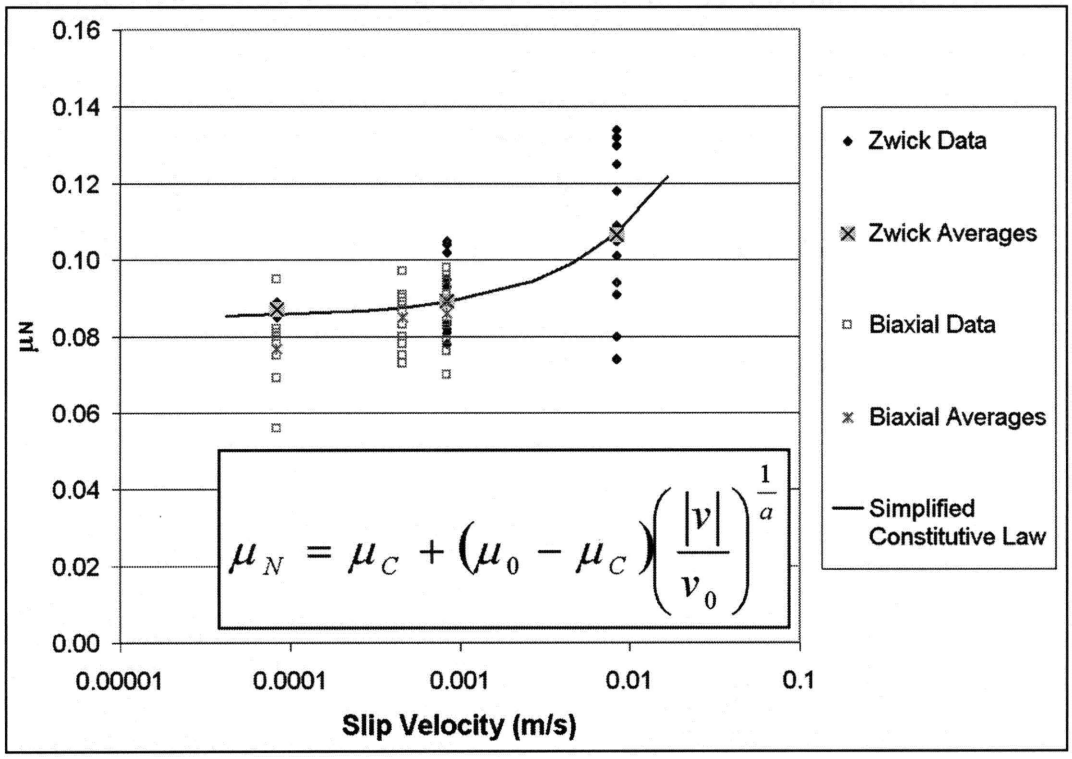

Figure 5-5 Power-law viscosity requires μ_N relation that approximates experimental data well

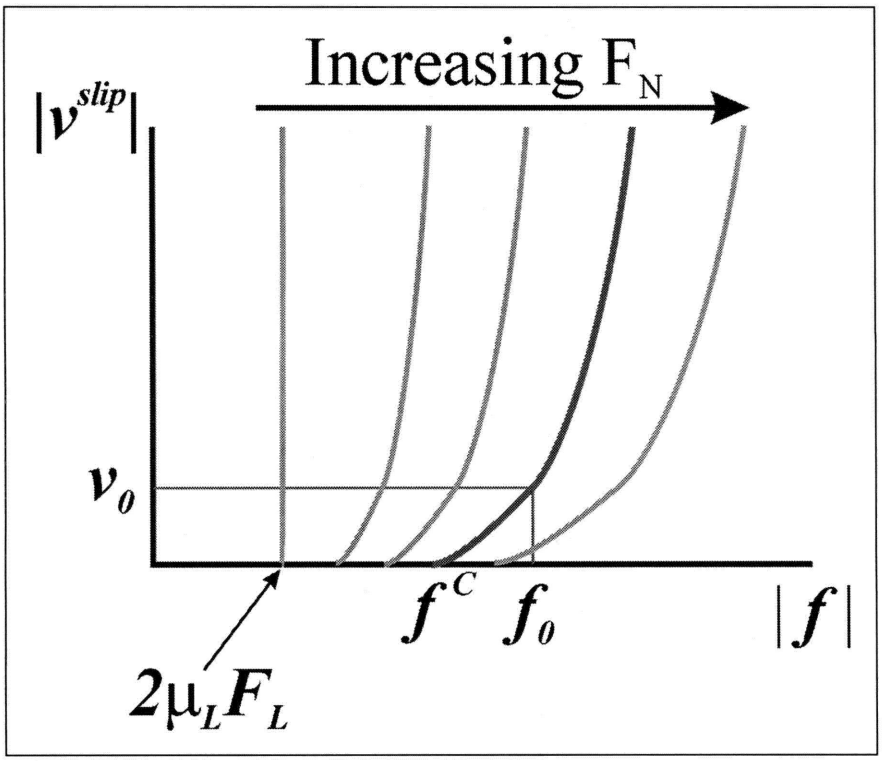

Figure 5-6 Behavior of simplified slip constitutive law

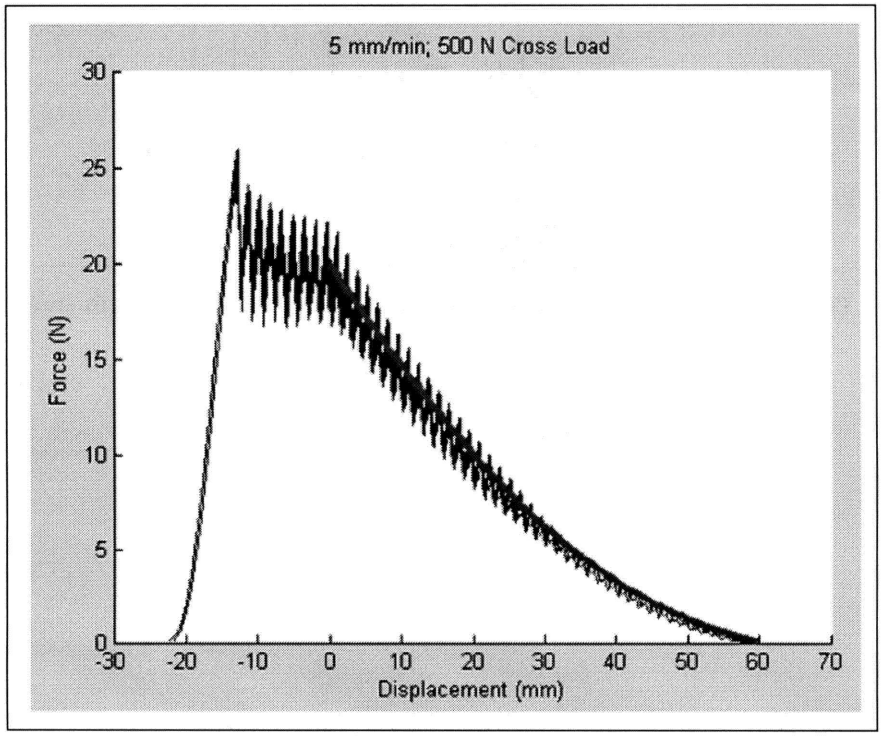

Figure 5-7 Comparison of pullout response predicted using analytical model and simplified slip constitutive law to experimental data at 5 mm/min

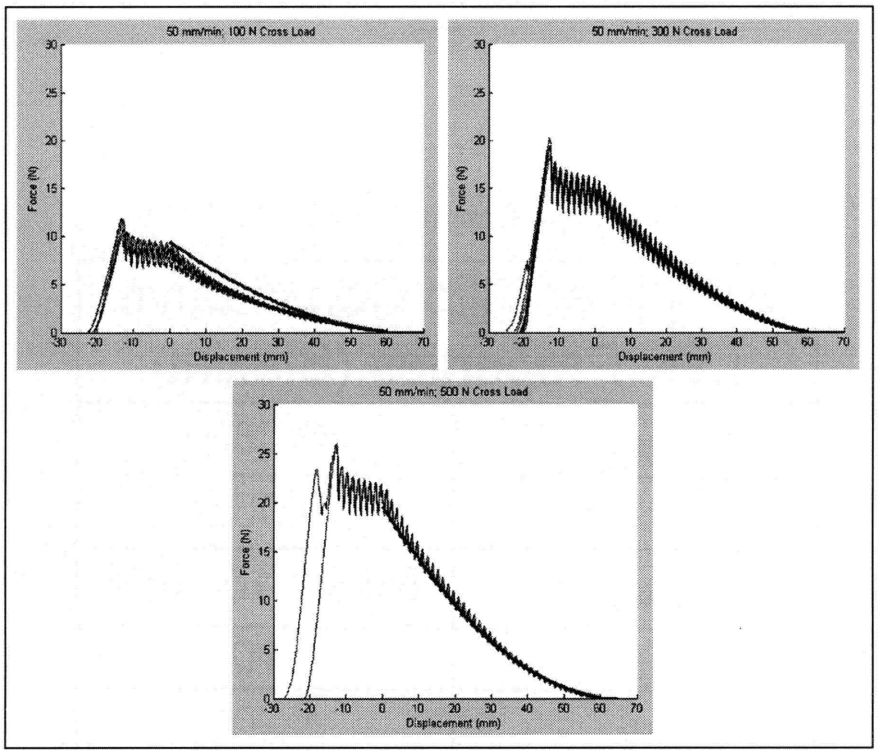

Figure 5-8 Comparison of pullout response predicted using analytical model and simplified slip constitutive law to experimental data at 50 mm/min

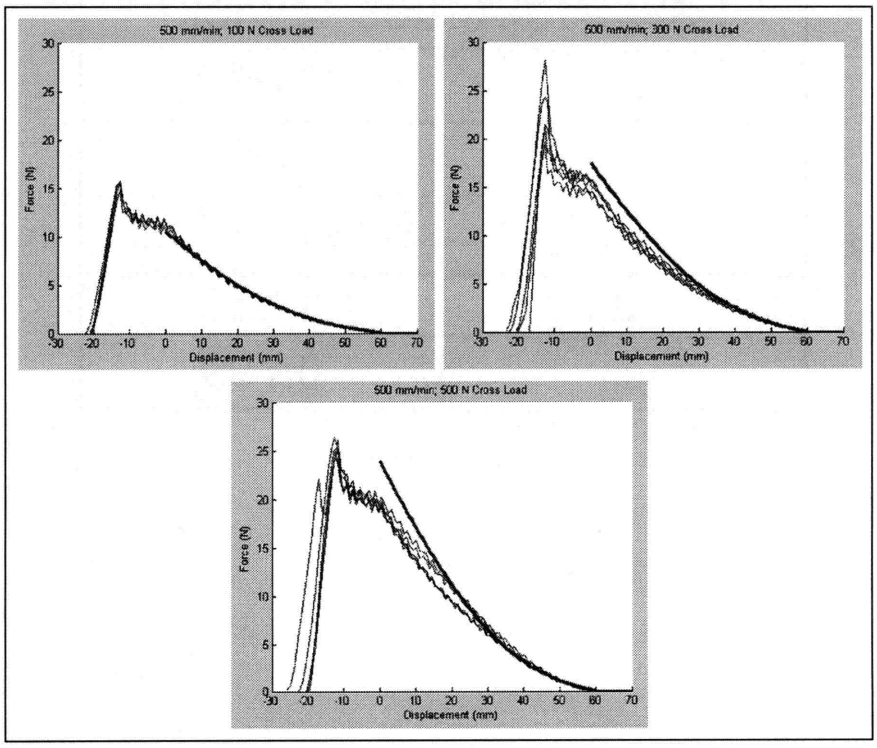

Figure 5-9 Comparison of pullout response predicted using analytical model and simplified slip constitutive law to experimental data at 500 mm/min

Table 5-1 Properties for simplified slip constitutive law

Simplified Slip Constitutive Law Properties (Biaxial)	
μ_c	0.080
μ_0	0.005
v_0	8.33×10^{-4} m/s
a	1.107
μ_L	1.200

Simplified Slip Constitutive Law Properties (Zwick)	
μ_c	0.085
μ_0	0.004
v_0	8.33×10^{-4} m/s
a	1.351
μ_L	0.799

Chapter 6
Implementation of Continuum Slip Model

6.1 Challenges of Implementing Continuum Slip

Chapter 5 describes a theory for capturing yarn slip in a continuum fabric model. The forces that drive slip, f_i, are calculated from the gradients of yarn tension **Grad**(T_i) according to Equation (5.19). When they become sufficiently large, these forces cause the yarns to begin to slip at velocities v_i^{slip}, according to the constitutive law given in Equations (5.21) and (5.29). The slip velocities of the stretched yarns v_i^{slip} can be converted into SLIDY velocities v_i using Equation (5.3). The unstretched yarn lengths ℓ_i evolve at a rate $\dot{\ell}_i$ that is proportional to the gradients of the SLIDY velocities, **Grad**(v_i), according to Equation (5.13). The yarn lengths at a given time are calculated by integrating the evolution rates $\dot{\ell}_i$ forward through time from known starting values ${}^0L_i$. Implementing this theory into a finite element framework presents a number of complex challenges.

The most significant challenge arises from the fact that traditional finite element frameworks are well suited only for use with "local" material models—there is an assumption that the response of a material at a given location depends only on the gradient of deformation (or the strain) and on other quantities, such as stresses, state variables, etc, evaluated at that location. Traditional finite element frameworks are not generally well suited for theories where the material response at a point depends on gradients of quantities other than the deformation. According to the slip continuum theory described in Chapter 5, the material response depends on the unstretched yarn lengths ℓ_i, which evolve based on the gradients of slip velocities, which are driven by gradients of tension. So the material response depends on the gradient of the gradient of the yarn tensions.

Unfortunately, the yarn tensions (like the stresses) are not calculated as smooth, continuous fields, but rather are calculated at discrete locations within the finite element mesh—the integration points of the elements. In order to implement the slip theory, a method must be devised for estimating a smooth tension field from these discrete values so that the slip velocities can be calculated, and for estimating a smooth velocity field from the calculated slip velocities so

that the evolution of the unstretched yarn lengths can be calculated at the integration points. Estimation of these smooth fields is complicated by three factors.

First, for an arbitrary finite element mesh of quadrilateral elements, the integration points are located at non-regular locations, as is shown in Figure 6-1. It is much more difficult to estimate smooth fields in multiple dimensions when the points at which the field values are sampled are not located on a regular lattice.

Secondly, the numeric locking problem discussed in Appendix C introduces small oscillatory errors into the tension values calculated at the integration points, which do not vanish as the mesh is refined. These errors cause larger errors into the calculated gradients, especially where the mesh is refined and the integration points are close together, and can even result in the appearance false gradients. When these inaccurate tension gradients are used to calculate slip velocities, the errors are further magnified, because the slip velocities in Kevlar® fabrics are very sensitive to variations in the tension gradients. When the gradients of the erroneous slip velocities are calculated, the error is magnified again, especially in areas where the mesh is refined.

Thirdly, in many applications it is most important to accurately measure slip near the edges of a fabric, especially if the redistribution of loads near a clamp or a damaged area of fabric are being investigated, or if yarn pullout or weave unraveling are being simulated. However, it is more difficult to accurately estimate the gradient of a field near the edge of the region where the field is sampled. A method of estimating the gradients must be adopted which allows for realistic boundary conditions on the tensions and slip velocities to be applied, to ensure that slip near the edges of the model is captured accurately.

We have developed a number of different methods for calculating the tension and slip velocity gradients and implementing the slip theory into the commercial finite element code ABAQUS. None of these methods is completely satisfactory; better numerical methods need to be developed for implementing a non-local material model that suffers from numerical locking into a finite element framework. However, our methods are sufficient for validation of the slip theory against several physical cases, despite some persistent numerical inaccuracies.

6.2 Hybrid Element Implementation

In order to calculate tension and slip velocity gradients in a finite element framework, we first tried developing hybrid elements which estimate smooth, continuous fields that approximate the calculated tensions and slip velocities at the integration points and that are interpolated over each element from tension and velocity degrees of freedom. The gradients of these fields can be

calculated from the degrees of freedom and the gradients of the interpolation functions. This method is attractive because it allows slip velocities and yarn length evolution rates to be calculated element by element, as compared to other methods that require the fabric state to be calculated over a patch of multiple elements before gradients can be determined and slip calculations can be made. Integration of the evolution of the unstretched yarn lengths forward through time can be performed implicitly if the slip velocities and evolution rates are calculated using this method, while for other methods explicit time integration with very small time steps is the best alterative. Although this approach ultimately proved unsatisfactory due to numeric issues introduced by the locking problem described in Appendix C, we nevertheless detail the method under the expectation that further investigation may lead to numerical techniques that eliminate the locking problem.

We begin with the hybrid element formulation described in Appendix B. This element formulation introduces a mean amplitude field to the element with corresponding additional degrees of freedom $\tilde{A}_a$, and uses these degrees of freedom to calculate the amount of crimp interchange that occurs everywhere in the element. This formulation is more computationally efficient that a purely displacement-based formulation and is easier to implement in the presence of inelastic phenomena such as slip. We then introduce additional fields that are used to estimate smooth projected tension fields within the element in order to calculate the tension gradients. For each yarn family, we introduce a set of interpolation functions $N_a^T(\mathbf{X})$ that describe the estimated projected tension field $\hat{T}$ at any point $\mathbf{X}$ within the element, given a set of n_T tension degrees of freedom $\hat{T}_a$:

$$\hat{T}(\mathbf{X}) = \sum_{a=1}^{n_T} N_a^T(\mathbf{X})\hat{T}_a \,. \tag{6.1}$$

These interpolation functions may be different from the functions that are used to interpolate displacements or mean amplitudes. It is more convenient to estimate the projected tension field $T\cos\beta$ instead of just the tension field T because the slip driving force f depends on the gradient of the projected tension, according to Equation (5.19). Unlike the tension fields described in Appendix C, which were intended to eliminate the element locking problem, the tension fields described by Equation (6.1) are "informational" fields in that they are not directly used to calculate the stress or the through thickness forces. Stress and through thickness force are determined from actual tension values T that are calculated at the integration points from the yarn stretches. Consequently, the reaction forces associated with the displacement and mean amplitude

fields will have no dependence on the projected tension degrees of freedom $\hat{T}_a$ and the corresponding terms of the stiffness matrix will be zero.

In order to solve for the additional degrees of freedom, we must develop corresponding equilibrium equations. Since the estimated projected tension fields should approximate the actual projected tension values $T\cos\beta$ calculated at the integration points, we introduce the following equilibrium equation in strong, or local, form:

$$\hat{T}(\mathbf{X}) = T(\mathbf{X})\cos\beta(\mathbf{X}). \tag{6.2}$$

The corresponding weak or integral form is obtained by multiplying this expression by an arbitrary admissible test function $\overline{T}$ and integrating over the element:

$$\int_e \overline{T}\left\{\hat{T}(\mathbf{X}) - T(\mathbf{X})\cos\beta(\mathbf{X})\right\} dV = 0. \tag{6.3}$$

For any estimated field $\hat{T}(\mathbf{X})$, there will be residual generalized forces R_a^T that are conjugate to each of the degrees of freedom $\hat{T}_a$. These forces are determined by choosing a test function $\overline{T}$ that is interpolated from test degrees of freedom $\overline{T}_a$ according to Equation (6.1), and then choosing successive sets of test degrees of freedom $\overline{T}_a = \delta_{ab}$ for $b = \{1,2,\ldots n_T\}$. This gives n_T residuals associated with each of the n_T tension degrees of freedom:

$$R_a^T = \int_e N_a^T \left\{\hat{T}(\mathbf{X}) - T(\mathbf{X})\cos\beta(\mathbf{X})\right\} dV. \tag{6.4}$$

Because integration in a finite element code is typically performed numerically, this integral expression can be rewritten as a sum over the integration points:

$$\begin{aligned} R_a^T &= \sum_q \left(N_a^T \left\{ \sum_{b=1}^{n_T} N_b^T \hat{T}_b - T\cos\beta \right\} \right)\Bigg|_q w_q J_q \\ &= \sum_q N_a^T\Big|_q \left\{ \sum_{b=1}^{n_T} N_b^T\Big|_q \hat{T}_b - T_q \cos\beta_q \right\} w_q J_q \end{aligned}. \tag{6.5}$$

Here w_q is the integration weight associated with integration point q, J_q is the element isoparametric Jacobian at q, and T_q and β_q are the actual tension and crimp angle, respectively, calculated at integration point q, which depend on the displacement and mean amplitude degrees of freedom of the element. Refer to a finite element text such as Bathe [1996] for further details regarding numeric integration. Note that the same integration orders need not be used for evaluating the tension field residuals and the displacement and mean amplitude residuals. However, using different integration orders for different residuals would require multiple sets of

integration points per element. Not only would this practice cause the memory storage requirements for such an element to become large, but it would also pose challenging questions regarding how the evolution of the state variables for the two sets of integration points should be calculated. For simplicity, we assume the same integration order for all residual equations, sufficiently large so that the displacement equations are fully integrated (since reduced integration is known to introduce spurious deformation modes into the fabric element, as is discussed in Appendix C).

When all residuals R_a^T are zero, the corresponding set of nodal tension degrees of freedom $\hat{T}_a$ generate an estimated tension field $\hat{T}(\mathbf{X})$ that best approximates $T(\mathbf{X})$. These degrees of freedom can be calculated by the Newton-Rhapson algorithm used by implicit finite element codes, provided that the variations of all the residuals with all degrees of freedom are known. Because the through thickness forces and the stresses do not depend on $\hat{T}(\mathbf{X})$, the residuals associated with the displacements u_j and the mean amplitude $\tilde{A}$ have no dependence on $\hat{T}_a$ and hence the corresponding variations are all zero:

$$K_{jab}^{UT} \equiv \frac{\partial R_{ja}^U}{\partial \hat{T}_b} = 0, \tag{6.6}$$

$$K_{ab}^{AT} \equiv \frac{\partial R_a^A}{\partial \hat{T}_b} = 0. \tag{6.7}$$

R_{ja}^U and R_a^A give the residuals associated with displacement of displacement node a in the j-direction, and with a change in mean amplitude at amplitude node a, respectively. The variations associated with the residuals R_a^T are given below:

$$\begin{aligned} K_{ajb}^{TU} &\equiv \frac{\partial R_a^T}{\partial u_{jb}} = \sum_q N_a^T\big|_q \frac{\partial (T_q \cos\beta_q)}{\partial u_{jb}} w_q J_q \\ &= \sum_q N_a^T\big|_q \frac{\partial (T\cos\beta)}{\partial F_{jK}} N_{b,K}^U\big|_q \; w_q J_q \end{aligned}, \tag{6.8}$$

$$\begin{aligned} K_{ab}^{TA} &\equiv \frac{\partial R_a^T}{\partial \tilde{A}_b} = \sum_q N_a^T\big|_q \frac{\partial (T_q \cos\beta_q)}{\partial \tilde{A}_b} w_q J_q \\ &= \sum_q N_a^T\big|_q \frac{\partial (T\cos\beta)}{\partial \tilde{A}} N_b^A\big|_q \; w_q J_q \end{aligned}, \tag{6.9}$$

$$K_{ab}^{TT} \equiv \frac{\partial R_a^T}{\partial \hat{T}_b} = \sum_q N_a^T\big|_q \; N_b^T\big|_q \; w_q J_q . \tag{6.10}$$

Here u_{jb} is the displacement of displacement node b in the j-direction, F_{jK} give the components of the deformation gradient $\mathbf{F}$, N_a^U gives the interpolation functions associated with the displacement degrees of freedom at displacement node a, N_a^A gives the interpolation function associated with the mean amplitude degree of freedom $\tilde{A}_a$, and $N^U_{a,K}$ gives the gradient of N_a^U in the K-direction in the reference configuration. The residuals given in Equation (6.5) and the variations given in Equations (6.8) - (6.10) are added to the element residual vector and stiffness matrix, respectively, and the resulting hybrid element formulation can be used to determine the additional tension degrees of freedom.

Once these tension degrees of freedom are known, the gradients of the estimated projected tension fields can be readily calculated:

$$\mathbf{Grad}\left(\hat{T}\right) = \sum_{K=1}^{2}\sum_{a=1}^{n_T} N^T_{a,K}\hat{T}_a \mathbf{e}_\mathbf{K} \,. \tag{6.11}$$

Here $\mathbf{e}_\mathbf{K}$ is a unit vector in the reference configuration K-direction, and $N^T_{a,K}$ is the gradient of the interpolation function N_a^T in the reference configuration K-direction.

At each integration point, the through-thickness and locking forces F_N and F_L are known, as are the yarn stretches λ and quarter-wavelengths p. $\mathbf{Grad}(\hat{T})$, which approximates $\mathbf{Grad}(T\cos\beta)$, can be evaluated, and so the SLIDY velocity v_i can then be calculated using Equations (5.19), (5.29), and (5.3). However, in order to calculate the evolution of the unstretched yarn lengths ℓ using Equation (5.13), the gradient of v_i must be determined. We therefore repeat the procedure outlined above to estimate a smooth v_i field. Suitable interpolation functions N_a^V are introduced that allow smooth estimated SLIDY velocity fields $\hat{v}$ to be calculated from SLIDY velocity degrees of freedom $\hat{v}_a$:

$$\hat{v}(\mathbf{X}) = \sum_{a=1}^{n_V} N_a^V(\mathbf{X})\hat{v}_a \,. \tag{6.12}$$

We require that the difference between the calculated SLIDY velocities v and the estimated SLIDY velocity fields $\hat{v}$ vanish at the integration points, which result in a set of residuals that must be zero:

$$\begin{aligned} R_a^V &= \int_e N_a^V \{\hat{v}(\mathbf{X}) - v\} dV \\ &= \sum_q N_a^V\big|_q \left\{\sum_{b=1}^{n_V} N_b^V\big|_q \hat{v}_b - v_q\right\} w_q J_q \end{aligned} \,. \tag{6.13}$$

v_q is the SLIDY velocity that is calculated at integration point q. The variations of R_a^V with respect to the displacement, mean amplitude, and tension degrees of freedom are:

$$K_{ajb}^{VU} \equiv \frac{\partial R_a^V}{\partial u_{jb}} = \sum_q N_a^V\big|_q \ \frac{\partial v_q}{\partial u_{jb}} w_q J_q \,, \tag{6.14}$$

$$K_{ab}^{VA} \equiv \frac{\partial R_a^V}{\partial \tilde{A}_b} = \sum_q N_a^V\big|_q \ \frac{\partial v_q}{\partial \tilde{A}_b} w_q J_q \,, \tag{6.15}$$

$$K_{ab}^{VT} \equiv \frac{\partial R_a^V}{\partial \hat{T}_b} = \sum_q N_a^V\big|_q \ \frac{\partial v_q}{\partial \hat{T}_b} w_q J_q \,, \tag{6.16}$$

Note that v depends on the weave deformation gradient $\mathbf{F}$ and hence on the displacements because F_N, F_L, and p depend on $\mathbf{F}$. v depends on $\tilde{A}$ because F_N and F_L depend on $\tilde{A}$. v depends on the nodal tension degrees of freedom $\hat{T}_a$ because it depends on the slip driving force f: as $\hat{T}_a$ vary, **Grad**($\hat{T}$) varies and hence f varies.

If an explicit evolution scheme for ℓ is used, the value of ℓ for the current increment, $\ell^{t+\Delta t}$, is determined by the size of the increment Δt and the evolution rate $\dot{\ell}^t$ at the end of the previous increment:

$$\ell^{t+\Delta t} = \ell^t + \Delta t \dot{\ell}^t \,. \tag{6.17}$$

Such an approach typically requires very small values for Δt in order to ensure accuracy and stability, and hence can be very computationally expensive. In this case, the value of ℓ that is used to calculate stresses, through thickness force, etc., will not depend on the estimated SLIDY velocity fields calculated during the current increment and hence none of the residuals other than $R_a{}^V$ will depend on the SLIDY velocity degrees of freedom $\hat{v}_a$. Consequently, $K^{UV} = K^{AV} = K^{TV} =$ 0. Furthermore, the variation of $R_a{}^V$ with respect to $\hat{v}_b$ will only have a single term:

$$K_{ab}^{VV} \equiv \frac{\partial R_a^V}{\partial \hat{v}_b} = \sum_q N_a^V\big|_q \ N_b^V\big|_q \ w_q J_q \,. \tag{6.18}$$

However, an advantage of this hybrid element approach is that it permits an implicit evolution scheme for ℓ. In other words, if the evolution rate at the end of the previous increment is given by $\dot{\ell}^t$ and the rate at the end of the current increment is calculated to be $\dot{\ell}^{t+\Delta t}$ from the estimated SLIDY fields, then the length for the current increment $\ell^{t+\Delta t}$ can depend on both rates according an approximate implicit integration scheme such as the trapezoidal rule below:

$$\ell^{t+\Delta t} = \ell^t + \frac{\Delta t}{2}\left(\dot{\ell}^t + \dot{\ell}^{t+\Delta t}\right). \tag{6.19}$$

Such an algorithm permits much larger time increments and guarantees stability. However,

because the stresses, through thickness force, etc., depend on $\ell^{t+\Delta t}$, which now depend on $\dot{\ell}^{t+\Delta t}$ and hence on the estimated SLIDY fields, all of the residuals will now depend on $\hat{v}_a$ and K^{UV}, K^{AV}, and K^{TV} will no longer be zero. Furthermore, K^{VV} will have additional terms:

$$K_{ab}^{VV} \equiv \frac{\partial R_a^V}{\partial \hat{v}_b} = \sum_q N_a^V\Big|_q \left(N_b^V\Big|_q - \frac{\partial v_q}{\partial \hat{v}_b} \right) w_q J_q \,. \tag{6.20}$$

The resulting element stiffness matrix will be neither sparse nor symmetric. Our numerical trials indicate that convergence is not guaranteed and may be extremely slow. Further research into the numerical behavior of this system is necessary.

We still must address the choice of suitable interpolation schemes for $\hat{T}$ and $\hat{v}$. Interpolation using piecewise polynomial functions is most common. However, the oscillatory noise in the tension data calculated from the locking phenomenon described in Appendix C limits the order of the polynomials that can be chosen. For example, consider the simple one dimensional case shown in Figure 6-2. In this case, the tension field increases linearly from 0.8 to 1.0 along one element of unit length, remains constant at 1.0 along a second element, and decreases linearly to 0.8 along a third. This tension is sampled at three Gauss integration points, which is consistent with full integration of an element with quadratic displacement interpolation. In the cases shown at the top of the figure, the tension is sampled accurately. In the cases shown at the bottom, oscillatory noise has been added to the sampled tensions: the outside integration points have been increased by a random value between 0 and 0.1, and the central integration point has been decreased by a random value between 0 and 0.1. Such noise is consistent with the noise generated by the numeric locking phenomenon. In the noise free cases, both a continuous linearly interpolated estimated tension field and a continuous quadratically interpolated estimated tension field exactly reproduce the real tension fields. In the presence of noise, the linear estimated field still closely approximates the real tension field. However, the quadratic estimated field conforms to the oscillatory noise and indicates oscillating tensions and large, artificial gradients. Such problems are even more severe when discontinuous interpolation fields are used, and when the estimated field is approximated over a two dimensional domain, as it is in actual elements. In general, in order to avoid large, artificial gradients from the oscillatory noise, the estimated tension fields must be interpolated at a lower polynomial order than the displacement fields, as the interpolation order of the displacement fields determines the order of integration and hence the number of Gauss integration points per element.

The simplest possible interpolation scheme, which is discussed in greater detail in Section 6.5, is to treat the estimated tension and SLIDY velocity fields as piecewise constant over each

element, so that $n_T = n_V = 1$ and N^T and N^V are equal to unity. This is equivalent to finding the average value of tension and SLIDY velocity over the element. However, a field that is constant over an element has no gradients, so use of such an interpolation scheme would never result in slip. The next simplest scheme would be to assume that the fields vary linearly over each element, with three degrees of freedom describing the linear variation in two dimensions:

$$\hat{T} = \hat{T}_1 + \hat{T}_2 X + \hat{T}_3 Y \,. \tag{6.21}$$

The fields yielded by this scheme are discontinuous at the element boundaries We experimented with such an interpolation scheme and were met with limited success. The chief shortcoming of this scheme is that the gradients it predicts are extremely sensitive to small errors in the tension values sampled at the integration point values, especially when the mesh is significantly refined, so the oscillatory noise from the locking phenomenon resulted in tension gradients with large errors.

Interpolation schemes that are continuous across element boundaries proved to be less sensitive to errors at individual integration points. The continuous bilinear and biquadratic interpolation schemes used for traditional finite elements (see Bathe [1996]) are not suitable for representing fields that are specific to a particular material direction in an anisotropic material, because they cannot accurately represent certain common physical situations, as is described in Appendix D. We therefore developed an interpolation scheme that is continuous across element boundaries and that can accurately represent fields specific to a specific material direction. We refer to this scheme as "chordal interpolation" because it involves linearly interpolating along a chord parallel to the material direction that connects points on the element edges. The field values at these points are interpolated either linearly or quadratically from the nodal field values at the end points of each element edge. When the material directions are aligned with the edges of a rectangular element, chordal interpolation is equivalent to linear interpolation in one direction and either linear or quadratic interpolation in the other. Because we commonly use a biquadratic interpolation scheme for displacement interpolation, we limit the chordal interpolation scheme to linear interpolation along the element edges. The chordal interpolation scheme is discussed in detail in Appendix D.

We investigated a wide variety of different hybrid element formulations, including formulations that combined bicubic, biquadratic, or bilinear displacement interpolations with biquadratic, bilinear, or linear chordal tension and velocity interpolations, and with different orders of integration. As is described in Appendix C, some of these formulations suffer more severely from the numeric locking phenomenon than the fully integrated biquadratic displacement based elements do. Some exhibit spurious modes that caused extremely unrealistic

displacements to be predicted or that caused the element stiffness and the tension gradients to be severely underestimated. The most successful element formulation used biquadratic interpolation for the displacement and mean amplitude degrees of freedom, linear chordal interpolation for the tension and velocity degrees of freedom, and nine integration points to ensure that the displacement residual equations were fully integrated. This element suffered from the numeric locking phenomenon, but not as severely as some of the formulations, exhibited no spurious modes, and predicted realistic (although somewhat noisy) tension and velocity fields in all physical cases investigated.

This element was ultimately unsatisfactory. Because the estimated tension fields were continuous but not smooth across element boundaries, the tension gradient along a given yarn is constant within each element but abruptly changes at each element boundary. Furthermore, numerical errors caused oscillations in the estimated tension fields—tension would be overpredicted in one element and underpredicted in the next (although the net error integrated over the elements is necessarily zero). It is not clear if these oscillations are caused by the numeric locking problem or other instabilities in the hybrid element formulation. They result in abruptly changing tension gradients from one element to the next, and in some cases even created "saw-tooth" shaped estimated tension fields, with tension increasing across one element, decreasing across the next, then increasing again, etc. The corresponding slip velocities would therefore also vary abruptly from element to element and could oscillate from positive to negative along subsequent elements. This in turn would cause the model to predict large yarn length evolution rates near the element boundaries, which cause the yarns "bunch up" along the element boundaries. The resulting predictions of the fabric mesostructural evolution is therefore highly mesh dependent and non-physical. This behavior is shown in Figure 6-3 for the bias-extension case with a very fine mesh. Even though the tension contours appear reasonably smooth, a great deal of oscillatory noise is evident in the SLIDY, velocities, and the true yarn length evolution rates are outweighed by erroneously large values at the element boundaries.

6.3 Fourier Smoothing Techniques

The problems with the hybrid elements stemmed from the fact that the fields they predicted were non-smooth. Higher order interpolation functions that yield smooth functions are more adversely affected by the oscillatory noise from numeric locking. Therefore, we investigated other means of smoothing the estimated tension and velocity fields. One common method of smoothing a data field is to approximate the field with a surface constructed of splines. This

procedure is straightforward in one dimensional domains and in two dimensional domains where the sampled points are regularly spaced, as is shown at the top of Figure 6-1. However, it is extremely challenging to generate a smooth field using splines on a two dimensional domain with irregularly positioned data points, such as a model arbitrarily meshed with quadrilateral elements shown at the bottom of Figure 6-1. Therefore, we investigated non-spline techniques for smoothing the data fields.

The first such technique that we investigated involves transforming the tension data from a spatial domain to a frequency domain using fast Fourier transforms. The transformed data can then be passed through a filter to eliminate any noise that appears above a given cutoff frequency. In other words, any features that have a length scale smaller than a certain value can be eliminated. When small length scale features, such as abrupt peaks or troughs in tension at the element edges, are eliminated, the data is smoothed. The filtered data can then be transformed back into the spatial domain and analyzed. Examples of these transformations are shown in Figure 6-4 for a state of tension predicted in the bias-extension case, and in Figure 6-5 for a state of tension predicted in the slit-damage case using a quarter-symmetry model. These test cases are described in detail in Sections 2.10 and 2.11, respectively. Note that these fields are plotted in the reference configuration geometry. Provided that a sufficient filter size is chosen, the noise in the tension fields can be smoothed and the mesh-dependent erroneous slip velocities and yarn length evolution rates can be eliminated. In the un-filtered cases on the left of the figures, the mesh-dependent oscillations in the driving force are visible, as are the large yarn length evolution rates at the element boundaries. After sufficient filtering, both cases qualitatively predict realistic velocity fields and yarn length evolution rates that are consistent with experimental observations. In the bias case, slip velocities grow along the diagonal lines that experimental samples separate along, and yarn length evolution rates become positive at the edges of the strip, indicating that the weave at the edges will being to unravel. In the slit-damage case, two modes of slip develop around the slit, as is described by Godfrey and Rossettos ([1998] and [1999]) and in Sections 2.10.

However, this method suffers from several problems. First, the smoothing process tends to blunt large tension concentrations, so the smoothed tension contours may underestimate slip that actually occurs. As is evident in Figure 6-4 and Figure 6-5, the greater the smoothing, the more tension concentrations are artificially reduced. Secondly, in order to eliminate the mesh-dependent noise, the smoothing method must filter out features that have a length scale equal to the characteristic length scale of the elements. However, in many cases real slip-driven phenomena, like the redistribution of tension concentrations at the tip of a slit or the unraveling of

the weave at the edge of the bias-extension sample, occur over only a few yarns. Since the fabric cannot be treated as a continuum at length scales smaller than a few yarns, the mesh cannot be refined to smaller length scales and still give realistic results. Consequently, the smallest possible characteristic element length will be the same size as the length scale over which some slip phenomena occur. Therefore, these slip phenomena will be filtered out along with the numeric noise. Finally, this smoothing technique introduces errors into the smoothed fields near the boundaries, which are apparent in Figure 6-5. These errors are magnified when the gradients are calculated. As discussed previously, it is often most important to accurately calculate slip near the fabric edges.

6.4 Virtual Shell Coupling

The next smoothing approach that we investigated was motivated by conceptualizing the tension fields as three dimensional surfaces whose heights vary as a functions of position on a two dimensional plane. The non-smooth, noisy tension data is represented by a rough surface with sharp peaks and valleys. Our goal is to determine a smooth surface without any sharp peaks that approximates the rough surface as closely as possible. Provided that the variations in height are small, this can be accomplished by bending a thin, elastic plate into a shape that closely approximates the rough surface. We therefore developed a method of estimating smooth gradients by using shell elements whose out-of-plane displacement degrees of freedom are coupled to the nodal tensions calculated by the fabric elements. This approach is attractive because shells are inherently non-local; since rotations are continuous across element boundaries, the response of a given element to out of plane deformations is influenced by the response of the neighboring elements. The out-of-plane displacement fields will always be smooth, and the gradients of those fields can be calculated from the shell rotations.

We refer to this technique as virtual shell element coupling, and we explored two slightly different implementations. The algorithm for the first implementation is shown in Figure 6-6. Hybrid fabric elements with tension degrees of freedom are used. These elements also possess degrees of freedom corresponding to estimated locking force and through-thickness force fields, and lack SLIDY velocity degrees of freedom. The tension, locking force, and through-thickness force degrees of freedom serve as a means of extrapolating the actual tensions, locking forces, and through-thickness force calculated at the integration points to the corner nodes in a manner that eliminates the oscillations introduced by numeric locking. These fields are interpolated using a linear chordal interpolation scheme described Appendix D and therefore are continuous from

element to element but not smooth. Two "tension shell" models (one for each yarn family) that are topologically identical to the real model are constructed out of thin shell elements composed of a linear elastic material, and then constrained against rigid body motion. The out-of-plane displacements of the tension shell nodes are connected to base nodes using linear spring elements. The out-of-plane displacements of these base nodes are coupled to the tension degrees of freedom in the fabric elements using multi-point constraints, scaled so that the shell deformations remain small.

The base nodes and spring elements are used because, if the shell nodes were coupled directly to the tension degrees of freedom, the shell surface would not smooth the tension field. By separating the shell nodes from the base nodes with springs, the shell elements are free to assume a smoother shape with a lower energy cost than that prescribed by the non-smooth nodal tension values. However, the more the shape of the tension shells deviate from the actual tension field, the greater the energy cost in the connecting springs. By varying the ratio of the connecting spring stiffness to the flexural rigidity of the shells, different amounts of smoothing can be achieved. However, the total stiffness of the composite system consisting of the shell elements and the springs must be significantly smaller than the stiffness associated with varying the tension degrees of freedom in the real model. Otherwise, the resistance of the shells to deformation will feed back to the real model and adversely affect the calculation of the estimated tension fields, since the multi-point constraints that couple the shells transfer force in both directions.

Boundary conditions on tension are applied to both the fabric elements and the tension shells. For example, when yarns intersect a free edge, the tension in those yarns should be zero. Both the appropriate tension degrees of freedom in the fabric elements and the out-of-plane displacements of the appropriate tension shells can be constrained to be zero on free edges to capture this boundary condition.

Two more topologically identical "velocity shell" models are created to calculate smooth slip velocity fields. Like the tension shells, the velocity shells are constrained against rigid body motion and are coupled in the out-of-plane direction to a set of base nodes with linear springs. The rotational degrees of freedom of the tension shells are then used to calculate the tension gradients at the nodes, which are used in conjunction with the locking force and through-thickness force degrees of freedom from the fabric elements to calculate slip velocities according to the slip constitutive law given in Equation (5.29). These slip velocities are coupled to the out-of-plane displacements of the base nodes attached to the velocity shells. Appropriate boundary conditions on slip velocity are applied (e.g. zero slip velocity at clamped edges). Like the tension shells, the stiffness associated with the velocity shell nodes must be significantly smaller than the

stiffness associated with rotations of the tension shells and the stiffness associated with the nodal locking force and through-thickness force degrees of freedom of the fabric elements, in order to avoid feedback. Unfortunately, because the displacements of the velocity shells are coupled to these quantities through a nonlinear slip constitutive law, it can be difficult to quantify the relative stiffnesses of the two structures.

The nodal rotations of the slip velocity shells can be used to calculate the SLIDY velocity gradients and the corresponding unstretched yarn evolution rates. These values can be written to an output file at the end of each increment and read in at the beginning of the next increment in order to explicity calculate the evolution of the unstretched yarn lengths. The subroutine that calculates the fabric element behavior interpolates between the evolution rates at the nodes to find the evolution rates at each integration point, and calculates the evolution of the unstretched yarn lengths explicitly.

This method proved more effective than the Fourier transform smoothing described in the preceding section. Figure 6-7 shows the predicted tension, slip velocity, and yarn length evolution rate fields in both the bias-extension test and the slit-damage test. The same physically realistic contours that were evident from the Fourier-smoothed plots appear, but most of the noise and non-physical numerical artifacts have been eliminated without significantly blunting the tension concentrations (some blunting is inevitable in any smoothing process) or introducing error near the boundaries. In fact, the application of accurate boundary conditions is a major benefit of the virtual coupled shell method. However, three chief problems with this method remain. First, it is difficult to determine appropriate numerical parameters, such as the factors that scale tension and slip velocity before applying them as displacements, the stiffness of the coupling springs, the thickness of the shells, and the properties of the materials that compose the shell elements. These parameters must yield stiffnesses that are small enough to avoid feedback but large enough so that resulting global stiffness matrix does not become ill conditioned. Secondly, this method is extremely expensive, both in computational cost and in memory requirements, since n fabric elements require an additional $4n$ shell elements. Finally, it does not completely eliminate mesh-dependent numeric noise and oscillations from one element to the next, as is evident in the plot of the bias-extension case in Figure 6-7. Though these errors are much smaller than those in the unsmoothed data, they are significant enough to prevent accurate, physically realistic slip fields from being predicted in all but the most simple cases.

We modified the coupled virtual shell element method to try to further reduce these errors. The process of extrapolating estimated tension values to the nodes by interpolating them as continuous fields over the element introduces some of the numeric noise. If the tensions are

instead averaged over each element, the resulting tension values are much more accurate and less noisy. The average tensions in an element are calculated by placing a node at each element center and introducing just one "informational" degree of freedom $\hat{T}$ per element for each tension field. The residual associated with this degree of freedom is the difference between its value and the values of the project tensions integrated over the element, as calculated from the integration point values:

$$R_T = \int_e \left(\hat{T} - T\cos\beta\right) dV = \hat{T}V_e - \sum_q T_q \cos\beta_q J_q w_q \,, \tag{6.22}$$

where $T_q\cos\beta_q$ is the projected tension calculated at integration point q, J_q is the isoparametric Jacobian, associated with integration point q, w_q is the weight associated with integration point q, and $V_e = \sum_q J_q w_q$ is the volume of the element (unit thickness is assumed). When this residual vanishes, the value $\hat{T}$ will reflect the average value of $T\cos\beta$ over the element. This can equivalently be thought of as estimating a projected tension field $\hat{T}$ that is piecewise constant over each element and discontinuous between elements. The interpolation functions associated with this a field, $N^T(\mathbf{X})$, are equal to unity and Equation (6.5) reduces to Equation (6.22).

Piecewise constant fields are unable to exhibit oscillatory behavior over an element and hence completely eliminate the oscillations in the tension fields that stem from numeric locking of the fabric elements, discussed in Appendix C. They also do not introduce "saw-tooth" oscillations from one element to the next; since the estimated tension field is not required to be continuous across elements, it is calculated as accurately as possible in every element. Therefore, no smoothing is necessary. Instead, the virtual shell elements are used to calculate continuous fields from the averaged data, since the estimated tension fields are discontinuous and piecewise constant and cannot directly be used to calculate gradients. Once the averaged projected tensions are imposed on the coupled virtual shells as displacements, the gradients can be calculated from the virtual shell rotations.

Because the tensions that are to be applied as displacements to the shell elements are now located at the center of the real elements, the shell mesh must be refined so that shell nodes lie at the centers of the fabric elements. For each fabric element, four shell elements are used, with corner nodes at the corners, mid-edges, and centers of the fabric elements. Because there are now unconstrained shell nodes between the constrained nodes, and because the averaged projected tension data do not require smoothing, base nodes and spring elements are unnecessary—the averaged projected tension values at the element centers can be scaled and directly applied to the corresponding shell nodes as out-of-plane displacements. The locking and through-thickness

forces are also averaged at the centers of the real elements and are used with the projected tension gradients from the tension shell rotations to calculate slip velocities. The scaled slip velocities are then applied directly to the appropriate velocity shells, which are topologically identical to the tension shells. The rotations of the velocity shells can be used to calculate the velocity field gradients and the yarn length evolution rates, which are written to an output file and read in and applied in the next increment, as described above.

This second coupled virtual shell method was more accurate and had less noise than the first method. Provided suitable values for the shell material properties, shell thicknesses, and tension and velocity scale factors were used, the model predicted stable, physically realistic slip contours with almost no numeric noise. For simple cases where the mesh did not need significant refinement to capture phenomena that occur over small length scales, this method was effective. However, it also suffered from several problems. First, it was even more computationally expensive than the first method, requiring *16n* shell elements for models with n fabric elements. Secondly, in certain situations the shells would buckle in complex three-dimensional modes that would sometimes generate non-physical slip velocities or yarn evolution rates. The most significant problem with both coupled virtual shell methods is the choice of suitable values for the shell material properties, shell thicknesses, and tension and velocity scale factors.

In order to predict smooth fields that are accurate and physically realistic, three conditions must hold for the tension shells. First, the shells must behave as "thin" shells—i.e. the shell bending stiffness must be much smaller than the shell transverse shear stiffness so that the shells accommodate deformation through bending rather than through transverse shearing. Secondly, the out-of-plane displacements of the shell elements must be small enough so that membrane effects in the shells remain negligible. Thirdly, the shells must have small enough stiffness so that feedback through the coupling is negligible and the shell stiffness does not affect the estimated tension field calculation. Specifically, the force residual that results from varying the out-of-plane displacement of one of the shell nodes must be small compared to the residual that results from a corresponding variation (scaled appropriately) of the corresponding tension degree of freedom.

The bending stiffness k_B of a shell element composed of a linear elastic material scales with $E_T t_T^3 / L_e^2$, where E_T is the Young's modulus of the tension shell, t_T is the tension shell thickness, and L_e is the characteristic length of the shell element. The transverse shear stiffness k_{TS} of a shell scales with Gt, where G is the shear modulus, which generally scales with E for a constant Poisson's ratio. Therefore, the thin shell requirement gives:

$$\frac{k_B}{k_{TS}} << 1 \Rightarrow \frac{C_1 \frac{E_T t_T^{\,3}}{L_e^2}}{C_2 E_T t_T} << 1 \Rightarrow \frac{t_T}{L_e} < \Re_1 . \tag{6.23}$$

In order to maintain thin shell behavior, the ratio of the shell thickness t to the characteristic element length L_e must remain smaller than some unknown constant $\Re_1$.

The easiest way to ensure that membrane forces remain negligible is to constrain only as many of the in-plane shell degrees of freedom as are necessary to prevent rigid body motion, and then to ensure that the maximum change in out-of-plane displacement $(\Delta u_3)_{shell}$ imposed on adjacent shell nodes is less than the distance between those nodes. This can be ensured by requiring:

$$\left(u_3^{\max}\right)_{shell} = K_T \hat{T}_{\max} < L_e . \tag{6.24}$$

Here $(u_3^{\max})_{shell}$ is the maximum displacement applied to any shell node, $\hat{T}_{\max}$ is the maximum projected tension anywhere in the model, and K_T is the scale factor that transforms the projected tensions into displacements of the virtual shell nodes. It is assumed that, since fabrics cannot support compressive stresses, $\hat{T}_{\min} = (u_3^{\min})_{shell} = 0$.

Assuming negligible transverse shear displacements and negligible membrane effects, the residual force associated with varying the out-of-plane displacement of one of the shell nodes scales with $k_B\ (u_3)_{shell} = k_B\ (K_T\ \hat{T})$. From Equation (6.22), the residual in the fabric element associated with variation of $\hat{T}$ scales with $\hat{T} V_e = \hat{T} L_e^2$ (unit thickness is assumed). The requirement that the stiffness of the fabric element be much larger than the stiffness associated with out-of-plane shell displacements gives:

$$\frac{\frac{\partial\left(k_B K_T \hat{T}\right)}{\partial \hat{T}}}{\frac{\partial\left(\hat{T} L_e^2\right)}{\partial \hat{T}}} << 1 \Rightarrow \frac{K_T E_T t_T^{\,3}}{L_e^4} < \Re_2 . \tag{6.25}$$

The ratio must be smaller than a second unknown constant $\Re_2$.

The same three requirements hold for the velocity shells. The thin shell requirement gives:

$$\frac{k_B}{k_{TS}} << 1 \Rightarrow \frac{C_1 \frac{E_V t_V^{\,3}}{L_e^2}}{C_2 E_V t_V} << 1 \Rightarrow \frac{t_V}{L_e} < \Re_1 . \tag{6.26}$$

Here E_V and t_V are the modulus and thickness of the velocity shells, respectively. The requirement for negligible membrane effects gives:

$$\left(u_3^{\max}\right)_{shell} = K_V v_{\max} < L_e , \tag{6.27}$$

where K_V is the scale factor that converts velocities into out-of-plane displacements of the velocity shells, and v_{max} is the maximum SLIDY velocity calculated over the entire model. The relative stiffness requirement is much more challenging to bound for the velocity shells, because the displacements of the slip velocity shells are related to the rotations of the tension shells and to the locking and through-thickness forces from the real elements in a nonlinear manner. The residual associated with a small rotation φ of the tension shell is proportional to $\varphi E_T\, t_T^3$. The residual associated with a small change of out-of-plane displacement u_3 of the velocity shells scales with $u_3\, E_V\, t_V^3 / L_e^2 = (K_V v)\, E_V\, t_V^3 / L_e^2$, the product of the displacement and shell bending stiffness. The slip driving force f scales with φ / K_T. However, the slip velocity v and the slip driving force f are related by the nonlinear constitutive law. Requiring that the velocity shells be significantly less stiff than the tension shells gives:

$$\frac{\dfrac{\partial\left(K_V v \dfrac{E_V t_V^3}{L_e^2}\right)}{\partial v} \dfrac{\partial \hat{v}\left(f, F_N, F_L\right)}{\partial f} \dfrac{\partial f}{\partial \varphi}}{\dfrac{\partial\left(\varphi E_T t_T^3\right)}{\partial \varphi}} << 1 \tag{6.28}$$

$$\Rightarrow \frac{1}{L_e^2} \frac{K_V}{K_T} \frac{E_V t_V^3}{E_T t_T^3} < \hat{\Re}_3\left(f, F_N, F_L\right)$$

Here $\Re_3$ is not a constant, but a function that depends on the values of the slip driving force and the force degrees of freedom.

$\Re_1$ and $\Re_2$ can be determined by conducting parametric studies with varying values of t_T and $K_T E_T$ for a fixed element size L_e. When transverse shear deformation of the shells become negligible, t is sufficiently small relative to L_e. When feedback effects vanish, $K_T E_T\, t_T^3$ is sufficiently small compared to L_e^4. $\Re_3$ for a particular range of f, F_N, and F_L present in a model can be approximated by conducting parametric studies with varying values of $K_V E_V$ for a model that exhibits the appropriate range of values of θ, F_N, and F_L, with a fixed element size L_e.

These requirements create problems when the mesh is refined. As the mesh is refined by some factor R, the thin shell requirement requires the shell thicknesses t_T and t_V be reduced by R as well. The negligible membrane effects require that the scale factors K_T and K_T also be reduced by R. The requirement for negligible tension shell stiffness compared to the real elements will automatically be satisfied, because both the numerator and the denominator will be decreased by a factor of R^4. However, the requirement for negligible velocity shell stiffness compared to the tension shell stiffness requires that E_V be reduced by a factor of R^2. In principle, these requirements can all be satisfied by making t_T, t_V, E_T, E_V, K_T, and K_V all very small. However, the global stiffness matrix becomes ill-conditioned and the residuals associated with the shell elements become immeasurably small if the shell stiffnesses become too much smaller than the stiffnesses associated with the real elements. The tension shells undergo a net reduction of stiffness of R^2 and the velocity shells undergo a net reduction of stiffness of R^3 when the mesh is refined by a factor R. The requirement that the global stiffness matrix be well conditioned and the residuals be measurable, when combined with the other requirements on the coupled virtual shell method, place a numeric restriction on the refinement of the mesh. The slip theory relies on the assumption that the mesh can be sufficiently refined. Unfortunately, in all but the simplest of the validation cases we examined, the mesh could not be sufficiently refined to accurately capture the slip-driven phenomena that were of interest. Therefore, even though the virtual coupled shell method was effective in eliminating most of the numeric problems that degraded the accuracy of the slip-enabled model, it ultimately proved unusable in complex cases which require a fine mesh.

6.5 Quadratic Gradient Estimation on Element Patches

Since none of the sophisticated techniques for estimating smooth tension and slip velocity fields discussed in the preceding sections were completely successful, and since all were computationally expensive, we adopted a less sophisticated, more computationally efficient approach for calculating tension and velocity gradients. We essentially use a second order finite difference approach to estimate the gradients at the center of an element based on the average field values at that center and at the centers of the neighboring elements.

We restrict our analyses to cases where the mesh consists only of quadrilateral elements. In the first step of any analysis, the element nodal connectivity matrix and the reference-configuration coordinates of every node in the model are stored. For every element e, the four elements that share its four edges are identified. We define the element that shares the edge between its first and second corner nodes to be the element "below" it., the element that shares its

second and third corner nodes to the element "to the right", the element that shares its third and fourth corner nodes to be the element "above" it, and the element that shares its first and fourth corner nodes to be the element "to the left". We designate these elements as e_{V-}, e_{H+}, e_{V+}, and e_{H-} respectively. This convention is for the sake of record keeping and does not necessarily correspond to the orientation of the elements relative to the global coordinate frame. From the nodal coordinates, the reference configuration distances from the center of element e to its mid-edge nodes, and then from these mid-edge nodes to the centers of the adjacent elements are calculated and designated as s_V^-, s_H^+, s_V^+, and s_H^-, shown in Figure 6-8. The reference configuration unit vectors $\mathbf{n_H}$ and $\mathbf{n_V}$ that give the orientations of the chords connecting the "left" and "right" mid-edge nodes and the "bottom" and "top" mid-edge nodes, respectively, are also calculated.

Let T be any of the fields whose gradient must be calculated, such as the projected tension field. The average values of this field are calculated at the element centers using Equation (6.22), as is detailed in the preceding section. The values at the centers of the elements e, e_V^-, e_H^+, e_V^+, and e_H^- are designated as T, T_V^-, T_H^+, T_V^+, and T_H^- respectively, shown in Figure 6-8. The field gradient is calculated by assuming that the field varies quadratically from the center of an element on one side of e, through the center of e, to the center of the element on the other side of e, along lines where one element isoparametric coordinate is constant (i.e. along the straight line segments connecting the center nodes to the mid-edge nodes). For details regarding isoparametric coordinates in elements, refer to a finite element text such as Bathe [1996]. This assumption is reasonable assuming that the mesh is sufficiently refined and not too severely distorted; highly distorted elements and abruptly changing element sizes can introduce errors into the calculation. The quadratic equation $T = a_2X^2 + a_1X + a_0$ that fits the three calculated field values along either the H- or V-direction can be found by solving the following system of equations:

$$\begin{aligned} a_2\left(s^+\right)^2 + a_1 s^+ + a_0 &= T^+ \\ a_0 &= T \\ a_2\left(-s^-\right)^2 - a_1 s^- + a_0 &= T^- \end{aligned} \quad . \tag{6.29}$$

The gradient of the field at the center of element e, projected along the $\mathbf{n_H}$ or $\mathbf{n_V}$ direction, is given by the a_1 value from this system when it is solved for the H- or V-direction, respectively. The components of **Grad**(T) in a Cartesian coordinate system, which are the gradients of the T field along the reference configuration X- and Y-directions, can be found by solving a second system of equations:

$$\begin{aligned}\mathbf{Grad}(T)\cdot\mathbf{n}_{\mathbf{H}} &\equiv \frac{\partial T}{\partial X}n_{HX}+\frac{\partial T}{\partial Y}n_{HY}=\frac{\partial T}{\partial s_H}=a_{1H}\\ \mathbf{Grad}(T)\cdot\mathbf{n}_{\mathbf{V}} &\equiv \frac{\partial T}{\partial X}n_{VX}+\frac{\partial T}{\partial Y}n_{VY}=\frac{\partial T}{\partial s_V}=a_{1V}\end{aligned}. \tag{6.30}$$

The unknowns are $\partial T/\partial X$ and $\partial T/\partial Y$, the components of **Grad**(T).

This procedure is performed at the end of each time increment to determine the projected tension gradient **Grad**($T\cos\beta$) and the corresponding slip driving force f at time t, according to Equation (5.19). This driving force, along with the normal force between the yarns and the locking forces (which are also averaged at the node centers according to the method described by Equation (6.22)) are used to calculate a slip velocity v^{slip} at every element center according to the constitutive law that relates f and v. The velocity v^{slip} is converted to a SLIDY velocity v using Equation (5.3). The gradient estimation process is then repeated for the velocity values to estimate the slip velocity gradient and the corresponding evolution rate of the unstretched yarn length $\dot{\ell}_i$ at time t, as described by Equation (5.13). The unstretched yarn lengths at the end of the next time increment, at time $t + \Delta t$, are calculated explicitly at all integration points in the element according to:

$$\ell^{t+\Delta t} = \ell^t + \Delta t\dot{\ell}^t. \tag{6.31}$$

Although explicit calculation of the evolution of the unstretched yarn lengths requires very small time steps to ensure stability, it is necessary due to the impossibilities of implementing an implicit evolution scheme within a commercial finite element code where the full equilibrium tension field is accessible only for the previous time increments.

6.6 Boundary Conditions

Special provisions must be made near the boundaries of the mesh. The finite difference scheme described in the preceding section requires the field values at the centers of neighboring elements on both sides of an element. We assume that the mesh is sufficiently refined so that an element always has at least two neighbors—one in the H-direction and one in the V-direction. However, when an element e lies at the boundary of the mesh, there will be no neighboring element on one side (or on two sides, if it is a corner element). Using only one neighbor to estimate a gradient can result in inaccurately calculated gradients. It is frequently most important to accurately capture yarn slip in the regions near the boundaries, for example, in cases where yarns pull out of the weave, where the weave unravels, or where slip alleviates large tension concentrations generated by slit-like damage. Therefore, we must develop suitable boundary

conditions for the tension and slip velocity fields T_i and v_i that are used to calculate evolution of ℓ_i.

Several types boundary conditions are possible, shown in Figure 6-9. All of these boundary conditions can be captured by treating the element as if it were neighbored by another "phantom" element beyond the boundary with appropriate tension and velocity field values. We assume that the distance s from the center of e to the center of the phantom element is the same as the distance from the center of e to the center of its actual neighbor on the other side—in other words, we assume that the phantom elements mirror the mesh across the center of e.

The simplest case occurs when the yarns intersecting an edge are free. In this case, the unwoven tails of the yarns extending beyond the weave and the model boundaries are unloaded. Consequently, the neighboring phantom element will have zero tension: $T = 0$. Since there are no forces beyond the boundary resisting the flow of the loose yarns, the slip velocity in the phantom element will be the same as the slip velocity in e: $v = v_e$.

The next case is when the fabric is clamped or encased. In this case, we assume that some crossover points are held in the clamps as well as the yarns. The tension and velocity in the neighboring phantom element must be defined. Since this element would be completely encased by the clamp, we take the slip velocity in the phantom element to be zero: $v = 0$. Tension should not be taken to be zero, since this would imply an abrupt drop in tension at a clamp, which is not the case. We take the phantom element tension to be equal to the tension in the element adjacent to the clamp: $T = T_e$. This is consistent with a tension gradient that approaches zero at the clamp, which implies zero slip velocity at the clamp.

In the third case, we assume the yarns to be gripped beyond the last set of crossover points. This case may arise in various situations—for example, during a yarn pullout test. In this case, the yarns may be under tension beyond the boundary. We expect that tension in the yarn beyond the weave can be different from the tension at the center of the edge element (otherwise the tension gradient at the edge would be zero and yarn slip, and thus yarn pullout, could never occur). We assume that similar effects that cause tension to increase (or decrease) by some amount ΔT from the center of the element e's actual neighbor, element $e+1$, to the center of e, will cause the tension to increase or decrease by the same amount from the center of e towards the center of the phantom element, so $T = 2T_e - T_{e+1}$. Note that this is equivalent to calculating the tension gradient at e by finding the gradient between e and $e+1$. As in the case of the free edge, we expect that the yarn slip velocity beyond the boundary will be the same as it is just inside the boundary, so $v = v_e$.

The next case can occur when one edge of a fabric is hemmed or sewn, so that the edge is free but the yarns cannot slip. In this case, the slip velocity in the phantom element is zero: $v = 0$. The tension at the edge must also be zero, so $T = 0$ as well.

The final case occurs when the boundary represents a line of symmetry. In this case the phantom element is a real element that is a mirror image of element e. Tension in the phantom element is the same as the tension in element e: $T = T_e$. Slip velocity must be equal and opposite to the slip velocity in e: $v = -v_e$. Note that this permits evolution of yarn lengths across a line of symmetry, which is physically realistic—the crossover points at the centerline of some symmetric fabric specimen can undergo a net loss or gain of yarn material, although the slip velocity at the exact centerline must of course be zero.

Two other issues must be addressed near the boundaries. First, when a yarn family is parallel to an edge, the gradients of fields along that yarn family should be insensitive to the boundary conditions associated with that edge. However, if the mesh is distorted, numeric effects can create a dependence in the gradients along the parallel yarn family on the boundary condition. For example, consider the case shown in Figure 6-10 where a yarn family parallel to a free edge is carrying a large, constant load, and passes through a distorted element with one edge on the free edge boundary. Because the load carried by the yarn is large, and the free edge condition requires that tension be zero in the phantom neighbor, there will be a large gradient calculated in the $\mathbf{n}_V$ direction. If the element were rectangular, the $\mathbf{n}_V$ direction would be normal to the yarn family orientation ${}^0\mathbf{g}$, and the large V-direction gradient would not affect the calculation of the tension gradient along the yarn. However, since the element is distorted, $\mathbf{n}_V$ will have a small but nonzero projection on ${}^0\mathbf{g}$, and hence a very large tension gradient V-direction will introduce error into the gradient calculation along ${}^0\mathbf{g}$. To avoid this problem, the gradient estimation algorithm checks if the yarn family in question is parallel to any boundary in the reference configuration before applying the boundary condition. If it is, a special "parallel family" boundary condition is applied instead, where $T = 2T_e - T_{e+1}$ and $v = 2v_e - v_{e+1}$. In other words, we calculate the gradient along the $\mathbf{n}_H$ or $\mathbf{n}_V$ direction using only the element value and the value at the actual neighbor $e+1$.

The final issue that must be addressed near a boundary concerns the nodal displacements on that boundary. Since the nodal displacements correspond to the displacements of the crossover points, not the displacements of the yarn material, the nodal displacements at an edge must be defined according to constraints on the crossover points. In the case of a free or sewn edge, the crossover points at the boundary are free to move, so the nodal displacements u should be unconstrained. In the case of a clamped edge, some crossover points are gripped along with the yarn material, so the nodal displacements must be constrained: $u = 0$.

Along a line of symmetry, displacements parallel to the symmetry line should be unconstrained. Displacements perpendicular to a line of symmetry should neither be constrained to be zero nor left free. The continuum length scale is assumed to be sufficiently large that there may be many crossover points in the vicinity of a given location. A pair of crossover points that straddle a line of symmetry may separate away from one another. Hence the nodes that lie on a line of symmetry should be permitted to displace away from the line of symmetry, provided this displacement is accompanied by slip of yarn material past the node (and hence past the associated crossover point) towards the line of symmetry so that the net flow of yarn material through the line of symmetry is zero. Consequently, the displacement of a node that initially lies on a line of symmetry must be constrained by:

$$u - s = 0, \tag{6.32}$$

where s is the total length of yarn material that has flowed past the node towards the line of symmetry, and u is the displacement away form the line of symmetry. In the case where yarns beyond a fabric edge are clamped and subjected to some imposed displacement $\overline{u}$ normal to the fabric edge (e.g. during a yarn pullout test), the displacement u of the edge nodes in the same direction should be constrained by:

$$u - s = \overline{u}, \tag{6.33}$$

where s is the total yarn length that has slipped past the edge node out of the fabric. When no slip occurs, $s = 0$ and displacement of the yarn that extends out of the fabric will cause corresponding displacement of the crossover points at the edge of the fabric. Once slip occurs, $s > 0$ and the displacement of the crossover points, described by u should be less than that of the yarns, described by $\overline{u}$. These constraints are applied through a user defined MPC subroutine.

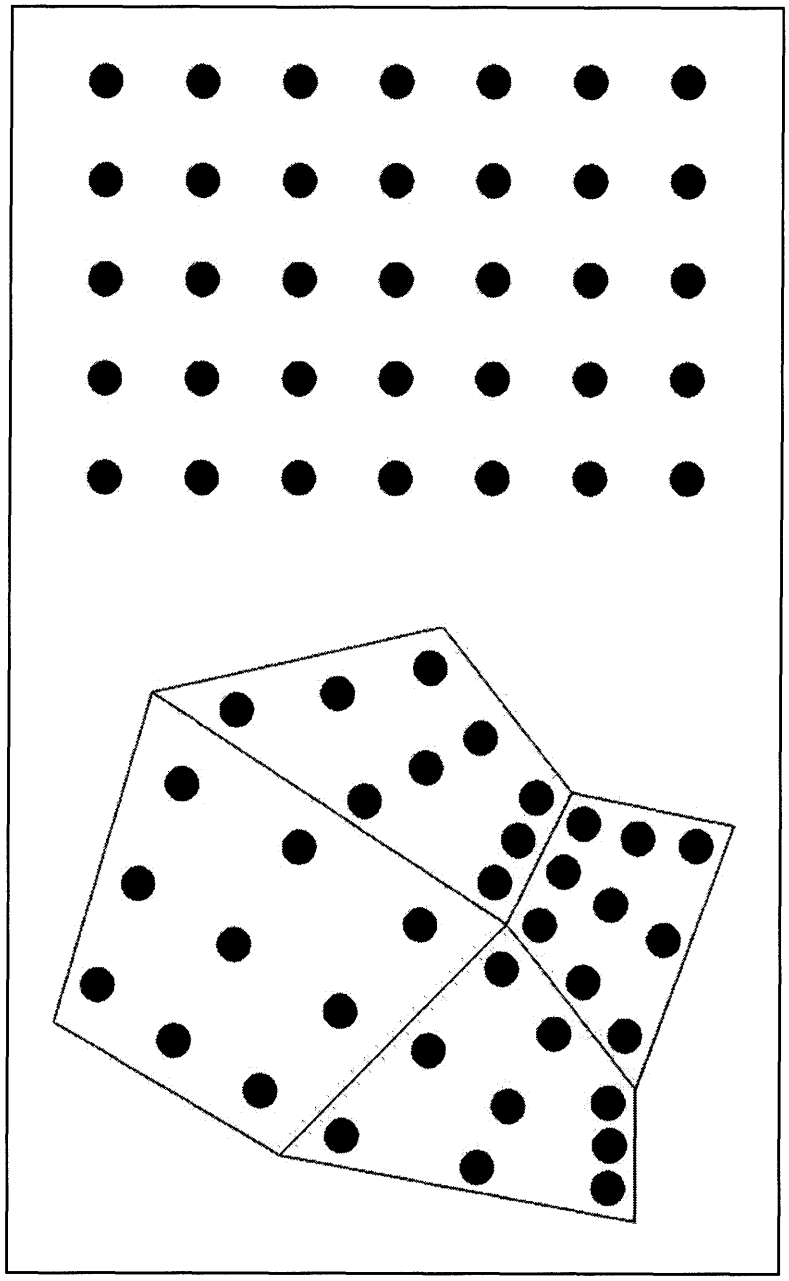

Figure 6-1 Regularly located points versus irregularly location integration points in an arbitrary finite element mesh

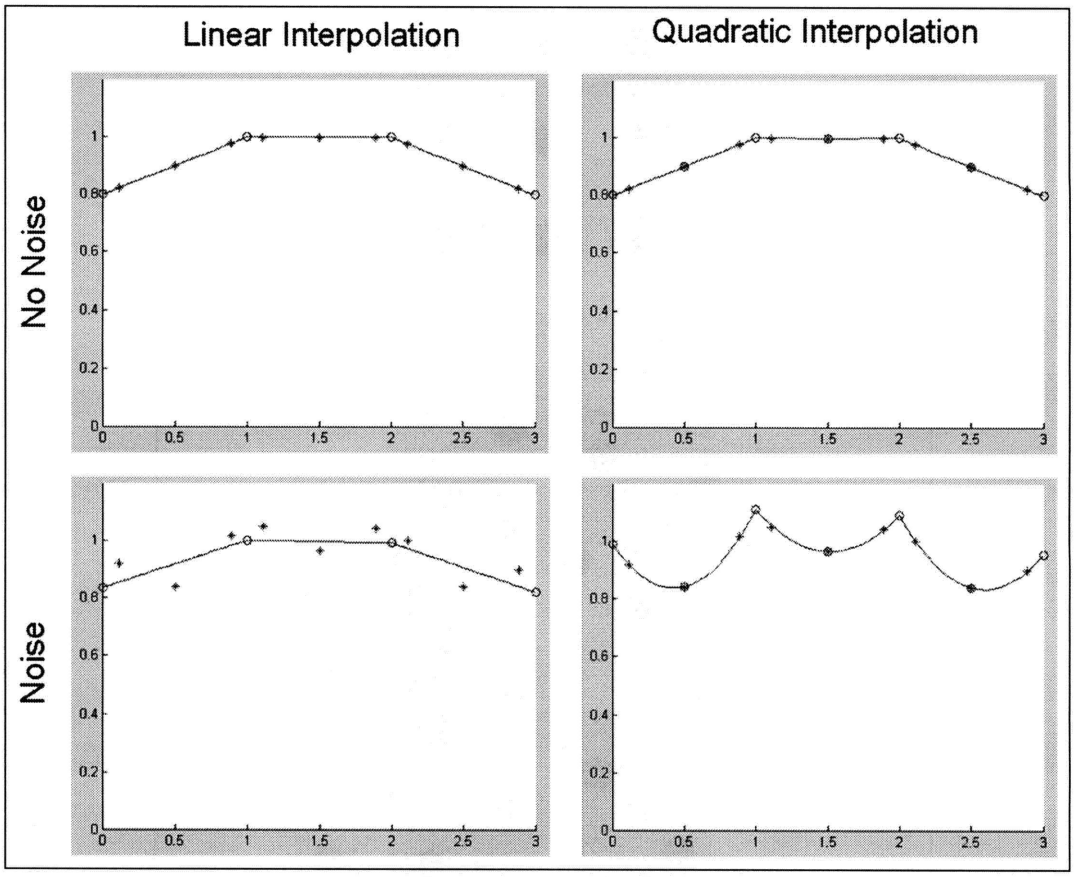

Figure 6-2 One dimensional interpolation with and without noise

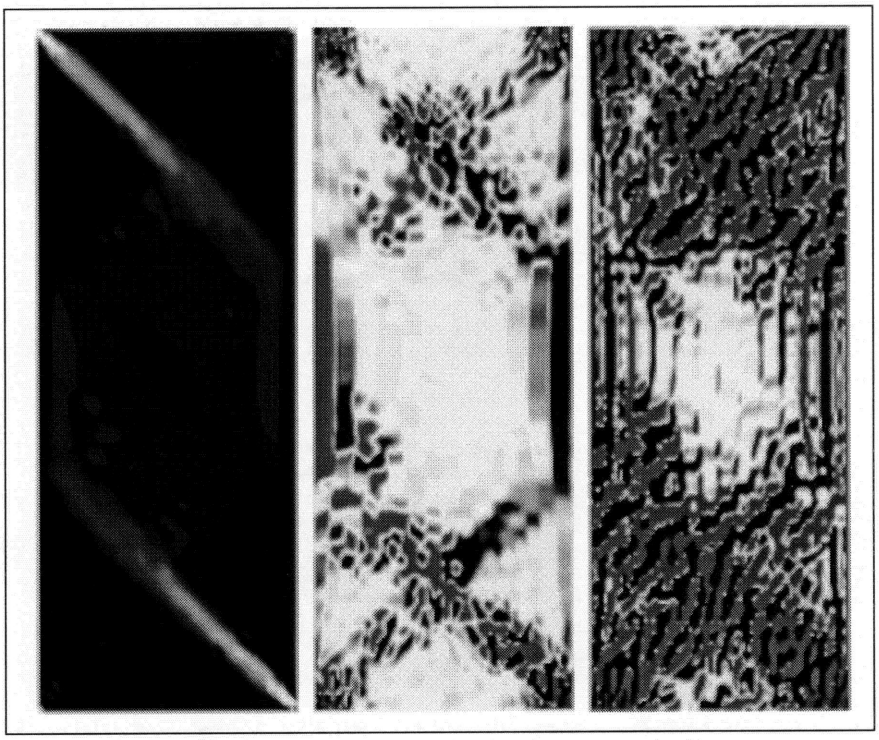

Figure 6-3 Tension, slip driving force, and unstretched yarn length evolution rates in bias-extension test using hybrid elements

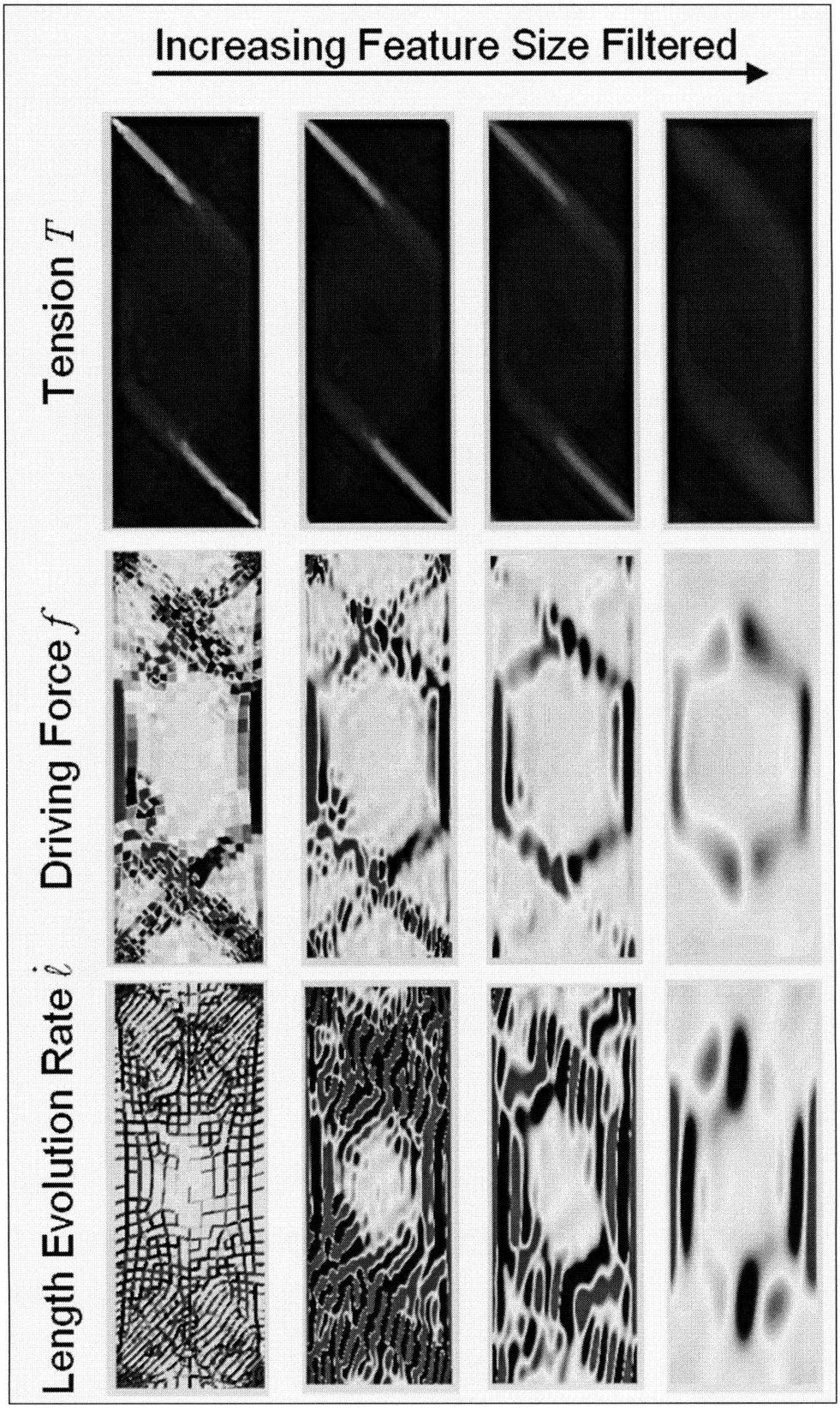

Figure 6-4 Tension, slip driving force, and yarn length evolution rates in bias-extension test, filtered to smooth features with increasingly large length scales

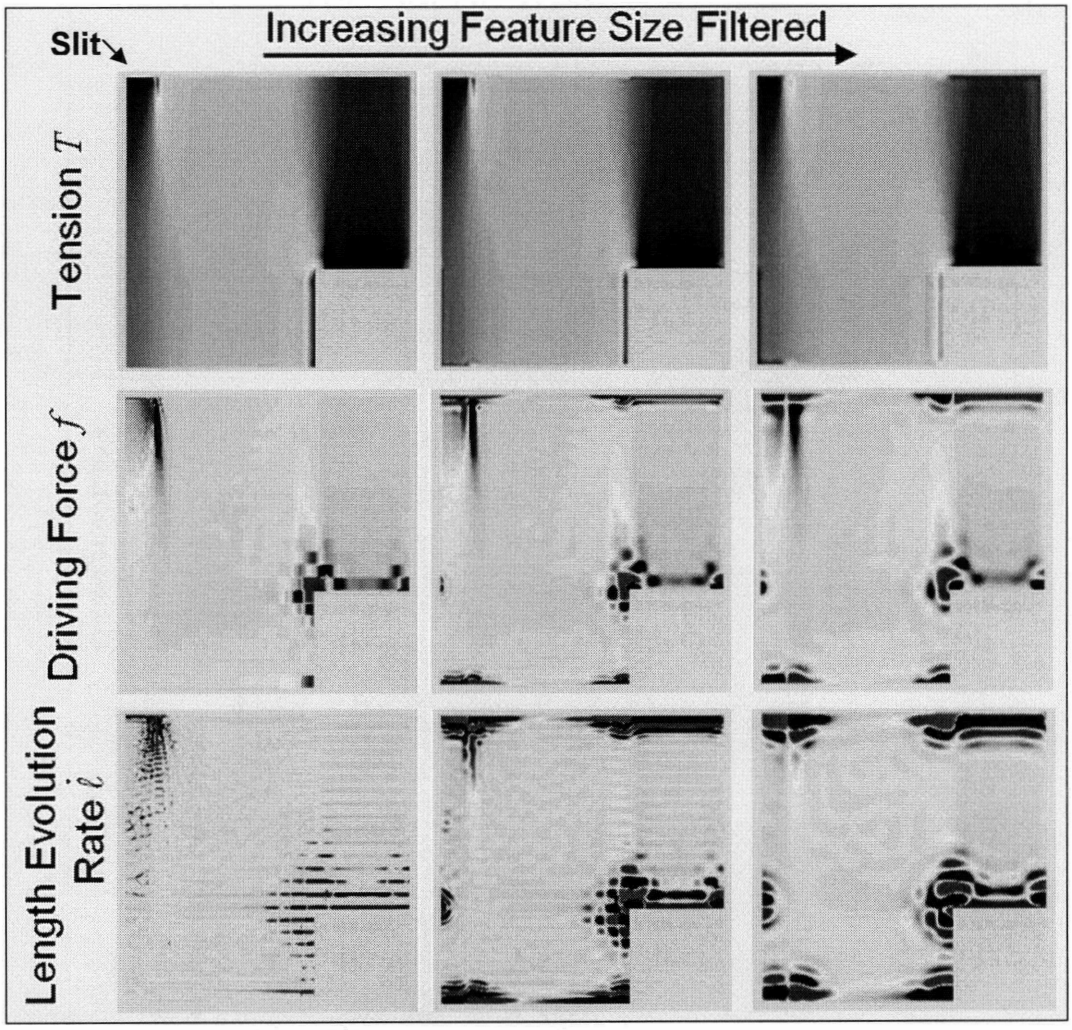

Figure 6-5 Tension, slip driving force, and yarn length evolution rates in slit-damage test, filtered to smooth features with increasingly large length scales

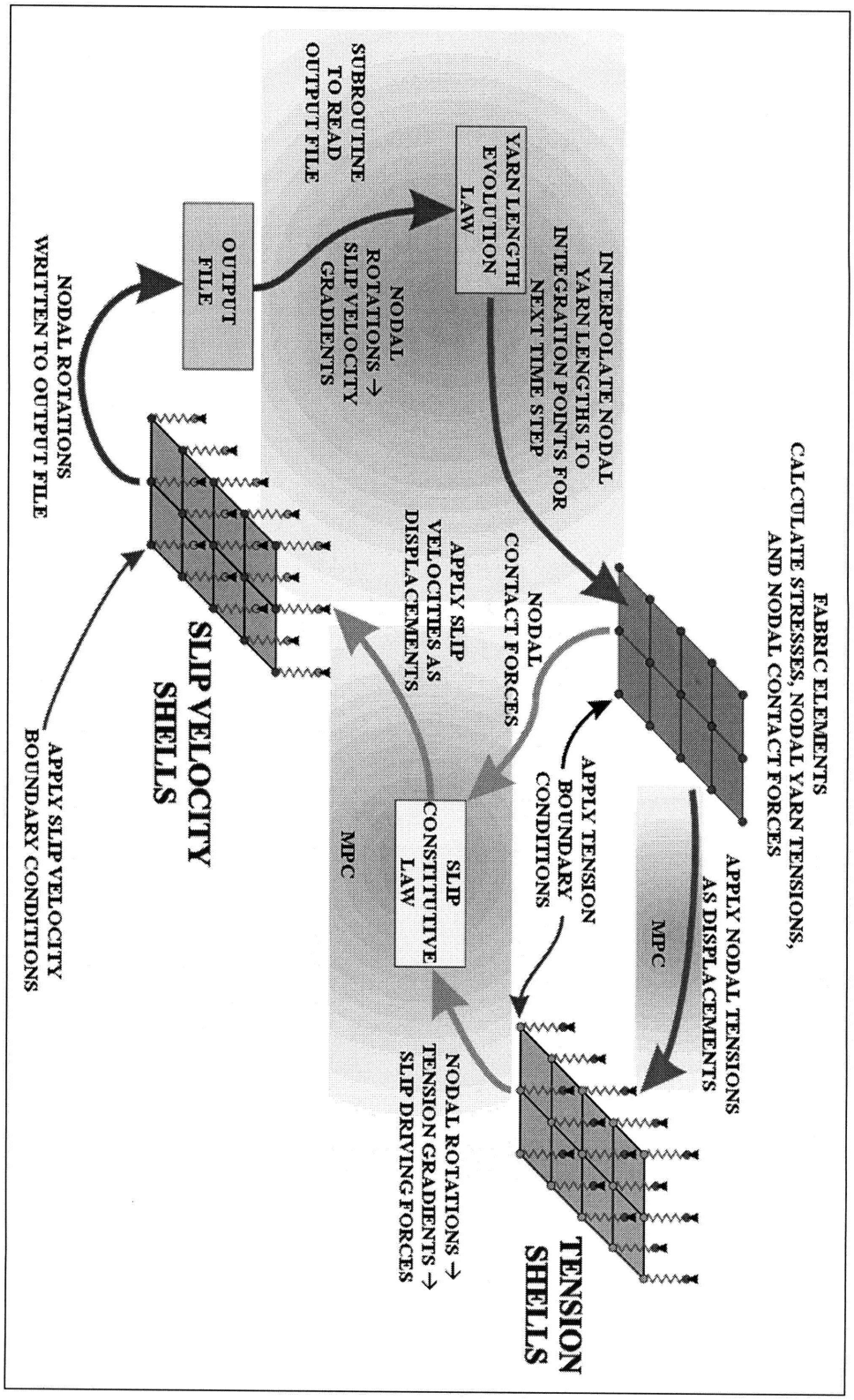

Figure 6-6 Algorithm for calculating smooth tension and slip velocity fields using coupled virtual shell elements

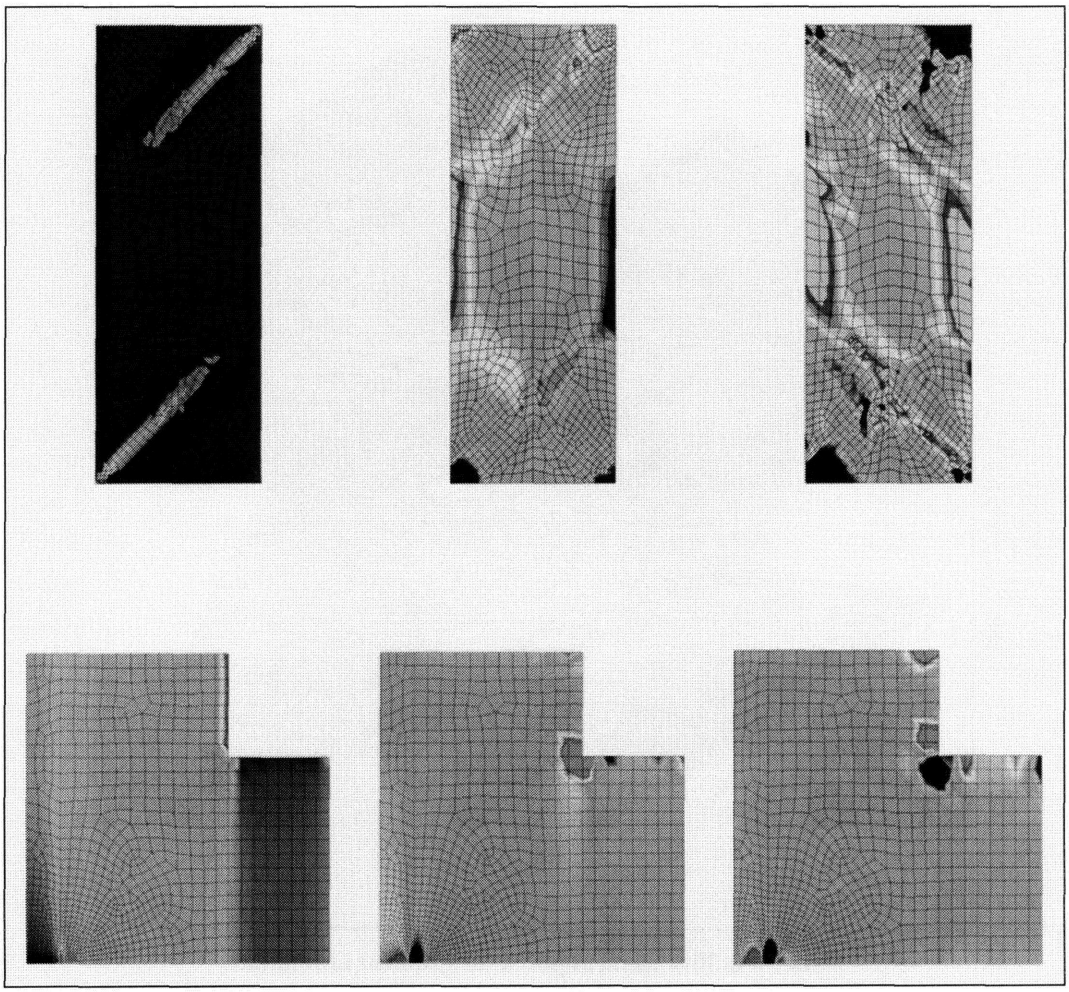

Figure 6-7 Tension, slip driving force, and yarn length evolution rates in bias-extension test and in slit-damage test, calculated using virtual shell coupling method

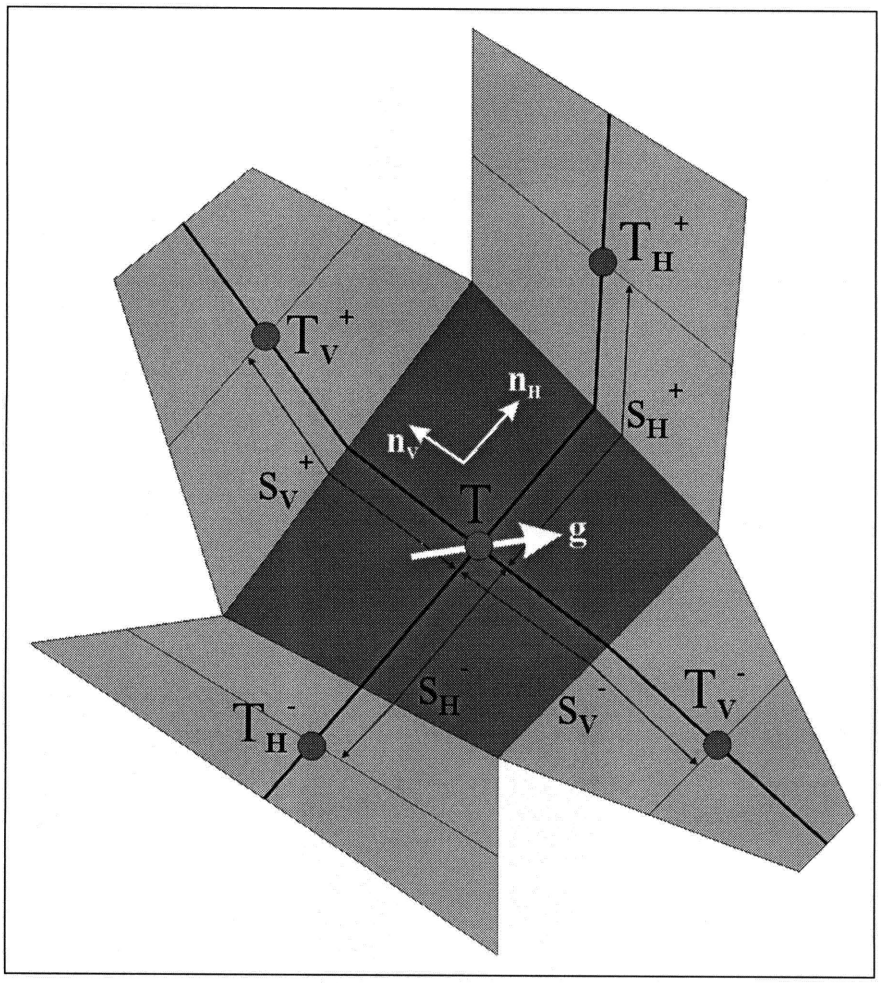

Figure 6-8 Five element patch for gradient estimation

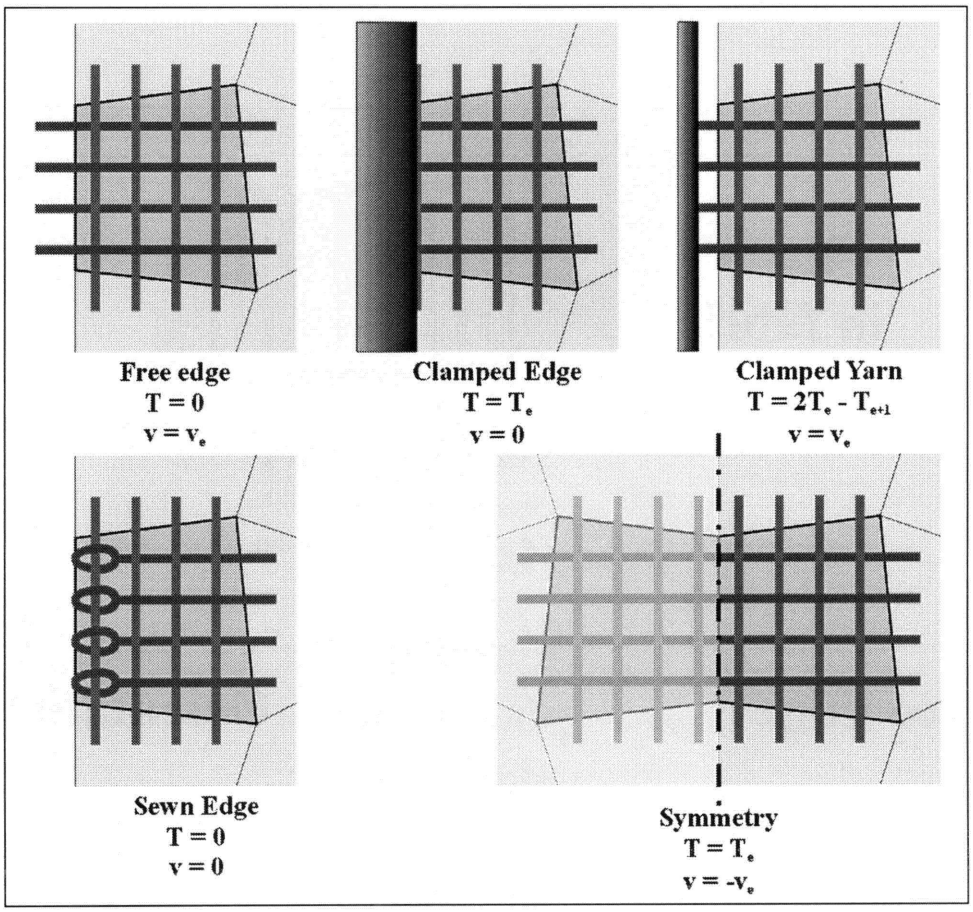

Figure 6-9 Possible boundary conditions

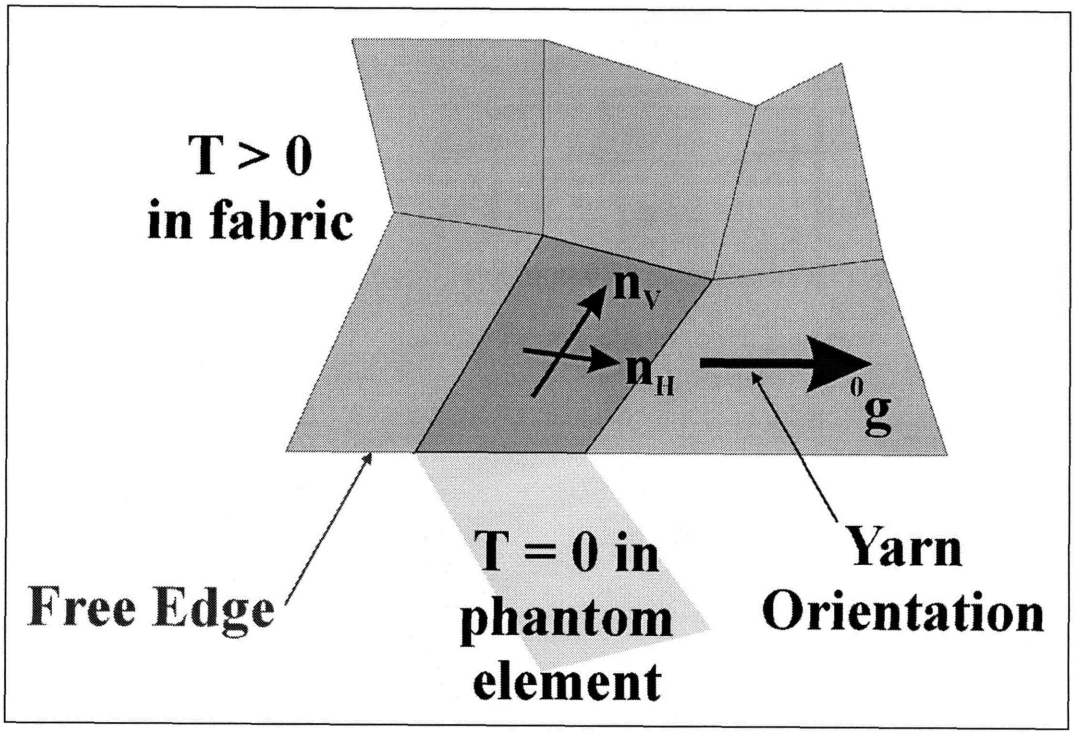

Figure 6-10 Irregular mesh at a boundary can cause erroneous gradients to be calculated for yarns parallel to edge

Chapter 7
Validation of Slip Theory

7.1 Numerical Problems with the Slip Theory Implemented into an Implicit Finite Element Code

The slip-enabled fabric model was implemented into an implicit finite element code, ABAQUS/Standard. This code was initially chosen because its architecture is more easily customized, through the use of user-defined subroutines, than that of many other available implicit or explicit commercial finite element codes, including ABAQUS/Explicit. ABAQUS/Standard is well suited to finding equilibrium solutions to steady state problems and is an effective tool for validating the fabric models in most cases. However, explicit codes are often better suited for transient, time-dependent problems, like many problems that involve yarn slip in fabrics. After performing several implicit analyses to validate the slip-enabled model, we concluded that the model would be far more effective if it were implemented into an explicit code. The main reasons leading to this conclusion are described below.

Because the slip velocities and the evolution of the unstretched yarn lengths are calculated from yarn tension gradients, which are calculated over multiple elements, it is significantly easier to integrate the evolution of the unstretched yarn lengths forward in time using a purely explicit integration procedure, described by Equation (6.31). However, when an explicit integration procedure is used, the time increment Δt must be small in order to ensure accuracy and stability. If the chosen time increment size is too large, the slip formulation become unstable, and large, wildly oscillating slip velocity fields and nonphysical displacement predictions result. Many small increments are typically required for any given analysis to ensure accuracy and stability. Usually, when explicit integration schemes are used, the increased computational cost of the large number of increments is offset by the smaller computational cost of each explicit calculation, compared to implicit calculations. However, when an explicit integration procedure is included in a formulation that is implemented into an implicit finite element code, then a large number of computationally expensive increments are necessary.

As a result, the computational costs associated with the slip-enabled model with explicit integration of the unstretched yarn lengths, implemented into the implicit ABAQUS/Standard framework, are large. Since our goal is to validate the slip theory, not to develop a commercially viable finite element tool with minimal computational costs, we used the implementation in

ABAQUS/Standard. The computational costs can be reduced somewhat by modifying the slip-constitutive relation so that smaller slip velocities are calculated, since the maximum acceptable size of the time increment depends, in part, on the magnitude of the yarn length evolution rates, and these depend on the gradients of the slip velocities. While this approach is unsuitable for dynamic analyses of transient phenomena, it is effective for the quasi-static validation cases that we consider. However, even for quasi-static cases, there is a limit on how small the slip velocities can be, since excessively slow velocities prevent the steady-state solution from being achieved over the course of the analysis.

Consequently, some analyses have prohibitively large computational costs. When there is very little resistance to slip in certain parts of the model, slip velocity gradients can become large and the required time increments to ensure stability become so small that 10^8 or more increments are necessary to conduct an analysis. In these cases, the computational cost of the analysis is prohibitively large. In general, large slip velocities occur in analyses involving large slip displacements, greater than several times the characteristic length of the weave structure $2p$. Consequently, we do not model cases with large slip displacements or include pullout or unraveling effects using the ABAQUS/Standard model implementation, since these cases are too computationally expensive to analyze. We limit validation cases to cases where small slip displacements result in the redistribution of loads. We recommend implementation of the slip-enabled model into an explicit finite framework so that problems with large slip displacements can be considered.

In addition to the requirement for very small time increments, use of explicit slip integration in an implicit code can introduce another numerical problem. As is described in Appendix B, convergence difficulties can occur when the slip-free formulation is used to model cases where one family carries extremely large tensions (on the order of 150 N, in excess of the yarn strength) and the other carries near zero tensions. This problem relates to how the model captures crimp interchange. In such cases, the highly tensioned yarn family becomes nearly flat, and its crimp amplitude and crimp angle approach zero, as the crimp amplitude and angle of the other yarn family approach finite values. A scaling function is used so that all real values for the mean amplitude degree of freedom correspond to an admissible range of mean amplitudes. However, use of this scaling function causes the sensitivity of the through-thickness forces to variations in the mean amplitude to decrease when one yarn family is flattened, which can, in extreme cases, result in an ill-conditioned stiffness matrix and in convergence difficulties. These difficulties are compounded by numerical inaccuracies in the through-thickness force and corresponding

stiffness terms, which are introduced as the crimp amplitude of one family becomes small, because large tensions are multiplied by the sine of very small crimp angles.

This problem only occurs in rare, unrealistic loading cases for the slip-free model. Unfortunately, it is exacerbated by the presence of slip. In regions where yarn tensions differ greatly between the two families and one family becomes almost flat, the through thickness force becomes small and inaccurate. Consequently the resistance to slip at that point becomes very small and unstable. Slip velocities can then become large and variable, so slip velocity gradients can become artificially large. Explicit integration of the corresponding artificially large evolution rates of the unstretched yarn lengths can result in artificially small tensions, or even negative tensions. Such erroneous tensions cause the residuals associated with the through-thickness forces to become unacceptably large, but these residuals cannot be reduced by variation of the mean amplitude degree of freedom because the scaling function makes them insensitive to this degree of freedom. Therefore, they must be reduced by unrealistic distortions of the mesh. This problem propagates because small or negative tensions result in near-zero or negative through thickenss forces, which provide little resistance to slip and result in abruptly changing slip velocities, which in turn require smaller time increments and cause yarn lengths to evolve so that tensions become even more negative. Eventually, the solution begins to diverge. In the presence of slip, the algorithmic instability associated with the crimp interchange phenomenon can occur at much smaller tensions than in the slip-free case, and limits the maximum loads which can be applied in certain analyses.

7.2 Raked Strip

We first attempted to validate the slip continuum model by devising a very simple case where slip effects are carefully controlled and easily predicted. In this case, shown in Figure 7-1, a vertically oriented rectangular strip with the yarn families aligned with the edges is clamped at each end. The top edge is displaced by some distance δ. The vertical displacements of the nodes lying on the horizontal centerline are constrained to be less than $\delta/2$ (a value of $\delta/3$ was used); this simulates the effect of a rake pushed through the fabric constraining the crossover points from displacing the entire $\delta/2$ distance that they would if they were unconstrained. This case was analyzed for both a slip-free case, where the yarn evolution rates were set to zero regardless of the slip driving forces, and a case with slip enabled.

We examined both the resulting tension contours throughout the strip and the reaction forces on the clamps and the rake. The reaction forces are shown in Figure 7-2 and the tension contours

in the vertically oriented yarns are shown in Figure 7-3. In the slip-free case, the rake essentially acts as a clamp, because the crossover points are constrained and the yarn material deforms in an affine manner with the crossover points. In this case, the top half of the strip must support larger strains than the bottom half, and hence is subjected to much larger tensions. This also causes the top half to undergo larger lateral deformations due to crimp interchange. No transfer of tension is possible through the rake because no slip is allowed. The bottom clamp is subjected to a very small load—the majority of the downward load which opposes the upwards load on the top edge is supported by the rake, across which there is a very large tension gradient.

When slip is allowed, the response changes dramatically. The fabric no longer supports large tension gradients across the rake—gradients cause the yarns to slip past the rake, and as they slip the yarns stretch and hence the tensions that the yarns carry become more evenly distributed. Both lateral displacements and axial yarn tensions are nearly equal in the top and bottom halves of the specimen. Because slip limits the tension gradient the specimen can support across the rake, the load that the rake can bear is also limited and the reaction at the rake drops to a small value (equal to the sum of the critical slip resistances f^C at all the rake-supported crossover points), compared to the loads on the ends. Yarn tension is now transferred from the top half of the sample to the bottom half, and so the bottom clamp now sees a greater load, comparable to the load on the top clamp minus the small load on the rake. The total load at the top clamp is lower than in the slip-free case, because it is not necessary to force such large stretches upon such short sections of yarns.

These responses are physically realistic and the loads predicted by the analysis in the two cases can be quantitatively verified by simple calculations. The slip implementation works for this very simple case, where a localized tension gradient is applied uniformly across a strip to cause one yarn family to slip in a predictable fashion. We now examine more complex cases to further validate the slip model.

7.3 Yarn Pullout

We next simulated yarn pullout tests of the type described in Chapter 4. In these tests, a sample of fabric is subjected to a cross load by a lateral displacement parallel to one yarn family. One or more of the crossing yarns are then gripped and pulled from the fabric, while either the lateral displacement or the lateral load are held constant. Analysis of this kind of test was significantly afflicted by the numerical problems identified in Section 7.1. Near the free end of the pulled yarn, tensions are necessarily small. Small tensions correspond to small contact forces

F_N between the yarns, and hence there is very little resistance to slip. As a result, the slip velocities predicted by Equation (5.29) can become very large once the critical resistance to slip has been exceeded by the driving force f, and become very sensitive to small variations in f, as is shown in Figure 5-6. Therefore, small spatial variations in f can result in very large slip gradients, and the time increment necessary for stability in this region becomes extremely small. In some cases, the convergence problems associated with the flattening of one yarn family while the other carries low tensions also afflicted this analysis, in regions near the free edges far from the pulled yarn. These convergence difficulties manifested at similar load levels to the load levels where the necessary time steps became very small, just after steady-state slip was initiated. We therefore simulated yarn pullout tests only up to the point where the critical resistance to slip was reached at all points along the yarn and steady state slip was initiated.

Two sets of analyses were conducted for two different geometries. The first set of tests re-creates the pullout tests described in Chapter 4 performed using the pneumatic apparatus. The model, shown in Figure 7-4, had a width equivalent to 85 crossing yarns and was subjected to a constant 100 N nominal cross load (about 1.2 N/yarn). A displacement rate of 50 mm/min was applied to a section of the model equal in width to a single yarn, using the appropriate boundary conditions described in Chapter 6 for a clamped yarn. Because a fine mesh was necessary in the vicinity of the pulled yarn, a non-uniform mesh of variable density was used in order to reduce computational costs. This analysis was conducted using both the slip-free and the slip-enabled models. For the slip-enabled case, the parameter μ_0 in Equation (5.29) was increased by two orders of magnitude in order to scale down the slip velocities calculated, which allowed larger time increments to be used and reduce the computational cost of the analysis, as is described in Section 7.1. The slip velocities were still sufficiently large so that the results reach the steady state response.

The progression of the tension distribution (for both cases) and the velocity distribution (for the slip-enabled case) along the pulled yarn at different times are shown in Figure 7-5 and Figure 7-6, respectively. For the slip-enabled case, the tensions increase smoothly up until approximately the t = 4~5 s states, while nonzero slip velocities propagate downwards along the pulled yarn from the gripped end to the free end. Once the free end begins to slip, the entire yarn quickly accelerates. At this point, the shape of the tension distribution is the same as the shape of the yarn pullout curves shown in Figure 5-7 - Figure 5-9, which is expected. At this point, we would expect the velocity along the entire yarn to slip at the applied steady-state pull rate. However, once the velocities near the free end, where there is very little resistance to slip, become nonzero, the necessary time increment size for stability of the explicit integration algorithm becomes very

small, smaller than the time increment that was actually used in the analysis. Large, nonphysical oscillations appear in both the velocity and the tension profile and the model prediction becomes inaccurate.

Figure 7-5 shows that the tension gradients supported along the pulled yarn are lower in the slip-enabled case than in the slip-free case, at equivalent levels of tension (recall that as tension increases, resistance to slip increases and hence the yarns in the slip-enabled model can support larger tension gradients when they carry larger tensions). However, tensions in the pulled yarn are actually larger in the slip-enabled case. The reason is apparent in Figure 7-7, which shows tension contours in both the slip-free and slip-enabled model at a time where the slipping yarn in the slip-enabled model approaches the steady state configuration. In the slip-enabled case, the pulled yarn is flattened and stretched due to the tension it carries. It slips relative to its neighbors and transfers very little of the tension it carries to them. In the slip-free case, the pulled yarn cannot flatten and stretch without transferring some load to its neighbors, and consequently the applied load is shared across a wider section of fabric and the load carried by just the pulled yarn is lower. However, the macroscopic resistance to deformation of the entire structure is smaller in the slip-enabled case, as is evident in Figure 7-8.

The loads in Figure 7-8 are larger than the tensions in Figure 7-7 because when a finite element is displaced, the load transmitted to its corner nodes has contributions from the stress (i.e. the yarn tensions) in both that element and in the neighboring elements. Consequently, the predicted reaction force will be larger than the product of the force per unit width in the pulled element and the element width.

One shortcoming of this pullout model was that its irregular mesh caused the finite difference gradient estimation algorithm to predict non-physical tension gradients, and hence slip velocities, in certain areas. In order to eliminate these effects, and to build a more computationally efficient model which could be run with a smaller time increment and hence capture more of the pullout behavior before stability was compromised, we constructed a smaller model that had a uniform mesh and that represented a square of fabric that was only 20 yarns by 20 yarns. This model is shown in Figure 7-9. It has a regular mesh, so the non-physical slip velocities introduced by mesh irregularities are eliminated. It also has fewer elements, and hence is more computationally efficient and can be analyzed using a smaller time increment. A very small time increment was used in order to ensure stability for a larger portion of the analysis. A cross load of 24 N (1.2 N/yarn) was applied to the sample, and was then maintained by either load or constant displacement conditions.

The smaller embedded yarn length led to much smaller tensions necessary before the initiation of slip over the entire yarn length. Smaller tensions mean a larger area with little slip resistance, and hence the stability problem was worse for this model. Even with the smaller time increments, oscillations in the tension and velocity distributions along the pulled yarn indicated that the stability limit had been exceeded, as is shown in Figure 7-10 and Figure 7-11. In this case, the analysis was continued beyond the onset of instabilities. As the excessively large time steps cause artificially large slip velocities to be calculated, extreme yarn slip occurs through the lower portions of the specimen. As excessive amounts of yarn flow to the top portion of the specimen, the large tensions in the pulled yarn are relaxed and the tension field along the entire yarn drops. Loads are transferred to neighboring yarns and slip velocities also drop. The macroscopic load-displacement curve, shown in Figure 7-12, which had been leveling off towards the steady-state condition, begins to increase again, since the decreasing yarn slip velocities cease to accommodate the increasing displacements. This case illustrated the importance of maintaining stability in order to achieve accurate results.

In the displacement controlled case, cross tensions are larger, since tension in the pulled yarn is transferred to the crossing yarns via the crimp interchange effect. In this case, the larger cross tensions increased the resistance to slip, and hence the time increment used was sufficiently small to maintain stability until just after the steady-state conditions were achieved. Figure 7-13 shows the load-displacement curve for this case, for both the slip-free and the slip-enabled models. The loads are larger than in the force-controlled case, because the higher cross tensions lead to greater slip resistance. The load in the slip-free case increases rapidly since the system has very little compliance. The slip-enabled model predicts a far more compliant response that reaches a steady-state load as the entire yarn begins to slip at the imposed displacement rate. Unfortunately, shortly after this point was reached the numeric problems detailed in Section 7.1 prevented further analysis.

The model also predicts realistic unstretched yarn length contours throughout the analysis, as is shown in Figure 7-14. At the top edge, the pulled yarn drags the leading crossing yarns away from the rest of the specimen, slipping along the untensioned yarns that neighbor the pulled yarn. At the bottom edge, the trailing crossing yarns try to remain straight and hence separate from the rest of the sample, again slipping along the untensioned yarn tails. This response was observed during the pullout trials described in Chapter 4. Both these phenomena increase the amount of yarn material between crossing yarns, and hence the yarn length increases. At the same time, the central portion of the pulled yarn tends to flatten and stretch where it is under tension, slipping

past its neighbors and through the crossing yarns. Hence the amount of unstretched yarn length between crossing yarns decreases.

These analyses demonstrate that the model can predict observed and physically realistic phenomena in the yarn pullout tests, provided that a small enough time increment is used so that the explicit integration of the evolution of the unstretched yarn lengths is stable. Oscillations in the tension and velocity fields and non-physical behaviors are predicted when the time increments are too large. The model predicts realistic yarn length evolutions, yarn tension distributions, slip velocities, and force-displacement behaviors up until the point where steady-state conditions are achieved. At this point, the necessary time increment for stability becomes so small that the slip enabled model implemented into an implicit code becomes too computationally expensive.

7.4 Slit-Damage in a Biaxially Loaded Specimen

As shown by Godfrey and Rossettos ([1998] and [1999]) and discussed in Section 2.11, slip plays an important role in the propagation of damage in biaxially stressed fabrics. When a fabric with a slit consisting of consecutive breaks in parallel yarns is biaxially loaded, the broken yarns tend to pull apart. This creates a tension concentration at the tip in the slit, as the first unbroken yarn must support tensions that are much larger than the nominal tension far from the slit, much like a crack in an elastic solid creates a stress concentration at the crack tip. We successfully predicted the tension fields, including the tension concentration, using the slip-free model, as is described in Section 2.11. In a fabric where no slip occurs (e.g. because a coating bonds yarns together where they cross), these tension concentrations can lead to fast propagation of slit-like damage and catastrophic failure. Godfrey and Rossettos have shown that when slip can occur (e.g. in an uncoated fabric), two modes of slip develop. The broken yarns slip through the weave away from the slit, but as they do so they drag the crossing yarns with them, and these crossing yarns slip upwards along the unbroken yarns at the ends of the slit. This second mode of slip alleviates the tension concentration and can prevent catastrophic failure, similar to the manner in which plasticity can alleviate stress concentrations at a crack tip and prevent fracture. We have experimentally verified the presence of two modes of slip by conducting experiments on biaxially loaded Kevlar® fabrics with slit-like damage and measuring the slip fields around the slit using image analysis software, shown in Figure 7-15. We then simulated these experiments using the slip model to verify that our model predicts the same phenomena.

We conducted tests using two different model geometries. We used the quarter-symmetry cruciform geometry described in Section 2.11, which has an irregular mesh, and also a more

detailed half-symmetry model of just the region near a slit, with a uniform mesh. The quarter-symmetry model had symmetry-type boundary conditions along the two lines of symmetry, with the ends of the cruciform arms clamped and the sides of the cruciform arms left free. The appropriate boundary conditions on the tensions and slip velocities described in Chapter 6 were applied to all edges. The nodes on the lines of symmetry were allowed to displace away from the line of symmetry, which corresponds to crossover points that straddle the symmetry line moving away from one another, provided the yarns slip past the nodes so that there is zero net flow of yarn material at the line of symmetry. Biaxial loading is applied by applying a horizontal displacement to the clamp at the right-hand side of the cruciform while holding the displacement of the top clamp constant. The crimp interchange effect transfers load from the horizontal yarn family to the vertical yarn family and causes both families of yarns to be loaded. The geometry of the half-symmetry model is shown in Figure 7-16. It is 5.08 x 3.81 cm. The bottom edge of the model, which contains a 1.27 cm slit at its center, is a line of symmetry, and symmetry boundary conditions are applied to this edge. Equal displacements are applied normal to the other three edges (displacements parallel to the edges are unconstrained). Clamped yarn boundary conditions, described in Chapter 6, are enforced on these edges.

Both models predict the expected slip phenomena. Figure 7-17 shows the slip displacements of the vertical yarns predicted by the quarter-symmetry cruciform model when the applied horizontal strain is approximately 1.1 %. Both modes of slip are clearly visible. The yarns that intersect the slit have positive slip displacements, indicating that they have slipped upwards past the crossing yarns. The model indicates negative slip displacements of the yarns at the end of the slit, indicating that the yarns have slipped downwards past the crossover points (or, actually, that the crossover points have slipped upwards along the yarn).

This slip mode tends to reduce the tension concentration at the tip of the slit. Figure 7-18 shows the reaction force at the node at the end of the slit as a function of time for both the slip-free and the slip-enabled case. This reaction force is proportional to the tension concentration that results from the slit. The force in the slip-enabled case is smaller, indicating that slip has reduced the tension in the first unbroken yarn, which is consistent with the conclusions of Godfrey and Rossettos. This reduction is also evident in Figure 7-19, which shows the tension distribution in the vertical yarns measured along the horizontal line of symmetry in front of the slit shortly after the onset of slip in the slip-enabled case, and at the same load in the slip-free case. Not only does slip reduce the tension concentration immediately in front of the slit, but it distributes the tensions over a larger section of fabric, just as plasticity distributes stresses over a larger section of an elastic-plastic material at the tip of a crack. Figure 7-19 shows the conditions shortly after the

onset of slip; at larger loads after large slip displacements have occurred this reduction in the tension concentration will be more significant. The half symmetry model with the uniform mesh gives the same results, and its uniform mesh eliminates artificial slip contours far from the slit that result from numerical errors in the gradient estimation scheme.

As in the yarn pullout case, it is computationally feasible to conduct these simulations only up to the point where large slip displacements begin to occur, when the broken yarns that intersect the slit start to pullout out of the weave. At this point, the slip velocity gradients become large and very small time steps become necessary. The algorithmic instability discussed in Section 7.1, which occurs when one yarn family carries much larger tensions than the other, also limited these analyses, especially in the half-symmetry model. The weakly tensioned vertical yarns near the center of the slit exhibit this instability. The highly tensioned crossing yarns are nearly flat and the through-thickness forces are negligible, so the weakly tensioned vertical yarns begin to undergo very rapid slip velocities near the slit. Integration of the corresponding yarn lengths cause very large unstretched yarn lengths to evolve, which place the yarns unrealistically in compression and eventually prevent convergence to a realistic solution, since the through-thickness forces cannot be equilibrated.

7.5 Bias-Extension

The final case that we simulated in order to validate the slip model was the bias extension test, described in Chapter 2. In this test, shown in Figure 7-20, a strip of fabric is cut so that its yarn families are oriented at 45° to the load direction. The strip is then pulled and the yarns rotate relative to one another to align with the applied load. Chapter 2 describes how the slip-free model accurately captures the interesting phenomena in this test, up to the onset of slip. Initially, slip only occurs at the corners, where the edges of the strip are gripped and where there is a large tension concentration. The weave tends to pull apart and separate from the grips at these points. After very large deformations, the yarn rotation is arrested by locking forces as the yarns jam against one another, and the resulting tensions that develop drive more extensive yarn slip fields that causes the weave to unravel at the edges of the strip and that causes the strip to be pulled apart along diagonal lines along the yarns that intersect the strip corners, as is shown in Figure 7-20.

We simulated this test using the slip enabled model. The model captures the early stages of slip near the corners well, as shown in Figure 7-21. The model predicts that the weave will begin

to separate and pull away from the grips, starting at the corners and working inward, reducing the tension concentration at the corners. This is consistent with experimental observations.

Unfortunately, the current implementation of the model cannot be used to simulate the later stages of slip, where the weave unravels and the fabric separates along diagonal bands. This is partly due to the very small time step necessary once slip velocities and slip velocity gradients become large, as id discussed in Section 7.1. However, there is another numerical problem with the model that precludes the advanced stages of this analysis. As the fabric shear angle becomes large, both the slip-free and the slip-enabled models encounter convergence difficulties. Increasingly small time increments are necessary to prevent divergence of the Newton-Rhapson algorithm, regardless of whether slip is enabled or not. At large loads, these difficulties prevent the analysis from converging. These load levels are relatively large, corresponding to applied loads of over 100 N for a 3.5 x 9.5 cm strip, but are not sufficient to initiate the advanced stages of slip that pull the sample apart. Since problem is encountered for both the slip-free and the slip-enabled model, it is not a result of the slip implementation. In fact, slip delays the onset of the convergence difficulties slightly.

We attribute these convergence difficulties to the inaccurate geometric and constitutive assumptions used to capture shear and locking effects at large shear rotations. The truss geometry described in Chapter 2 that is used for the model is relatively simplistic; for example, it does not include the effects of yarn wrapping, which combine with locking effects to exert additional resistance to relative yarn rotation and likely arrest yarn rotation sooner than the current model predicts. The truss geometry and constitutive laws that are assumed to capture the locking effects are admittedly inaccurate: the trusses are oriented differently than the actual contact forces would be, and relatively simple constitutive laws were used to describe the response of these trusses to compression. This model was developed to be accurate for moderate shear angles, where the errors associated with these assumptions is relatively small. At the large shear angles that are present when the advanced stages of slip initiate, the locking trusses become extremely compacted and wrapping effects become important, so the errors become more severe. In order to simulate the advanced stages of slip in bias-extension, a model with a far more accurate and detailed representation of the weave geometry and the locking effects must be developed.

We note that the tension fields and corresponding driving forces that develop in the model prior to convergence failure are consistent with the failure patterns shown in Figure 7-20. Figure 7-22 shows the warp yarn tensions near the end of the analysis (plotted on the undeformed mesh), with the contour range reduced to show more detail in the center of the strip, and the corresponding slip driving forces calculated from these tensions. These slip driving forces are

only on the order of 0.25 N at this point, which is too small to overcome static resistances to slip. But it is evident that, as they increase with the macroscopic load, they will drive the slip fields that will cause the strip to unravel and separate in the experimentally observed manner shown in Figure 7-20. Along the two edges of the strip, the warp yarn driving forces will tend to cause slip velocities up and to the right at the left edge, and down and to the left at the right edge, which will result in the yarn ends pulling into the strip and the weave unraveling along the edges. At the lower left and upper right regions bounding the central portion of the strip, the driving forces will cause bands of slip that are consistent with the weave separating just downstream of these bands. The weft slip driving forces (not shown) indicate the same trends on the opposite sides of the strip. Therefore, even though the current ABAQUS/Standard implementation of the slip-enabled model cannot simulate these advanced slip stages, it does predict loads that are consistent with the observed experimental failure patterns.

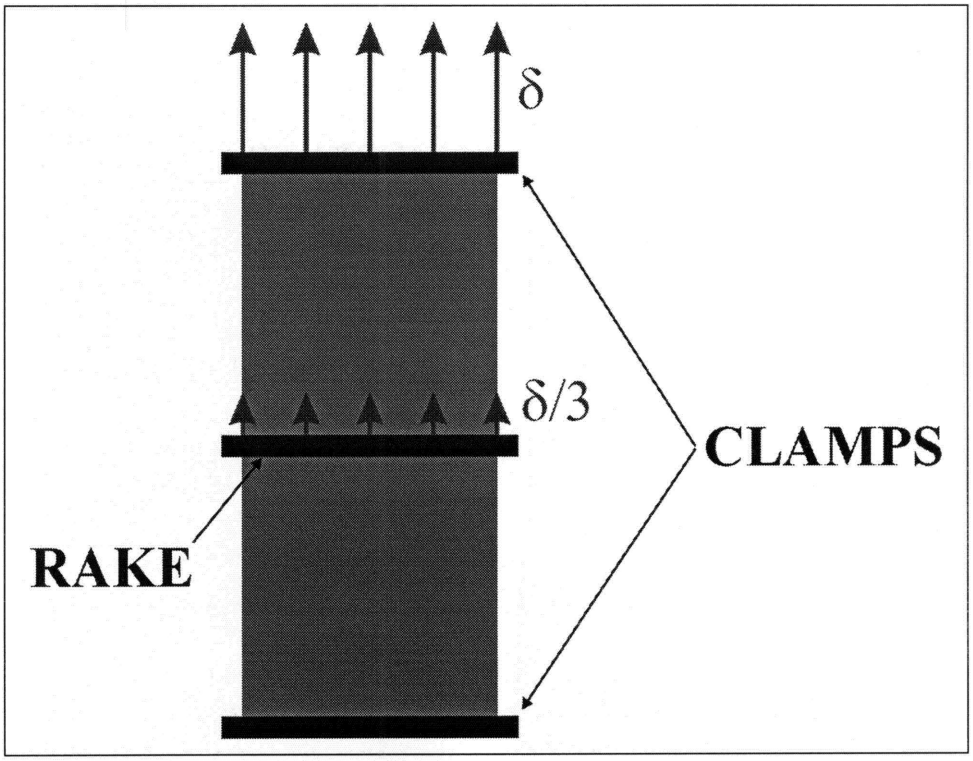

Figure 7-1 Schematic of raked strip slip validation case

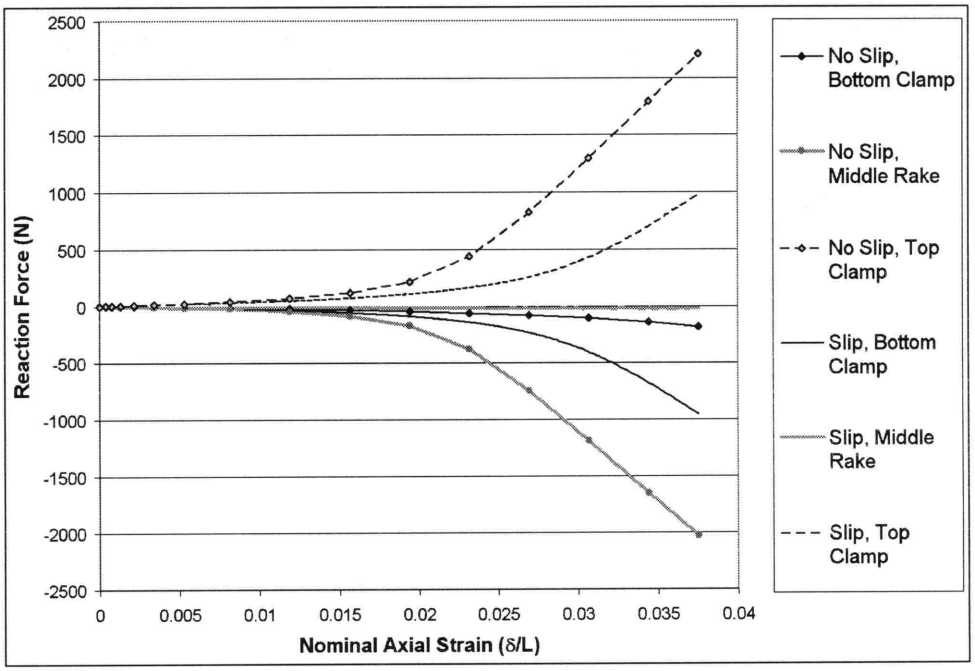

Figure 7-2 Predicted reaction forces in raked strip test

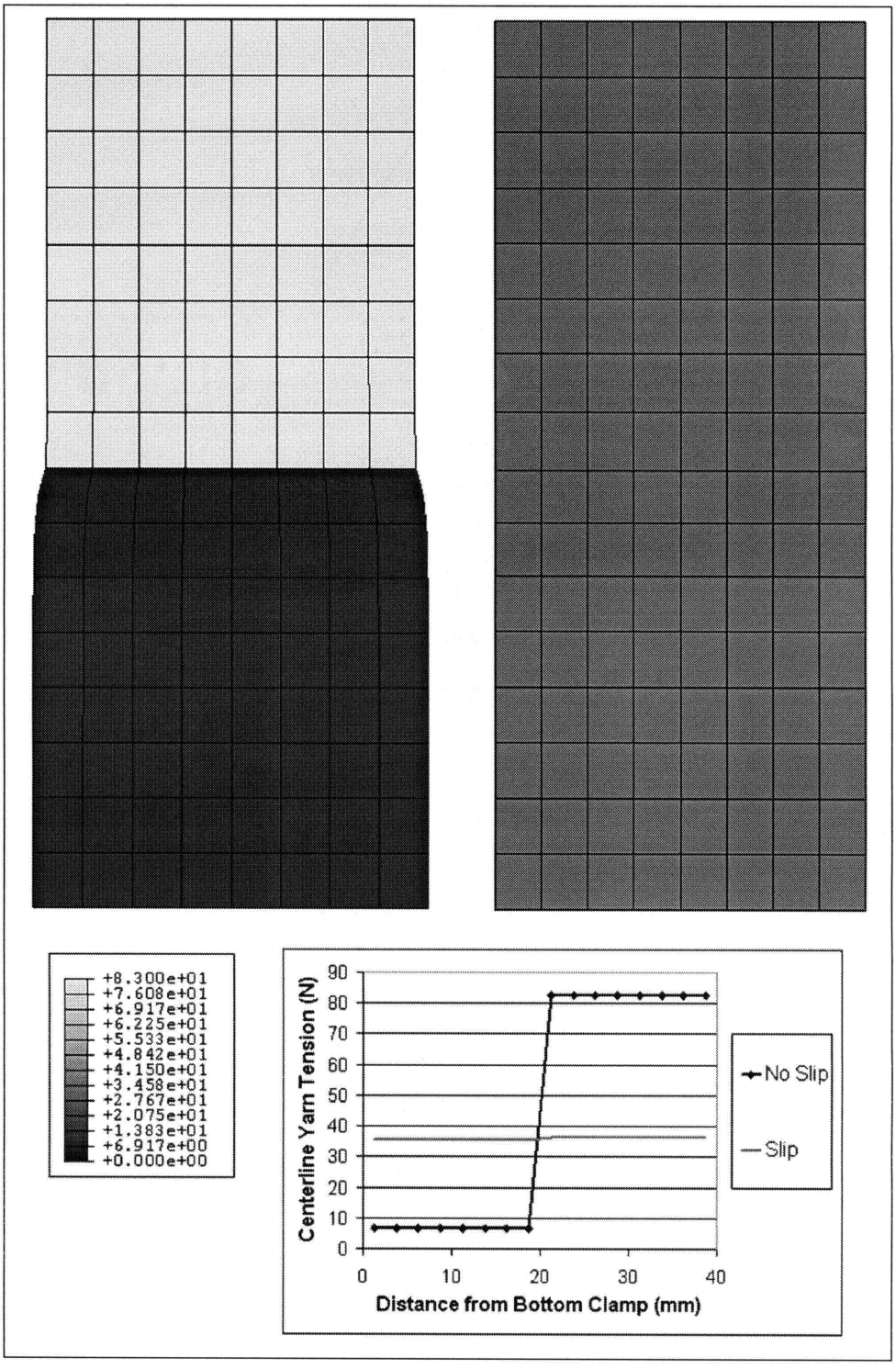

Figure 7-3 Tension contours in raked strip test

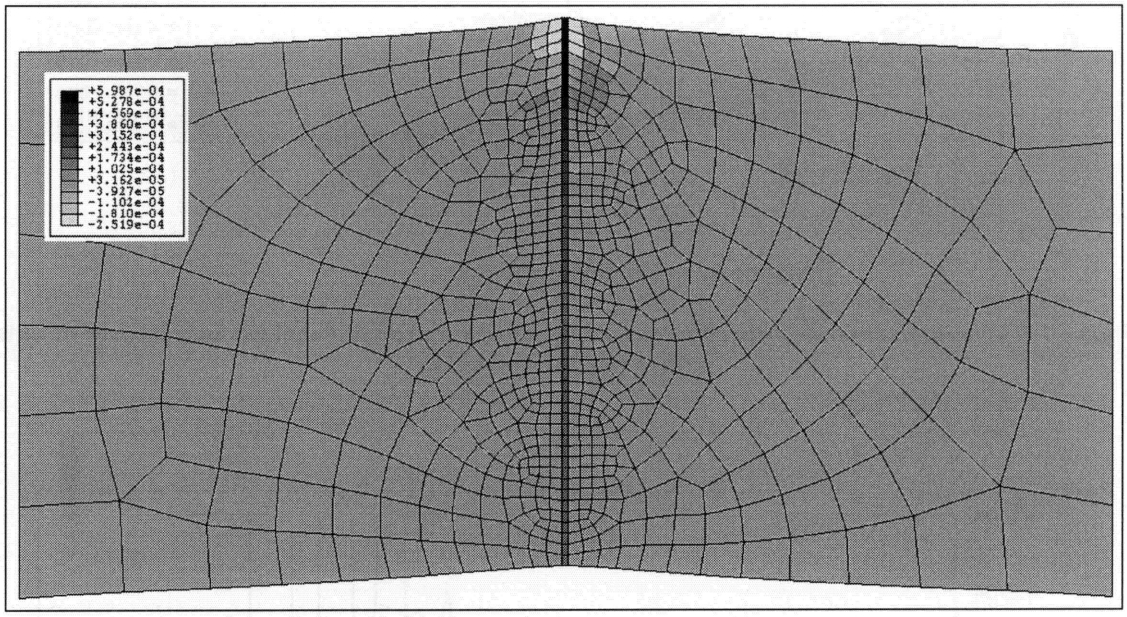

Figure 7-4 Yarn pullout model, with slip velocity contours as pulled yarn approaches steady state

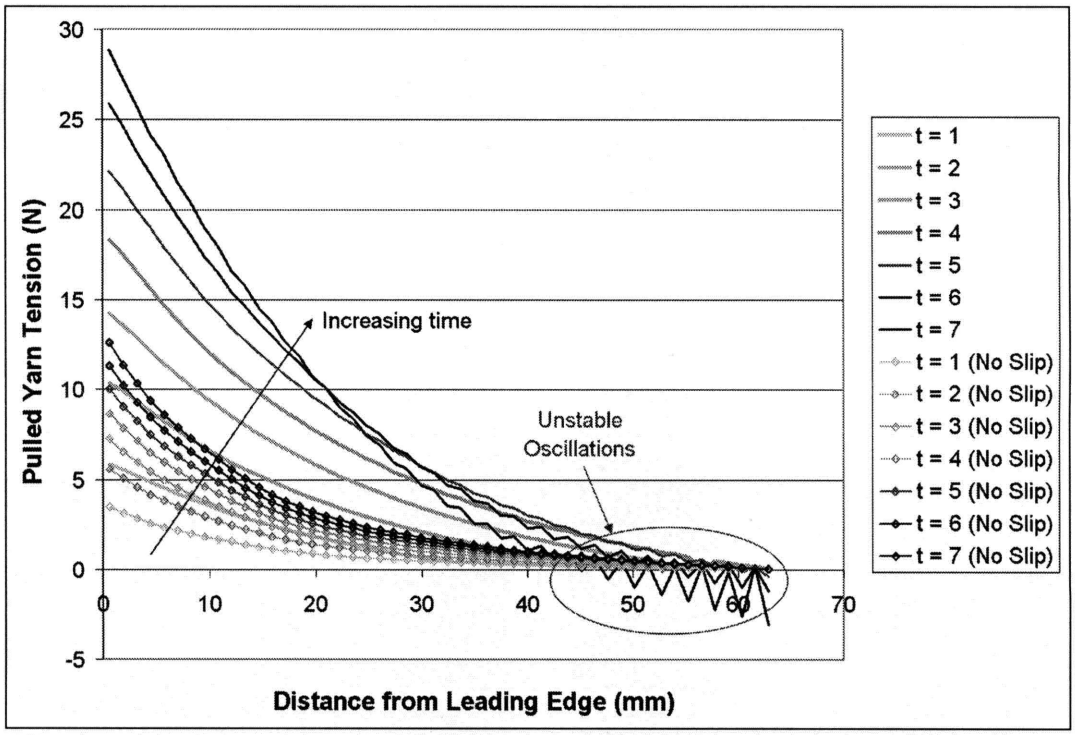

Figure 7-5 Evolution of tension distributions along pulled yarn for slip-enabled and slip-free models in yarn pullout simulation

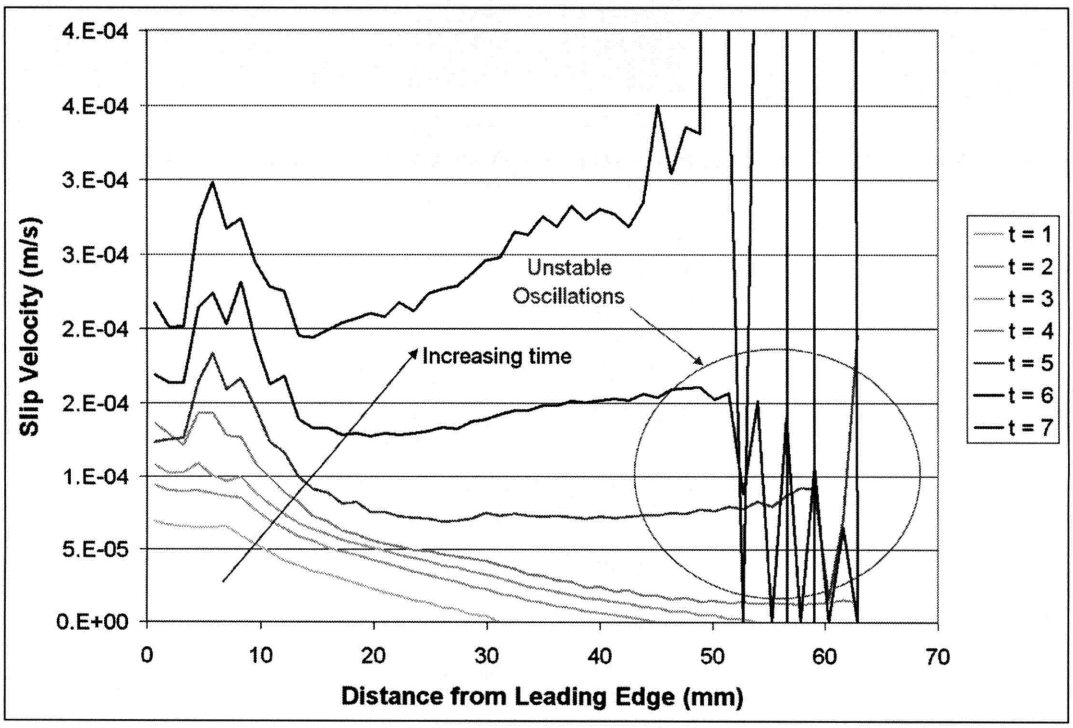

Figure 7-6 Evolution of velocity distributions along pulled yarn for slip-enabled model in yarn pullout simulation

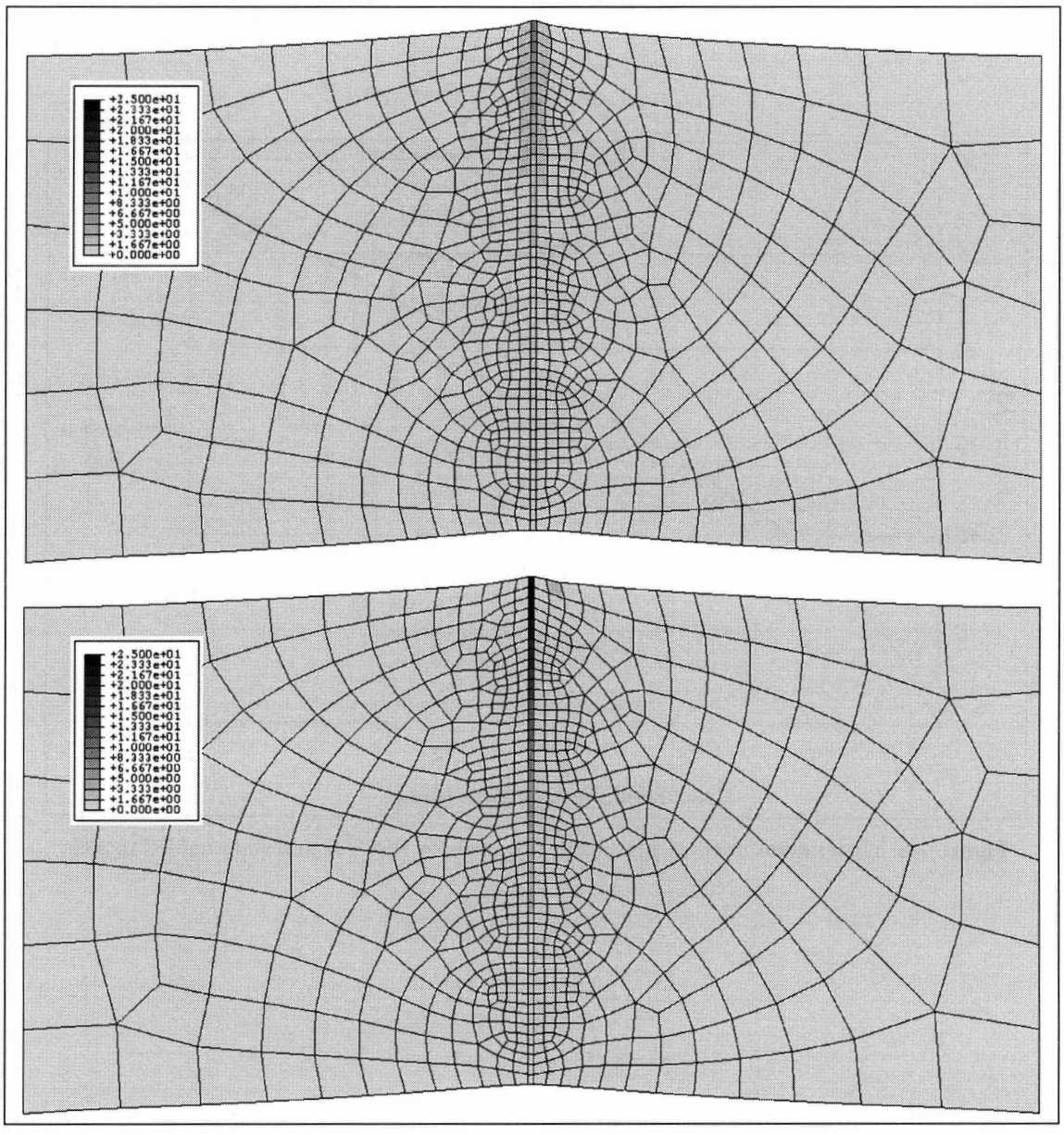

Figure 7-7 Tension contours in slip-free (top) and slip-enabled (bottom) model in yarn-pullout simulation

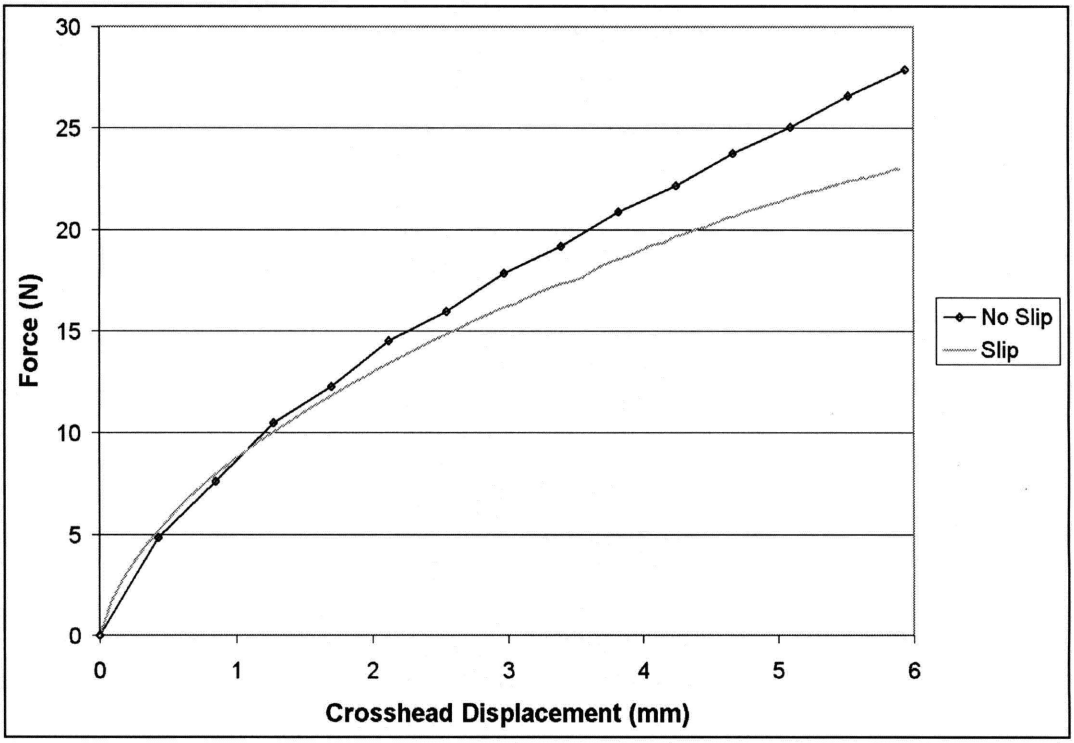

Figure 7-8 Yarn pullout load-displacement response for slip-free and slip-enabled models

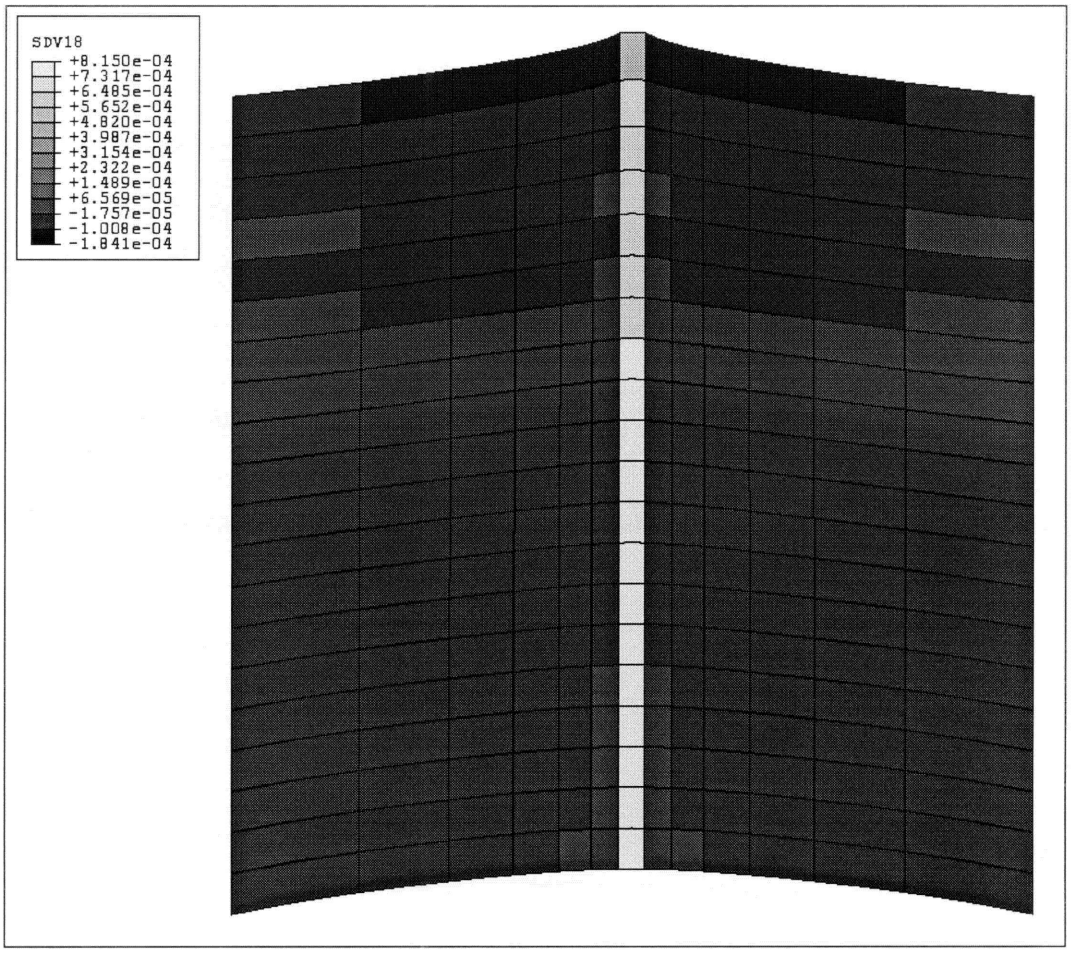

Figure 7-9 Small yarn pullout model, with slip velocity contours as pulled yarn approaches steady state

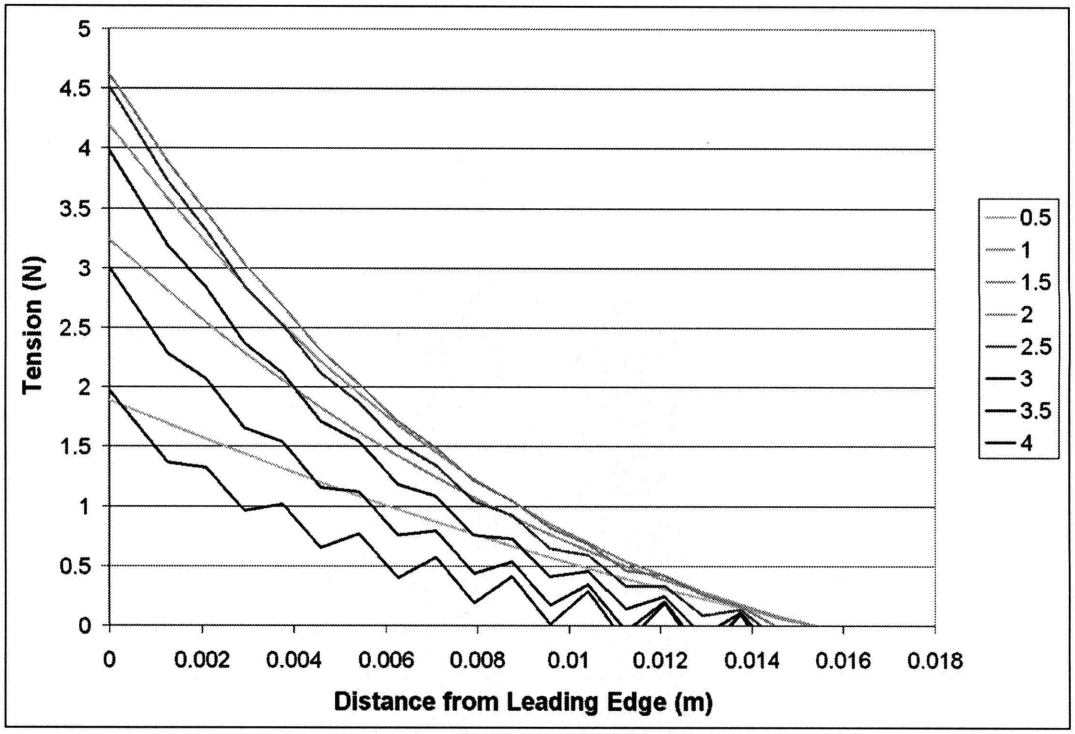

Figure 7-10 Evolution of tension distributions along pulled yarn in unstable small pullout simulation

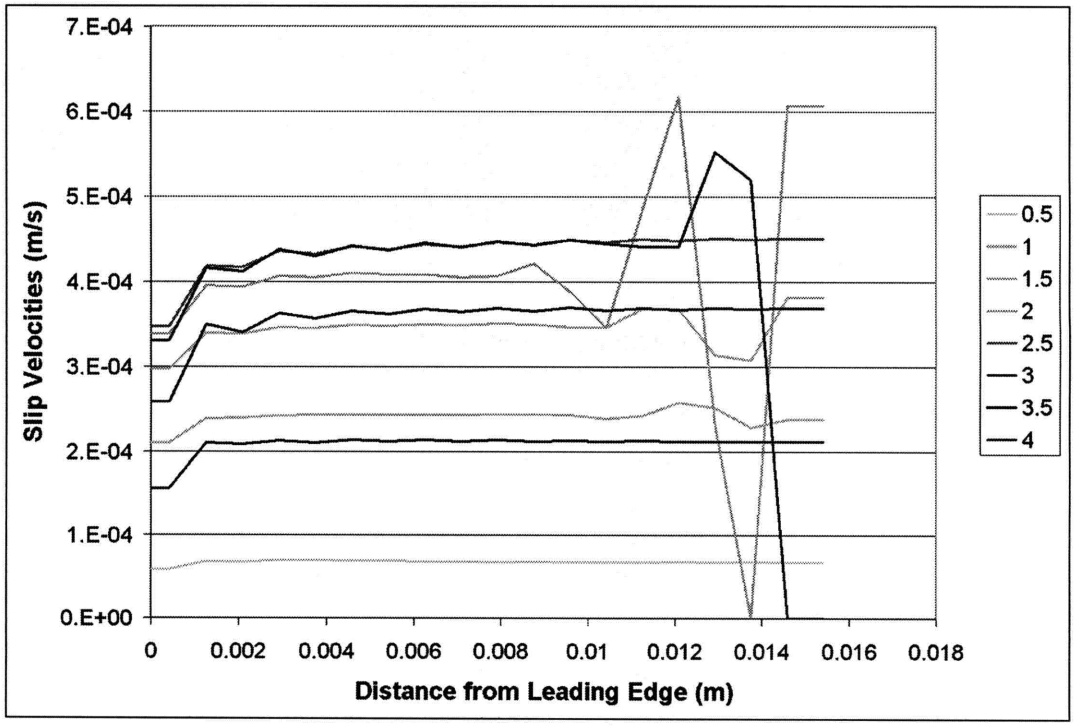

Figure 7-11 Evolution of velocity distributions along pulled yarn in unstable small pullout simulation

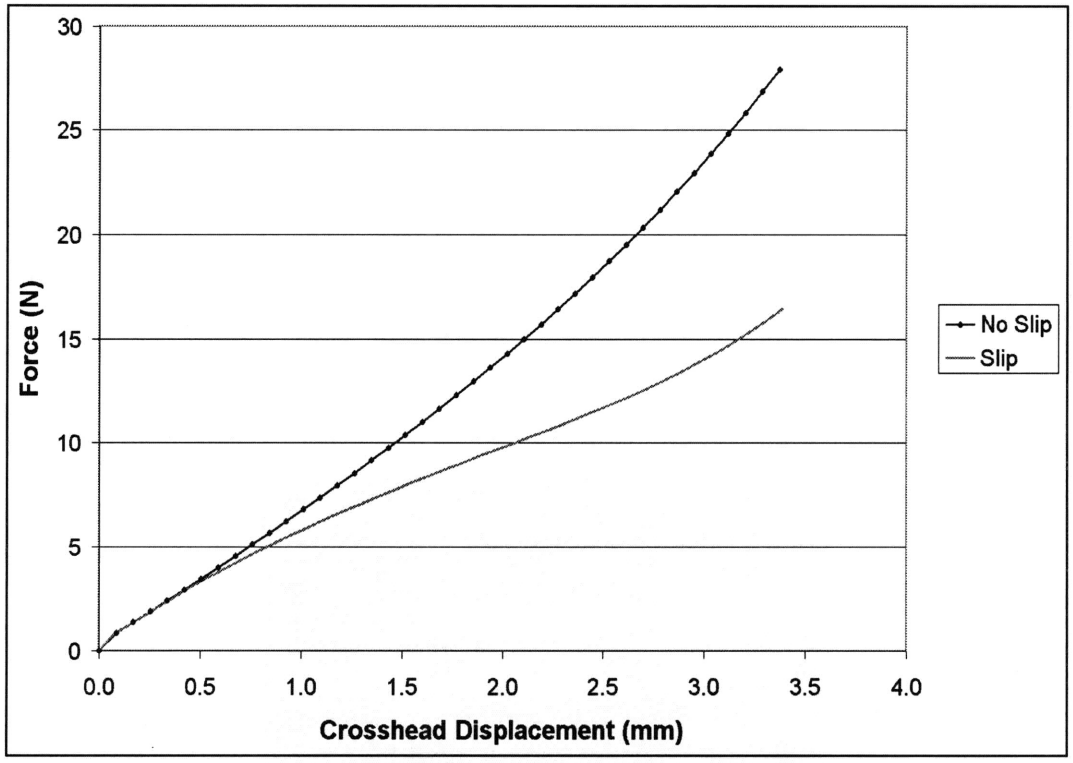

Figure 7-12 Yarn pullout load-displacement response in unstable small pullout simulation

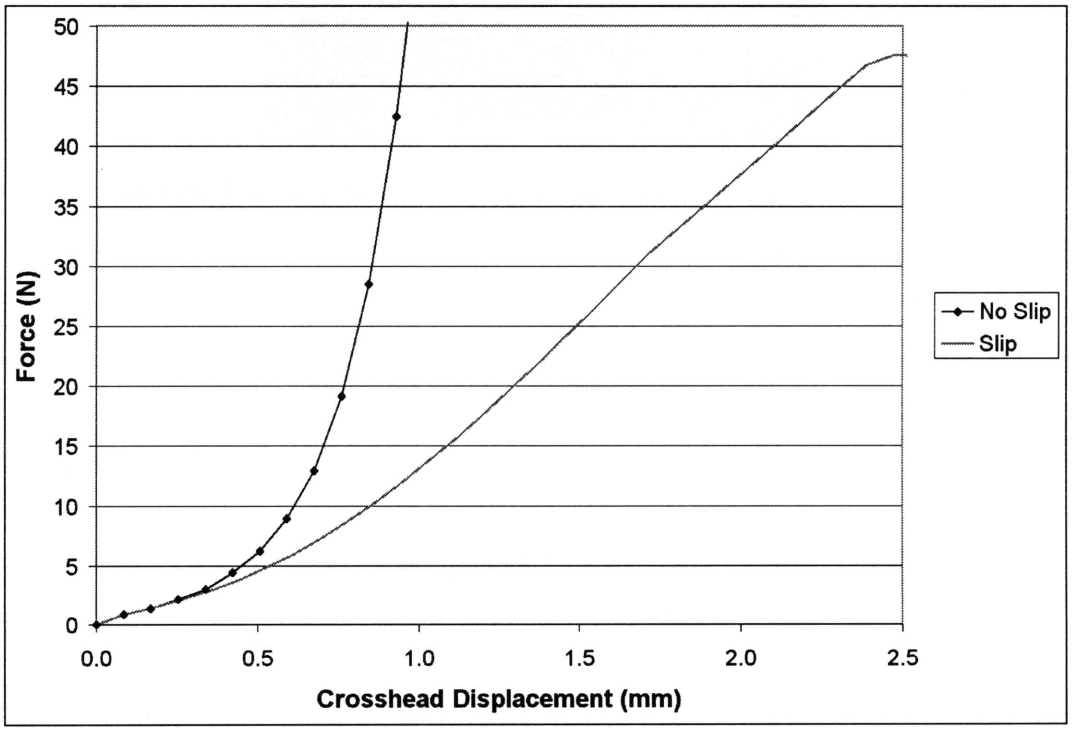

Figure 7-13 Yarn pullout load-displacement response in stable small pullout simulation with fixed lateral displacement

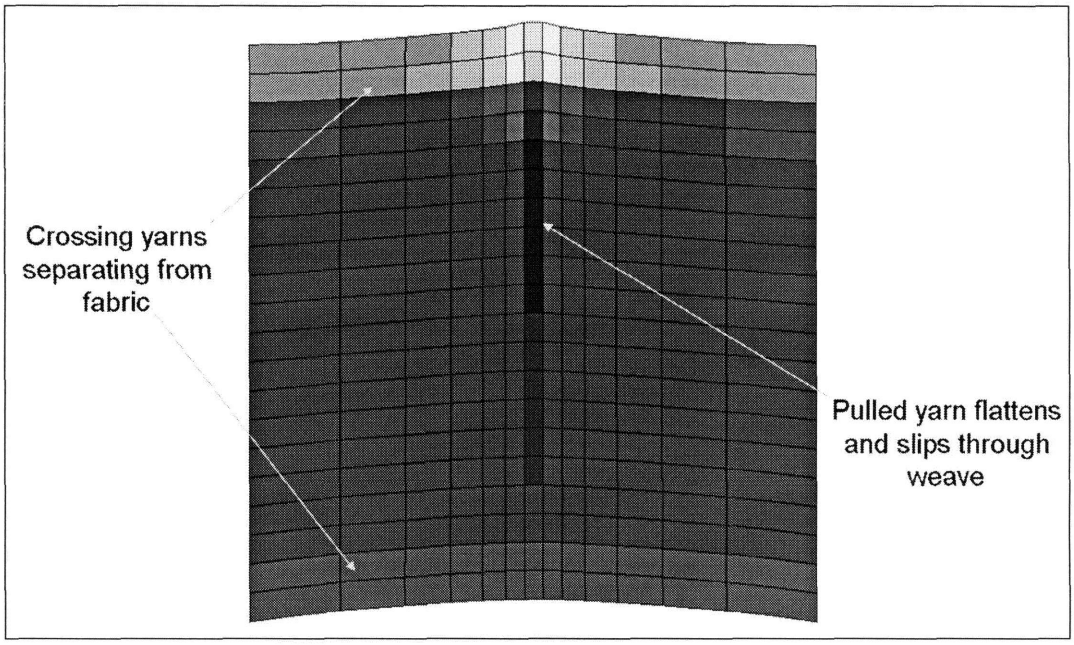

Figure 7-14 Unstretched yarn length contours in small pullout simulation

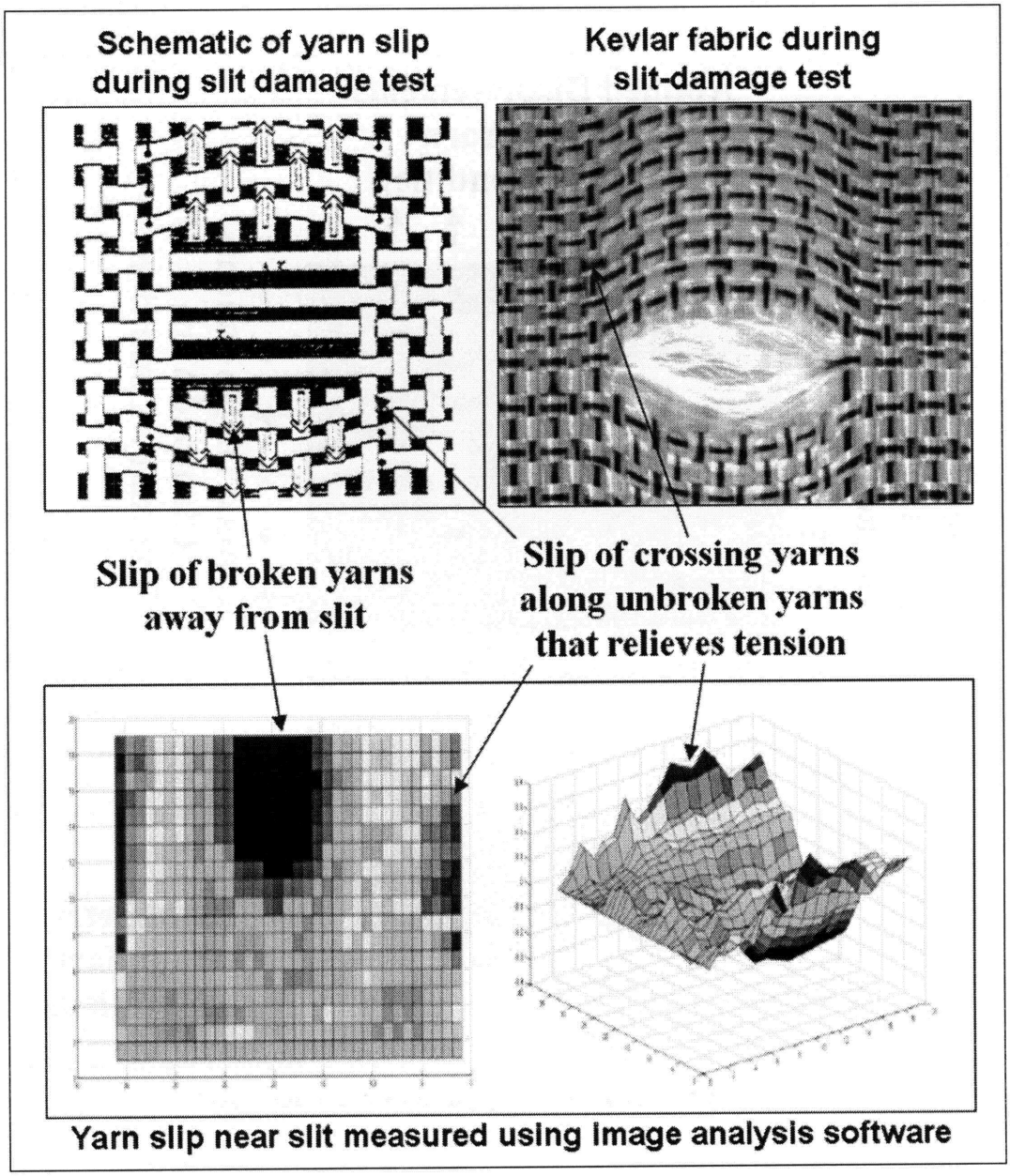

Figure 7-15 Experimentally observed slip fields around a slit in a biaxially stressed fabric

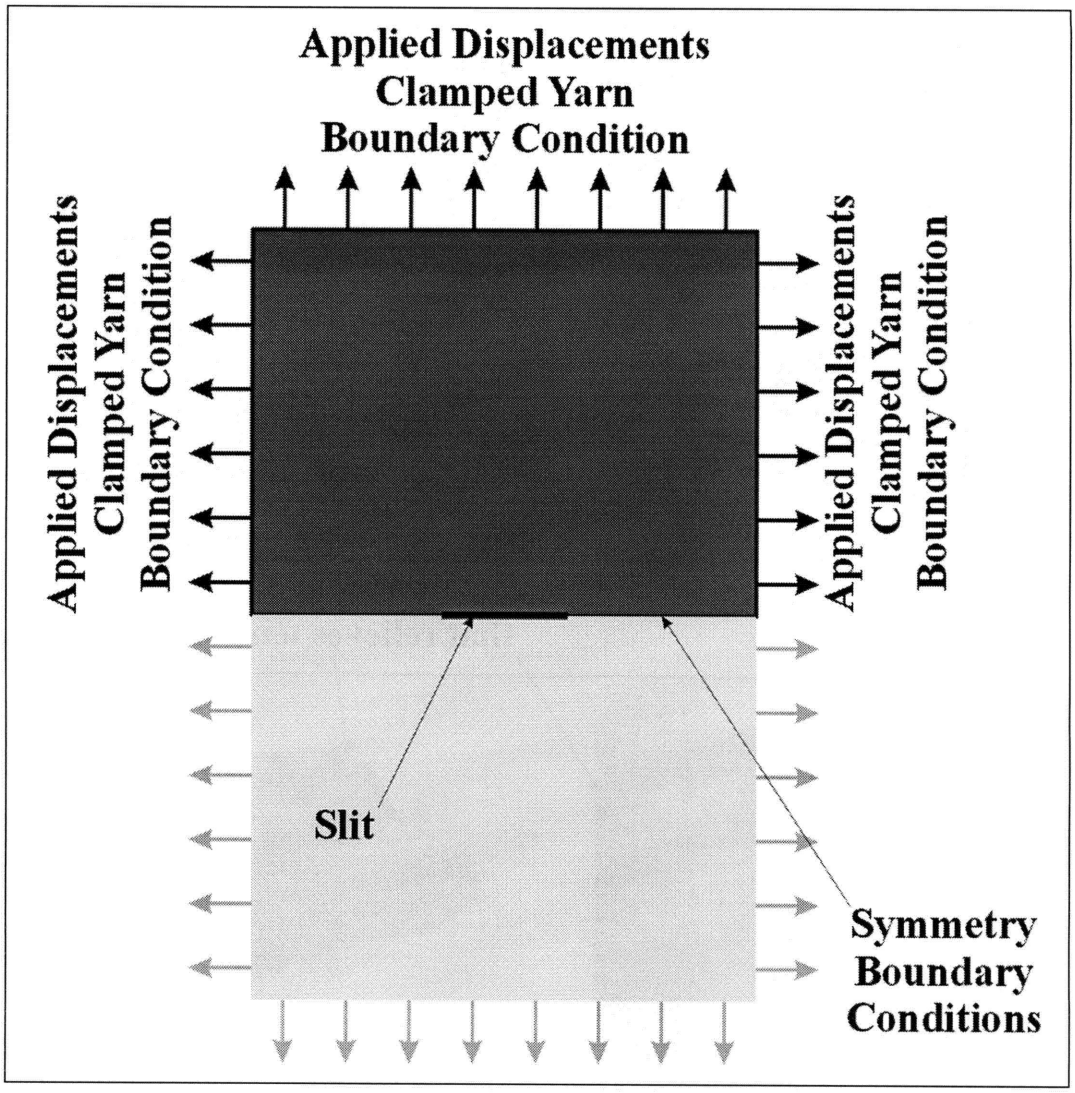

Figure 7-16 Geometry of half-symmetry slit-damage model

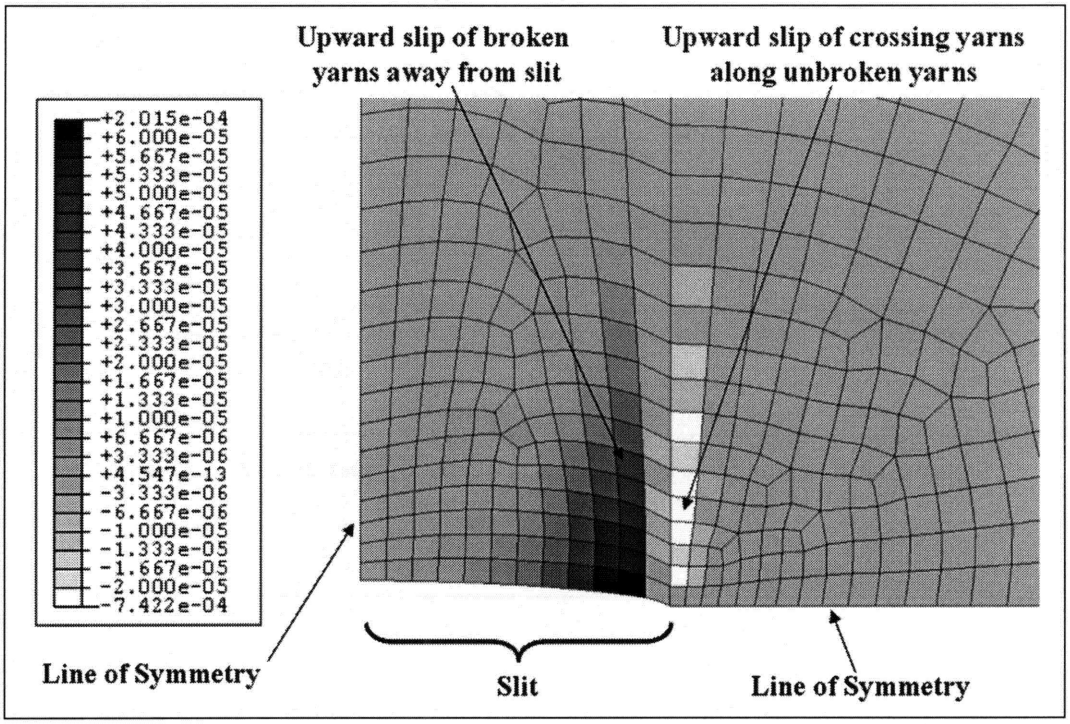

Figure 7-17 Slip displacement of yarns around slit predicted by quarter-symmetry model

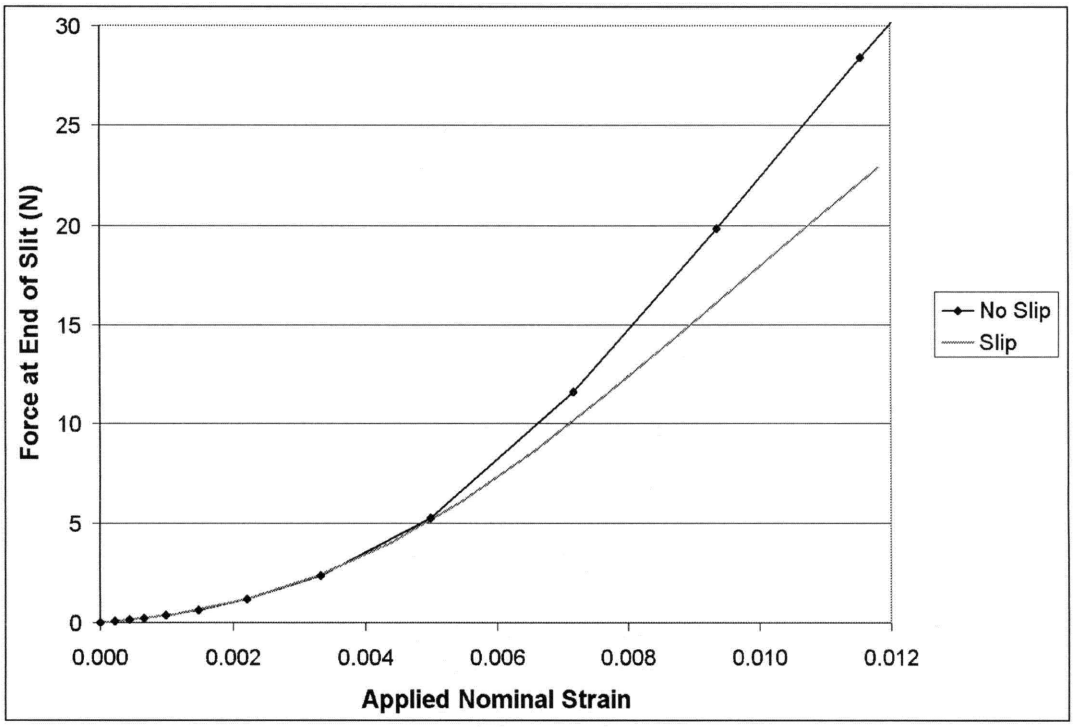

Figure 7-18 Reaction force at end of slit predicted by quarter-symmetry model

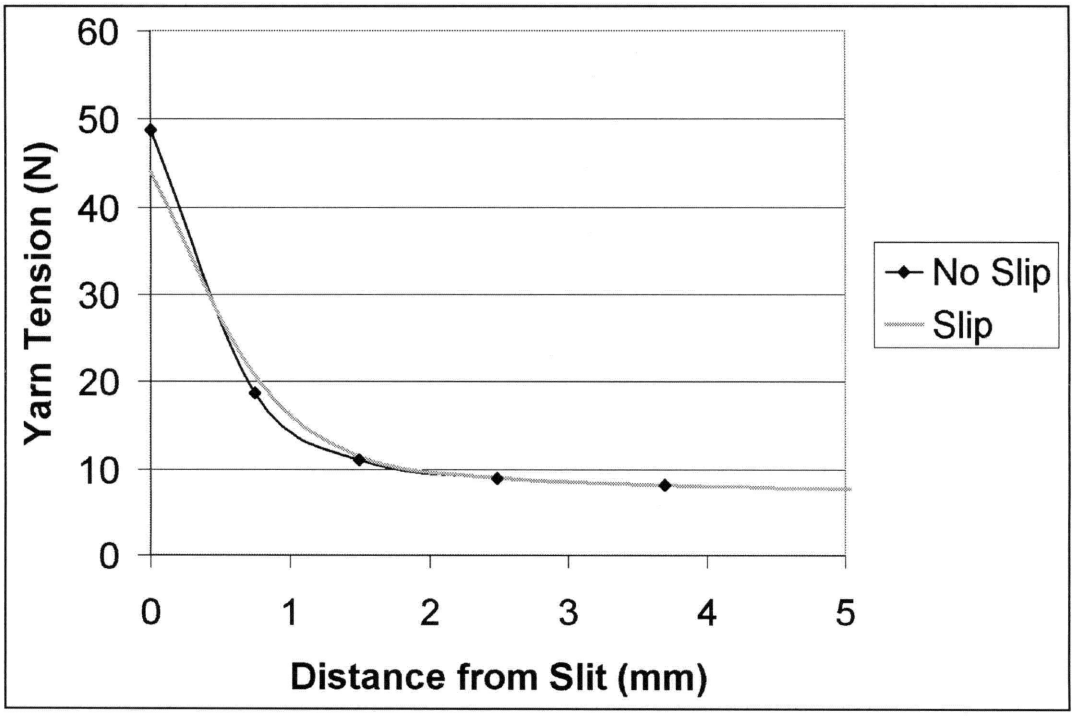

Figure 7-19 Vertical yarn tension distribution along horizontal line of symmetry in front of slit

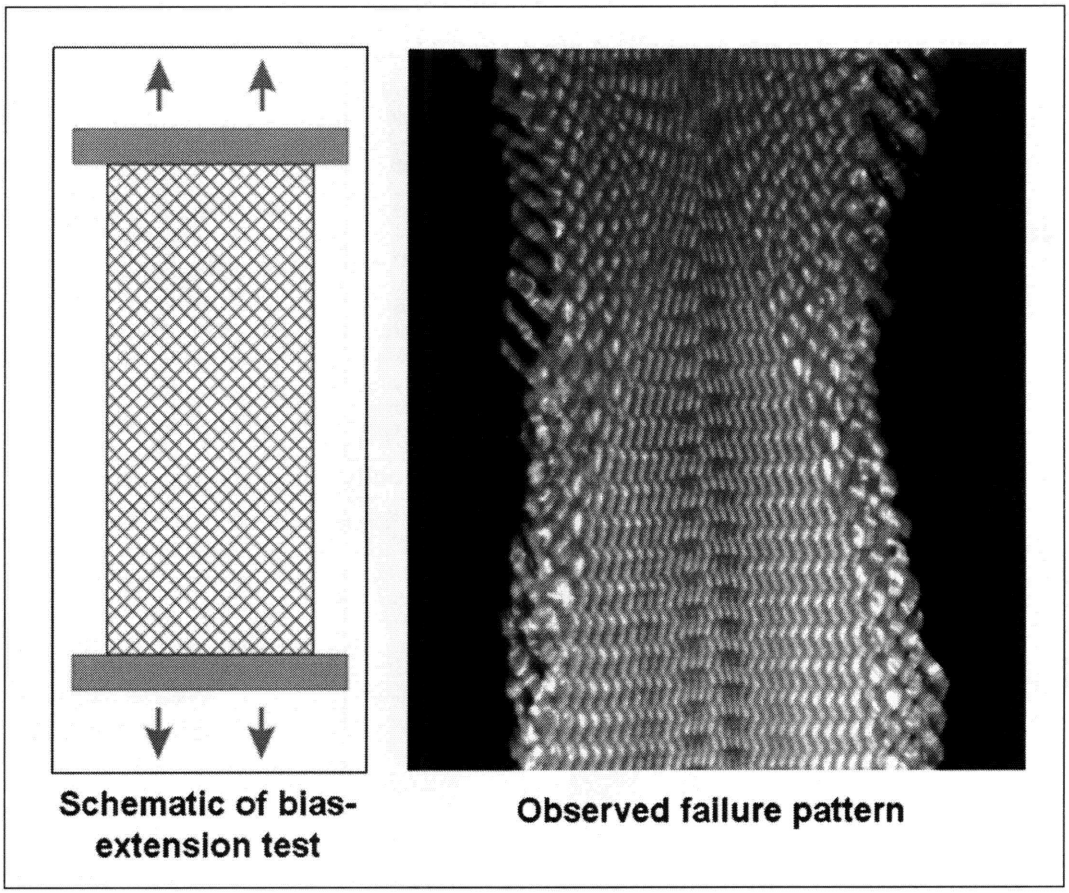

Figure 7-20 Bias-extension test

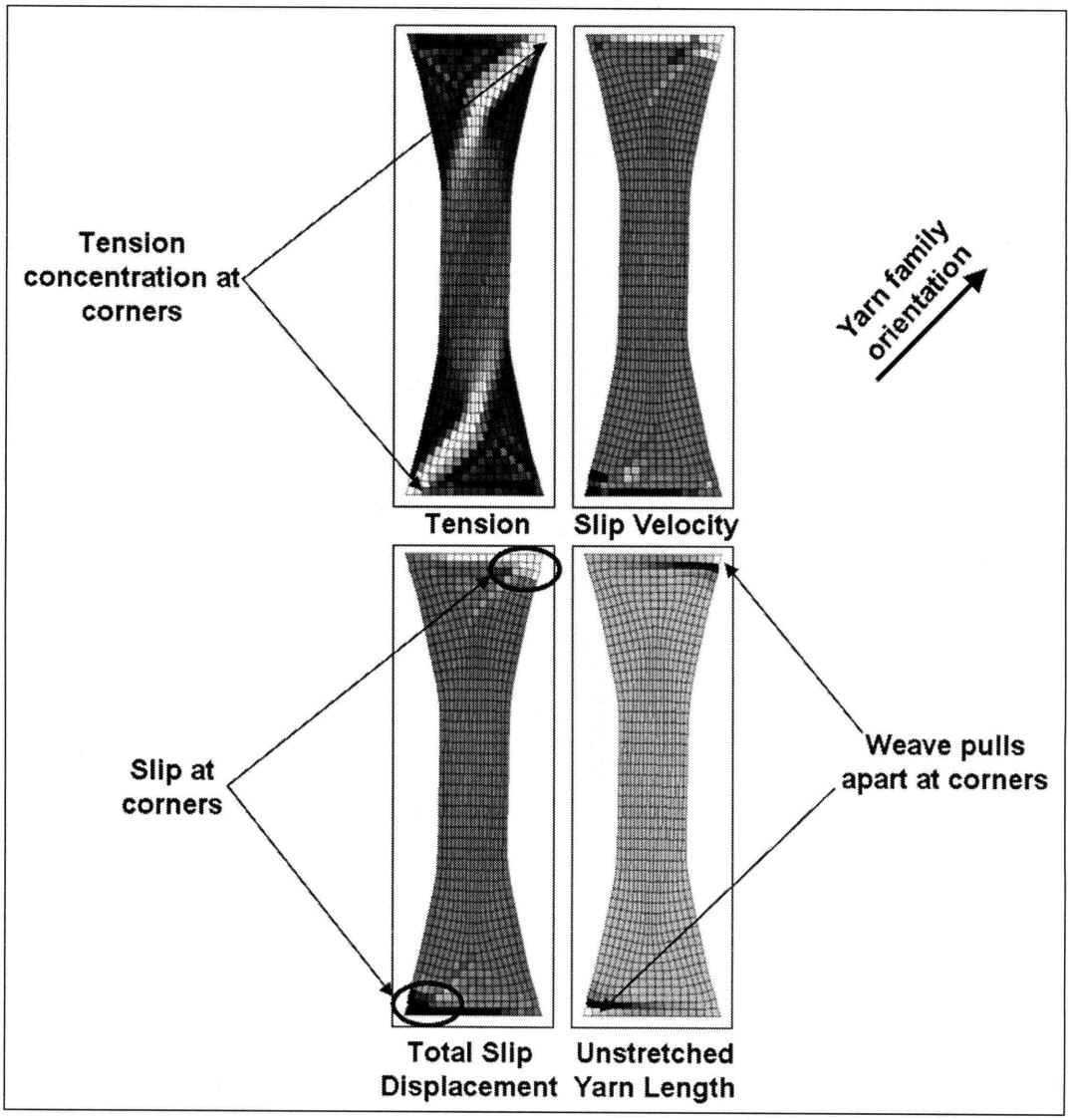

Figure 7-21 Tension, slip-velocity, slip displacement, and unstretched yarn length of the warp yarn family (oriented 45° to horizontal in reference configuration) during early stages of slip

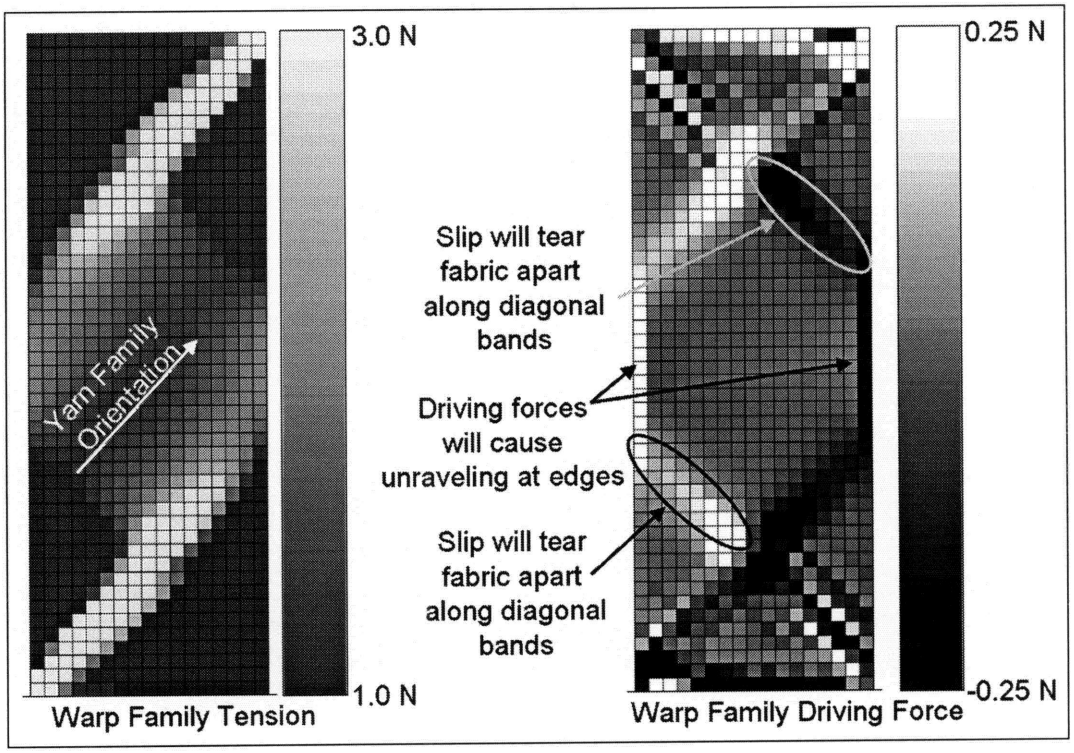

Figure 7-22 Warp direction yarn tensions and slip driving forces in a bias-extension test

Chapter 8
Summary and Recommendations

8.1 Summary

We have proposed a unified approach for modeling the mechanical response of a woven fabric at different length scales. The approach consists of choosing a characteristic geometry and representative unit cell that represents the weave, and appropriate constitutive relations that describe the response of the components of the unit cell. The model can be tailored to different applications through this choice of geometry and constitutive relations—more detailed and complex relations allow different fabric deformation mechanisms to be captured with increased accuracy, at the expense of increased computational cost. The configuration of the weave mesostructure is then related to the state of macroscopic deformation by enforcing local equilibrium within the unit cell, which can be accomplished either by enforcing the local equilibrium equations at the macroscopic scale, or by finding the mesostructural configuration which is consistent with the given deformation history that has the minimum stored elastic energy. Once the mesosturctural configuration is determined the meso-level forces such as yarn tensions and bending moments can be calculated. These forces are then transformed into equivalent continuum stresses at the macroscopic scale through equilibrium arguments. In order to validate this approach, we developed a fabric model that is specialized to modeling the in-plane quasi-static slip-free behavior of a particular plain weave Kevlar® fabric. We measured the appropriate material properties and then compared the model predictions to experimental observations in a variety of different two-dimensional load cases, e.g. uniaxial extension, bias-extension, biaxial tension in the vicinity of slit-like damage. The model was in good agreement with experiments up until the onset of slip and failure.

We next extended the model to three dimensions, by developing an anisotropic shell implementation. Because the fabric is not actually a thin homogeneous structure, but rather a thin three dimensional network being approximated as a shell, the shell behavior cannot be determined by integrating the material behavior through the shell thickness. Instead, we characterized the nine independent modes of deformation of an anisotropic shell, and the corresponding nine generalized forces. The planar model was assumed to describe the membrane response of the shell, irregardless of the out-of-plane shell deformations. Various other simplifying assumptions defined the through-thickness and transverse shear responses of the shell. We conducted bending

experiments on single yarns and on fabric samples, twist experiments on fabric samples, and detailed finite element analyses of fabrics subjected to bending and twist, where every yarn was modeled discretely. These experiments and analyses revealed the mechanisms that control bending and twist of fabrics, and allowed constitutive relations that describe bending and twist response to be characterized. For the Kevlar® fabric we examined, a linear bending response and a bilinear twist response were used. The shell implementation was then used to predict the fabric response in various load cases where out-of-plane deformations occur, and these predictions favorably compared to experimental observations.

We next explored the phenomenon of yarn slip in fabrics. Yarn-to-yarn friction and yarn pullout experiments were used to characterize the frictional behavior that resists slip of yarns in a fabric. The yarn-to-yarn friction tests were not suitable for quantitatively measuring the frictional forces that resist slip in a fabric, because the geometry of the test is significantly different from the geometry of a yarn in a weave, but the tests are useful to determining a range of reasonable friction coefficients and for evaluating any potential rate dependence of frictional effects. The friction tests indicated that friction is slightly rate dependent. We then developed a simplified analytical model that permits the load-displacement response measured in a yarn pullout test to be predicted from a hypothesized constitutive law for frictional resistance to slip in a fabric. If the model prediction can be fit to the experimental results using the same constitutive properties for a variety of loading conditions, the hypothesized constitutive law is descriptive. By fitting the model prediction to the experimental measurements, we determined a sufficiently descriptive constitutive law to validate the slip model. The associated constitutive parameters are consistent with the yarn-to-yarn friction tests.

We developed a slip-enabled continuum fabric model by describing the fabric continuum in a novel manner. In the presence of slip, a single deformation mapping can not be used to describe the motion of all the yarn material, since the two yarn families do not move affinely with one another. One approach is to use a separate deformation mapping for each yarn family. However, using this approach makes it is difficult to accurately capture yarn interactions at the crossover points that control mechanisms such as crimp interchange and locking. Therefore, we use a single mapping that describes the motion of the weave crossover points. The spatial gradient of this mapping is not a deformation gradient in the traditional sense, since it does not map the motion of material points. The motion of the yarn material relative to the crossover points is given by velocity fields. With this description, the same modeling approach and unit cell that were used for the slip free model can be used for the slip-enabled model. However, as the yarns slip through the weave, the unloaded configuration of the unit cell evolves throughout the weave.

We derive equations that describe this evolution as a function of the gradient of slip velocity along the yarn families. We determine the meso-level forces that drive these slip velocities at the mesostructural scale and derive their dependence on the gradient of the tensions along the yarn families. The slip velocity can be related to the driving force using a constitutive law that is determined from yarn pullout experiments.

Because the evolution of the fabric behavior depends on gradients of slip velocities, which are calculated from driving forces that depend on gradients of yarn tensions, the proposed slip theory is non-local. Implementation of a non-local theory into a commercial finite element framework is challenging, primarily because of difficulties in determining gradients from tension and velocity values that are calculated at irregularly spaced integration points in the presence in numeric noise. We explored various methods for determining these gradients, including the use of hybrid elements, spatial filtering and smoothing techniques, and coupling the displacements of shell elements to the tension and velocity values. Ultimately the most effective and computationally efficient method involved averaging the tension (or velocity) values at the centers of the elements, and then estimating the gradients using a finite difference technique over patches of elements. This method is inaccurate when the mesh is distorted, and requires appropriate boundary conditions be applied to the tension and velocity fields, but it allowed the slip approach to be validated. We developed boundary conditions for a free edge, a clamped edge, an edge where yarns but not crossover points are clamped, and lines of symmetry.

We validated the slip-enabled model by simulating four cases where slip occurs—a rake test where a rake through the fabric causes slip, a yarn pullout test, a biaxial tension test around a region containing slit-like damage, and a bias-extension test. The model effectively predicts small slip displacements that redistributes tensions. All the slip fields predicted in these cases were in good agreement with experimental observations. Unfortunately, numerical problems prevented analyses involving large slip displacements from being conducted. Most of these problems stem from the use of an explicit integration scheme for the evolution of the yarn lengths while the model is implemented into an implicit finite element framework. We recommend that the slip formulation be implemented into an explicit framework in order to analyze a wider variety of load cases.

8.2 Recommendations for Continued Work

We recommend a number of different avenues for further research into these topics. Slip-free models of the type described in Chapter 2 are very useful for many applications, but the model

that we have developed was specialized for plain weave Kevlar® fabrics subjected to small to moderate shear deformations. The simplified truss geometry used is adequate to validate the model and capture the behaviors that were of particular interest to us, but has known shortcomings. More accurate (although more computationally intensive) geometries have been proposed, e.g. by Warren [1992], Sagar *et al.* [2003] or Nadler *et al.* [2006]. Employment of a more accurate geometric representation would make the model more accurate in certain cases where phenomena that cannot be captured by the simple truss geometry are important, such as wrapping effects, although the computational cost of the model would be increased. Some fabric applications may also require more complex constitutive relations to describe the response of the components of the unit cell; for example, some fabrics may be woven of yarns that exhibit nonlinear, inelastic behavior when stretched. The model would especially benefit from more accurate geometric and constitutive relations that describe to the locking phenomenon, since these improvements would allow it to be used in applications where shear angles become large. The current model gives inaccurate results and eventually fails to converge at large shear angles largely because the locking behavior is not faithfully represented by the assumed geometry and constitutive relations.

A key component of the model is the determination of the mesostructural configuration that corresponds to a macroscopic state of deformation. We have described two methods for accomplishing this—minimization of the conditional energy function, described in Chapter 2 and King [2003], and introduction of global degrees of freedom that describe the unit cell configuration, such as a mean amplitude, which is described in Appendix B. We have not explored other methods, such as using Lagrange multiplier methods or penalty methods, which could prove to be more robust or efficient. Alternatively, the methods we did explore could be optimized further—different minimization algorithms or different choices of global degrees of freedom might prove to be more effective. Developing better methods of relating the mesostructural configuration to the macroscopic deformation could eliminate the problem described in Appendix B, where convergence difficulties arise from numeric problems when one family of yarns becomes straight through the application of uneven tensions.

Extension of the same modeling approach to other weave structures requires the development of different unit cell geometries. Fabrics can be woven into many weave structures other than plain weaves, such as basket, twill, and satin weaves, shown in Figure 8-1. The repeating unit cells associated with these weaves are more complex that the unit cell associated with a plain weave, even if simple truss-based geometries are used to represent them. For example, Figure 8-2 shows a truss representation of a 2-2 twill weave, with the representative unit cell. Because

this unit cell lacks the symmetry of the plain weave unit cell, more than five parameters are necessary to define its configuration. Consequently, different methods will be necessary for determining the mesostructural configuration from the macroscopic deformation gradient. If the conditional energy minimization approach described in Chapter 2 is employed, the conditional energy must be re-derived for each unit cell geometry, and different algorithms may prove more effective at finding the preferred state where the conditional energy is minimized. If a global degree of freedom approach is used, more degrees of freedom than just the mean amplitude would be necessary, and the corresponding equilibrium equations must be carefully derived. In addition, the unit cell components intersect the unit cell boundaries in different ways than in the plain weave, so the macroscopic stress tensor associated with a given set of meso-level forces must be re-derived.

The extension of the model to three dimensional behavior encompassed a number of simplifying assumptions, and it may be valuable in some applications to relax some of these assumptions. For example, it was assumed that the membrane response of the fabric was decoupled from out-of-plane deformations. However, bending or twisting a fabric to large curvatures (so that the radius of curvature approaches the size of the characteristic unit cell) could impact the locking response. Applied through-thickness stresses, which can arise during fabric composite forming operations or in multilayer fabric structures such as ballistic armors, affect the through-thickness forces in the weave and therefore can affect crimp interchange and the membrane response in some fabrics. Since both locking forces and through-thickness forces are known to resist yarn slip, out-of-plane deformations can affect the slip-response of a fabric as well. The analysis of fabric composite forming operations and ballistic impacts on multi-layered armors also requires an effective means of modeling fabric-to-fabric or fabric-to-surface contact. Rebouillat [1998] shows that the tribological properties of the surface of a woven fabric are different from the properties of individual yarns. Accurate surface interaction models must be developed, and the effect that these interactions have on the mechanical behavior of the fabric must be determined.

The shell model used to capture the effects of bending and twist resistance is significantly more computationally expensive than a membrane implementation that omits these resistances. For a given application where the three-dimensional deformations of fabrics are of interest, the importance of the bending and twist resistance must be evaluated so that an appropriate choice between a membrane and shell implementation can be made. In other words, criteria for when the bending and twist resistances can be neglected must be established. Further study of the bending and twist responses themselves could also be useful. Currently, the bending and twist responses

must be measured experimentally from fabric samples, because of the complexity of the phenomena that control them. Ideally, the bending and twist response of the fabric should be predicted from the weave structure and the properties of the individual yarns or fibers.

Further study of yarn slip is necessary. More extensive yarn friction tests and yarn pullout tests that investigate a wider variety of geometries and a wider range of input parameters would allow a much more detailed understanding of frictional effects that control yarn slip. The frictional response at large rates are of especial interest if slip is to be included in a model used for simulating ballistic impacts. Apparatuses capable of measuring high rate friction coefficients or pullout responses must be devised and constructed. The analytical model used to relate a frictional constitutive law to the measured pullout response described in Chapter 4 can also be improved. The simulations of the pullout test discussed in Chapter 7 imply that some of the assumptions of this model, most notably the assumptions that negligible slip occurs perpendicular to the pulled yarn and that the average crossing yarn spacing $2p$ remains constant along the yarn throughout the test, may not be accurate. Refinement of the analytical model could result in a better fit between the analytical model and the experimentally measured curves, and hence in more accurate slip constitutive relations. Further study of the pullout tests, both through numerical simulation or more detailed observation of the experimental trials, would aid this refinement. More complex forms of the slip constitutive relation could also be used; for example, the time-dependent relaxation of the cross sections and the corresponding variation of the locking forces described in Appendix A could be taken into account. Further exploration of this relaxation phenomenon may also be of interest.

The slip implementation described in Chapter 6 is not ideal. In particular, the finite difference method used for gradient estimation is prone to error, especially near the edges of the model and in regions with a non-uniform mesh. A more accurate method of calculating tension and slip-velocity gradients is required. One effective method would be to develop a non-local element is capable of predicting accurate tension and velocity gradients at its integration points. We investigated a few element formulations with tension and slip velocity degrees of freedom that could calculate tension and velocity gradients, but these elements introduced non-physical oscillations into the solution that may relate to the numerical locking problem discussed in Appendix C. Eliminating the numeric locking problem is vital to the development of a robust non-local element, and would also improve the accuracy of the slip-free model. A robust non-local element would more accurately determine gradients and predict slip than the current finite difference method, and it would allow the tension and velocity gradients to be determined on an element-by-element basis. Determining the gradients on an element-by-element basis would

make implicit integration of the yarn length evolution feasible, which would permit larger time increments and more computationally efficient analyses. Also, it would facilitate the implementation of rate-independent slip constitutive models, which cannot be easily implemented when the evolution of the yarn lengths are calculated explicitly.

The most significant work that should be pursued is the implementation of both the slip-free and the slip-enabled models into an explicit finite element framework. Although suitable for validation of the modeling techniques, implicit codes are poorly suited to studying ballistic impacts and fabric composite forming, which are two of the most interesting contemporary fabric applications. They also suffer from convergence problems under certain conditions. Furthermore, as long as an explicit integration scheme is used to integrate the evolution of the unstretched yarn lengths in the presence of slip, it is undesirable to implement the model into an implicit framework, as this combines the large computational cost per increment of implicit analyses with the large number of very small increments necessary for stability of an explicit integration scheme. An explicit implementation would be much more computationally efficient in many cases, and would be able to model a much larger range of applications, including applications involving large three dimensional deformations and contact, such as fabric composite forming, and applications with large slip displacements, such as yarn pullout tests. When an explicit implementation is developed for transient dynamic analyses, care must be taken in developing appropriate equilibrium relations for the fabric mesostructure that take inertial effects into account. Care must also be taken in deriving the appropriate mass matrix for the fabric, so that not only the inertia associated with the in-plane location of yarn material is included, but also inertia associated with the three dimensional motions of the yarns within the unit cell.

Once large slip deformations can be simulated, fabric failure can be included in the model formulation. Failure due to yarn pullout and weave unraveling in the slip-enabled model can be implemented in the following way. The yarn length between any weave point and the free ends of the yarn can be calculated in the reference configuration. Since the yarn velocity past the weave point is known throughout the history of the analysis, the amount of yarn that has slipped past that point can be calculated at each time increment. When the free end of the yarn reaches the weave point, the effects of the yarn on the mechanical response of the fabric at that point can be removed, e.g. by reducing the effective yarn stiffness at that point to a very small value. This is equivalent to imagining that every yarn has an thread of a very compliant material extending infinitely from its end. Once a yarn is pulled out of an element, appropriate boundary conditions on the tension and velocity fields in the neighboring elements must be imposed. It is possible that yarns of both families may be pulled from an element. In this case, the element can be

deactivated. Because yarns never spontaneously weave themselves into a fabric, additional elements that are not present in the reference configuration never need be generated.

Failure due to yarn breakage can be accomplished in a similar manner. Once the breaking strength or breaking strain of a yarn is exceeded at a given weave point, the effects of the yarn on the mechanical response of the fabric can be removed, e.g. by reducing the yarn stiffness to a very small value. Appropriate boundary conditions on the tension and velocity fields must be imposed on the neighboring elements. If the pullout of the broken yarn is of interest, the model must re-calculated the yarn length between every affected weave point and the new free ends of the yarn each time a break is detected.

A final avenue of research involves the combination of this fabric model and other material models to simulate the behavior of composite systems. For example, a simple fabric composite model could be developed by combining the fabric model in series with a hyperelastic material model that represents the composite matrix. More advanced composite models could be developed by modifying the fabric and matrix models to take into account coupling and delamination effects between the two mechanical system. A model of an armor system consisting of multiple layers of fabric and other materials could be assembled by combining the fabric elements with elements that model the response of the other components, with appropriate interactions defined. The continuum implementation of the fabric model is extremely versatile in that it can be easily combined with other continuum models to simulate advanced composite systems.

Further development of fabric modeling techniques along the avenues described here will result in a robust fabric model that can predict the mechanical behavior of practically any woven fabric system at both the macroscopic scale and the mesoscale, in a wide variety of applications that may involve large three-dimensional deformations, yarn slip, and fabric failure.

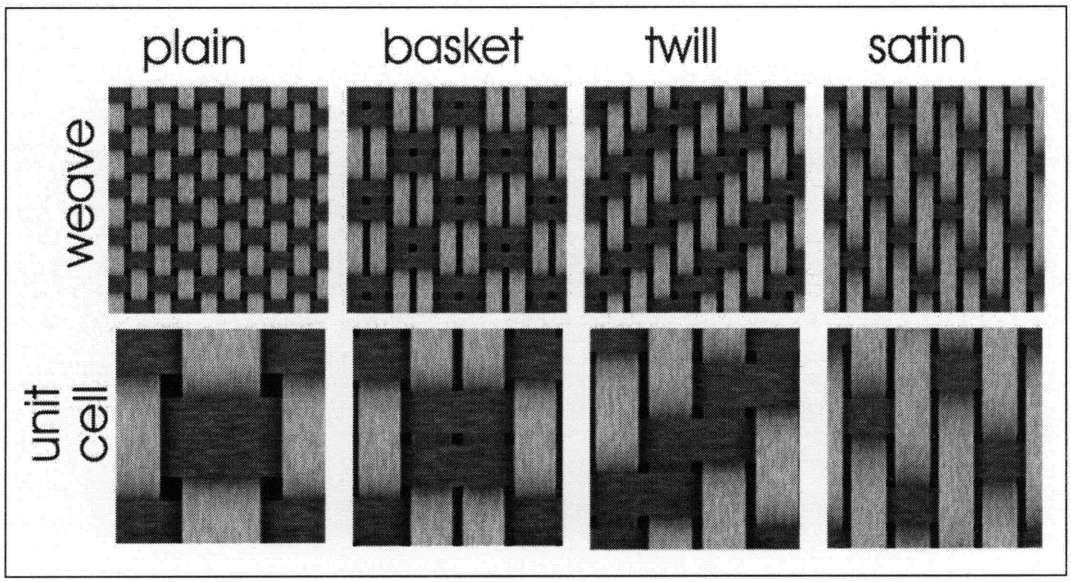

Figure 8-1 Examples of different fabric weaves

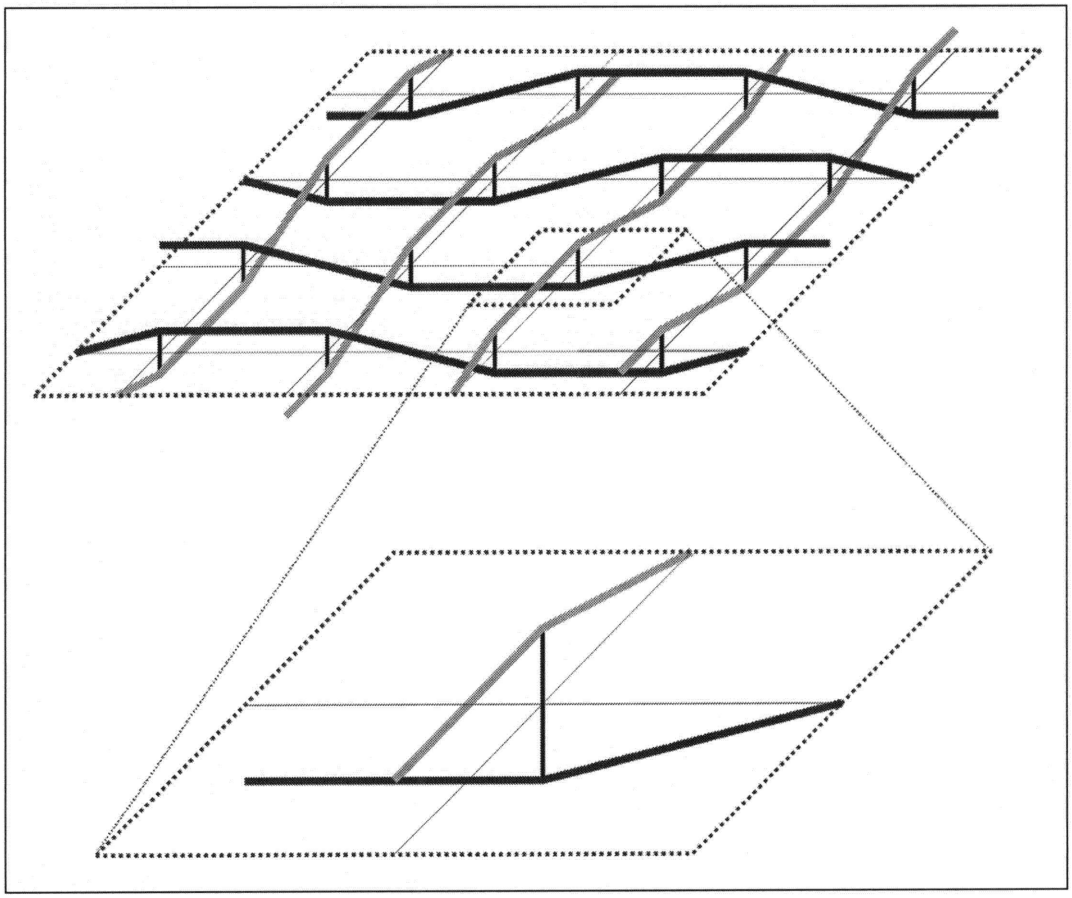

Figure 8-2 Truss representation of 2-2 twill weave, with representative unit cell

References

Baseau E., "Finite Deformation of Elastic-plastic Filamentary Networks", *International Journal of Nonlinear Mechanics* 38:1473-1479, 2003.

Bathe K.J., *Finite Element Procedures,* Prentice Hall, Upper Saddle River, NJ, 1996.

Bathe K.J. and Chapelle D., *The Finite Element Analysis of Shells: Fundamentals*, Springer-Verlag, 2003.

Belytschko T., Liu W.K., and Moran B., *Nonlinear Finite Elements for Continua and Structures*, Wiley, 2000.

Ben Boubaker B., Haussy B., and Ganghoffer J.F., "Discrete Models of Woven Structures: Stability and Draping Analysis", *C.R. Mecanique* 330:871-877, 2002.

Boisse P., Borr M., Buet K., and Cherouat A., "Finite Element Simulations of Textile Composite Forming Including the Biaxial Fabric Behavior", *Composites Part B* 28B:453-464, 1997.

Boisse P., Buet K., Gasser A., and Launay J., "Meso/macro-mechanical Behavior of Textile Reinforcements for Thin Composites", *Composites Science and Technology* 61(3):395-401, 2001.

Breen D.E., House D.H., and Wozny M.J., "A Particle-Based Model for Simulating the Draping Behavior of Woven Cloth", *Textile Research Journal* 64(11):663-685, 1994.

Chen B., Lang E.J., and Chou T., "Experimental and Theoretical Studies of Fabric Compaction Behavior in Resin Transfer Modeling", *Materials Science and Engineering* A317:188-196, 2001.

Cherouat A. and Billouet J.L., "Mechanical and Numerical Modelling of Composite Manufacturing Processes: Deep-drawing and Laying-up of Thin Pre-imprognated Woven Fabrics", *Journal of Materials Processing Technology* 118:460-471, 2001.

Godfrey, T.A., and Rossettos, J.N., "Damage Growth in Pre-Stressed Plain Weave Fabrics", *Textile Research Journal* 68(5):359-370, 1998.

Godfrey, T.A., and Rossettos, J.N., "The Onset of Tear Propagation in at Slits in Stressed Uncoated Plain Weave Fabrics", *Journal of Applied Mechanics – Transactions of the ASME* 66(4):926-933, 1999.

Gommers B., Verpoest I., and Van Houtte P., "Modelling the Elastic Properties of Knitted-Fabric-Reinforced Composites", *Composites Science and Technology* 56:685-694, 1996.

Grosberg P., "The Mechanical Properties of Woven Fabrics Part II: The Bending of Woven Fabrics", *Textile Research Journal* 36(3):205-211, 1966.

Hearle J.W.S., Grosberg P., and Backer S., *Structural Mechanics of Fibers, Yarns, and Fabrics*, Wiley-Interscience, New York, 1969.

Kato S., Yoshiro T., and Minami H., "Formulation of Constitutive Equations for Fabric Membranes Based on the Concept of Fabric Lattice Model", *Engineering Structures* 21:691-708, 1999.

Kawabata S., Niwa M., and Kawai H., "The Finite Deformation Theory of Plain Weave Fabrics Part I:The Biaxial Deformation Theory", *Journal of the Textile Institute* 64(1):21-46, 1973.

Kawabata S., Niwa M., and Kawai H., "The Finite Deformation Theory of Plain Weave Fabrics Part II:The Uniaxial Deformation Theory", *Journal of the Textile Institute* 64(2):47-61, 1973.

Kawabata S., Niwa M., and Kawai H., "The Finite Deformation Theory of Plain Weave Fabrics Part III: The Shear Deformation Theory", *Journal of the Textile Institute* 64(2):62-85, 1973.

King M.J., "An Energy-Based Constitutive Model for the In-Plane Mechanical Behavior of Woven Fabrics", Master's Thesis, Massachusetts Institute of Technology, 2003.

King M.J., Jearanaisilawong P., and Socrate S., "A Continuum Constitutive Model for the Mechanical Behavior of Woven Fabrics", *International Journal of Solids and Structures* 42:3867-3896, 2005.

MacGlockton M.A., Cox B.N., and McMeeking R.M., "A Binary Model of Textile Composites: III Hight Failure Strain and Work of Fracture in 3D Weaves", *Journal of the Mechanics of Physics and Solids* 51:1573-1600, 2003.

McGuinness G.B., and O Bradaigh, C.M., "Development of Rheological Models for Forming Flows and Picture-Frame Shear Testing of Fabric Reinforced Thermoplastic Sheets", *Journal of Non-Newtonian Fluid Mechanics* 73:1-28, 1997.

Mohammed U., Lekakou C., Dong L., and Bader M.G., "Shear Deformation and Micromechanics of Woven Fabrics", *Composites Part A* 31:299-308, 2000.

Nadler B. and Steigmann D.J., "A model for frictional slip in woven fabrics", *C.R. Mecanique* 331:797-804, 2003.

Nadler B., Papadopoulos P., and Steigmann D.J., "Multiscale constitutive modeling and numeric simulation of fabric material", *International Journal of Solids and Structures* 43(2):206-221, 2006.

Ng S., Tse P., and Lau K., "Numerical and Experimental Determination of the In-Plane Elastic Properties of 2/2 Twill Weave Fabric Composites", *Composites Part B* 29B:735-744, 1998.

O'Rourke J., *Computational Geometry in C*, Cambridge University Press, New York, 1998.

Pan, N. and Yoon, M., "Behavior of Yarn Pullout from Woven Fabrics: Theoretical and Experimental", *Textile Research Journal* 63(11):629-637, 1993.

Peirce F.T., "The Geometry of Cloth Structure", *Journal of the Textile Institute* 28(3):T45-T96, 1937.

Peng, X.Q., Cao, J., Chen, J., Xue, P., Lussier, D.S., and Lui, L., "Experimental and Numerical analysis on normalization of picture frame tests for composite materials", *Composites Science and Technology* 64:11-21, 2004.

Peng, X.Q., Cao, J., "A Continuum-Mechanics Based Non-Orthogonal Constitutive Model for Woven Composite Fabrics", *Composites Part A* 36(6):859-874, 2005.

Press W.H., Teukolsky S.A., Vettering W.T., and Flannery B.P., *Numerical Recipes in FORTRAN: The Art of Scientific Computing*, 2nd ed., Cambridge University Press, Cambridge, 1992.

Rattensperger H., Eberhardsteiner J., and Mang H.A., "Numerical Investigation of High Pressure Hydraulic Hoses with Steel Wire Braid", IUTAM Symposium on Computational Mechanics of Solid Materials at Large Strains 407-416, 2003.

Raun X. and Chou T., "Experimental and Theoretical Studies of the Elastic Behavior of Knitted Fabric Composites", *Composites Science and Technology* 56:1391-1403, 1995.

Realff M.L., "Mechanical Properties of Fabrics Woven from Yarns Produced by Different Spinning Technologies", Ph.D. Thesis, Massachusetts Institute of Technology, 1992.

Realff M.L., Boyce M.C., and Backer S., "A Micromechanical Model of the Tensile Behavior of Woven Fabric", *Textile Research Journal* 67(6):445-459, 1997.

Rebouillat, S., "Tibological Properties of Woven Para-aramid Fabrics and Their Constituent Yarns", *Journal of Material Science* 33:3293-3301, 1998.

Reese S., "Anisotropic Elastoplastic Material Behavior in Fabric Structures", IUTAM Symposium on Computational Mechanics of Solid Materials at Large Strains 201-210, 2003.

Roylance D., Wilde A., and Tocci G., "Ballistic Impact of Textile Structures", *Textile Research Journal* 43(1):34-41, 1973.

Roylance D., Chammas P., Ting J., Chi H., and Scott B., "Numerical Modeling of Fabric Impact", in Proceedings of the National Meeting of the ASME, 1995.

Sagar T.V., Potluri P., and Hearle J.W.S., "Mesoscale Modelling of Interlaced Fibre Assemblies Using Energy Method", *Computational Material Science* 28:49-62, 2003.

Sagar T.V. and Potluri P., "Computation of Bending Behavior of Woven Structures Using Optimization Techniques", *Textile Research Journal* 74(10):879-886, 2004.

Shim V.P.W., Tan V.B.C., and Tay T.E., "Modelling Deformation and Damage Characteristics of Woven Fabric Under Small Projectile Impact", *International Journal of Impact Engineering* 16(4):585-605, 1995.

Shim V.P.W., Lim C.T., and Foo K.J., "Dynamic Mechanical Properties of Fabric Armour", *International Journal of Impact Engineering* 25:1-15, 2001.

Shockey D.A., Elrich D.C., and Simons J.W., "Improved Barriers to Turbine Engine Fragments: Interim Report I", DOT/FAA AR-99/8,I, 1999.

Shockey D.A., Elrich D.C., and Simons J.W., "Improved Barriers to Turbine Engine Fragments: Interim Report II", DOT/FAA AR-99/8,II, 1999.

Shockey D.A., Elrich D.C., and Simons J.W., "Improved Barriers to Turbine Engine Fragments: Interim Report III", DOT/FAA AR-99/8,III, 2001.

Shockey D.A., Elrich D.C., and Simons J.W., "Improved Barriers to Turbine Engine Fragments: Interim Report IV", DOT/FAA AR-99/8,IV, 2002.

Shockey D.A., Elrich D.C., and Simons J.W., "Improved Barriers to Turbine Engine Fragments: Final Annual Report", DOT/FAA AR-99/8,V, 2002.

Spencer, A.J.M., "Theory of Invariants", In *Continuum Physics*, Vol I (Eringin, A.C. ed.) Academic Press, New York, 239-353, 1971.

Steigmann D.J., "Equilibrium of Prestressed Networks", *IMA Journal of Applied Mathematics* 48(2):195-215, 1992.

Tabiei A. and Ivanov I., "Computational micro-mechanical model of flexible woven fabric for finite element impact simulation", *International Journal of Numerical Methods in Engineering* 153:1259-1276, 2002.

Tanov R.R. and Brueggert M., "Finite Element Modelling of non-Orthogonal Loosely Woven Fabrics in Advanced Occupant Restraint Systems", *Finite Elements in Analysis and Design* 39:357-367, 2003.

Termonia Y., "Impact Resistance of Woven Fabrics", *Textile Research Journal* 74(8):723-729, 2004.

Warren W., "The Large Deformation Elastic Response of Woven Kevlar Fabric", *Polymer Composites* 13(4):278-284, 1992.

Xue P., Peng X., and Cao J., "A Non-orthogonal Constitutive Model for Characterizing Woven Composites", *Composites Part A* 34:183-193, 2003.

Appendix A
Cyclic Shear and Viscoelastic Locking

A.1 Cyclic Shear Tests

One of the chief advantages of the continuum modeling approach for fabrics is that it can be easily tailored to a variety of different applications. Because the weave mesostructure and component constitutive relations that the model is based upon are physically motivated, the fabric model can be customized to include all deformation mechanisms that are relevant to a specific application, and exclude any that are unimportant in order to improve computational efficiency. If a specific component of the weave mesostructure is not represented with sufficient accuracy to capture a phenomenon of interest, the model can be easily modified to include the appropriate mechanisms.

An example of this versatility is the manner in which the model is easily modified to accurately capture cyclic shear. As discussed in Chapter 2, the shear deformation in fabrics is accommodated primarily by "trellising" rotation of the yarn families, and the response to shear deformation is dominated by the resistance to this rotation and by locking effects. The shear response can be characterized using a shear frame apparatus, shown in Figure 2-10. In order to gain a deeper understanding of the physical mechanisms that control the response to shear, we conducted a series of cyclic shear tests. In these tests, a cruciform fabric specimen is sheared in one direction by applying a positive displacement to the top corner of the shear frame. The displacement direction is then reversed and an identical negative displacement is applied at the same rate. The process is repeated with displacements of increasing magnitude. Positive displacements correspond to larger applied rotation angles than negative displacements, due to the test kinematics. The rotation angles applied to the specimen for these tests are shown in Figure A-1 as a function of time.

The experimentally measured load-displacement curve is shown in Figure A-2. Like the monotonic shear tests described in Chapter 2 the cyclic shear test indicates that the fabric exhibits a very stiff elastic response until the load reaches some critical load corresponding to a critical moment M_c at each crossover point. At this point the response becomes far more compliant as the yarns rotate at the crossover points. This rotation is resisted primarily by friction and hence dissipates energy; it is accompanied by very little increase in stored elastic energy or load. As

locking effects begin to dominate, the load increases and the response becomes increasingly stiff. When the applied displacement is reversed, the data exhibits an abrupt drop in load, probably indicating elastic unloading of some kind. The load gradually becomes negative and reaches a load corresponding to a moment of $-M_c$ at each crossover point when the test passes through the point of zero applied displacement. This is consistent with the hypothesis that $M_c = M_0$, the moment required in the absence of locking forces to cause the yarns to rotate relative to one another at the rate at which the test is conducted. The test exhibits the same trends in the negative direction; however, the peak loads are not as large because the applied rotation angles are smaller in this direction, as is evident from Figure A-1. Interestingly, when the specimen is re-loaded in subsequent cycles, smaller loads result at given applied displacements than during previous cycles. This indicates that some component of the weave mesostructure is evolving from cycle to cycle, and that this change is not completely reversed over consecutive cycles.

A.2 Deficiency of Original Model

The original model described in Chapter 2 does not capture the cyclic shear behavior accurately, as shown in Figure A-3. It predicts the loading curves of the final cycle fairly well, but fails to capture the unloading behavior or the drop in load over subsequent cycles. The model predicts that far less energy is dissipated during the load cycles (as measured by the area enclosed by the load-displacement loops) than actually is dissipated. In order to understand why the model behaves in the way it does, we examine in detail the mechanisms included in the model that resist shear deformation, and the component constitutive relation associated with these mechanisms.

Shear deformation corresponds to relative rotation of the yarn families. A change in angle between the yarn families must be accommodated a some combination of two mechanisms, shown in Figure 2-8—either the yarns must bend in an "S"-shape between crossover points or they must rotate past one another where they cross. These two mechanisms are driven by the same applied moment. However, relative yarn rotation can also cause locking forces to increase. The total resistance to yarn rotation will be the sum of the moment that drives s-bending and rotation at the crossover point and the moment that arises from locking effects, as is shown in Figure 2-9. The S-bending mechanism is assumed to be linear elastic, according to Equation (2.17). The response to yarn rotation at the crossover points is assumed to obey a power law dissipative relation given in Equation (2.18). Locking occurs when the yarn cross sections are compacted, which was assumed to be an elastic phenomenon that could be described by Equation (2.19).

This representation of the shear resistance will exhibit the response to loading and unloading shown in Figure A-4. In the absence of locking effects, shearing the fabric causes the reaction moment to increase linearly to some critical moment M_0 corresponding to the resistance to relative yarn rotation at the appropriate rate of deformation. Once this moment is reached, the moment remains constant. When the deformation is reversed, the load immediately decreases linearly to $-M_0$, and then remain constant until the deformation is reversed again. The difference between the loading and unloading curve is $2M_0$ at all points where elastic loading and unloading do not take place. When a nonlinear elastic locking element is added, the two responses are additive and the moment increases continuously as increasing deformation is applied, but the difference between the loading and unloading curves remains $2M_0$ because the additional element is purely elastic. Subsequent cycles will always pass through the same load at the same level of displacement. This behavior is evident in the model's prediction of the cyclic shear test shown in Figure A-3.

A.3 Improved Model

The facts that the difference between any given loading and unloading curve does not remain a constant and subsequent cycles have less load at the same level of displacement indicate that there is another mode of dissipation in the fabric. We hypothesized that the additional dissipation stems from inelastic deformation of the yarn cross sections during the locking process. The yarns are composed of a large number of untwisted fibers. As the fabric is cycled to increasingly large shear angles, the yarn cross sections increasingly deformed and compacted. However, they may not elastically return to their original configuration upon the removal of load. Instead, changes in shape to the yarn cross sections may be accompanied by dissipation of energy from inter-fiber frictional effects, which would cause the yarn cross sections to deform in a manner that could be described by a viscous or visco-elastic relation. This would account for the behaviors observed in the cyclic shear tests. Once the fabric is loaded to a given shear angle, a small reduction in the applied shear angle would immediately relieve most of the locking forces, since the compacted cross sections would not immediately re-expand and maintain locking contact. The locking forces dropping rapidly would cause the total load to drop almost to zero. The net load then becomes negative as the load required to drive the dissipative element in the opposite direction exceeds any residual positive locking forces. On subsequent cycles, the cross sections still would not have returned to their original uncompacted shape, and so at the same level of deformation, locking

forces would smaller than they were during the first cycle, resulting in the observed drop in load over subsequent cycles.

Once we identify a component whose constitutive response could be causing the predicted behavior to be erroneous, the model can be modified appropriately. We modified the model to capture the features of the cyclic shear test by replacing the elastic locking truss in the unit cell model with a visco-elastic element, shown schematically in Figure A-5. As in the original model, the element has an elastic spring that represents the locking contact between the yarns, with a nonlinear constitutive response that can be described using Equation (2.19). The parameter ${}^0d$ that appears in Equation (2.19) represents the perpendicular distance between yarn centers when their cross sections first come into contact and defines the unloaded length of the locking spring. As the cross sections are inelastically compacted, ${}^0d$ will become smaller and reduce the force in the locking spring. Therefore, the spring representing locking contact is placed in series with a dissipative element whose resistance to deformation represents the resistance of the yarn cross sections to inelastic compaction.

The yarns are assumed to have oval cross sections, with a minor radius r measured through the fabric thickness and a major radius R measured in the plane of the fabric that characterize their shape in an unloaded configuration. The parameter ${}^0d$ increases with both R and r. We assume that as the yarns become inelastically compacted, R becomes smaller, and hence we characterize the unloaded cross sectional configuration and the value of ${}^0d$ with the value of R.

Experimental observations indicate that upon removal of load, the yarn cross sections will eventually return to their original shape, characterized by the major radius in the reference configuration ${}^0R$. We therefore include an elastic recovery spring element in parallel with the dissipative element. The force in this recovery spring is assumed to be proportional to the amount by which the yarn cross sections have been compacted:

$$F_{rec} = K_r(R^0 - R) \tag{A.1}$$

The new constitutive parameter K_r reflects the stiffness of the elastic recovery response, as the yarn cross section tends to return to the original configuration.

Since the yarns are composed of many fibers that interact with one another through friction, we expect that the unloaded cross sectional shape, characterized by R, cannot evolve instantaneously but rather has some viscosity that limits the rate of deformation. We assume that the rate of deformation $\dot{R}$ depends on the difference between the instantaneous locking force and the resisting recovery force. Because the yarns cross sections can only undergo a certain amount of compaction before all available free space is consumed, we limit the deformation of the cross section by the introduction of an exponential term that prevents the cross section from

compacting beyond a critical point. We arbitrarily selected the point where the cross section becomes circular: $R = r$. The model is relatively insensitive to the selection of this critical point, as long as it is physically reasonable. The evolution of the parameter R, which defines the response of the dissipative element, is:

$$\dot{R} = -A(e^{R-r} - 1)(F_L \cos\alpha - F_{rec}). \tag{A.2}$$

Here A is a new constitutive parameter that relates to the effective viscosity of the dissipative element, and F_L and α are the force carried by the locking truss and the inclination of the truss to the fabric midsurface, respectively, as described in Chapter 2. All of these material parameters can be determined by fitting the model prediction of the cyclic shear test to the experimentally measured results. The fitted material parameters imply that, in the absence of constraining locking forces, compacted yarn cross sections will return to their reference shape in a matter of tens of seconds, which is a sufficiently slow response to account for the observed phenomena.

The predictions of the modified model with evolving inelastic yarn cross sections and fitted material properties are shown in Figure A-6. Unlike the original model, the modified model captures both the large amount of energy dissipated in the loading-unloading cycles, and the drop in force at a given level of displacement over subsequent cycles. These results indicate that the additional deformation mechanisms which were implied by the cyclic shear experiments have been successfully included in the constitutive model. This highlights the flexibility of this modeling approach. Because the model is based on physically motivated components, increasingly complex behaviors are easily included simply by changing the constitutive response of the appropriate component. In this case, a purely elastic locking relation was unable to capture an observed physical behavior. Replacing this elastic component with a physically motivated visco-elastic component gave the model the ability to capture very complex physically observed phenomena with the addition of two material parameters, K_r and A.

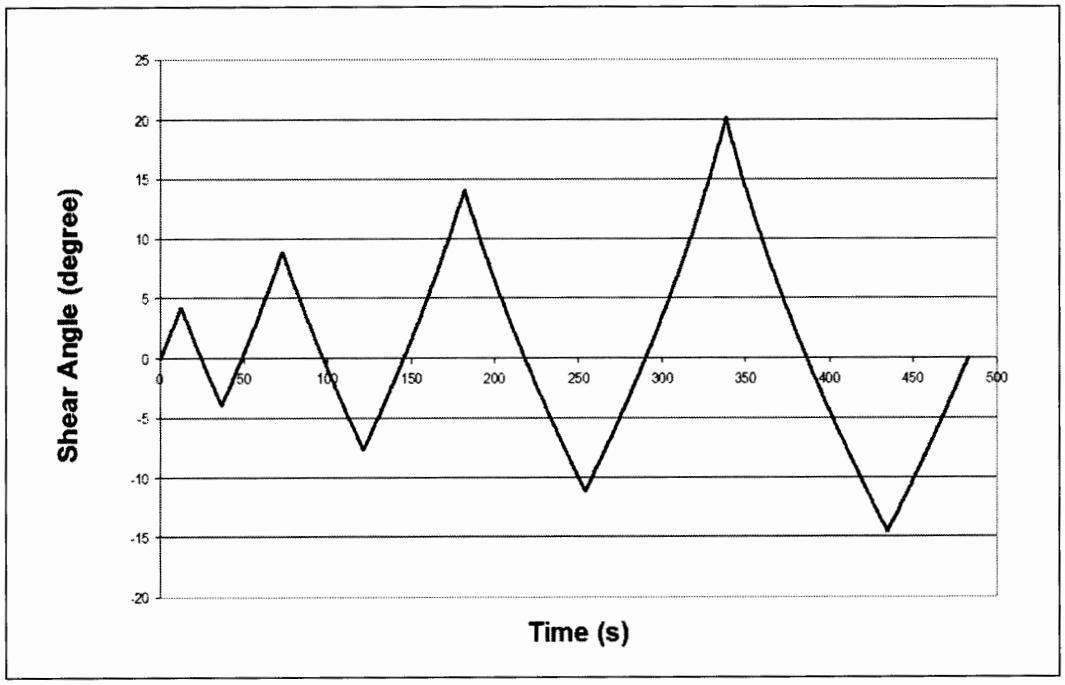

Figure A-1 Applied rotation angles in cyclic shear test

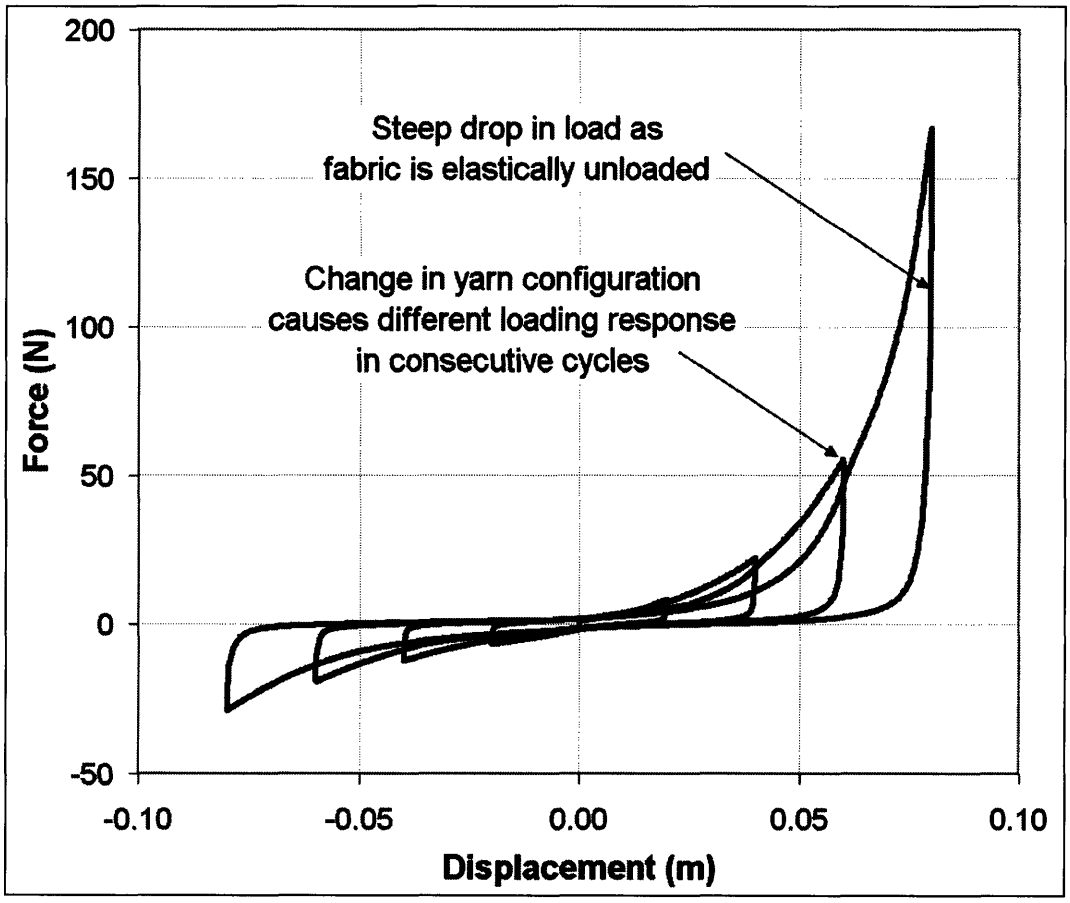

Figure A-2 Load-displacement response to cyclic shear

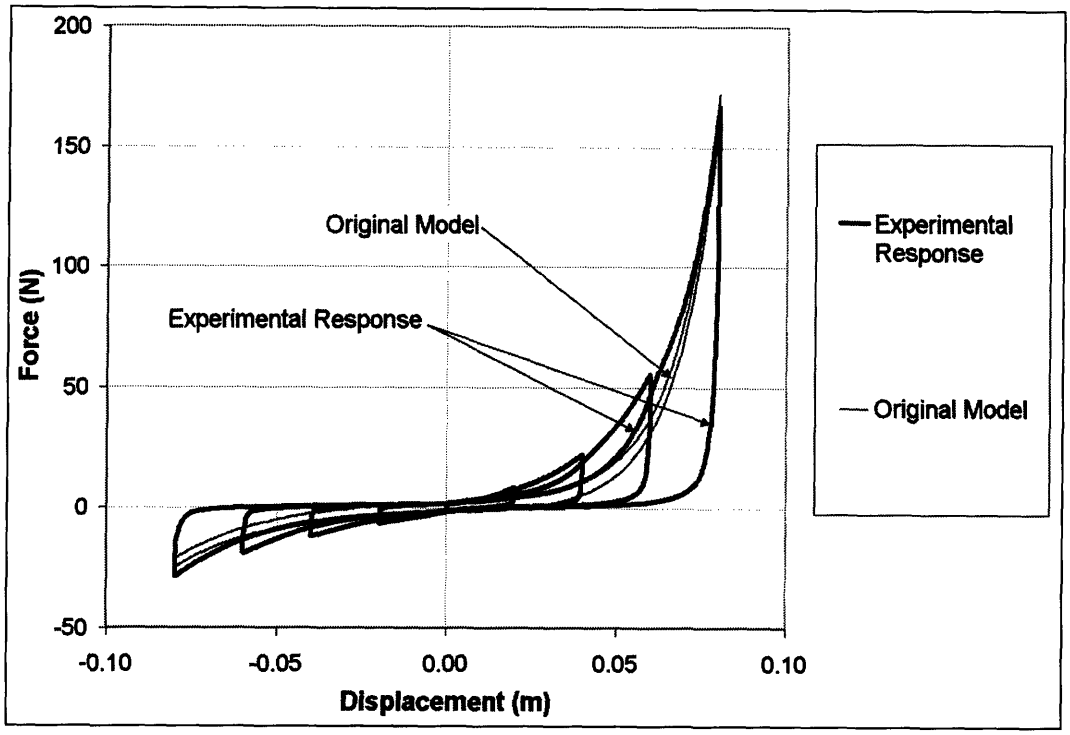

Figure A-3 Original model prediction of cyclic shear response

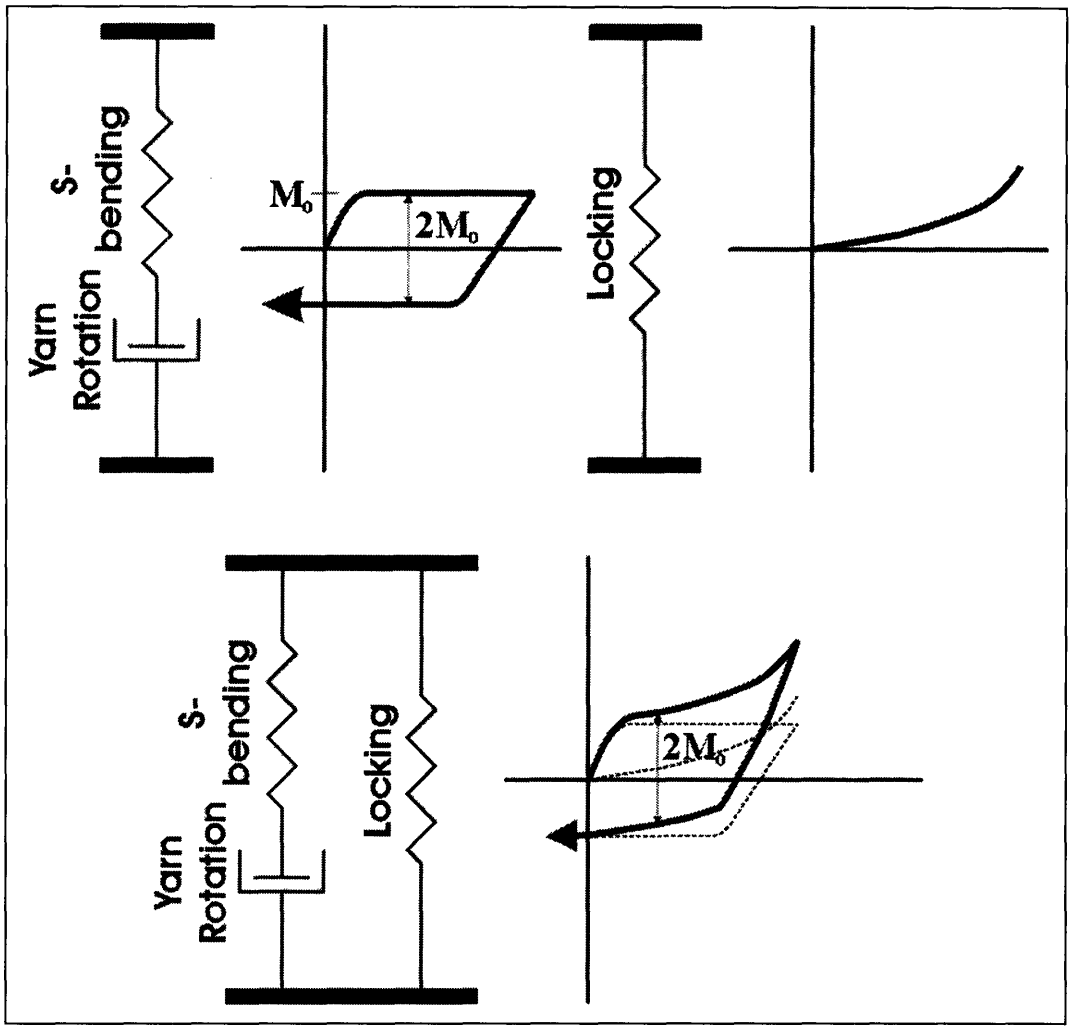

Figure A-4 Response of original model to loading and unloading

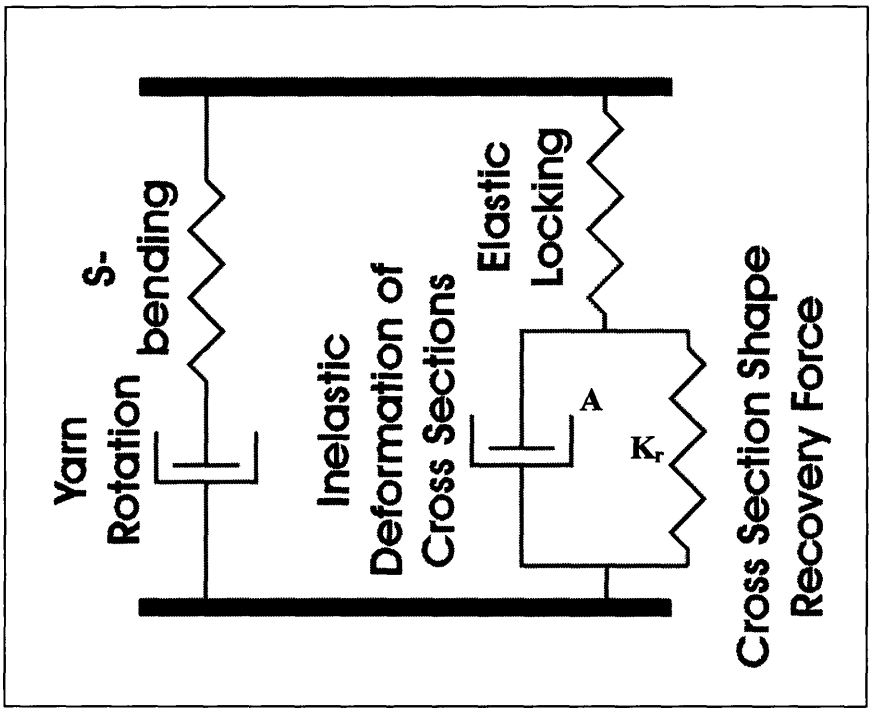

Figure A-5 Schematic of the resistances to shear deformation in the revised model, with a visco-elastic locking truss

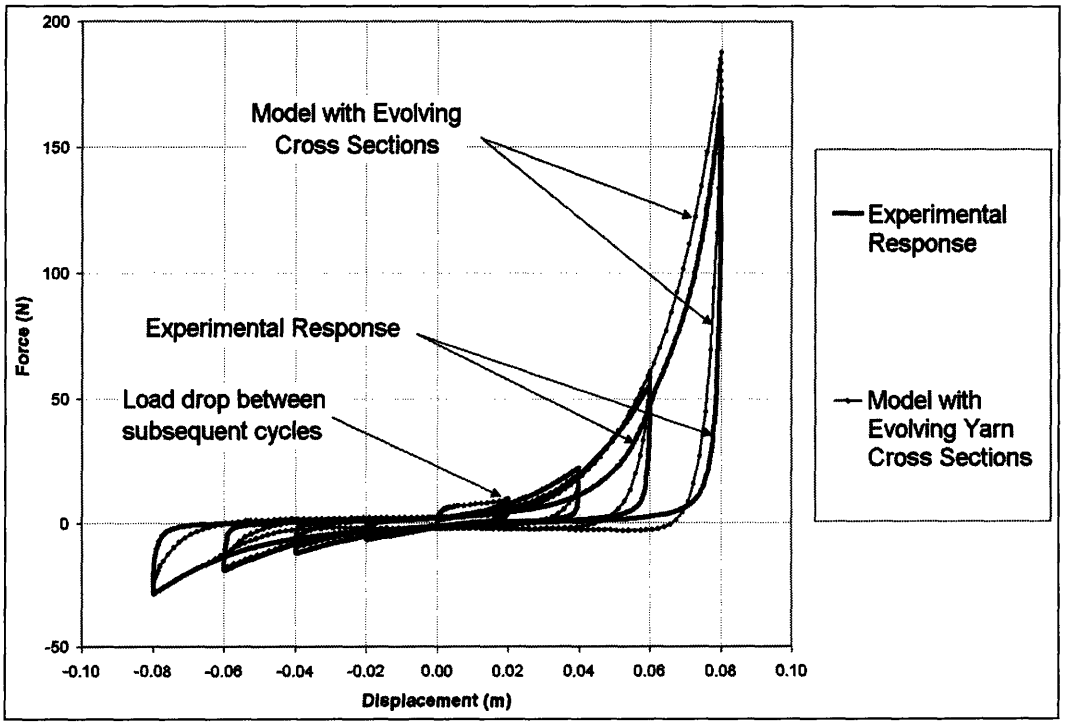

Figure A-6 Model prediction of cyclic shear response with evolving yarn cross sections

Appendix B
Reformulation of the Displacement-Based Modeling Approach with Mean Amplitude Degrees of Freedom

The slip-free model described in Chapter 2 is a displacement-based model. The macroscopic stresses and the evolution of the weave mesostructure depend only on the displacement field $\mathbf{u}(\mathbf{X})$ and on the corresponding deformation gradient $\mathbf{F}(\mathbf{X})$; when implemented into a finite element framework, the only nodal degrees of freedom are the x- and y-direction displacements u_x and u_y. In this model, the macroscopic deformation gradient $\mathbf{F}$ is used to find the corresponding configuration of the fabric unit cell at the mesostructural scale, which allowed meso-level forces and corresponding macroscopic stresses to be calculated. However, as is described in Section 2.6, the macroscopic deformation gradient alone does not explicitly determine the complete configuration of the unit cell. It describes only the in-plane stretches and shear of the unit cell; different configurations involving different yarn stretches and crimp angles are possible for the same deformation gradient. The displacement-based model described in Chapter 2 determined the unit cell configuration using an energy-based argument. Different configurations involve different amounts of elastic energy stored in the various unit-cell components (e.g. stretch of the trusses representing the yarns, compression crossover contact spring, compression of the locking trusses, etc.). The model determines the equilibrium configuration by finding the configuration with the minimum stored elastic energy, subject to the constraint that it must be compatible with the macroscopic deformation gradient.

Unfortunately, due to the complex functions describing the constitutive response of the various unit-cell components, there is no closed-form expression for the configuration giving the minimum stored elastic energy corresponding to a given deformation gradient. Therefore, this energy function had to be minimized numerically. Not only is this approach computationally expensive, but it becomes challenging when inelastic mechanisms such as yarn slip are included in the formulation. Therefore, we first re-formulate the model to use a different means of relating the mesostructural configuration to the macroscopic deformation and eliminate the energy minimization procedure.

As is described in Chapter 2 and King [2003], five independent parameters are necessary to characterize the configuration of the unit cell for the geometry that we have chosen. Three of

these parameters—the quarter-wavelengths of each yarn family p_i and the angle θ between yarn families—relate to the stretches and shear of the unit cell, and can be directly calculated from the deformation gradient $\mathbf{F}$ using Equations (2.20) and (2.21). The remaining two parameters relate to the amount of crimp in each yarn family. Either the two yarn truss lengths L_i, the two crimp amplitudes A_i, or the two crimp angles β_i can be used as the remaining two parameters that are necessary to completely determine the configuration of the unit cell. In the model described in Chapter 2, we chose the lengths L_i to be the free parameters; for the new formulation, it is mathematically more convenient to use the crimp amplitudes A_i.

We eliminate the need for energy minimization by introducing two additional field variables $\Delta A_i(\mathbf{X})$ at the macroscopic scale, which represent the change in the crimp amplitudes relative to the reference configuration. Hence the model degrees of freedom will include not only the displacements $\mathbf{u}$ but also the fabric crimp amplitudes ΔA_i. Rather than try to locally determine the values of A_i that correspond to a given deformation gradient $\mathbf{F}$ using energy minimization techniques, the mesostructural evolution and macroscopic stresses can be directly expressed as functions of the global fields $\mathbf{F}(\mathbf{X})$, $\Delta A_1(\mathbf{X})$, and $\Delta A_2(\mathbf{X})$. At any given point, if $\mathbf{F}$, ΔA_1, and ΔA_2 are known, the mesostructural configuration can be completely determined without locally minimizing a conditional energy function.

For every unknown field, there must be an equation that allows that field to be determined. In the displacement-based formulation, as in most two-dimensional finite element formulations, in-plane macroscopic equilibrium provides the two equations that allow the calculation of the two-dimensional displacement field. Equilibrium (in the absence of body forces) can be expressed in local, or strong form, as:

$$\begin{aligned} \frac{\partial}{\partial X_1} P_{11}(\mathbf{F}) + \frac{\partial}{\partial X_2} P_{12}(\mathbf{F}) = 0 \\ \frac{\partial}{\partial X_2} P_{21}(\mathbf{F}) + \frac{\partial}{\partial X_2} P_{22}(\mathbf{F}) = 0 \end{aligned} \quad . \tag{B.1}$$

The quantities P_{jK} are the components of the first Piola-Kirchhoff stress $\mathbf{P} = J\boldsymbol{\sigma}\mathbf{F}^{-1}$, where $\boldsymbol{\sigma}$ is the Cauchy stress and $J = \det(\mathbf{F})$. In integral or weak, equilibrium can be expressed as:

$$\int_{\Omega_0} \overline{\mathbf{F}} \cdot \mathbf{P}(\mathbf{F}) dV - \overline{W}^{ext} = 0, \tag{B.2}$$

where $\overline{\mathbf{F}}$ is the deformation gradient that corresponds to an arbitrary admissible virtual displacement field, $\overline{W}^{ext}$ is the external virtual work of boundary loads acting through the virtual displacements, and Ω_0 is the volume occupied by a body in the reference configuration. Given a

finite element discretization of Ω_0, the corresponding finite element equations can be calculated from the weak form equation. However, in the new formulation, the stress **P** now depends on ΔA_1 and ΔA_2 as well as on **F**, and hence two additional equations are necessary.

To determine the additional equations necessary to calculate these fields, we note that the state with the minimum stored elastic energy that we determined in Chapter 2 is the state at which the forces from the various components within the unit cell are internally in equilibrium with one another. Hence, in the desired state, local equilibrium equations at each end of the crossover spring must hold:

$$F_I = F_i^N . \tag{B.3}$$

Here F_I is the axial force carried by the crossover spring (positive when the spring is in compression), and F_i^N is the net through-thickness force applied to the end of the crossover spring from the yarn trusses (positive when acting inwards towards the fabric midplane). F_I is calculated from an appropriate constitutive relation and depends on the deformed length of the crossover contact spring, and hence can be determined from ΔA_1 and ΔA_2. F_i^N has dependencies on the tension carried by the yarns, the moments from the bending springs, and the forces from the locking spars:

$$F_i^N = 2T_i \sin\beta_i - 2F_{Lj}\sin\alpha_j\left(1+\frac{p_j|\cos\theta|\cos\beta_i}{L_i}\right)+2\left(\frac{k_{bi}\left(\beta_i-{}^0\beta_i\right)+M_{si}}{L_i}\right)\cos\beta_i . \tag{B.4}$$

For a yarn family i, T_i is the tension carried by the yarn truss of that family, F_{Lj} is the compressive force carried by the locking truss associated with the other yarn family, α_j is the angle which that locking truss makes with the fabric midplane, k_{bi} is the stiffness of the bending spring, and M_{si} is a small stabilizing moment that is added to the model to provide numerical stability, as described in Section 2.8. However, all these parameters can be directly determined if the configuration of the unit cell is known, and so F_i^N can be expressed as a function of **F**, ΔA_1, and ΔA_2.

Small virtual displacements of the ends of the crossover contact spring must do zero virtual work in the equilibrium state. We therefore multiply Equation (B.3) by virtual fields $\overline{\Delta A_i}$ and integrate over the body to convert the local equilibrium equations into integral or weak form equations:

$$\int_{\Omega_0}\overline{\Delta A_i}\left[F_I\left(\Delta A_1,\Delta A_2\right)-F_i^N\left(\mathbf{F},\Delta A_1,\Delta A_2\right)\right]dV = 0 . \tag{B.5}$$

These are the additional two equations (one for each yarn family i) necessary to solve for the two additional fields.

The fields ΔA_1 and ΔA_2 represent only one possible choice for the additional fields. Another convenient choice of fields with important physical significance is:

$$\begin{aligned} \widetilde{A} &\equiv \frac{\Delta A_1 - \Delta A_2}{2} \\ I &\equiv \Delta A_1 + \Delta A_2 \end{aligned} . \tag{B.6}$$

The parameter $\widetilde{A}$ gives the mean change in the crimp amplitude, which we subsequently refer to as the "mean amplitude". It can be used to quantify the total amount of crimp that one yarn family gained at the expense of the other yarn family. The negative sign appears because positive ΔA_1 and ΔA_2 values imply motion in opposite directions within the same unit cell. The parameter I give the total change in length of the crossover spring.

Adding the two equations given by Equation (B.5) together, substituting in these parameters, and re-arranging terms gives a different weak form equation:

$$\int_{\Omega_0} \left\{ \overline{\widetilde{A}} \left[F_2^N\left(\mathbf{F}, \widetilde{A}, I\right) - F_1^N\left(\mathbf{F}, \widetilde{A}, I\right) \right] + \bar{I} \left[F_I(I) - \frac{F_1^N\left(\mathbf{F}, \widetilde{A}, I\right) + F_2^N\left(\mathbf{F}, \widetilde{A}, I\right)}{2} \right] \right\} dV = 0 . \tag{B.7}$$

Because the virtual fields $\overline{\widetilde{A}}$ and $\bar{I}$ are arbitrary, they can be varied independently, and hence both terms enclosed in square brackets the above equation must be zero, yielding two equivalent strong or local form equations:

$$\begin{aligned} F_2^N &= F_1^N \\ F_I &= \frac{F_1^N + F_2^N}{2} \end{aligned} . \tag{B.8}$$

In other words, the local equilibrium equations that correspond to this choice of field parameters require that the through thickness forces associated with each yarn family must equate (i.e. equilibrium through the fabric thickness must be satisfied), and the force carried by the crossover contact spring must equal the average of the through thickness forces associated with each yarn family.

For many fabrics the yarns are sufficiently resistant to compaction that the crossover contact spring is orders of magnitude stiffer than any other unit cell components in compression. (When in tension the crossover spring is modeled as having near-zero stiffness, allowing the yarns to lose contact with one another. However, in all practical cases a fabric is loaded in tension, which corresponds to compression of the crossover spring, and hence this case does not generally arise). When the crossover contact spring is very stiff, the parameter I will be very small compared to ΔA_i and $\widetilde{A}$. In such cases, we can simplify the model and reduce computational costs by taking

the crossover contact spring to be inextensible, so $I = 0$. In this case, $\Delta A_1 = -\Delta A_2$ and F_1 can no longer be calculated from a component constitutive relation; it must be determined from F_1^N and F_2^N according to Equation (B.8). Since $I = 0$, any nonzero virtual $\bar{I}$ becomes inadmissible and the second half of Equation (B.7) vanishes. The problem is reduced to only one additional field variable, the mean amplitude $\tilde{A}$, and is characterized by the following equations in strong form:

$$\begin{aligned} &\frac{\partial}{\partial X_1} P_{11}\left(\mathbf{F}, \tilde{A}\right) + \frac{\partial}{\partial X_2} P_{12}\left(\mathbf{F}, \tilde{A}\right) = 0 \\ &\frac{\partial}{\partial X_2} P_{21}\left(\mathbf{F}, \tilde{A}\right) + \frac{\partial}{\partial X_2} P_{22}\left(\mathbf{F}, \tilde{A}\right) = 0, \\ &F_2^N\left(\mathbf{F}, \tilde{A}\right) - F_1^N\left(\mathbf{F}, \tilde{A}\right) = 0 \end{aligned} \tag{B.9}$$

and in weak form:

$$\begin{aligned} &\int_{\Omega_0} \bar{\mathbf{F}} \cdot \mathbf{P}\left(\mathbf{F}, \tilde{A}\right) dV - \bar{W}^{ext} = 0 \\ &\int_{\Omega_0} \bar{\tilde{A}}\left[F_2^N\left(\mathbf{F}, \tilde{A}\right) - F_1^N\left(\mathbf{F}, \tilde{A}\right)\right] dV = 0 \end{aligned} \tag{B.10}$$

This approach eliminates the energy minimization process, since the field variables $\mathbf{F}$ and $\tilde{A}$ now explicitly describe the complete configuration of the unit cell. The extra field variable is calculated by enforcing local through-thickness equilibrium at the macroscopic scale in addition to macroscopic in-plane equilibrium at every point. In this formulation we do not allow for the yarns to lose contact at the crossover point (since we assume $I=0$), but in cases where this phenomenon may be important, we can use the more complex weak from given in Equation (B.7).

Of course, a suitable discretization and interpolation scheme must be introduced to solve the additional weak form equation. For simplicity, we use the same finite element discretization and interpolation scheme that is used for $\mathbf{u}$. We assume that the field $\tilde{A}$ can be represented by a continuous bilinear or biquadratic interpolation of nodal values $\tilde{A}_a$ at each node a. Such interpolation functions are described in Bathe [1996].

The admissible values of the $\tilde{A}$ field are limited, because the crimp amplitude and crimp angle of either yarn family cannot become negative, since this would imply that the yarns were inverting in the weave. This limit is imposed numerically through the use of a scaling function:

$$\tilde{A} = \begin{cases} \tan^{-1}\left(\dfrac{\pi \tilde{A}^D}{2\ {}^0A_2}\right)\dfrac{2\ {}^0A_2}{\pi} & \tilde{A}^D \geq 0 \\ \tan^{-1}\left(\dfrac{\pi \tilde{A}^D}{2\ {}^0A_1}\right)\dfrac{2\ {}^0A_1}{\pi} & \tilde{A}^D < 0 \end{cases} . \tag{B.11}$$

Any value for the mean amplitude degree of freedom $\tilde{A}^D$ that is calculated at a given integration point is passed through this function to calculate the actual value $\tilde{A}$ that is applied in the material law. When $\tilde{A}$ is near zero, $\tilde{A}$ and $\tilde{A}^D$ will be approximately equal. As $\tilde{A}^D$ approaches positive or negative infinity, $\tilde{A}$ will approach the limiting values ${}^0A_2$ or ${}^0A_1$, respectively. This allows the mean amplitude degree of freedom to have any real value, which is necessary because the Newton-Rhapson algorithm used by implicit finite element codes may guess inadmissible values for this degree of freedom that lie outside the bounds.

We experimented with other numerical methods of preventing the Newton-Rhapson algorithm from guessing inadmissible values for the mean amplitude, including reduction of the time step when such values were guessed or creating a "hard stop" that applies arbitrarily large forces to prevent either family from becoming completely flat. All these methods worked equally well in most cases. In extreme cases, where one yarn family carried a large tension and the other carried very small tensions, the scaling function method proved most effective. However, even this method encountered problems in very extreme cases. As one yarn family becomes flat and its crimp amplitude and crimp angle approach zero, two effects occur. First, the calculated through-thickness force and corresponding stiffness terms associated with this yarn family become inaccurate, because numerical inaccuracies are introduced when the large tensions are multiplied by the sine of the very small crimp angles. However, the sensitivity of the through thickness force to changes in $\tilde{A}^D$ as $\tilde{A}^D$ increases in magnitude becomes small, since large variations in $\tilde{A}^D$ correspond to increasingly small variations in $\tilde{A}$. As the highly-tensioned yarns become increasingly flattened, the stiffness terms relating the through-thickness force residual to variations in the mean amplitude become very small and the stiffness matrix becomes ill conditioned.

Convergence problems in the Newton-Rhapson implicit scheme result from both these effects. For example, in regions of the plain weave Kevlar® model where one yarn family carries tensions in excess of approximately 150 N and the other yarn family carries near zero tensions, the solution begins to diverge and zero-pivot problems are sometimes reported by the analysis code, which are indicative of an inaccurate or ill-conditioned stiffness matrix. Since this generally

only occurs when tensions exceed the breaking strength of the Kevlar® yarns (approximately 100 N), more advanced methods to eliminate this problem were not investigated.

Appendix C
Numerical Locking in Fabrics

C.1 Locking-like Behavior in Strip Tests

Early in the modeling process, we noted a troublesome response predicted by the fabric material model in certain load cases. The finite elements would predict that the yarn tensions, and hence the stresses, would vary in a non-physical oscillatory manner that depended on the finite element mesh and the elements formulation used. Examples of these tension oscillations are shown in Figure C-1. These oscillations manifest in load cases with non-uniform strains, and they are most significant in cases where deformation is primarily accommodated through crimp interchange. The oscillations are a result of small oscillatory errors in the tension values (and hence in the stress) calculated at the integration points. In cases where the elements have three integration points along a given dimension, the extremal points would develop error in one direction and the central point would develop error in the opposite direction. In cases where there were only two integration points per dimension, they would develop errors in opposite directions. Although the magnitudes of these errors tend to be small compared to the actual tension values, especially when the tensions become large, the errors do not vanish as the mesh is refined. Reduced integration bilinear elements have only a single integration point and inherently assume constant tension (and stress) over the element; hence such elements do not exhibit oscillations.

In addition to the oscillatory tensions and stresses, equivalent meshes composed of elements with different formulations require different amounts of energy to be deformed to the same configuration, as shown in Figure C-1. Although lower order elements generally are stiffer than higher order elements, we noted that, in general, the elements that exhibited the most severe tension oscillations required the largest amount of energy to deform. The reduced integration bilinear elements, which cannot exhibit oscillations, require hourglass stiffness to control spurious hourglassing modes, but when the additional energy lost to this hourglass control is subtracted, these elements required the smallest amount of energy to deform. The differences in energy to deform the elements appear to be related to the tension oscillations.

This behavior resembles a well known phenomenon that occurs when fully integrated displacement-based elements are used to model incompressible or nearly incompressible materials. In such cases, the element predictions become inaccurate. Element stiffnesses become

artificially large as the bulk modulus increases, and the elements predict increasingly discontinuous, often oscillatory stress contours. This phenomenon is commonly referred to as numeric "locking" of the element, not to be confused with the "locking" phenomenon in fabrics that results when yarns cross sections jam against one another. The numerical locking problem associated with nearly incompressible materials develops when the stiffness associated with changes in volume is significantly larger (i.e. by several orders of magnitude) than the stiffness associated with isochoric deformations. Purely isochoric deformations result in relatively small stresses. However, small variations of the nodal displacements cause small variations in the volumetric strains, which result in large variations in the stresses, because the volumetric component of the stress becomes large. Consequently, the elements become artificially stiff, since small variations in the nodal displacements result in very large nodal forces, unless the strain variations that result from the nodal displacement variations happen to be purely isochoric.

Fabrics are not incompressible. They typically can undergo significant volume changes (assuming constant thickness) under very little applied load. The crimp interchange process is not volume conservative—the effective Poisson's ratio associated with this mechanism varies but is significantly less than 0.5, and approaches zero as one yarn family becomes completely straightened. The trellising process by which fabrics accommodate in plane shear also results in significant changes in volume, despite the fact that stresses generally remain small until the fabric jams. However, like a nearly incompressible material, certain modes of fabric deformation are orders of magnitude stiffer than other modes, especially for fabrics woven from a high-stiffness material such as Kevlar®. Because the tensile modulus of the yarns is so large, any mode of deformation that requires the yarns of either family to be stretched is much stiffer than any mode that can be accommodated by crimp interchange or by trellising. Any mode of deformation that is accommodated purely through these low-stiffness mechanisms will result in relatively small stresses. However, small variations of the nodal displacements result in deformation modes that cannot be accommodated purely through crimp interchange and trellising, and hence cause the yarns to become stretched. This results in large tensions and large stresses. Therefore, the elements will lock in a manner similar to that which afflicts nearly incompressible materials. If the yarn stiffnesses are reduced or the bending and trellising stiffnesses are increased so that the various deformation modes have similar stiffnesses, the numeric locking problem vanishes.

This explanation accounts for the oscillations in the tensions field. The oscillations occur when non-uniform strain fields are applied to the fabric, and are only significant compared to the actual tension magnitudes in cases where deformation is accommodated primarily through trellising and crimp interchange. Consider the case shown in Figure C-2. A strip of elements is

subjected to small, linearly increasing y-direction displacements, which impose a linearly varying axial strain field. X-direction displacements and hence transverse strains are unconstrained. As long as transverse strains are unconstrained and axial strains are small, the deformation can be accommodated purely by crimp interchange—no yarn stretch is necessary. However, the relationship between the imposed axial strain and the transverse strain that corresponds to no transverse yarn stretch is nonlinear, as is shown in Figure C-3. Even when axial strains that vary linearly across an element are imposed, the transverse strains that correspond to a pure crimp interchange deformation mode will vary nonlinearly across the element. Neither displacement-based elements with bilinear nor with biquadratic interpolation schemes can accommodate this nonlinear variation exactly. Consequently, no set of nodal displacements can yield a state of deformation that can be accommodated purely by crimp interchange at all integration points simultaneously. As is shown in Figure C-3, small deviations from the optimal strains will be present at every integration point. Because small variations in the strains away from a pure crimp interchange deformation mode result in yarn stretch, corresponding errors in the tension and stress will develop at the integration points. Because the stiffness associated with yarn stretch is so much larger than that associated with crimp interchange, the tension and stress errors will be significant compared to the tensions and stresses that develop in the physical case. The modes that minimize the tension errors, integrated over each element, involve the oscillatory tension fields that are evident in Figure C-1 and Figure C-2. When macroscopic modes of deformation that require yarn stretch are imposed, such as uniaxial extension to large strains or biaxial extension, the physical yarn tensions become large compared to the tension errors that develop in the model, and the locking problem becomes unimportant.

There are two methods commonly used to eliminate numerical locking problems in nearly incompressible materials—the use of reduced-integration elements and the use of hybrid elements. We investigated both methods and developed element formulations that did reduce or eliminate the observed locking errors in the tensions. A reduced-integration displacement-based biquadratic element with only four integration points greatly reduces the locking errors, and a bilinear element with only a single integration point eliminates them. Alternatively, the locking errors can be eliminated through the use of a hybrid element where the stress is calculated from tension fields as well as displacement fields, and where the tension fields are determined by introducing an additional equation to the finite element formulation that is derived from the constitutive law. Unfortunately, both of these formulations exhibited unacceptable spurious modes that led to non-physical displacement or tension fields in certain specific situations. These modes could not be eliminated without making convergence impossible or without re-introducing

the locking problem, because in certain situations the formulations that eliminate locking have no solution that satisfies all equilibrium equations without these spurious modes.

C.2 Reduced Integration Elements

To illustrate the spurious modes that develop for the reduced-integration elements, consider the test case shown in Figure C-4. The bottom edge of a unit square of material is constrained in the vertical direction. All horizontal displacements are unconstrained (except for one, to prevent rigid body motion). A vertical displacement δ is applied to one of the top corners of the square. Similar cases arise any time an abrupt change in boundary condition is applied along an edge; for example, in simulations of yarn pullout tests described in Sections 4.3 and 7.3, or of the slit-damage tests described in Sections 2.11 and 7.4. The exact solution for this test case is shown in Figure C-4, where the curvature of the deformed top edge depends on the ratio of the shear stiffness and the axial stiffness of the material. For a fabric, which has a relatively small shear stiffness, the vertical displacement of the top edge will decay very rapidly. To illustrate how the spurious modes develop, we choose a very simple material model with no coupling between the x- and y-direction behavior:

$$\begin{aligned} \sigma_{xx} &= K_{xx}\varepsilon_{xx} \\ \sigma_{yy} &= K_{yy}\varepsilon_{yy} \\ \sigma_{xy} &= K_{xy}\gamma_{xy} \end{aligned} \quad . \tag{C.1}$$

This material model might represent a composite with two families of non-interwoven fibers oriented parallel to the x- and y-directions, and some sort of interaction (from a matrix or from bonding where the fibers cross) that imparts shear resistance. This is very similar to a fabric material model, except that it excludes crimp interchange, yarn bending, fabric locking, and dissipative yarn rotation effects, all of which have relatively low stiffnesses associated with them.

If a single fully-integrated displacement-based bilinear element with four nodes is used to model the square of material in Figure C-4, it can be shown that the vertical displacement of the unconstrained top corner, δ_f, will be:

$$\delta_f = \frac{K_{xy} - 2K_{yy}}{K_{xy} + 4K_{yy}}\delta \, . \tag{C.2}$$

For a fabric, $K_{xy} << K_{yy}$, and as $K_{xy}/K_{yy} \rightarrow 0$, the solution will approach $\delta_f \rightarrow -\delta/2$. This implies that the first few elements adjacent to an abrupt boundary condition change may adopt a "bow-

tie" shape shown in Figure C-5 as the vertical displacements oscillate, but since $|\delta_f| < |\delta|$, the oscillatory displacements will decay, and as the mesh is refined, the finite element solution will approach the exact solution. This can also be shown for a fully-integrated displacement-based biquadratic element with eight nodes. In this case, as $K_{xy}/K_{yy} \rightarrow 0$, the vertical displacements δ_f, δ_c, δ_{sL}, and δ_{sR} of the nodes at the free corner, the center of the top edge, the center of the left edge, and the center of the right edge, respectively, approach:

$$\begin{Bmatrix} \delta_f \\ \delta_c \\ \delta_{sL} \\ \delta_{sR} \end{Bmatrix} \rightarrow \begin{Bmatrix} 0.323 \\ -0.165 \\ 0.5 \\ 0.162 \end{Bmatrix} \delta, \tag{C.3}$$

so the single element solution will take the shape shown in Figure C-6. Again, because the displacements are all smaller in magnitude than δ, they will decay over multiple elements and as the mesh is refined this solution will also approach the exact solution.

This is not the case for reduced-integration elements. For example, a reduced-integration displacement-based biquadratic element will take the following shape as $K_{xy}/K_{yy} \rightarrow 0$:

$$\begin{Bmatrix} \delta_f \\ \delta_c \\ \delta_{sL} \\ \delta_{sR} \end{Bmatrix} \rightarrow \begin{Bmatrix} 1 \\ -0.5 \\ 0.5 \\ 0.5 \end{Bmatrix} \delta. \tag{C.4}$$

This shape is shown in Figure C-7. In this configuration, σ_{yy} is nonzero at various locations throughout the element, but is exactly zero at the four integration points. Therefore, there will be no y-direction reaction forces at any of the nodes and the element can assume this deformed shape with no energy cost. It is therefore a spurious mode. Similarly, a reduced-integration displacement-based bilinear element can adopt a configuration where $\delta_f \rightarrow -\delta$ as $K_{xy}/K_{yy} \rightarrow 0$. In this configuration, σ_{yy} happens to be zero at the single integration point at the element center, and hence there are no reaction forces at the nodes. Because the displacements of the free corner node are equal in magnitude to the displacement of the constrained node for these elements, the displacement oscillations will not decay over multiple elements and the solution will not converge to the exact solution as the mesh is refined.

Of course, in a real fabric K_{xy} is nonzero, and there is also some coupling between x- and y-direction deformation through the crimp interchange effect. These mechanisms will impart some stiffness to the spurious modes. However, these phenomena have very small stiffnesses associated with them compared to the stiffness of the fabric parallel to the yarns. Consequently, reduced-integration fabric elements will tend to adopt the spurious modes to exploit the smaller energy costs. The stiffness of the elements will be severely underestimated, and the non-decaying displacement oscillations will result in unrealistic displacement predictions. This may account for the smaller stiffness associated with reduced integration elements shown in Figure C-1. The spurious modes and unrealistic oscillating displacement fields were evident when reduced integration elements were used to simulate the fabric behavior in both the slit-damage test and the yarn-pullout tests.

C.3 Hybrid Elements

The second method commonly used to eliminating numeric locking errors is the use of hybrid elements. For nearly incompressible materials, the stress is separated into hydrostatic and deviatoric components:

$$\begin{aligned} \boldsymbol{\sigma} &= \boldsymbol{\sigma}^{dev} + \boldsymbol{\sigma}^{h} \\ &= \boldsymbol{\sigma}^{dev} - p\mathbf{1} \end{aligned} \quad . \tag{C.5}$$

The hydrostatic stress (the negative pressure), is introduced as an additional solution field that is interpolated over each element from pressure degrees of freedom. In order to solve for this additional field, the hydrostatic constitutive law is introduced into the finite element formulation. For materials with a linear hydrostatic response to small volumetric strains, the pressure is given by:

$$p = -\kappa \varepsilon_V \,, \tag{C.6}$$

where ε_V is the volumetric strain and is calculated from the deformation gradient $\mathbf{F}$ according to:

$$\varepsilon_V \equiv \det \mathbf{F} - 1 \,. \tag{C.7}$$

For a nearly incompressible material, $\kappa \to \infty$, so the hydrostatic constitutive law is introduced to the finite element formulation in a weak form that remains well defined as the bulk modulus κ becomes arbitrarily large:

$$\int \overline{p} \left(\frac{p}{\kappa} + \varepsilon_V \right) dV = 0 \,, \tag{C.8}$$

Here $\overline{p}$ is an arbitrary admissible test function that is interpolated in the same manner as p. This

expression is enforced along with the equilibrium expressions, and the stress at any point is calculated by adding the interpolated pressure p to the deviatoric stress σ^{dev} calculated from the isochoric component of the deformation. As the bulk modulus becomes large, this formulation does not predict large variations in stress resulting from small, non-isochoric variations in the displacement field. Instead, it enforces the constraint that the volumetric strain should approach zero. It therefore eliminates the locking problem, provided that a suitable interpolation scheme is used for p.

A great deal of work has been devoted to deriving criteria that determine whether a given element formulation that uses various interpolation schemes for displacement and pressure will lock. Unfortunately, the bulk of this work pertains only to linear elastic material laws and small strain analyses. For nonlinear, finite strain analyses, numerical experimentation with different formulations is the only method currently available for determining if a given hybrid formulation will prevent locking. For more information about hybrid elements used to eliminate locking, refer to a finite element text such as Bathe [1998].

We followed a similar approach to develop a hybrid element to eliminate the numeric locking problem in our fabric elements. Numeric locking in fabrics occurs because the fabrics are nearly inextensible along the yarn family directions (when crimp interchange is not permitted) rather than nearly incompressible. Therefore, the stress is not separated into hydrostatic and deviatoric components, but rather into components that stem from yarn stretch, and components that stem from all other mechanisms:

$$\begin{aligned}\boldsymbol{\sigma} &= \boldsymbol{\sigma}^{T_1} + \boldsymbol{\sigma}^{T_2} + \boldsymbol{\sigma}^{other} \\ &= \hat{\boldsymbol{\sigma}}_1(T_1, \mathbf{F}) + \hat{\boldsymbol{\sigma}}_2(T_2, \mathbf{F}) + \boldsymbol{\sigma}_0\left(\mathbf{F}, \tilde{A}\right).\end{aligned} \tag{C.9}$$

We use the alternative formulation described in Appendix B, where the fabric configuration depends not only on the deformation gradient $\mathbf{F}$ but also on the mean amplitude $\tilde{A}$, which is interpolated from mean amplitude degrees of freedom and solved for by enforcing through-thickness equilibrium. This eliminates the need for minimizing the conditional energy to determine the fabric configuration, which is described in Chapter 2 and in King [2003], and allows the configuration to be determined directly and the stress to be decomposed. $\boldsymbol{\sigma}^{Ti}$ gives the component of stress that depends on the tension in yarn family i, which generally acts in the $\mathbf{g}_i \otimes \mathbf{g}_i$ direction. $\boldsymbol{\sigma}^{other}$ includes all other components of stress, including stress from yarn bending effects, jamming effects, and yarn rotation effects. Components of $\boldsymbol{\sigma}^{other}$ may act in any direction.

We introduce T_1 and T_2 as fields that are interpolated from tension degrees of freedom. Note that, unlike the "informational" tension degrees of freedom described in Section 6.2, these tension

degrees of freedom are "actual" degrees of freedom used to calculate the stress. The tension degrees of freedom are solved for by introducing constitutive laws in weak form into the finite element formulation. For linear elastic yarn behavior, the weak form constitutive laws are:

$$\int \overline{T}\left(\frac{T_i}{k_i} - \left(\hat{L}_i\left(\mathbf{F}, \widetilde{A}\right) - \ell_i\right)\right) dV = 0, \tag{C.10}$$

where $\overline{T}$ is an arbitrary admissible test function interpolated in the same manner as T_i; k_i is the stiffness of the yarn; L_i is the length of the stretched yarn in the deformed configuration, which depends on the deformation gradient $\mathbf{F}$ and the mean amplitude $\widetilde{A}$; and ℓ_i is the unstretched length of the yarn, which is equal to ${}^0L_i$ for the slip-free model. As the yarns become increasingly stiff and k_i becomes arbitrarily large, this formulation does not predict large variations of stress resulting from small variations in the displacement field that cause the yarns to be stretched. Instead, the formulation enforces a constraint that the yarns become inextensible. It therefore has the potential to eliminate the numeric locking problem, provided that suitable interpolation schemes are used for displacement and tension.

In general, interpolation schemes that successfully eliminate locking for nearly incompressible materials are schemes where pressure is interpolated using lower order polynomials than those used to interpolate displacement. For example, biquadratic displacement elements with discontinuous linearly interpolated pressures or with continuous bilinearly interpolated pressures are effective elements. We therefore considered similar element formulations for the hybrid fabric elements. We identified three elements in particular that appeared to eliminate the numerical locking problem. The first two were biquadratic displacement elements with nine displacement nodes and either discontinuous linear tension interpolation with three tension degrees of freedom per yarn family or continuous tension interpolation using the linear chordal interpolation scheme described in Appendix D. The second was a bicubic displacement element with twelve displacement nodes on the element edges and continuous tension interpolation using a quadratic chordal interpolation scheme.

Unfortunately, these elements also suffered from spurious modes and predicted unrealistic displacement and tension fields. We first consider the elements with biquadratic displacement interpolation and either discontinuous linear tension interpolation or continuous linear chordal interpolation. Both these formulations allow only linear tension variations across an element. Consider again the case shown in Figure C-4 and the following simple material law:

$$\begin{aligned} \sigma_{xx} &= K_{xx}\varepsilon_{xx} \\ \sigma_{yy} &= T \\ \sigma_{xx} &= K_{xy}\gamma_{xy} \end{aligned} \quad , \tag{C.11}$$

where T is the interpolated value of a tension field that describes the tension per unit width carried by fibers aligned in the y-direction, and can be solved for by enforcing the following weak form equation:

$$\int \overline{T}\left(\frac{T}{K_{yy}} - \varepsilon_{yy}\right) dV = 0 . \tag{C.12}$$

In the limiting case where K_{xy} is small compared to K_{yy}, the y-direction nodal forces will depend only on the tension distribution T. However, it can be shown that the only linear tension distribution that can simultaneously provide zero force residuals at all nodes for the applied tractions is one where $T = 0$ everywhere, as shown in Figure C-8, since the y-direction nodal forces must be zero both at the free corner and at the free nodes at the centers of the top and side edges. Therefore, the formulations that use linear tension distributions and biquadratic displacement interpolation must predict zero tension throughout the element in order to satisfy equilibrium. This is unrealistic because it implies that the y-direction nodal force is also zero at the constrained corner node—in other words, that it requires no force to deform the element. Uniformly zero tension does satisfy equilibrium (although unrealistically), but it must also be consistent with the displacement field according to the constitutive law integrated over the element given in Equation (C.12). For a biquadratic displacement field with nine nodes, there is a solution that satisfied this equation and results in $\varepsilon_{yy} = 0$ when averaged over the nine integration points:

$$\begin{aligned} \delta_f &= \delta \\ \delta_c &= \frac{-\delta}{2} \\ \delta_{sL} + \delta_{sR} + 4\delta_m &= 0 \end{aligned} \quad . \tag{C.13}$$

Here δ_f, δ_c, δ_{sL}, and δ_{sR} are defined as before, and δ_m is the vertical displacement of the node at the center of the element. The shape of one such mode is shown in Figure C-8. This mode will result in positive errors at some integration points, and corresponding negative errors at others, for zero net residuals. Note that not only is there a solution that satisfies the governing equations with an unrealistic, uniformly zero tension distribution, but that there an entire family of solutions that do so—any two of δ_{sL}, δ_{sR}, and δ_m can be arbitrarily varied as long as all three satisfy the given relation. Also note that because $\delta_f = \delta$, this solution will introduce non-decaying displacement

oscillations into a multi-element model, just as the reduced integration formulations did. We therefore see that any element family with biquadratic displacement interpolation and linearly varying tension fields can assume a configuration with uniformly zero tensions and unrealistic non-decaying displacement oscillations for no energy cost—in other words, such elements possess a spurious mode that prevents them from being used. It can be shown that the bicubic displacement elements with quadratically interpolated tension fields possess similar, although more complex spurious modes. These elements also predict uniformly zero tension distributions and non-decaying displacement oscillations as $K_{xy}/K_{yy} \rightarrow 0$.

Of course, in a real fabric, K_{xy} is not zero and there is coupling between the x- and y-directions through the crimp interchange mechanism, so the energy cost of assuming these modes is not quite zero. However, as mentioned previously, the stiffnesses associated with these mechanisms are much smaller than the stiffnesses associated with yarn stretch, and so the elements will choose the spurious modes because they are energetically inexpensive, and the model stiffness will be underestimated and unrealistic displacements will be predicted.

C.4 Failure to Control Spurious Modes

One common way of controlling spurious modes is to associate some artificial stiffness with any spurious modes that have no energy cost. This artificial stiffness is sometimes called "hourglass control stiffness" because it was originally applied to control spurious displacement modes that caused elements to assume an hourglass shape. Sufficient hourglass stiffness must be applied so that the energetic cost of assuming the spurious mode is greater than the energetic cost of assuming physically-realistic deformation modes. Unfortunately, this technique could not be applied to control the spurious modes that develop in either the reduced-integration displacement-based elements or the hybrid elements that we have explored so far. Sufficient hourglass control to eliminate the spurious modes cause the elements to begin to exhibit numerical locking problems again. Indeed, it is possible that no solution to the governing equilibrium equations exists for a formulation that is capable of eliminating locking. One of the techniques we investigated for eliminating the spurious modes was to square the errors at the integration points, so that spurious modes that have zero residuals due to positive error in some locations and negative error in others no longer exist. When this approach was implemented for the biquadratic displacement linear tension hybrid elements, the Newton-Rhapson implicit algorithm could not converge to a solution. Indeed, no physical solution is apparent for this formulation—no non-zero linear tension distribution can produce nonzero forces at the constrained corner node and

zero forces at all of the unconstrained nodes. Higher order tension distributions can do so, but when the same interpolation order is used for both the tension fields and the displacement fields, the numeric locking problem reappears, just as it does when the same interpolation order is used for both pressure and displacement fields in models of nearly incompressible materials.

C.5 Conclusions Regarding Numerical Locking

To date, we have been unable to develop an effective means of eliminating the numeric locking problem. It manifests as oscillatory errors in the tensions and stresses calculated at the integration points, and varying stiffness that depend on the element formulation used. The problem appears to stem from the large differences in stiffness between deformation modes that involve yarn stretch and deformation modes that can be accommodated by crimp interchange; when these stiffnesses are comparable, the problem vanishes. We have investigated both reduced-integration displacement-based element formulations and hybrid element formulations designed to eliminate numerical locking, and while we have successfully identified several formulations that eliminate the characteristic errors in tension, all of these formulations have spurious modes that cause the element stiffnesses to be underestimated and unrealistic displacement and tension fields to be predicted. Elimination of the spurious modes causes the locking problem to reappear or prevents convergence to a solution.

More research into this phenomenon is necessary. Although the tension errors are relatively small and are non-negligible only in the low-load regime before yarns have become significantly stretched, the oscillatory nature of the errors and the fact that they do not vanish with mesh refinement means that they introduce far more significant errors into tension values extrapolated to the element nodes and into tension gradients determined from the calculated tension values. Accurate extrapolation of the tensions and determination of the tension gradients are very important when yarn slip is included in a fabric model, because yarn slip is driven by the tension gradients and appropriate boundary conditions on the tension must be enforced at the edges of the model.

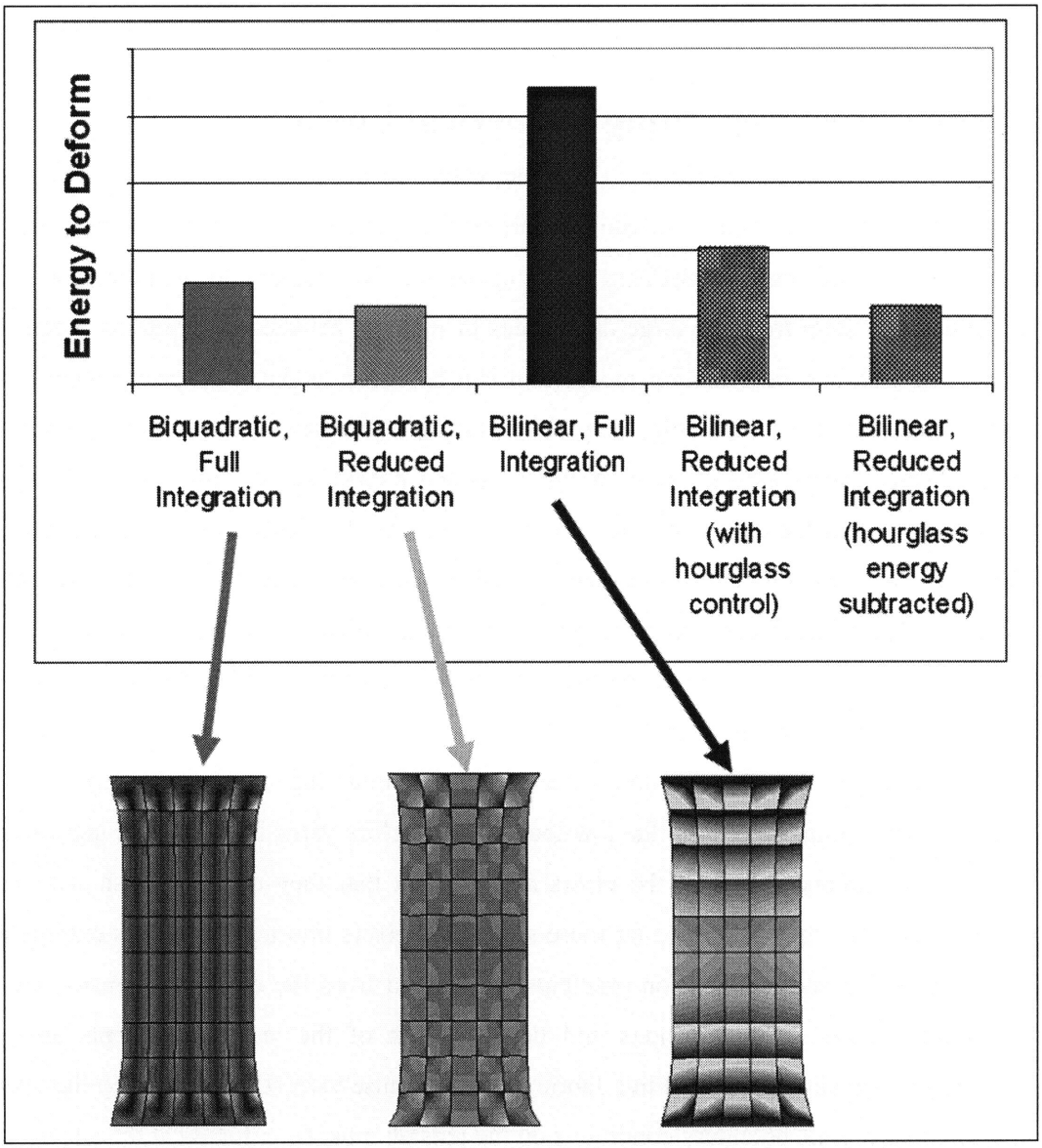

Figure C-1 Numeric locking in fabric elements; (Top) Energy to deform various elements; (Bottom) Yarn tension oscillations that appear in various elements

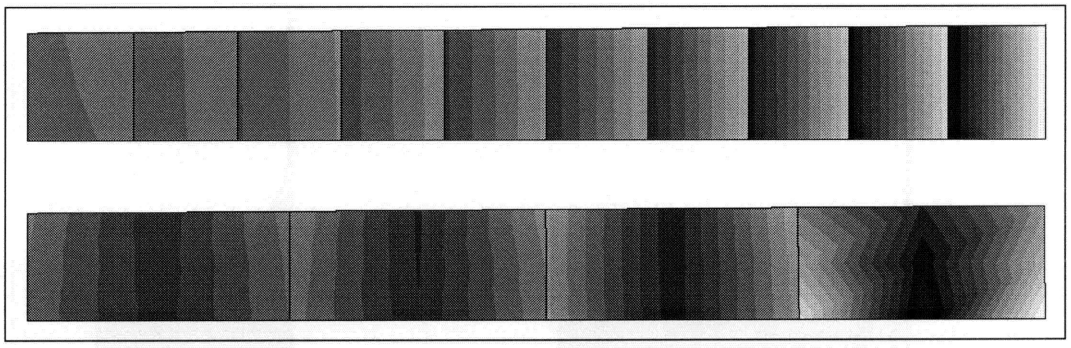

Figure C-2 Tension contours in bilinear (top) and biquadratic (bottom) fully-integrated displacement-based elements subjected to a linearly varying axial strain field

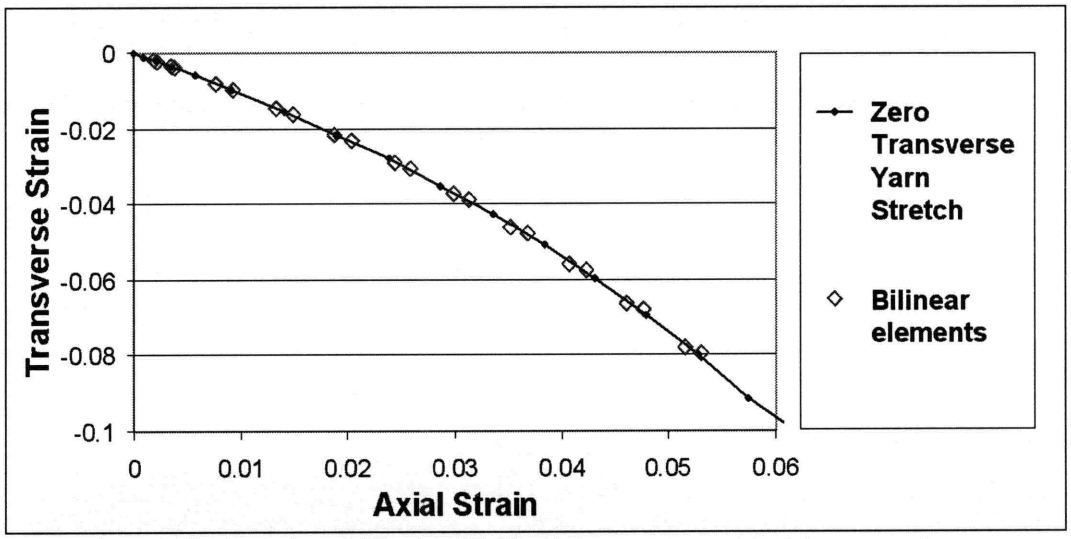

Figure C-3 Relationship between axial and transverse strains that can be accommodated purely through crimp interchange (no transverse yarn stretch), with strains in bilinear fully-integrated displacement-based elements subjected to a linearly varying axial strain field

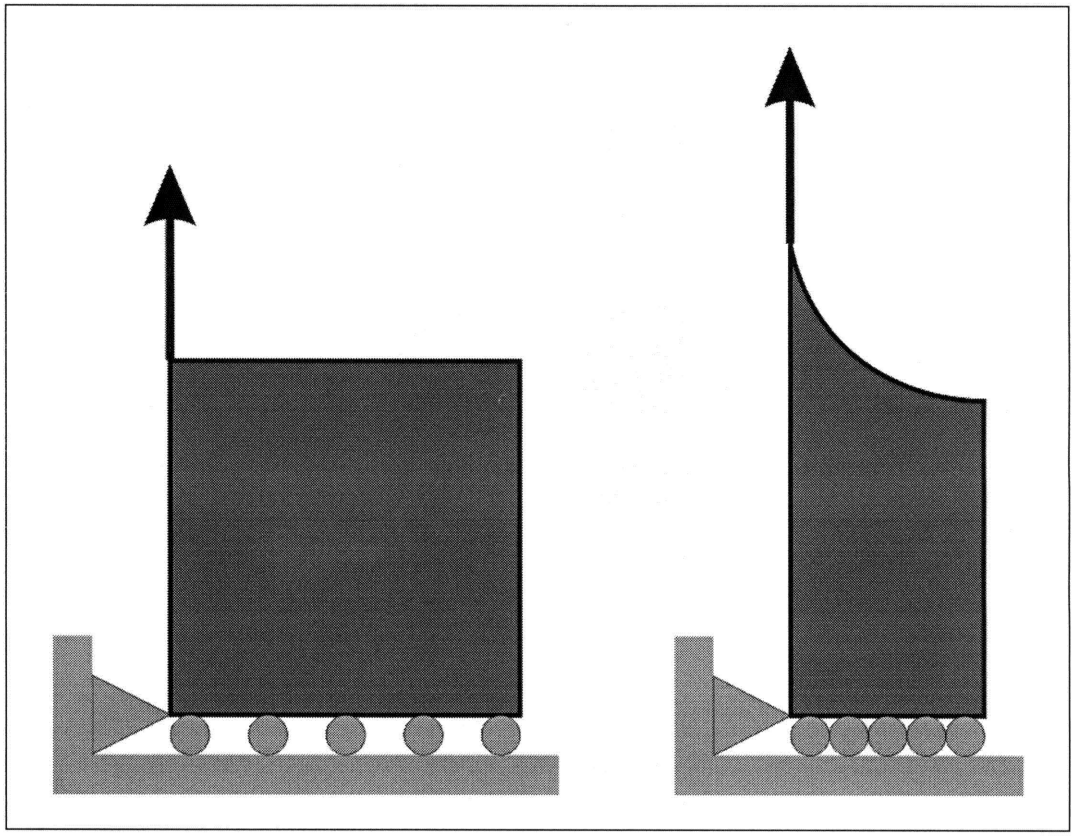

Figure C-4 Simple test case to illustrate spurious modes in element formulations used to eliminate numeric locking

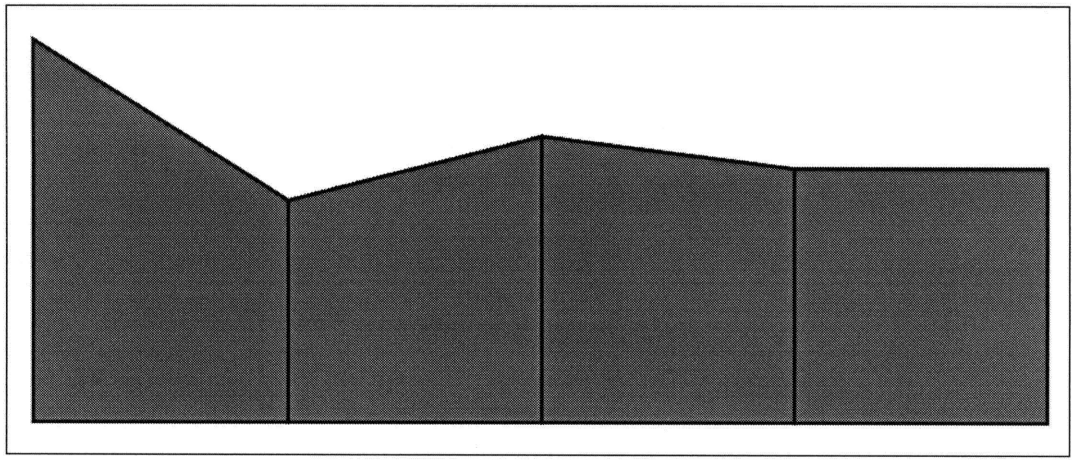

Figure C-5 "Bow-tie" deformation mode over first few elements for fully-integrated displacement-based bilinear element formulation

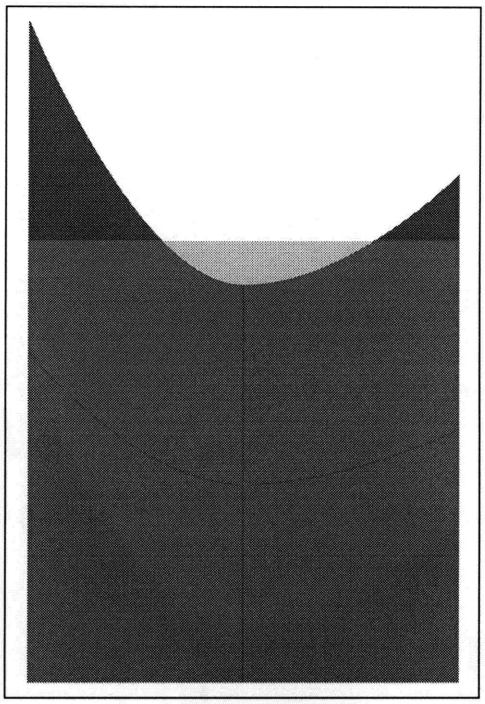

Figure C-6 Solution predicted by fully-integrated displacement-based biquadratic element

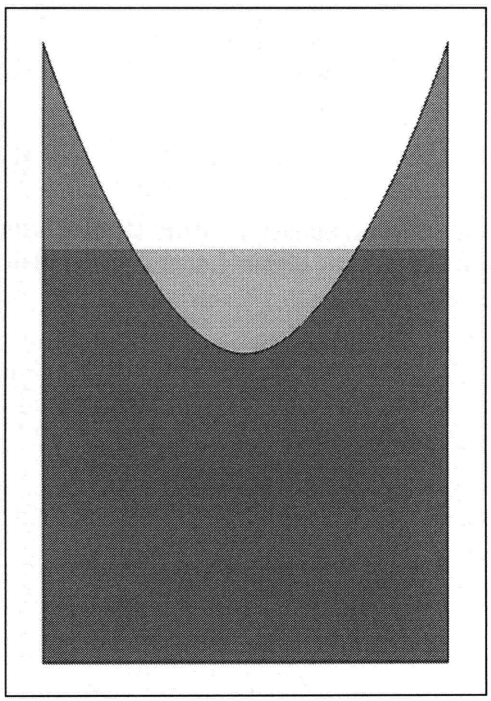

Figure C-7 Solution predicted by displacement-based biquadratic element with reduced integration

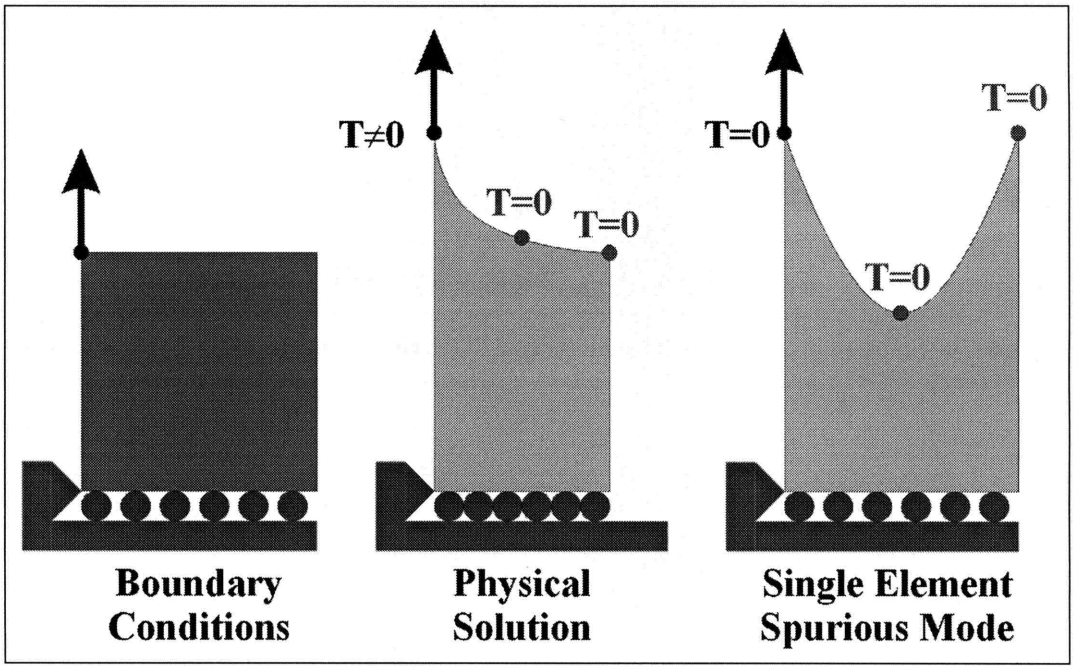

Figure C-8 Physical solution and spurious mode for hybrid element with a linear tension distribution and biquadratic displacement interpolation

Appendix D
Chordal Interpolation

D.1 Motivation

Finite element schemes rely on the discretization of a body into subdomains (elements). Suitable interpolation functions are chosen to evaluate fields at different points inside the element from the values of those fields at the element nodes. These nodal values are referred to as the nodal degrees of freedom. At any given material point $\mathbf{X}$ contained in an element e, the value of some field u can be expressed as a weighted sum of the nodal degrees of freedom $\hat{u}_a$:

$$u(\mathbf{X}) = \sum_a N_a(\mathbf{X})\hat{u}_a \,. \tag{D.1}$$

The weights are the interpolation functions N_a associated with each node a, and depend on position. They form a partition of unity and must have the following properties:

$$\sum_a N_a(\mathbf{X}) = 1 \quad \forall \mathbf{X} \in e\,, \tag{D.2}$$

$$N_a\left(\hat{\mathbf{X}}_b\right) = \delta_{ab}\,. \tag{D.3}$$

Here $\hat{\mathbf{X}}_b$ gives the location of node b, and δ_{ab} is the Kroneker delta (equal to unity when a=b and zero otherwise).

Continuum finite elements are sometimes used to represent anisotropic materials such as woven fabrics, which have preferred material directions (e.g. along the yarns) that may be oriented arbitrarily within the element. It is sometimes desirable to express quantities that are specific to these material directions as fields interpolated throughout the element from degrees of freedom at the nodes. For example, yarn tension in a hybrid fabric element could be represented as a continuous fields that is interpolated from nodal degrees of freedom. As described in Chapter 6, a continuous field can be estimated from discrete values calculated at the integration point values by requiring that the difference between the estimated field and the calculated values vanish when integrated over the element, which can be accomplished by introducing the following equation (given in weak form) to the finite element formulation to solve for the field degrees of freedom:

$$\int_V \bar{T}\left(\hat{T} - T\right) dV = 0. \tag{D.4}$$

Here T represents the field values calculated at the integration points, $\hat{T}$ is the estimated field evaluated by interpolating field degrees of freedom $\hat{T}_a$, and $\bar{T}$ is an arbitrary admissible test function.

Whatever interpolation schemes are used to represent a field, they must be able to accurately reproduce fields that physically occur, given a sufficiently refined mesh. The most commonly used interpolation schemes are bilinear and biquadratic schemes, which are effective for a wide variety of traditional displacement-based elements. These schemes are described in detail in several finite element texts, e.g. Bathe [1996]. Unfortunately, traditional bilinear and biquadratic interpolation schemes are not suitable for interpolation of material direction specific quantities unless the element is rectangular and the material directions are aligned with the element edges. For arbitrary meshes and arbitrarily oriented material directions, bilinear and biquadratic interpolation schemes cannot always capture realistic distributions of direction-specific quantities, such as yarn tensions in a fabric. For an example, consider the case shown in Figure D-1. Yarns in a woven fabric are oriented at a 45° angle to a square element. The yarns passing through the lower left and upper right corners of the element carry large tensions, while those passing through the other corners carry near-zero tensions. Yarn tension varies linearly in a direction perpendicular to the yarn direction, and is constant along the yarns. This is a very simple case that can physically occur in many situations (e.g. during yarn pullout tests, ballistic impacts, propagation of slit-like damage, or bias-extension tests, which are described in Chapter 2).

Neither a bilinear nor a biquadratic interpolation scheme is capable of capturing this simple physical case. Given the correct tension values at the element nodes (large positive tensions at two opposite corner nodes, near zero tensions at the other two corner nodes, and intermediate tensions at the midside nodes if they are present), these interpolation schemes yield a saddle shaped tension distribution, shown in Figure D-2. (We consider 8-node biquadratic interpolation schemes. A 9-node biquadratic interpolation scheme, with a node at the center of the element, produces a different but equally unsuitable distribution through the interior of the element.) This is an unrealistic distribution, as it implies that tension first decreases and then increases along each yarn, rather than remain constant. This interpolation scheme prevents tension from being correctly evaluated at both the nodes and at points within the element (e.g. the integration points) at the same time. It also prevents calculation of the realistic tension gradients along the yarns from the nodal tension values.

D.2 A Chordal Interpolation Scheme

We propose an alternative interpolation scheme for material direction specific fields, such as yarn tensions in a fabric. First, note that for a sufficiently refined mesh, field values evaluated on the element boundaries using linear or quadratic interpolation along the boundaries will be accurate, provided that the nodal values are accurate. Next, provided that the element in question is convex (a requirement for accurate finite elements in most cases case), any point within the element that is not on the element boundary will lie on a material direction vector that, when extended, passes through the element boundary at exactly two points. We postulate that it is reasonable to linearly interpolate values along the material directions between these two points, and that for a sufficiently refined mesh, these linearly interpolated values will be accurate.

We refer to this interpolation technique as "chordal interpolation", since we are interpolating along a chord that crosses the element. We designate the interpolation functions for this interpolation scheme as N_a^C , and define them in the following manner, analogous to Equation (D.1):

$$T(\mathbf{X}) \equiv \sum_a N_a^C(\mathbf{X},\mathbf{g})\hat{T}_a \,, \tag{D.5}$$

Note that the chordal interpolation function depends on the material point location **X,** and also on **g,** a unit vector that describes the in-plane orientation of the material direction in the reference configuration as it passes through **X**.

We follow the scheme described in O'Rourke [1998] to determine the end points of the chord—the points where a line through **X** parallel to the material direction crosses the element boundaries. We restrict this analysis to elements with straight edges in the reference configuration. (Extension to elements with curved edges is straightforward, although it involves complex algebra). Consider an arbitrarily shaped convex quad element with straight edges, as shown in Figure D-3, with corner nodes at positions $\mathbf{N_j}$ in the reference configuration. At any point **X** within the element there is a unit vector **g** that gives the in-plane material direction that passes through that point. We define the chord associated with **X** and **g** to be the straight line segment contained in the element that passes through **X** parallel to **g**. We assume that **g** remains constant along the chord—i.e. that the yarn or fiber that the chord represents is straight in the reference configuration. This assumption is reasonable provided the mesh is sufficiently refined.

Define a parametric vector function $\mathbf{p}(s) = \mathbf{X} + s\mathbf{g}$, which describes points on the chord that are distance s from point **X**. Consider one of the edges of the elements with endpoints $\mathbf{N_j}$ and $\mathbf{N_k}$. Define a second parametric function $\mathbf{q}(t) = \mathbf{N_j} + t(\mathbf{N_k} - \mathbf{N_j})$ that gives the percentage of the distance traveled along the edge from node $\mathbf{N_j}$ to $\mathbf{N_k}$. The intersection between the line containing

the chord and the line containing that edge lies where $\mathbf{p} = \mathbf{q}$. Hence we can establish a system of equations with two unknowns, s and t, the solution of which is given below. We designate m_1 and m_2 to be the coordinates of $\mathbf{N}_j$, n_1 and n_2 to be the coordinates of $\mathbf{N}_k$, g_1 and g_2 to be the components of $\mathbf{g}$, and x and y to be the coordinates of $\mathbf{X}$:

$$s = \left(-m_1 y - n_1 m_2 + n_1 y + x m_2 - x n_2 + m_1 n_2\right)/D, \tag{D.6a}$$

$$t = \left(-g_2 x - g_1 m_2 + g_1 y + g_2 m_1\right)/D, \tag{D.6b}$$

with

$$D = -g_1 m_2 + g_1 n_2 + g_2 m_1 - g_2 n_1. \tag{D.6c}$$

Note that it is possible for D to be zero, in which case s and t are undefined (they approach positive or negative infinity as D approaches zero). This indicates that the edge between $\mathbf{N}_i$ and $\mathbf{N}_j$ is parallel to $\mathbf{g}$ and hence the chord will never intersect that edge.

For $0 \le t \le 1$, the intersection point lies on the element edge. When t exactly equals 1 or 0, the intersection lies on one of the nodes. When $t < 0$ or $t > 1$, the line containing the chord intersects the line containing the edge outside of the element. Provided that the point $\mathbf{X}$ does not lie on a corner node or on an edge that is parallel to $\mathbf{g}$, there must be exactly two distinct points $\mathbf{X}_1$ and $\mathbf{X}_2$ where the chord intersects the element boundaries. In order to find $\mathbf{X}_1$ and $\mathbf{X}_2$, we find the intersections (s_1, t_1) and (s_2, t_2) that give two distinct points $\mathbf{X}_1$ and $\mathbf{X}_2$ with $0 \le t \le 1$. In the special case where $\mathbf{X}$ corresponds to one of the corner nodal locations $\mathbf{N}_i$, it is possible that there may be only one intersection point for certain vectors $\mathbf{g}$, which would be indicated by two of the intersection points having a t value out of the range $0 \le t \le 1$ and the other two intersections having $s=0$, meaning that they lie at the same point. In this case, $\mathbf{X}_1 = \mathbf{X}_2 = \mathbf{N}_j$. When $\mathbf{X}$ lies on an edge that is parallel to $\mathbf{g}$, (the D value for that edge is zero and two other admissible points have $t = 1$ or $t = 0$) we define $\mathbf{X}_1$ and $\mathbf{X}_2$ to be $\mathbf{N}_j$ and $\mathbf{N}_k$, the nodes at the ends of the parallel edge.

Once points $\mathbf{X}_1$ and $\mathbf{X}_2$ have been found, the value of $\hat{T}$ at these two points can be calculated using the traditional linear or quadratic interpolation functions along the edge:

$$\hat{T}(\mathbf{X}_i) = \sum_a N_a(\mathbf{X}_i)\hat{T}_a. \tag{D.7}$$

We interpolate linearly between these two points to find $\hat{T}(\mathbf{X})$:

$$\begin{aligned}\hat{T}(\mathbf{X}) &= \frac{|s_2|}{|s_1|+|s_2|}\hat{T}(\mathbf{X}_1)+\frac{|s_1|}{|s_1|+|s_2|}\hat{T}(\mathbf{X}_2) \\ &= \frac{|s_2|}{|s_1|+|s_2|}\sum_a N_a(\mathbf{X}_1)\hat{T}_a+\frac{|s_1|}{|s_1|+|s_2|}\sum_a N_a(\mathbf{X}_2)\hat{T}_a\,. \\ &= \sum_a\left(\frac{|s_2|}{|s_1|+|s_2|}N_a(\mathbf{X}_1)+\frac{|s_1|}{|s_1|+|s_2|}N_a(\mathbf{X}_2)\right)\hat{T}_a\end{aligned} \tag{D.8}$$

For the special case where $\mathbf{X}$ lies on a corner node, $\mathbf{X}_1 = \mathbf{X}_2$ and $s_1 = s_2 = 0$, so this expression will be undefined. To complete the theory, we can redefine s_1 and s_2 to be any partition of unity in this special case because $\hat{T}(\mathbf{X}_1)=\hat{T}(\mathbf{X}_2)$; $s_1 = s_2 = ½$ is convenient. However, note that when these interpolation schemes are used in a finite element analysis to evaluate fields at Gauss quadrature points, this special case will not arise, because Gauss quadrature points never lie on the corner nodes for quadrilateral elements.

By comparing Equation (D.8) to Equation (D.5), we see that the chordal interpolation functions N_a^C are:

$$N_a^C(\mathbf{X},\mathbf{g}) \equiv \frac{|s_2|}{|s_1|+|s_2|}N_a(\mathbf{X}_1)+\frac{|s_1|}{|s_1|+|s_2|}N_a(\mathbf{X}_2). \tag{D.9}$$

Note that s_1, s_2, $\mathbf{X}_1$, and $\mathbf{X}_2$ depend on $\mathbf{X}$ and $\mathbf{g}$, as well as the reference configuration coordinates of the corner nodes $\mathbf{N}_j$. The chordal interpolation functions will satisfy the properties given in Equations (D.2) and (D.3) provided that the interpolation function N_a that are used to interpolate along the edges satisfy these properties.

In some cases, the reference configuration gradients of interpolated fields along the material directions may be of interest. For example, in a fabric the gradient of tension along a yarn might be of interest, since this gradient drives yarn slip through the weave. If we define ξ to be a coordinate in the reference configuration measured along the material direction parallel to $\mathbf{g}$, the gradient of a field $\hat{T}$ along this direction is:

$$\frac{\partial \hat{T}}{\partial \xi} \equiv \mathbf{Grad}\left(\hat{T}\right)\cdot\mathbf{g}\,. \tag{D.10}$$

Since we assume a linear interpolation along the yarn, we can calculate this gradient in the following manner:

$$\frac{\partial \hat{T}}{\partial \zeta} = \frac{\hat{T}(\mathbf{X}_1) - \hat{T}(\mathbf{X}_2)}{s_1 - s_2} = \frac{\sum_a N_a(\mathbf{X}_1)\hat{T}_a - \sum_a N_a(\mathbf{X}_2)\hat{T}_a}{s_1 - s_2} = \sum_a \left(\frac{N_a(\mathbf{X}_1) - N_a(\mathbf{X}_2)}{s_1 - s_2} \right) \hat{T}_a \equiv \sum_a N_a^{C'} \hat{T}_a \quad , \tag{D.11a}$$

with

$$N_a^{C'}(\mathbf{X}, \mathbf{g}) \equiv \frac{N_a(\mathbf{X}_1) - N_a(\mathbf{X}_2)}{s_1 - s_2} . \tag{D.11b}$$

Note that we designate $\mathbf{X}_1$ to be the point that lies in the direction indicated by $\mathbf{g}$ relative to $\mathbf{X}$, and $\mathbf{X}_2$ to be the point in the direction indicated by $-\mathbf{g}$. If the nodal values $\hat{T}_a$ of some field that is chordally interpolated are known, these gradient interpolation functions can be used to calculate the reference configuration gradients of those fields along the material directions.

D.3 Implementation

Certain issues arise when these chordal interpolation functions are implemented into a computational framework. In many finite element codes, the bilinear or biquadratic shape functions are frequently expressed in terms of isoparametric coordinates (often designated as r and s) instead of global coordinates x and y, and the global coordinates of isoparametric locations within the element must be determined through isoparametric interpolation, as described in Bathe [1996]:

$$\begin{aligned} x(r,s) &= \sum_a N_a(r,s)\hat{x}_a \\ y(r,s) &= \sum_a N_a(r,s)\hat{y}_a \end{aligned} . \tag{D.12}$$

The locations of the Gauss quadrature points are often stored in isoparametric coordinates. Therefore, the first step in calculating the chordal interpolation functions is to convert coordinates of the Gauss quadrature points to global coordinates, so that Equation (D.6) can be used to find the corresponding ends of the chords through these points.

For each of the four edges, Equation (D.6) either gives s and t parameters or indicates that D is zero and s and t are undefined. Provided that the point in question lies within the interior of the element, there must be exactly two unique intersection points. However, it is possible that there may be three or even four edge intersections with $0 \le t \le 1$, if the chord intersects one or two of the corner nodes. When this occurs, the two unique intersection points $\mathbf{X}_1$ and $\mathbf{X}_2$ can be identified by identifying a pair of points with different s values.

When a point lies near an edge that is nearly parallel to the chord through that point, numeric round off error can create difficulties in the calculation of the intersection points. Consequently, logical tests for edges parallel to the chord must include suitable tolerances.

The endpoints of the chord $\mathbf{X}_1$ and $\mathbf{X}_2$ are calculated in global (x and y) coordinates. In order to calculate the chordal interpolation function using Equations (D.9) and (D.11b), it is necessary to evaluate the standard bilinear or biquadratic shape functions N_a at these points. However, as is mentioned above, in many codes the standard shape functions are expressed in terms of isoparametric coordinates (r and s). Therefore, the isoparametric coordinates of the end points $\mathbf{X}_1$ and $\mathbf{X}_2$ must be calculated. Equation (D.12) relates the isoparametric coordinates to the global coordinates; unfortunately, these relations do not have a closed form inverse. Therefore, the isoparametric coordinates and the corresponding values of the shape functions at points $\mathbf{X}_1$ and $\mathbf{X}_2$ must be calculated numerically using iterative techniques. Only then can the chordal interpolation functions be calculated using Equations (D.9) and (D.11b).

D.4 Validation of Chordal Interpolation Scheme

Chordal interpolation schemes can accurately represent any physically realistic field that is accurately represented by bilinear or biquadratic interpolation schemes, with the caveat that the chordal interpolation scheme can capture only linear variations along the material directions. They can also represent fields that cannot be accurately represented by bilinear or biquadratic schemes.

For cases where the material direction is parallel to parallel edges of a rectangular or trapezoidal element, the chordal interpolation scheme is equivalent to a bilinear scheme (or, if quadratic interpolation along the element edges is used, it is equivalent to a linear-quadratic scheme). For example, the field shown in Figure D-4, which increases linearly in the x- and y-directions, is accurately represented by both chordal and by traditional bilinear and biquadratic interpolation schemes. When the field increases linearly along a material direction oriented parallel to the y-direction and quadratically along the x-direction, a bilinear scheme cannot be represent it, but both a biquadratic and a chordal interpolation scheme (using quadratic interpolation along the edges) can, as shown in Figure D-5.

There are cases where neither the bilinear nor the biquadratic schemes can accurately represent a physical field that can be represented by a chordal interpolation scheme. For example, consider a case similar to the one described in Section D.1, where the material direction is oriented at 45° to the element, and where the field is constant along the material direction and

increases quadratically from zero at the upper left and lower right corners of the element to unity at the center of the element. As is shown in Figure D-6, only the chordal scheme (with quadratic interpolation along the edges) can accurately represent this field given correct values at the nodes.

The inability of the chordal interpolation scheme to capture nonlinear variations along the material direction means that there are certain cases where a finer mesh may be required than would be for a biquadratic scheme. However, because a biquadratic scheme will not always give correct results when the material directions are not aligned with the element edges, the chordal interpolation scheme provides greater flexibility when meshing a model of an anisotropic material with direction-dependent degrees of freedom, because arbitrarily shaped elements that are oriented arbitrarily with respect to the material directions can be used.

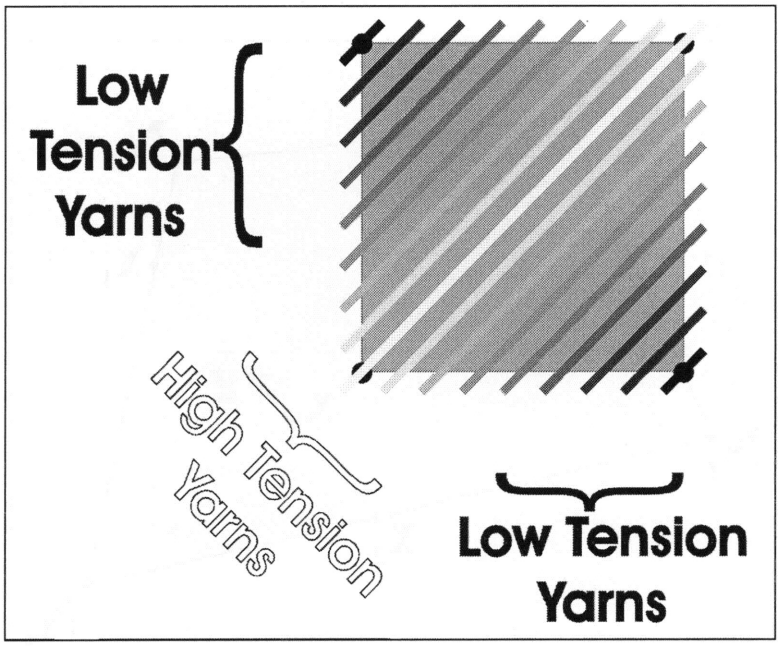

Figure D-1 A case where bilinear and biquadratic interpolations fail--yarns oriented diagonally across the element

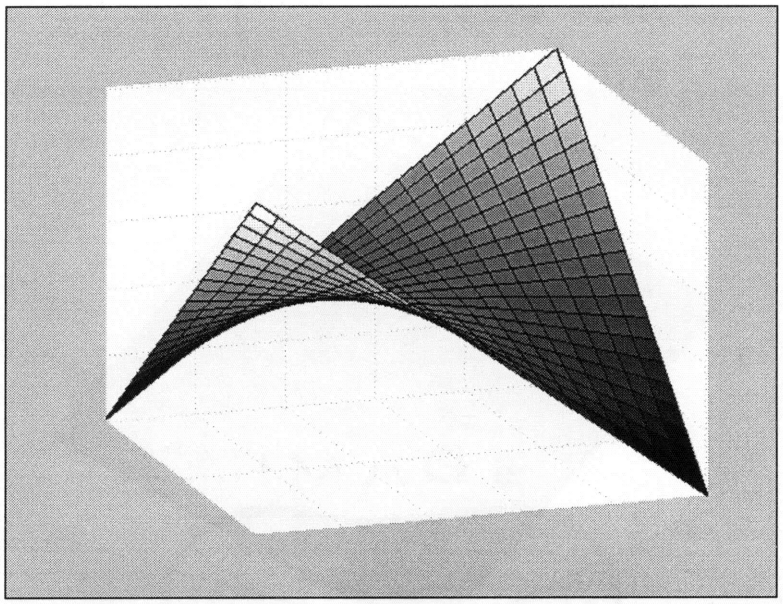

Figure D-2 Saddle distribution resulting from bilinear and biquadratic interpolation

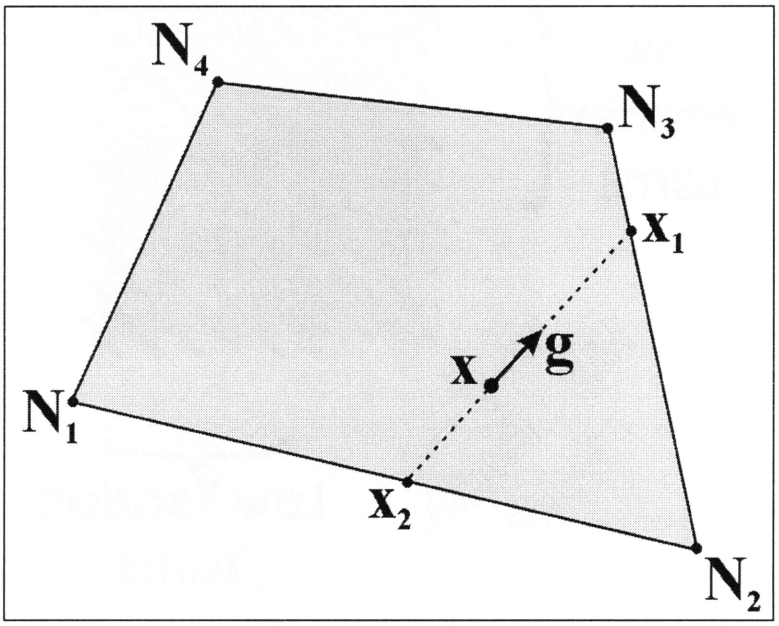

Figure D-3 Geometry of an arbitrary quad element with a chord parallel to a material direction

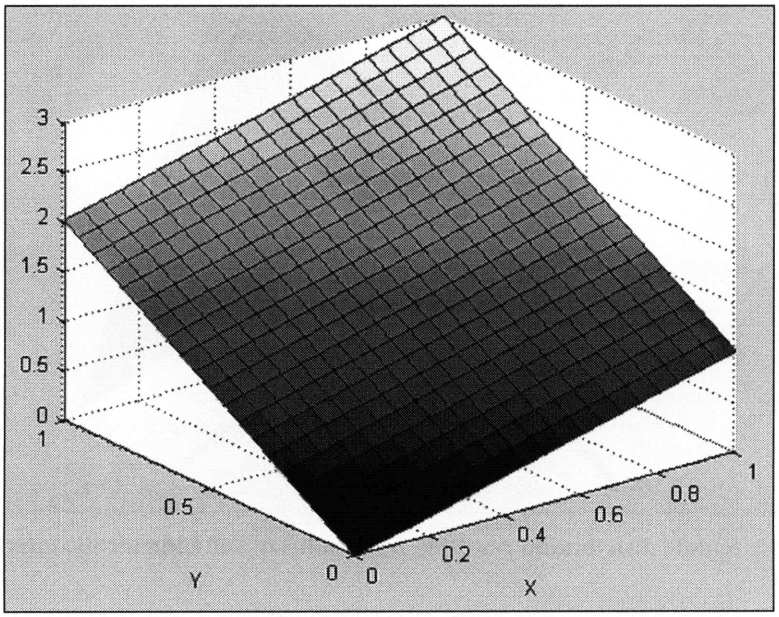

Figure D-4 Field increasing linearly in x- and y-directions

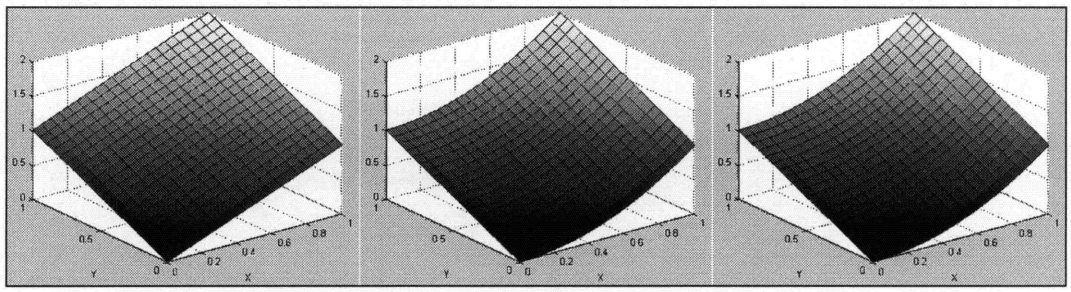

Figure D-5 Bilinear (left), biquadratic (middle) and chordal (right) interpolation of field that increases linearly along a y-oriented material direction and quadratically along the x-direction

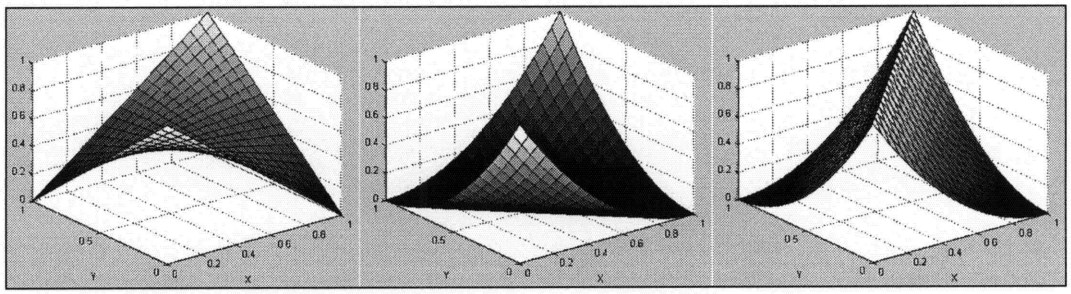

Figure D-6 Bilinear (left), biquadratic (middle), and chordal (right) interpolation of a field that is constant along a material direction oriented at 45° to the element, and increasing quadratically from the outside corners to the center of the element

Appendix E
Mechanical Drawings

The subsequent pages contain mechanical drawings for a fabric grip (used on the biaxial machine), the twist test apparatus described in Chapter 3, the yarn-to-yarn friction test apparatus described in Chapter 4, and the pneumatic apparatus used for pullout tests, also described in Chapter 4. All of these were designed and machined at MIT.

The fabric grip is designed to attach to a Deben biaxial tensile tester. Grips of this type proved to be very effective in all fabric experiments at gripping fabric specimens so that the fabric neither slips significantly in the grip nor is sheared or broken at the edge of the grip. The fabric is wrapped around a bar with a diamond-shaped cross section, and this bar is clamped between two jaws.

The twist test apparatus is designed to be attached to a cantilever texture analyzer uniaxial tester. Neither the cables nor the counterweights are shown in the drawings. Because the moving portion of the device is not rotationally symmetric about the twisting axis, the weight of the apparatus components affect the measured response. Consequently, a test must be performed with no specimen loaded so that the portion of the response that comes from the weight of the components of the apparatus can be subtracted from responses measured for various specimens.

The yarn-to-yarn friction test apparatus is designed to be attached to a Zwick uniaxial tensile tester. The weight used to apply the input tension is not shown. The pulleys (which are mounted on shoulder screws), threaded rods, thumbnuts, etc., are also not shown. These parts were ordered from McMaster-Carr.

The pneumatic apparatus is also designed to be attached to a Zwick uniaxial tensile tester. It employs fabric grips where the fabric is wrapped around a rod with a diamond-shaped cross section and clamped between two jaws. The pneumatic cylinders and the associated pneumatic tubing and hardware are not shown. These components were ordered from McMaster-Carr.

Fabric Grip

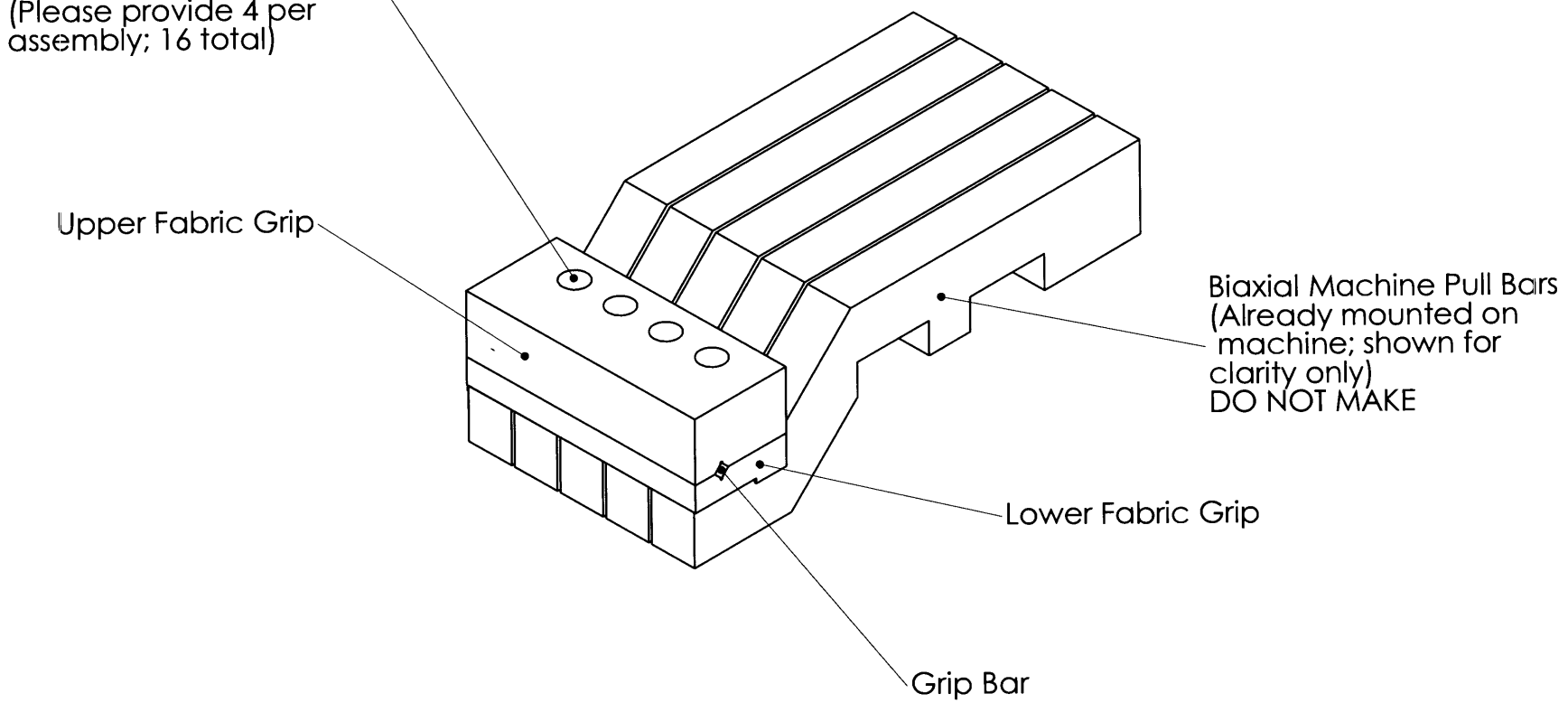

		UNLESS OTHERWISE SPECIFIED:		NAME	DATE
			DRAWN		
			CHECKED		
			ENG APPR.		
			MFG APPR.		
		INTERPRET GEOMETRIC TOLERANCING PER:	Q.A.		
		MATERIAL	COMMENTS: FOR QUESTIONS, CONTACT MICHAEL KING AT X40164 OR AT MKING@MIT.EDU		
NEXT ASSY	USED ON	FINISH			
APPLICATION		DO NOT SCALE DRAWING			

TITLE: Biaxial Grip Assembly 4 REQUIRED

SIZE	DWG. NO.	REV
A		

SCALE: 1:3	WEIGHT:	SHEET 1 OF 4

5 4 3 2 1

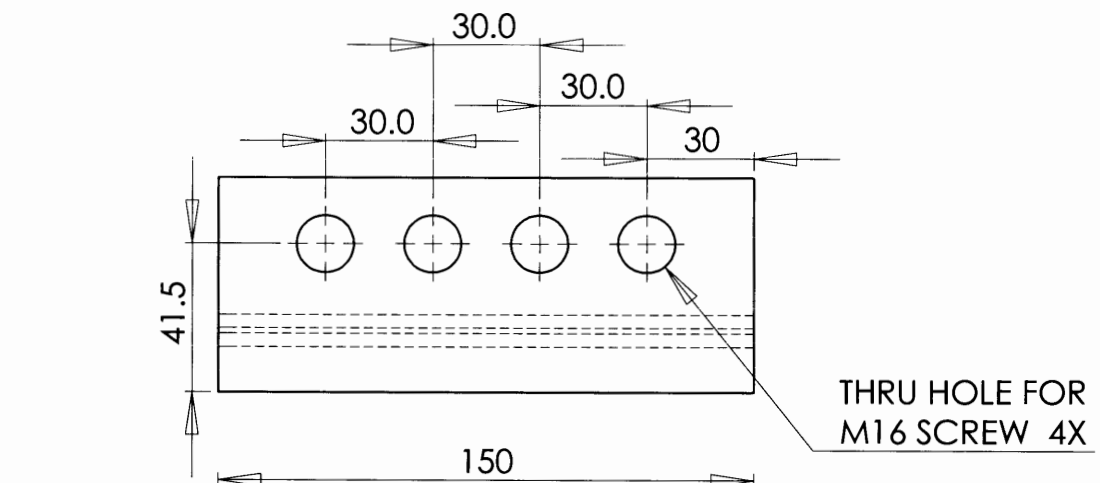

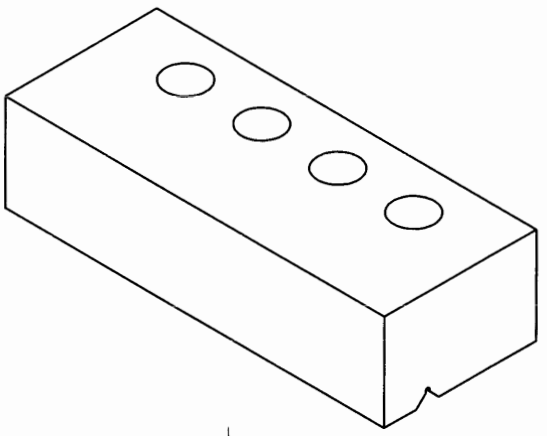

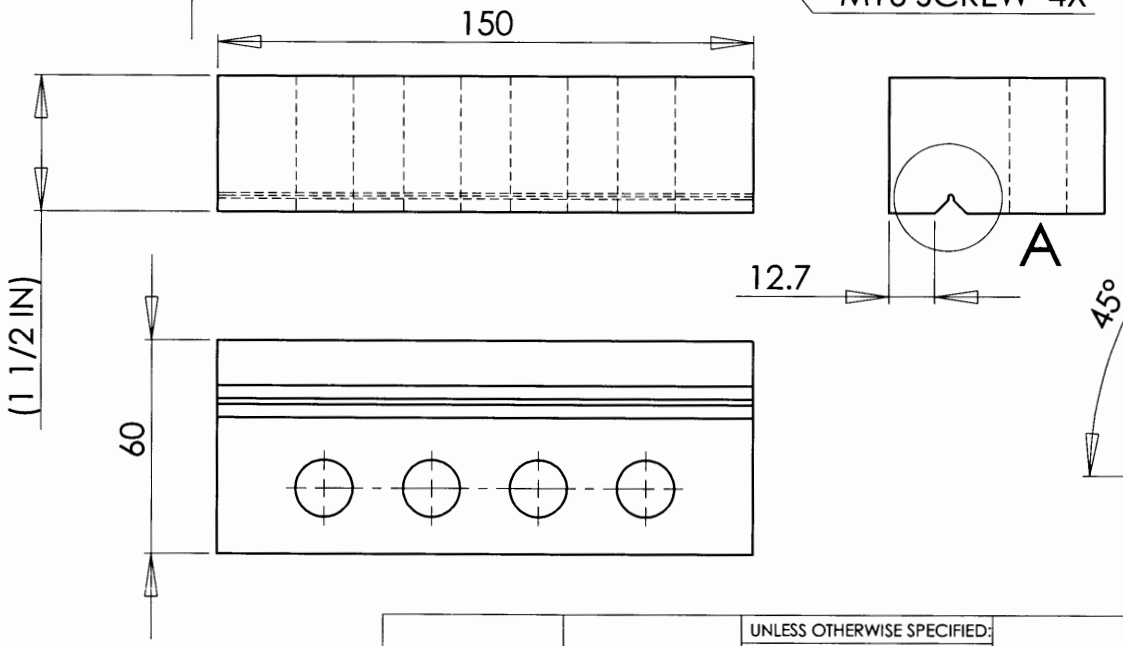

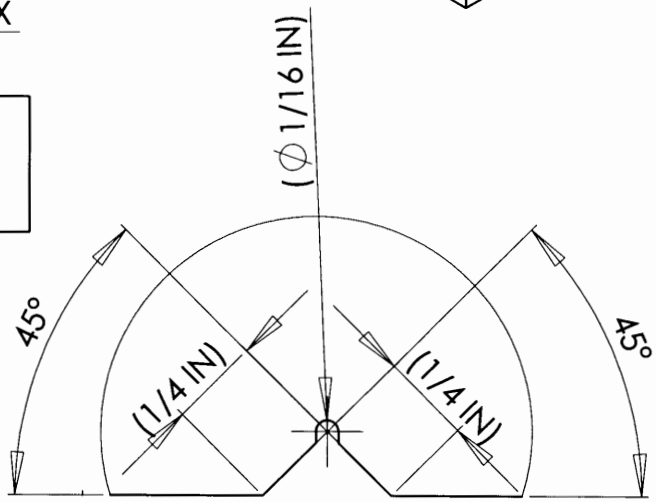

DETAIL A
SCALE 2 : 1

		UNLESS OTHERWISE SPECIFIED:		NAME	DATE
		DIMENSIONS ARE IN MM UNLESS UNLESS OTHERWISE NOTED TOLERANCES: X=±0.2 X.X = ±0.05 X.XX = ±0.02	DRAWN		
			CHECKED		
			ENG APPR.		
			MFG APPR.		
			Q.A.		
		MATERIAL STEEL 400 MPA MIN STRENGTH	COMMENTS: FOR QUESTIONS, CONTACT MICHAEL KING AT X40164 OR AT MKING@MIT.EDU		
NEXT ASSY	USED ON	FINISH			
APPLICATION		DO NOT SCALE DRAWING			

TITLE:
Upper Fabric Grip
for Biaxial Machine
4 REQUIRED

SIZE	DWG. NO.	REV
A		
SCALE: 1:2	WEIGHT:	SHEET 3 OF 4

5 4 3 2 1

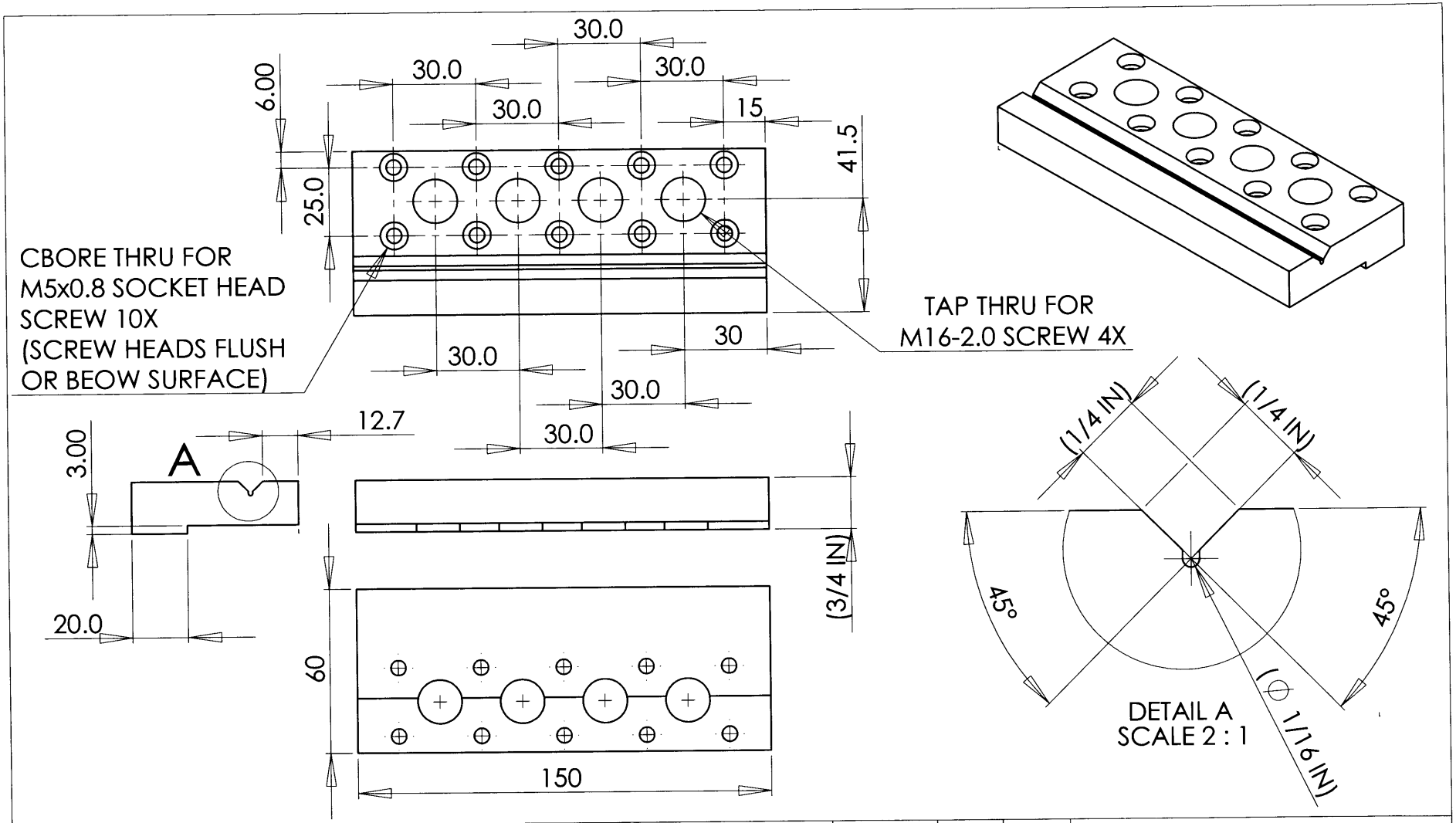

		UNLESS OTHERWISE SPECIFIED:		NAME	DATE
		DIMENSIONS ARE IN MM UNLESS UNLESS OTHERWISE NOTED TOLERANCES: X= ±0.2 X.X = ±0.05 X.XX = ±0.02	DRAWN		
			CHECKED		
			ENG APPR.		
			MFG APPR.		
			Q.A.		
		MATERIAL STEEL 400 MPA MIN STRENGTH	COMMENTS: FOR QUESTIONS, CONTACT MICHAEL KING AT X40164 OR AT MKING@MIT.EDU		
NEXT ASSY	USED ON	FINISH			
APPLICATION		DO NOT SCALE DRAWING			

TITLE: Lower Fabric Grip for Biaxial Machine: 4 REQUIRED

SIZE	DWG. NO.	REV
A		
SCALE: 1:2	WEIGHT:	SHEET 2 OF 4

5 4 3 2 1

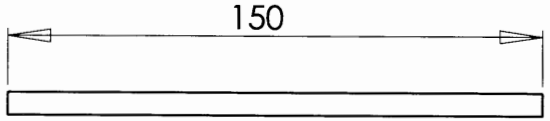

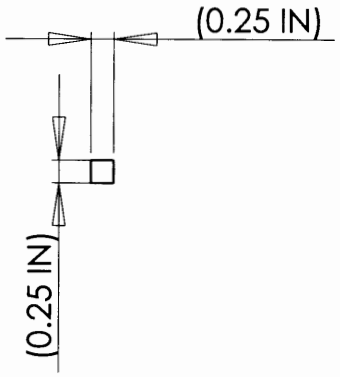

NEXT ASSY	USED ON	
APPLICATION		

UNLESS OTHERWISE SPECIFIED:
DIMENSIONS ARE IN MM UNLESS UNLESS OTHERWISE NOTED
TOLERANCES:
X= ±0.2
X.X = ±0.05
X.XX = ±0.02

MATERIAL
STEEL

FINISH

DO NOT SCALE DRAWING

	NAME	DATE
DRAWN		
CHECKED		
ENG APPR.		
MFG APPR.		
Q.A.		

COMMENTS:
FOR QUESTIONS, CONTACT MICHAEL KING AT X40164 OR AT MKING@MIT.EDU

TITLE:
Grip Bar
for Biaxial Machine
4 REQUIRED

SIZE	DWG. NO.	REV
A		

SCALE: 1:2 | WEIGHT: | SHEET 4 OF 4

5 4 3 2 1

Twist Test Apparatus

REVISIONS				
ZONE	REV.	DESCRIPTION	DATE	APPROVED

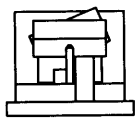

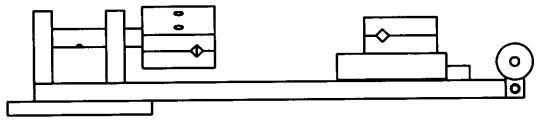

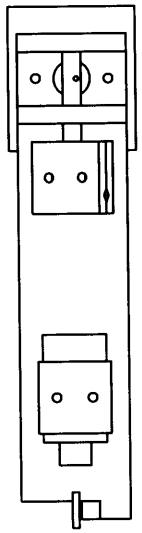

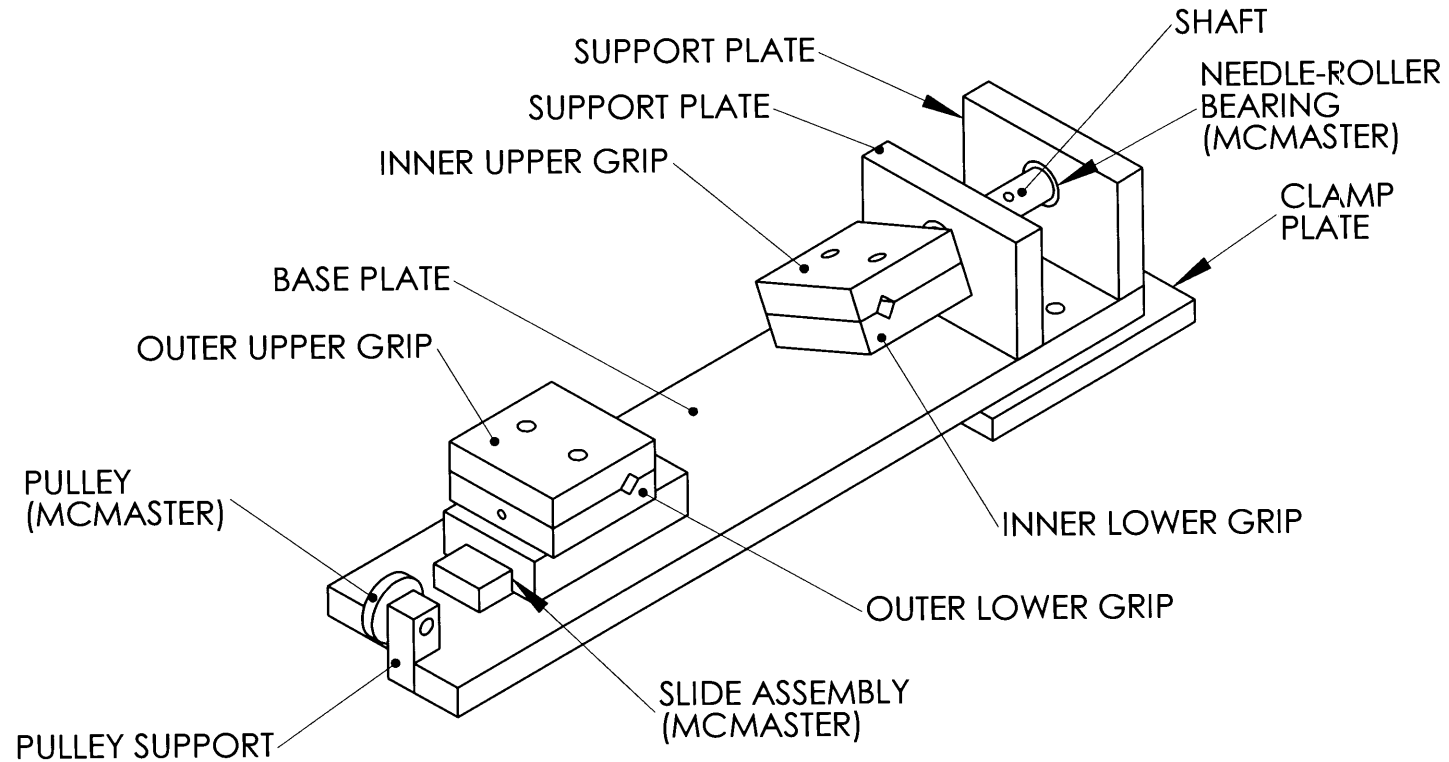

COMPONENT LIST
- BASE PLATE
- CLAMP PLATE
- SUPPORT PLATE (2X)
- SHAFT
- INNER LOWER GRIP
- INNER UPPER GRIP
- OUTER LOWER GRIP
- OUTER UPPER GRIP
- PULLEY SUPPORT
- GRIPPING BAR (2X)
- 0.25 DIA X 0.75 DOWEL PIN
- MISCELLANEOUS 1/4-20 AND #6-32 SOCKET HEAD CAP SCREWS

FROM MCMASTER
- SLIDE ASSEMBLY
- IDLER PULLEY
- NEEDLE-ROLLER BEARINGS (2X)

NEXT ASSY	USED ON
APPLICATION	

DIMENSIONS ARE IN INCHES
TOLERANCES:
FRACTIONAL ±
ANGULAR: MACH ± BEND ±
TWO PLACE DECIMAL ±
THREE PLACE DECIMAL ±

MATERIAL --

FINISH --

DO NOT SCALE DRAWING

	NAME	DATE
DRAWN		
CHECKED		
ENG APPR.		
MFG APPR.		
Q.A.		

COMMENTS:

MIT

TWIST TESTER ASSEMBLY

SIZE	DWG. NO.	REV.
A		
SCALE:1:5	WEIGHT:	SHEET 1 OF 1

REVISIONS				
ZONE	REV.	DESCRIPTION	DATE	APPROVED

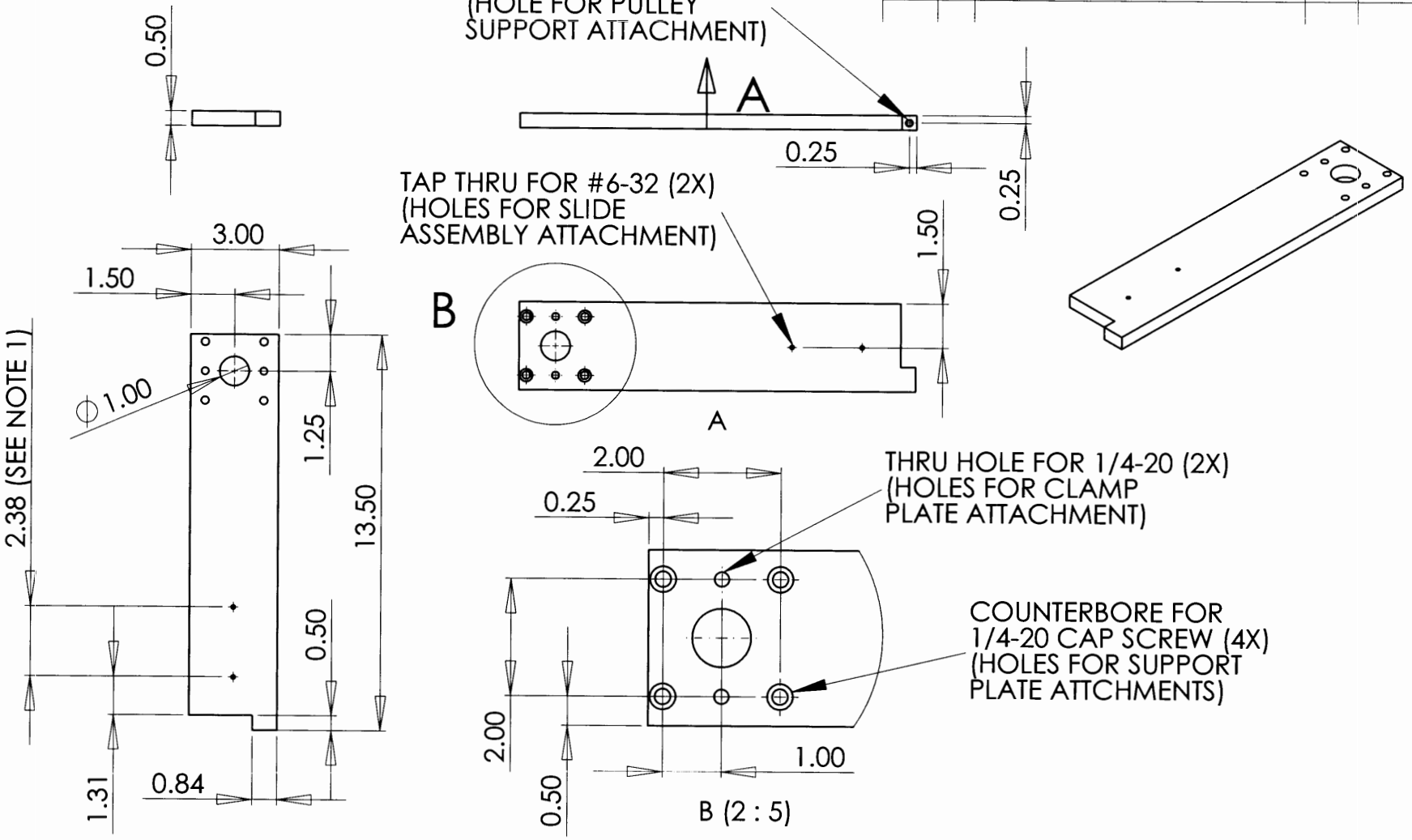

NOTES:
1. DIMENSION IS APPROXIMATE ENSURE THAT HOLE SPACING CORRESPONDS TO HOLES IN SLIDE ASSEMBLY

NEXT ASSY	USED ON	
APPLICATION		

DIMENSIONS ARE IN INCHES
TOLERANCES:
FRACTIONAL ±
ANGULAR: MACH ± BEND ±
TWO PLACE DECIMAL ±
THREE PLACE DECIMAL ±

MATERIAL ALUMINUM

FINISH --

DO NOT SCALE DRAWING

	NAME	DATE
DRAWN		
CHECKED		
ENG APPR.		
MFG APPR.		
Q.A.		

COMMENTS:

MIT

BASE PLATE

SIZE	DWG. NO.	REV.
A		
SCALE:1:5	WEIGHT:	SHEET 1 OF 1

REVISIONS				
ZONE	REV.	DESCRIPTION	DATE	APPROVED

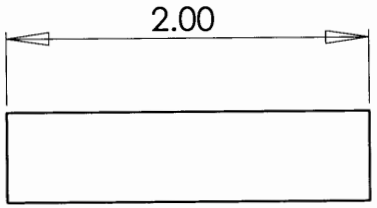

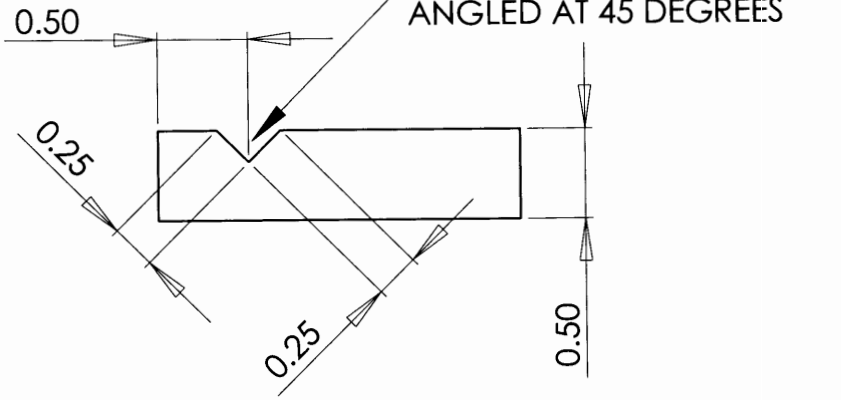

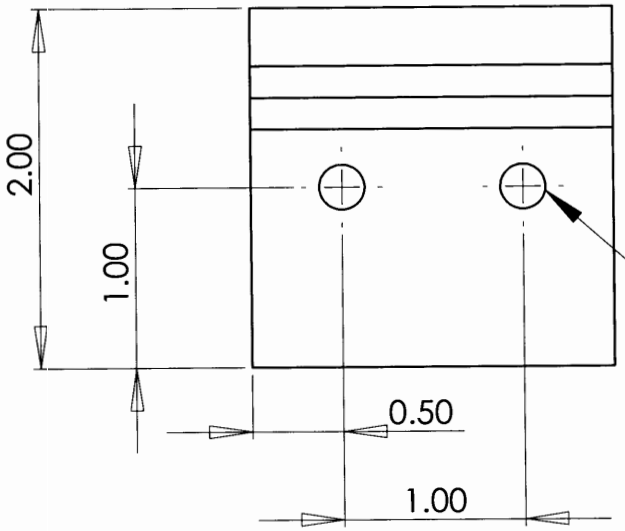

THRU HOLE FOR 1/4-20 (2X) (HOLES FOR OUTER LOWER GRIP ATTACHMENT)

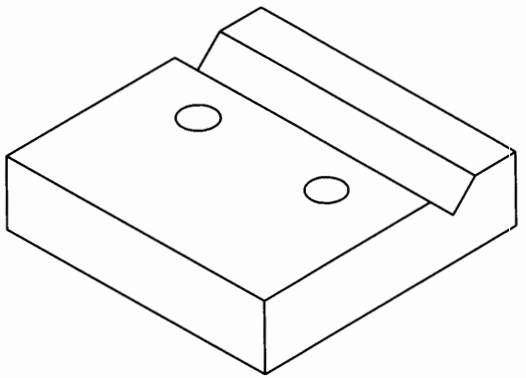

PROPRIETARY AND CONFIDENTIAL

THE INFORMATION CONTAINED IN THIS DRAWING IS THE SOLE PROPERTY OF MIT. ANY REPRODUCTION IN PART OR AS A WHOLE WITHOUT THE WRITTEN PERMISSION OF MIT IS PROHIBITED.

NEXT ASSY	USED ON
APPLICATION	

DIMENSIONS ARE IN INCHES
TOLERANCES:
FRACTIONAL ±
ANGULAR: MACH ± BEND ±
TWO PLACE DECIMAL ±
THREE PLACE DECIMAL ±

MATERIAL ALUMINUM

FINISH --

DO NOT SCALE DRAWING

	NAME	DATE
DRAWN		
CHECKED		
ENG APPR.		
MFG APPR.		
Q.A.		

COMMENTS:

MIT

OUTER UPPER GRIP

SIZE	DWG. NO.	REV.
A		
SCALE:1:1	WEIGHT:	SHEET 1 OF 1

ZONE	REV.	REVISIONS DESCRIPTION	DATE	APPROVED

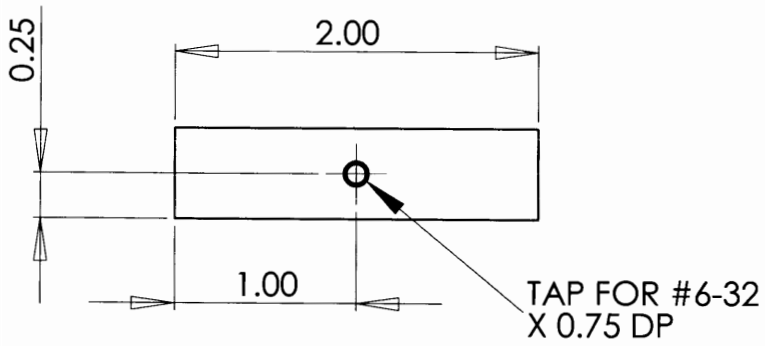

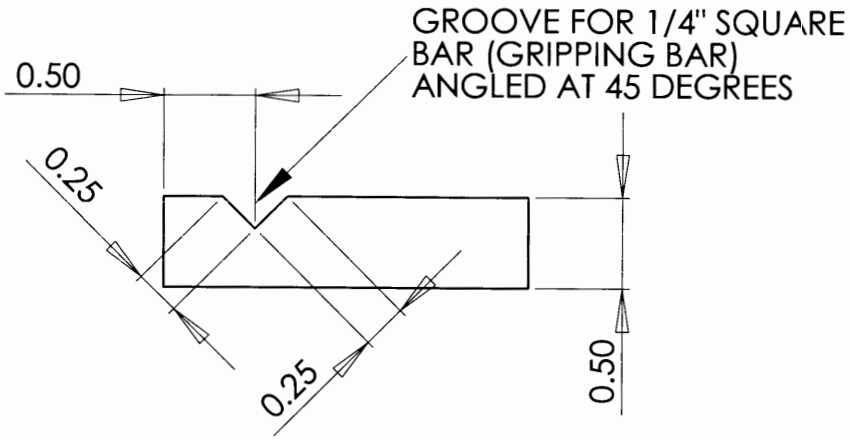

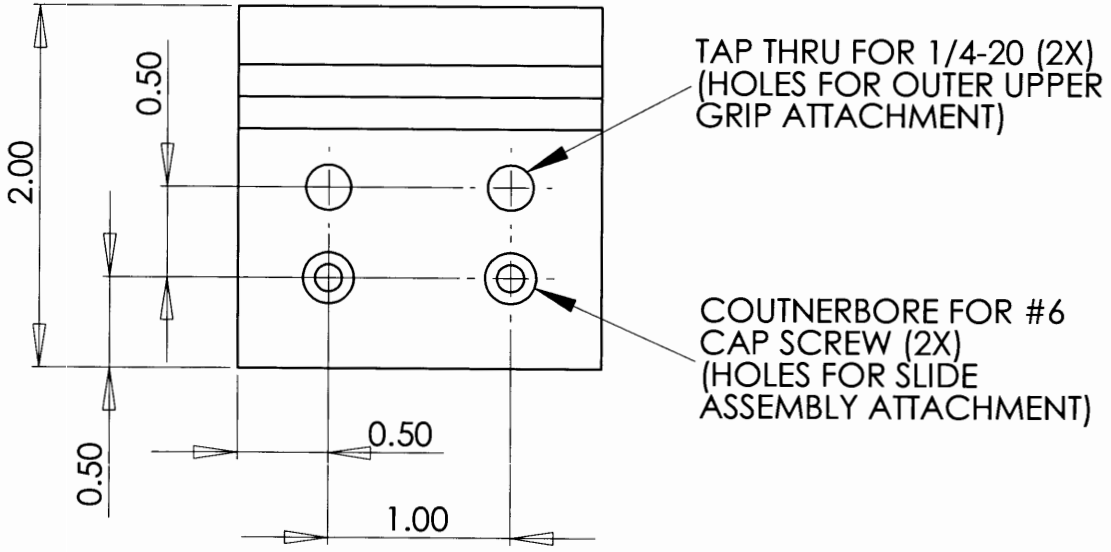

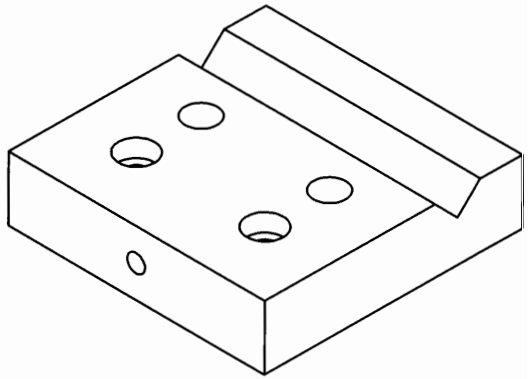

NEXT ASSY	USED ON
APPLICATION	

DIMENSIONS ARE IN INCHES
TOLERANCES:
FRACTIONAL ±
ANGULAR: MACH ± BEND ±
TWO PLACE DECIMAL ±
THREE PLACE DECIMAL ±

MATERIAL: ALUMINUM

FINISH: --

DO NOT SCALE DRAWING

	NAME	DATE
DRAWN		
CHECKED		
ENG APPR.		
MFG APPR.		
Q.A.		

COMMENTS:

MIT

OUTER LOWER GRIP

SIZE	DWG. NO.	REV.
A		

SCALE:1:1 | WEIGHT: | SHEET 1 OF 1

ZONE	REV.	REVISIONS DESCRIPTION	DATE	APPROVED

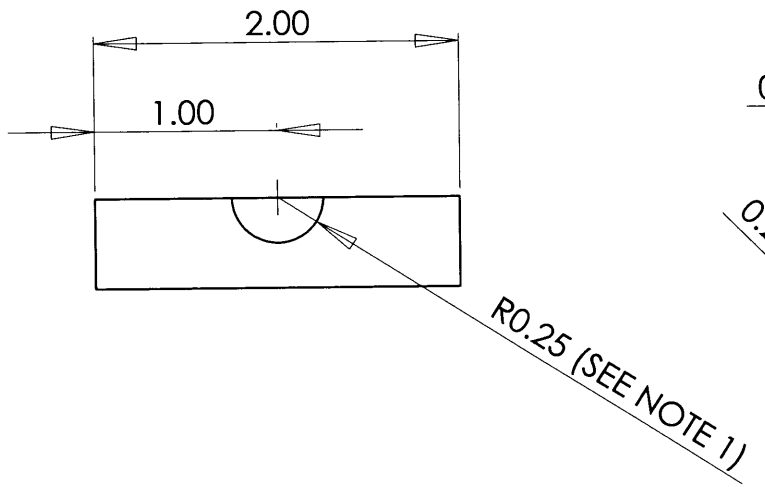

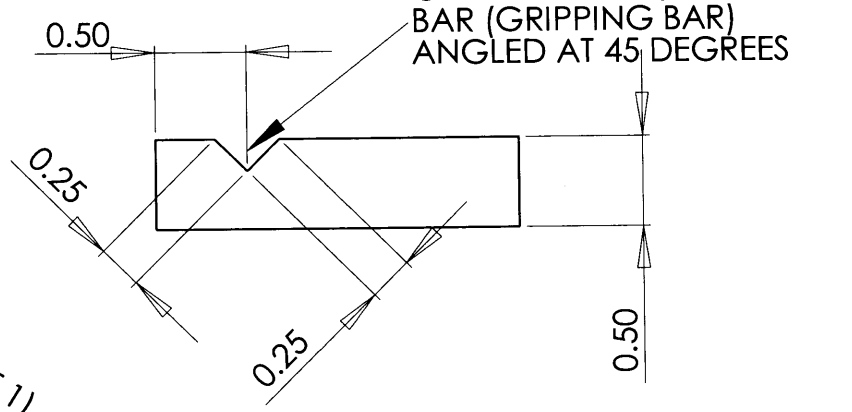

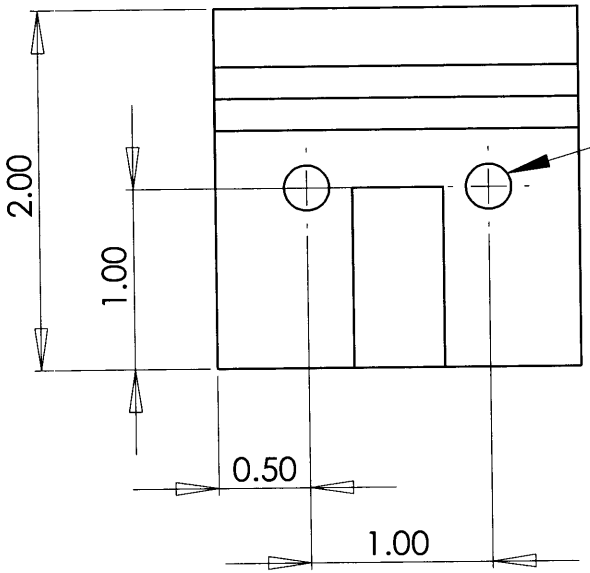

THRU HOLE FOR 1/4-20 (2X) (HOLES FOR INNER LOWER GRIP ATTACHMENT)

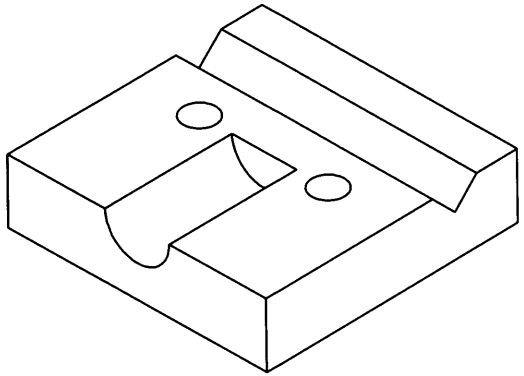

NOTES:
1. THERE SHOULD BE CLEARANCE FIT BETWEEN SHAFT AND INNER UPPER GRIP

NEXT ASSY	USED ON
APPLICATION	

DIMENSIONS ARE IN INCHES
TOLERANCES:
FRACTIONAL ±
ANGULAR: MACH ± BEND ±
TWO PLACE DECIMAL ±
THREE PLACE DECIMAL ±

MATERIAL: ALUMINUM

FINISH: --

DO NOT SCALE DRAWING

	NAME	DATE
DRAWN		
CHECKED		
ENG APPR.		
MFG APPR.		
Q.A.		

COMMENTS:

MIT

INNER UPPER GRIP

SIZE	DWG. NO.	REV.
A		
SCALE:1:1	WEIGHT:	SHEET 1 OF 1

ZONE	REV.	REVISIONS DESCRIPTION	DATE	APPROVED

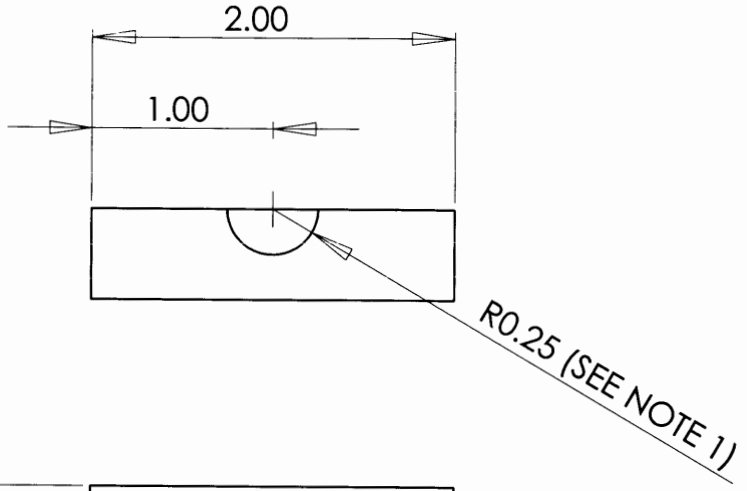

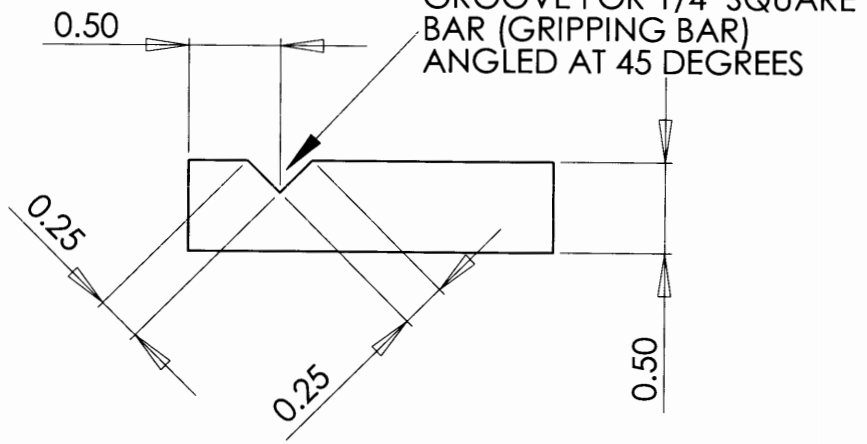

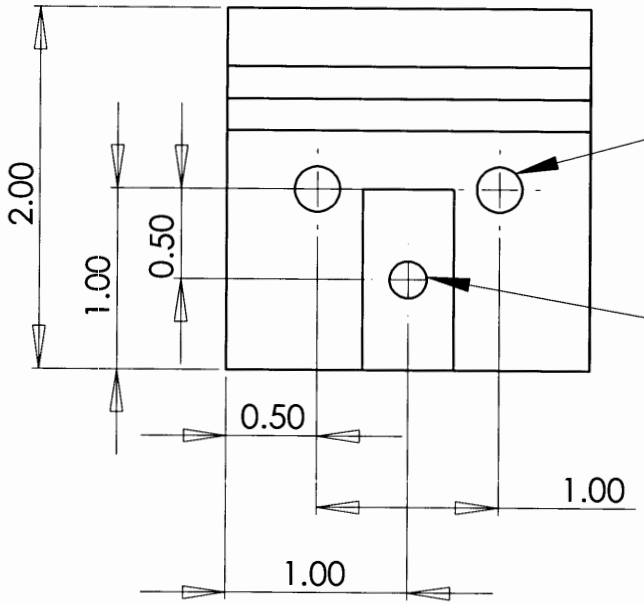

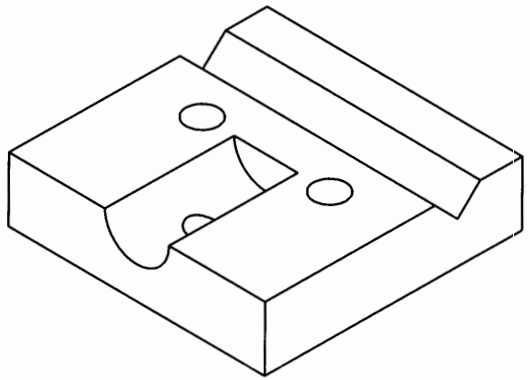

NOTES:
1. THERE SHOULD BE CLEARANCE FIT BETWEEN SHAFT AND INNER LOWER GRIP

NEXT ASSY	USED ON
APPLICATION	

DIMENSIONS ARE IN INCHES
TOLERANCES:
FRACTIONAL ±
ANGULAR: MACH ± BEND ±
TWO PLACE DECIMAL ±
THREE PLACE DECIMAL ±

MATERIAL ALUMINUM

FINISH --

DO NOT SCALE DRAWING

	NAME	DATE
DRAWN		
CHECKED		
ENG APPR.		
MFG APPR.		
Q.A.		

COMMENTS:

MIT

INNER LOWER GRIP

SIZE	DWG. NO.	REV.
A		

SCALE:1:1 | WEIGHT: | SHEET 1 OF 1

ZONE	REV.	REVISIONS DESCRIPTION	DATE	APPROVED

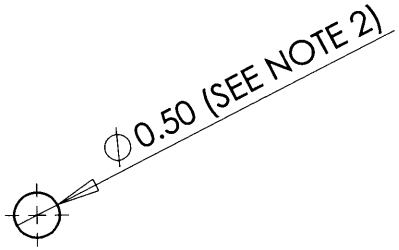

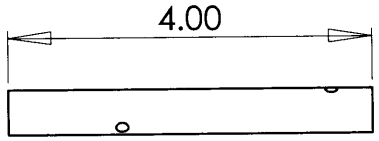

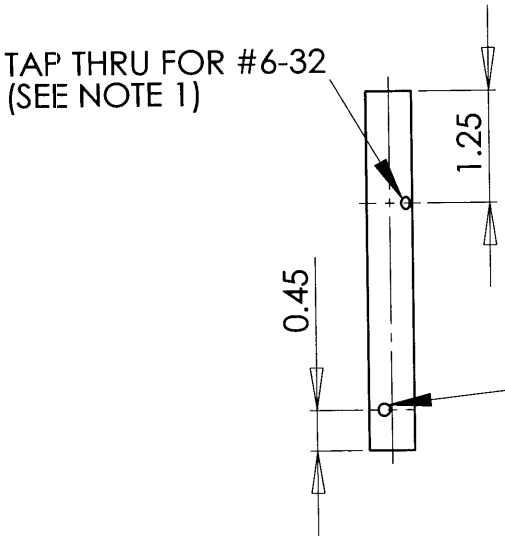

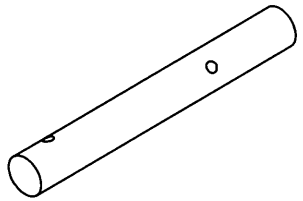

NOTES:
1. RELATIVE ORIENTATION OF HOLES IS NOT IMPORTANT AS LONG AS THEY ARE DIAMETRAL
2. SHAFT IS TO BE PRESS FIT INTO 1/2" ID NEEDLE-ROLLER BEARINGS

NEXT ASSY	USED ON
APPLICATION	

DIMENSIONS ARE IN INCHES
TOLERANCES:
FRACTIONAL ±
ANGULAR: MACH ± BEND ±
TWO PLACE DECIMAL ±
THREE PLACE DECIMAL ±

MATERIAL: STEEL
FINISH: --
DO NOT SCALE DRAWING

	NAME	DATE
DRAWN		
CHECKED		
ENG APPR.		
MFG APPR.		
Q.A.		

COMMENTS:

MIT

SHAFT

SIZE	DWG. NO.	REV.
A		
SCALE:1:2	WEIGHT:	SHEET 1 OF 1

ZONE	REV.	REVISIONS DESCRIPTION	DATE	APPROVED

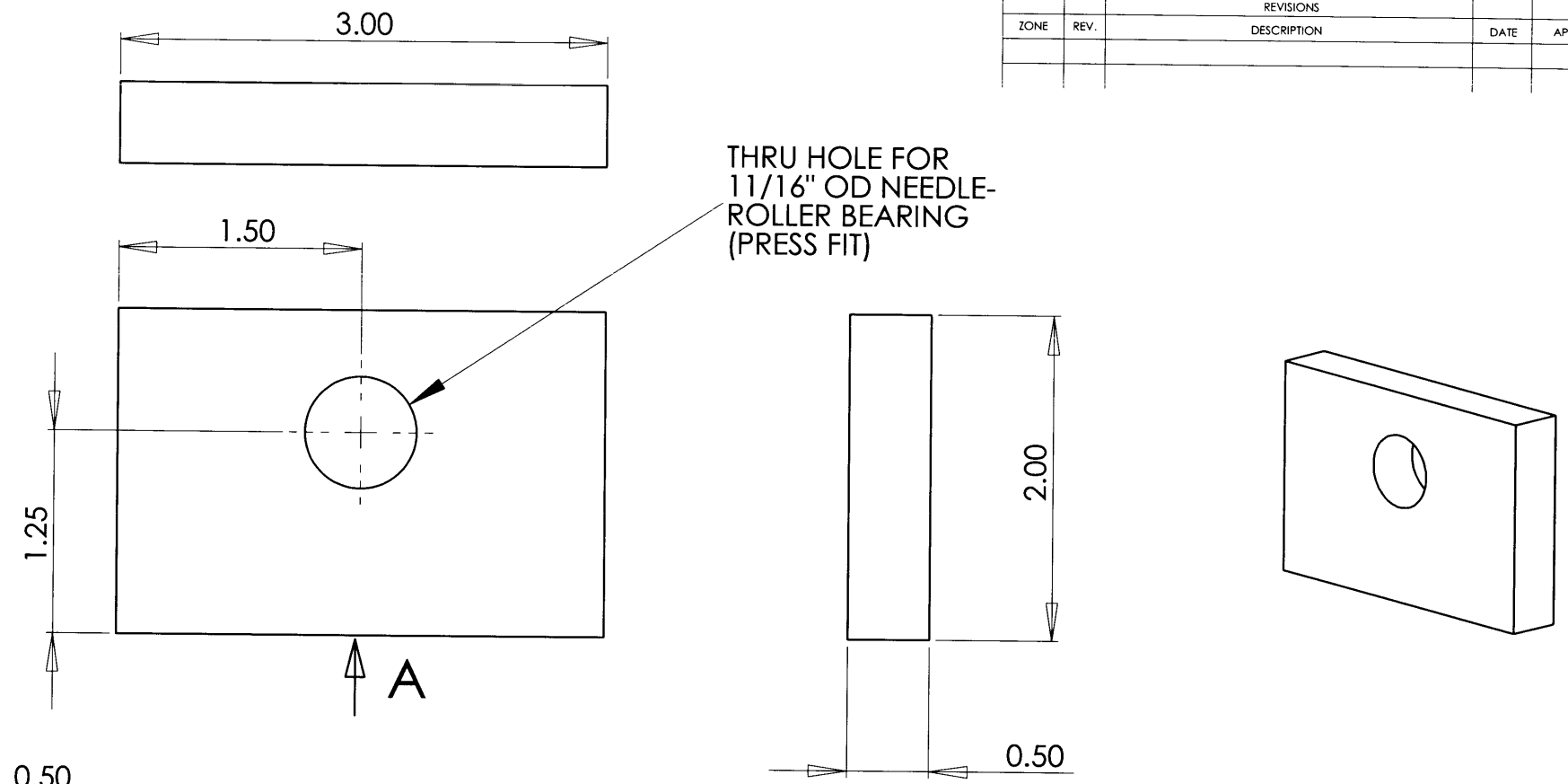

NEXT ASSY	USED ON
APPLICATION	

DIMENSIONS ARE IN INCHES
TOLERANCES:
FRACTIONAL ±
ANGULAR: MACH ± BEND ±
TWO PLACE DECIMAL ±
THREE PLACE DECIMAL ±

MATERIAL: ALUMINUM

FINISH: --

DO NOT SCALE DRAWING

	NAME	DATE
DRAWN		
CHECKED		
ENG APPR.		
MFG APPR.		
Q.A.		

COMMENTS:

MIT

SUPPORT PLATE (2X)

SIZE	DWG. NO.	REV.
A		

SCALE:1:1 | WEIGHT: | SHEET 1 OF 1

ZONE	REV.	REVISIONS DESCRIPTION	DATE	APPROVED

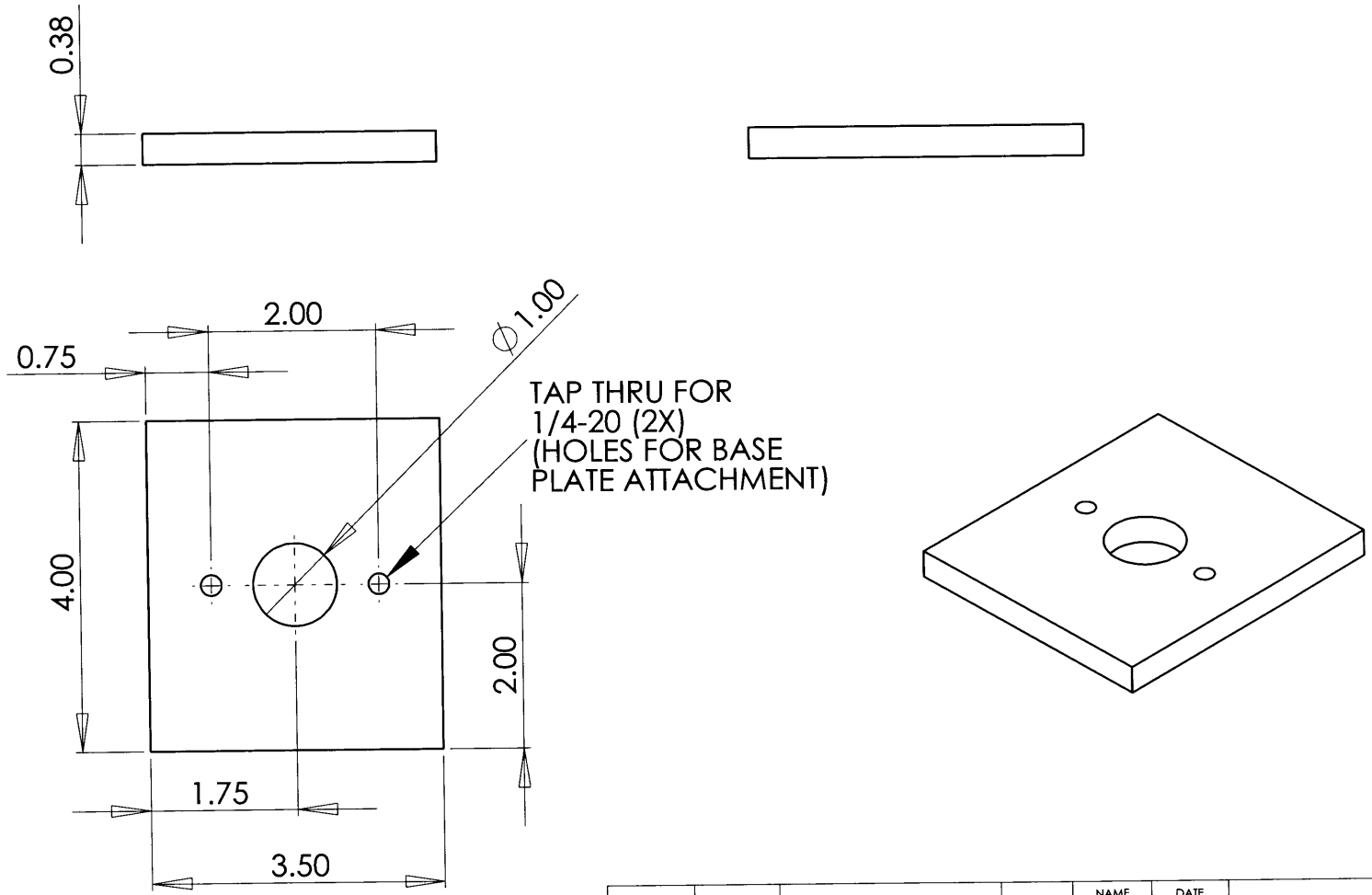

NEXT ASSY	USED ON
APPLICATION	

DIMENSIONS ARE IN INCHES
TOLERANCES:
FRACTIONAL ±
ANGULAR: MACH ± BEND ±
TWO PLACE DECIMAL ±
THREE PLACE DECIMAL ±

MATERIAL: ALUMINUM

FINISH: --

DO NOT SCALE DRAWING

	NAME	DATE
DRAWN		
CHECKED		
ENG APPR.		
MFG APPR.		
Q.A.		

COMMENTS:

MIT

CLAMP PLATE

SIZE	DWG. NO.	REV.
A		
SCALE:1:2	WEIGHT:	SHEET 1 OF 1

ZONE	REV.	REVISIONS DESCRIPTION	DATE	APPROVED

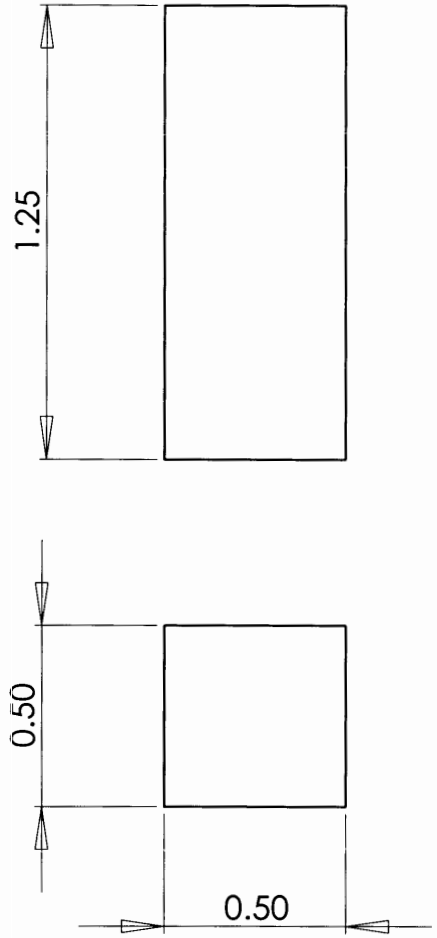

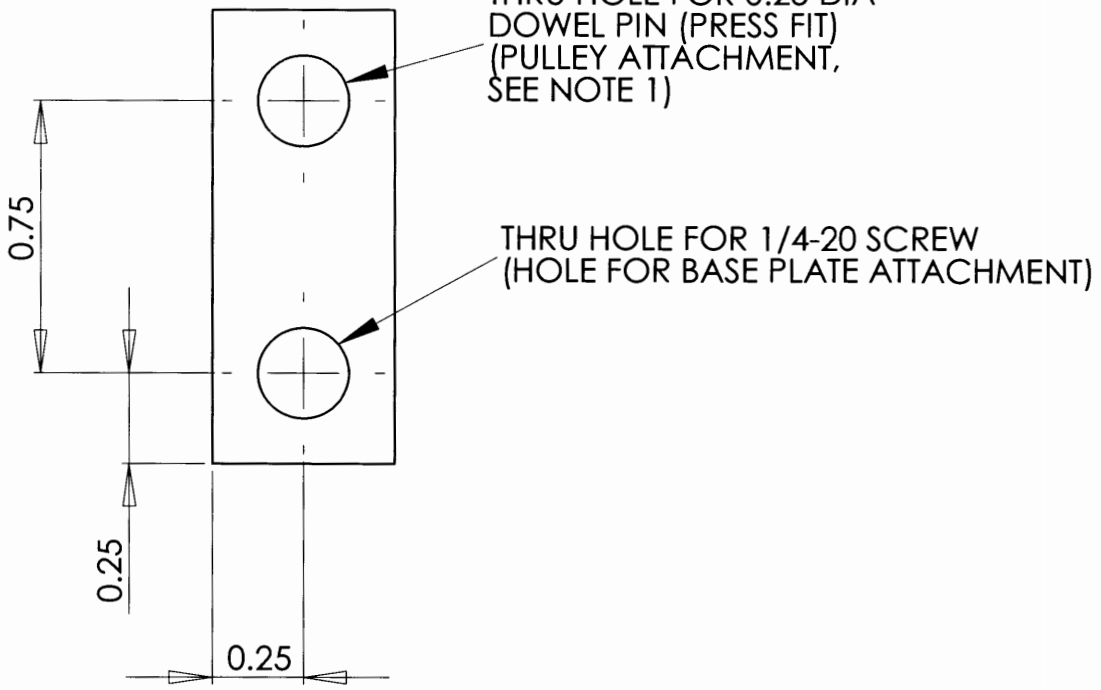

NOTES:
1. PULLEY IS ATTACHED BY PRESS FITTING ONTO 0.25 DIA X 0.75 DOWEL PIN, AND THEN PRESS FITTING PIN INTO SUPPORT

NEXT ASSY	USED ON
APPLICATION	

DIMENSIONS ARE IN INCHES
TOLERANCES:
FRACTIONAL ±
ANGULAR: MACH ± BEND ±
TWO PLACE DECIMAL ±
THREE PLACE DECIMAL ±

MATERIAL ALUMINUM

FINISH --

DO NOT SCALE DRAWING

	NAME	DATE
DRAWN		
CHECKED		
ENG APPR.		
MFG APPR.		
Q.A.		

COMMENTS:

MIT

PULLEY SUPPORT

SIZE	DWG. NO.	REV.
A		
SCALE:2:1	WEIGHT:	SHEET 1 OF 1

		REVISIONS		
ZONE	REV.	DESCRIPTION	DATE	APPROVED

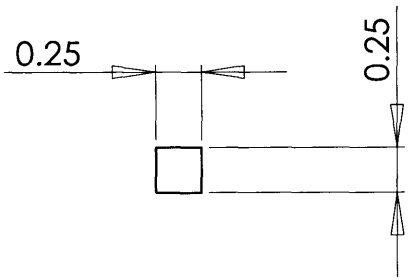

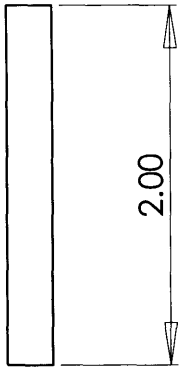

NEXT ASSY	USED ON
APPLICATION	

DIMENSIONS ARE IN INCHES
TOLERANCES:
FRACTIONAL ±
ANGULAR: MACH ± BEND ±
TWO PLACE DECIMAL ±
THREE PLACE DECIMAL ±

MATERIAL: ALUMINUM

FINISH: --

DO NOT SCALE DRAWING

	NAME	DATE
DRAWN		
CHECKED		
ENG APPR.		
MFG APPR.		
Q.A.		

COMMENTS:

MIT

GRIPPING BAR (2x)

SIZE	DWG. NO.	REV.
A		
SCALE:1:1	WEIGHT:	SHEET 1 OF 1

Yarn to Yarn Friction Test Apparatus

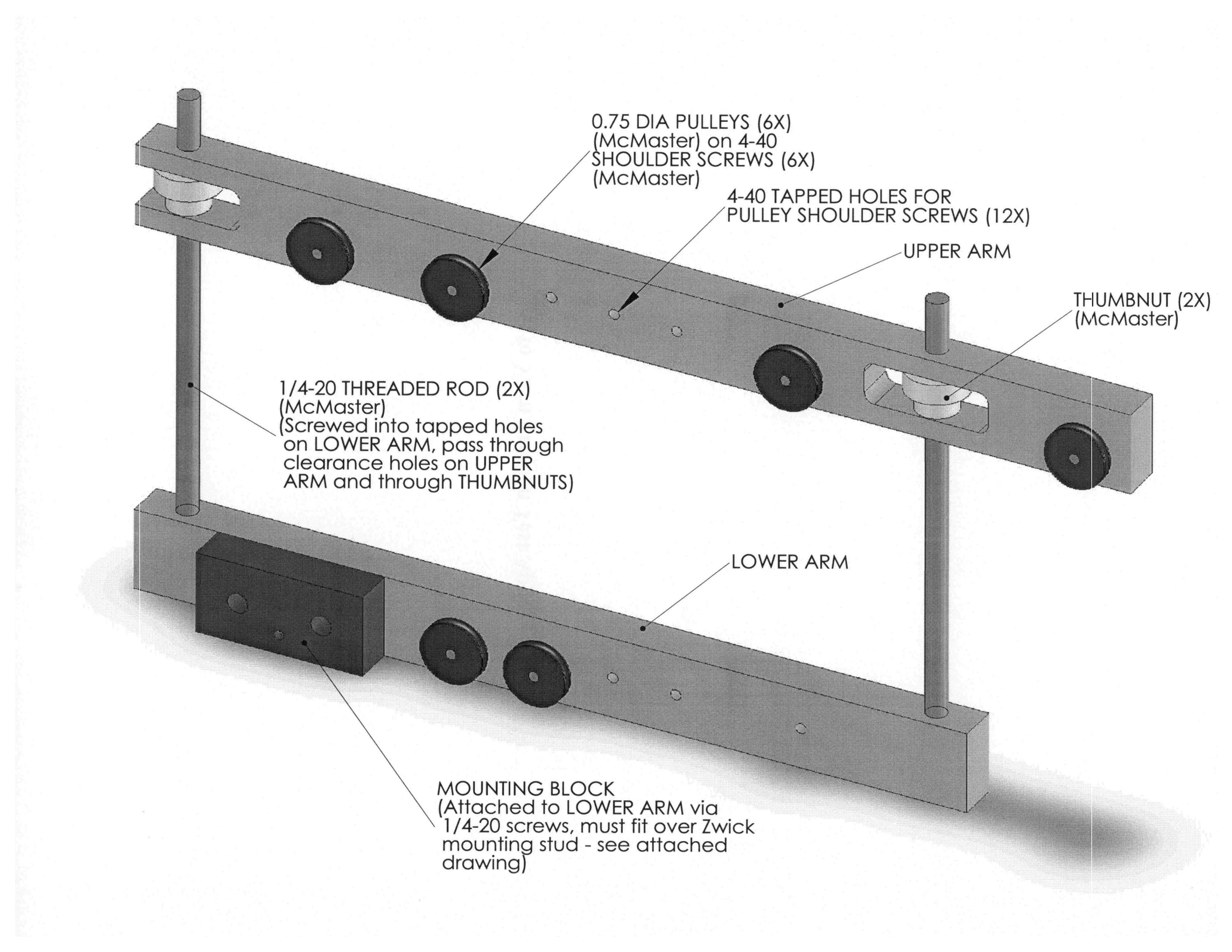
0.75 DIA PULLEYS (6X)
(McMaster) on 4-40
SHOULDER SCREWS (6X)
(McMaster)
4-40 TAPPED HOLES FOR
PULLEY SHOULDER SCREWS (12X)
UPPER ARM
THUMBNUT (2X)
(McMaster)
1/4-20 THREADED ROD (2X)
(McMaster)
(Screwed into tapped holes
on LOWER ARM, pass through
clearance holes on UPPER
ARM and through THUMBNUTS)
LOWER ARM
MOUNTING BLOCK
(Attached to LOWER ARM via
1/4-20 screws, must fit over Zwick
mounting stud - see attached
drawing)

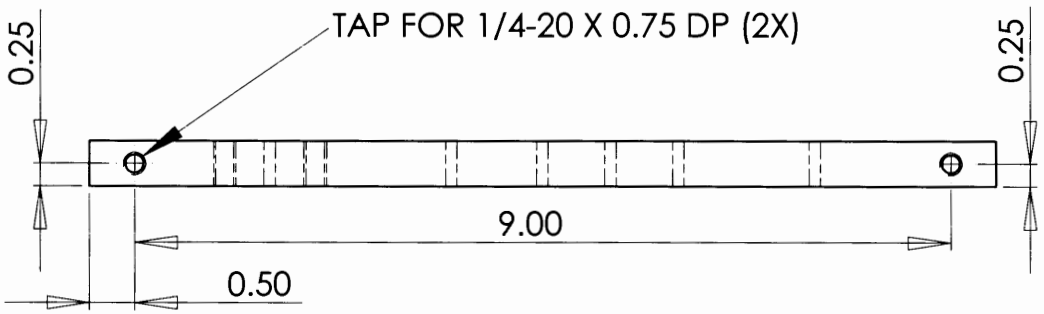

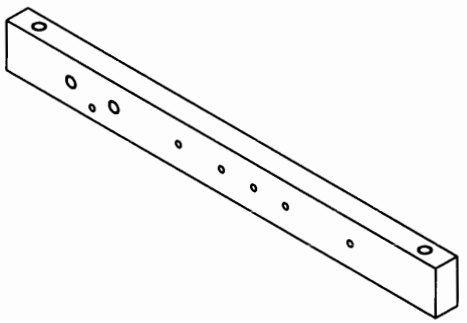

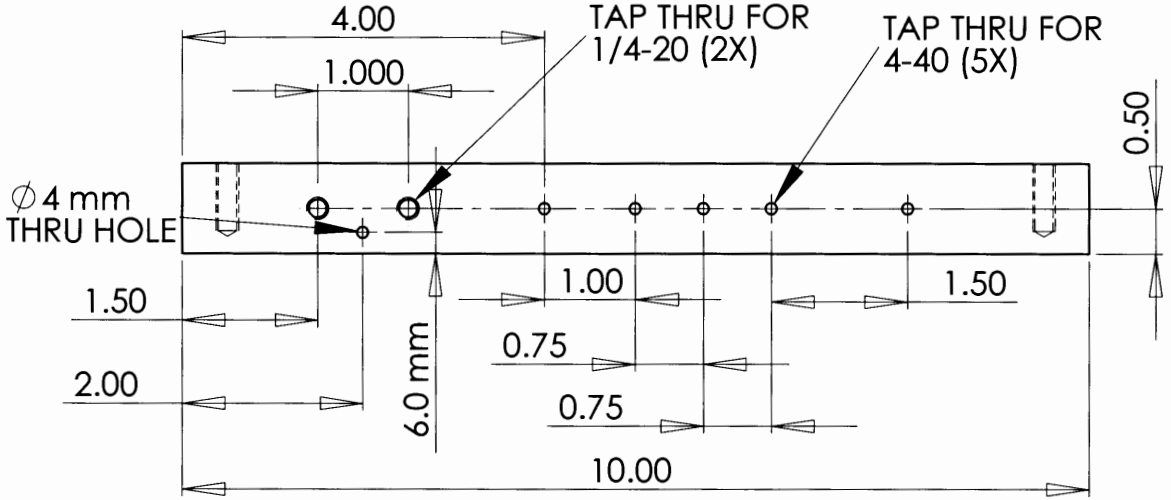

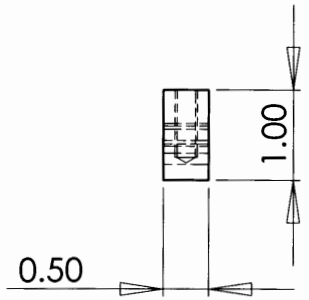

		UNLESS OTHERWISE SPECIFIED:		NAME	DATE
		DIMENSIONS ARE IN INCHES TOLERANCES: FRACTIONAL ± ANGULAR: MACH ± BEND ± TWO PLACE DECIMAL ± THREE PLACE DECIMAL ±	DRAWN	MJK	7/5/05
			CHECKED		
			ENG APPR.		
			MFG APPR.		
		INTERPRET GEOMETRIC TOLERANCING PER:	Q.A.		
		MATERIAL ALUMINUM	COMMENTS: For questions, contact Mike at mking@mit.edu or at X40164		
NEXT ASSY	USED ON	FINISH NONE			
APPLICATION		DO NOT SCALE DRAWING			

TITLE:

Lower Arm

SIZE	DWG. NO.	REV
A		

SCALE: 1:2	WEIGHT:	SHEET 2 OF 3

5 4 3 2 1

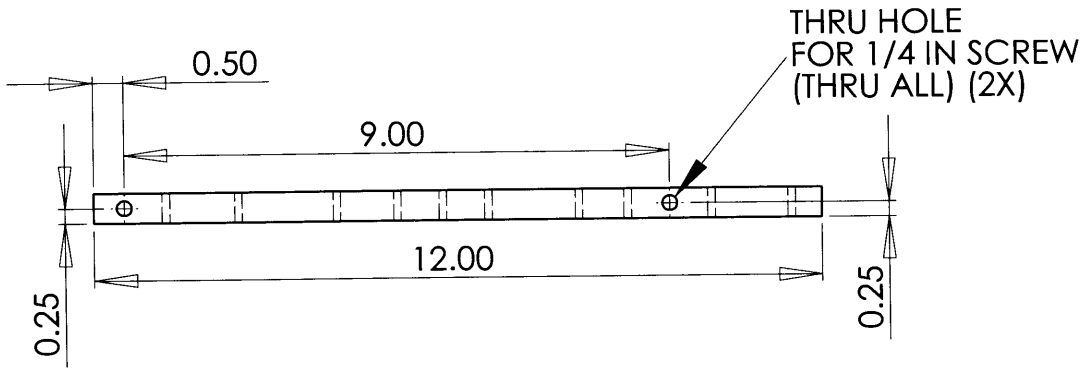

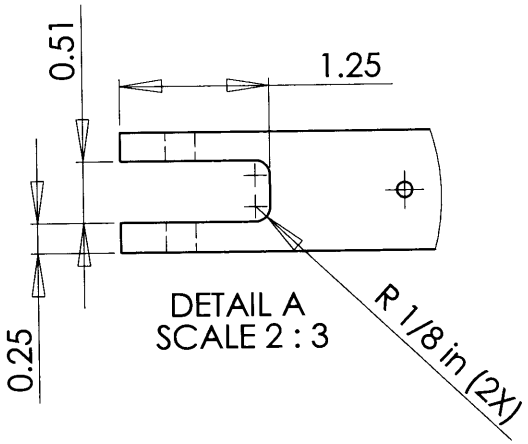

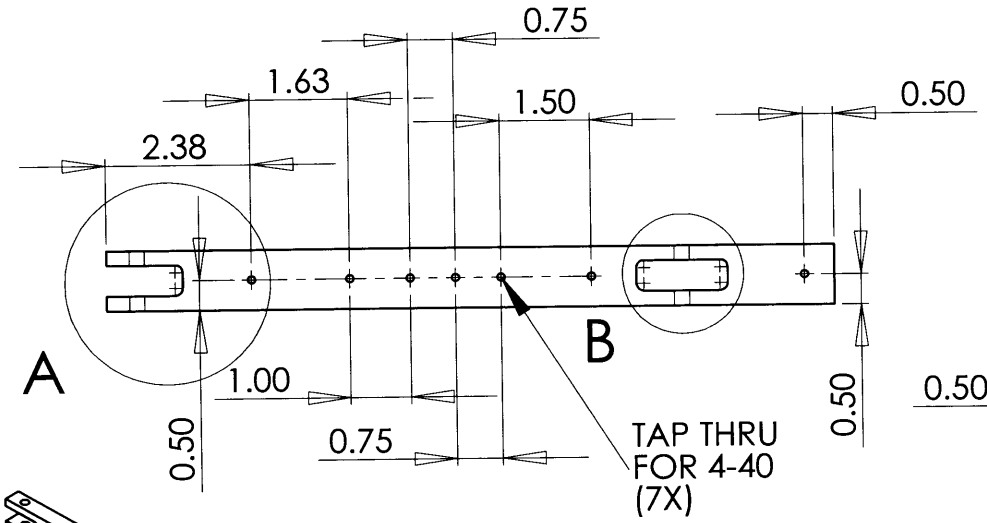

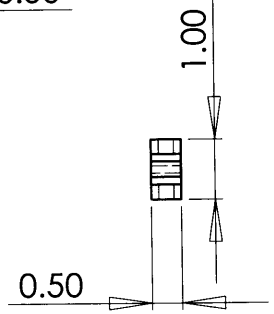

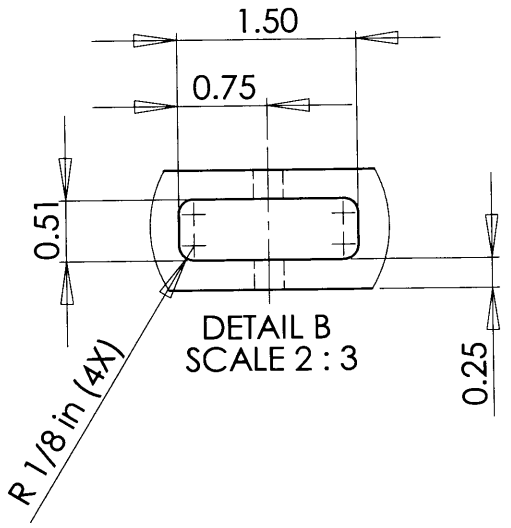

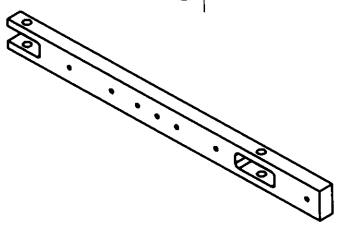

		UNLESS OTHERWISE SPECIFIED:		NAME	DATE
		DIMENSIONS ARE IN INCHES TOLERANCES: FRACTIONAL ± ANGULAR: MACH ± BEND ± TWO PLACE DECIMAL ± THREE PLACE DECIMAL ±	DRAWN	MJK	7/5/05
			CHECKED		
			ENG APPR.		
			MFG APPR.		
		INTERPRET GEOMETRIC TOLERANCING PER:	Q.A.		
		MATERIAL ALUMINUM	COMMENTS: For questions, contact Mike at mking@mit.edu or at X40164		
NEXT ASSY	USED ON	FINISH NONE			
APPLICATION		DO NOT SCALE DRAWING			

TITLE:

Upper Arm

SIZE	DWG. NO.	REV
A		
SCALE: 1:5	WEIGHT:	SHEET 3 OF 3

5 4 3 2 1

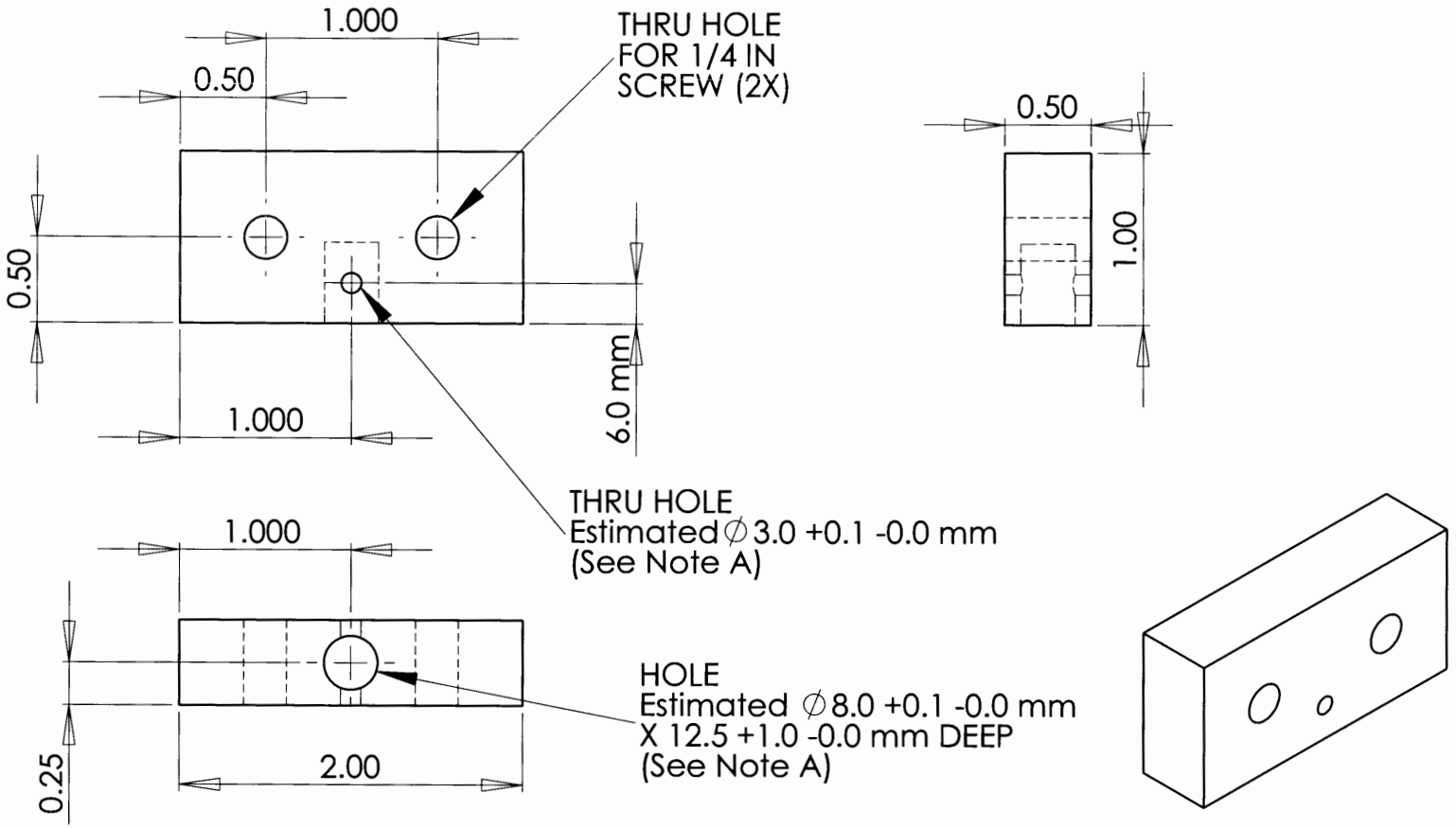

NOTE A
Hole dimensions and tolerances are estimates. This block must fit over Zwick mounting stud. A fastening pin must pass through the 3 mm thru hole and the hole in the mounting stud. All fits should be clearance fits only, with minimal play. The end of the 8 mm hole need not be flat, but it must be sufficiently deep. See attached sheet for dimensions of Zwick mounting stud and fastening pin.

		UNLESS OTHERWISE SPECIFIED:		NAME	DATE
		DIMENSIONS ARE IN INCHES TOLERANCES: FRACTIONAL ± ANGULAR: MACH ± BEND ± TWO PLACE DECIMAL ± THREE PLACE DECIMAL ±	DRAWN	MJK	7/5/05
			CHECKED		
			ENG APPR.		
			MFG APPR.		
		INTERPRET GEOMETRIC TOLERANCING PER:	Q.A.		
		MATERIAL ALUMINUM	COMMENTS:		
NEXT ASSY	USED ON	FINISH NONE	For questions, contact Mike at mking@mit.edu or at X40164		
APPLICATION		DO NOT SCALE DRAWING			

TITLE:

Mounting Block

SIZE	DWG. NO.	REV
A		

SCALE: 2:1	WEIGHT:	SHEET 1 OF 3

5 4 3 2 1

Pneumatic Biaxial Test Apparatus

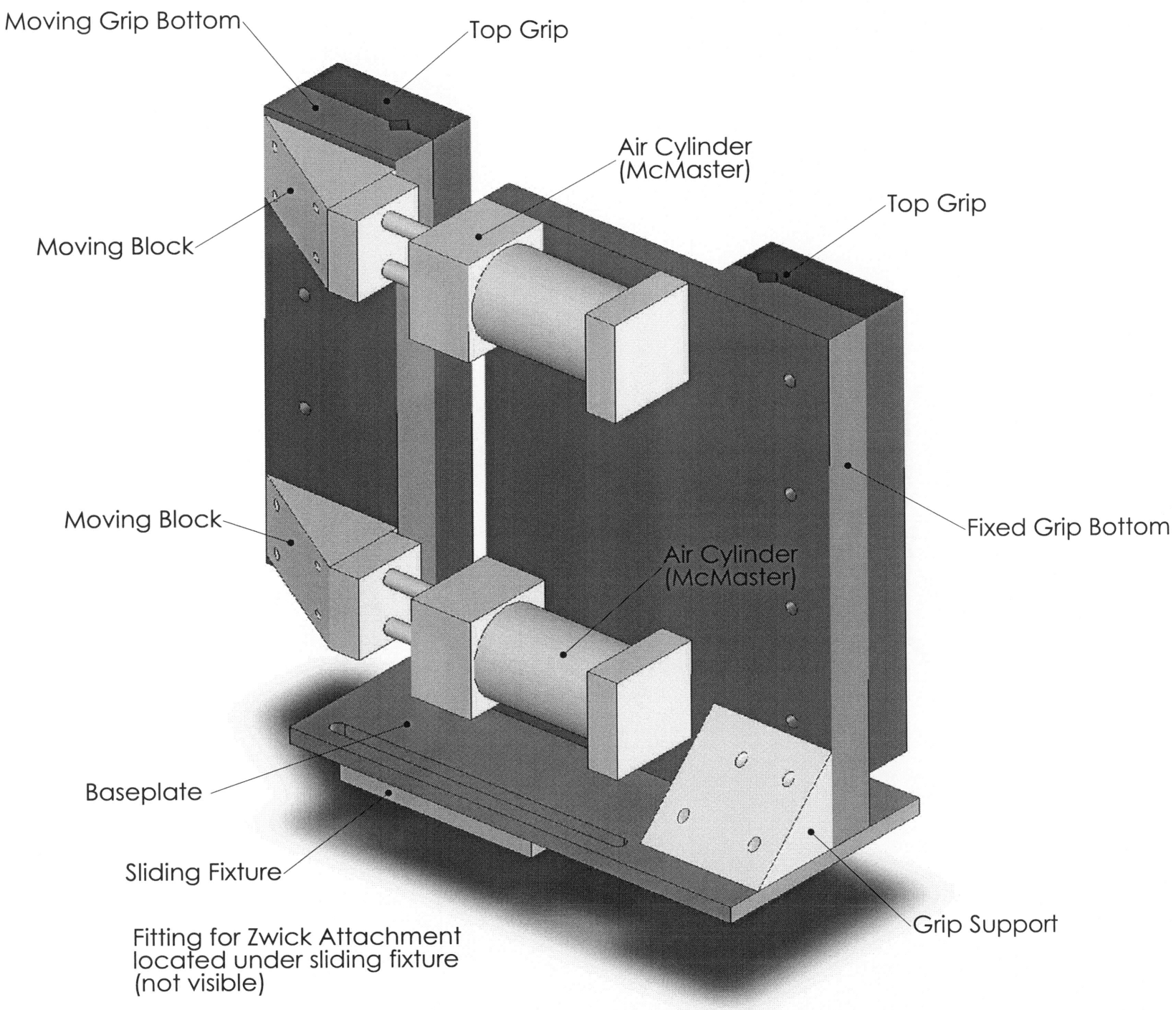
Moving Grip Bottom
Top Grip
Air Cylinder
(McMaster)
Top Grip
Moving Block
Moving Block
Fixed Grip Bottom
Air Cylinder
(McMaster)
Baseplate
Sliding Fixture
Grip Support
Fitting for Zwick Attachment
located under sliding fixture
(not visible)

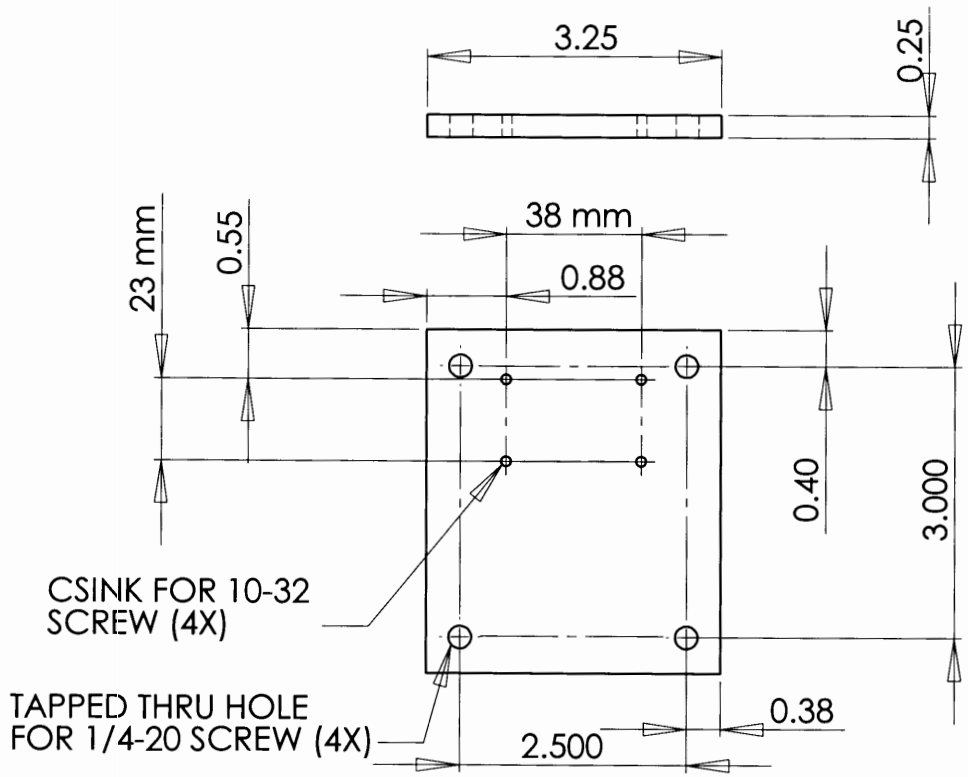

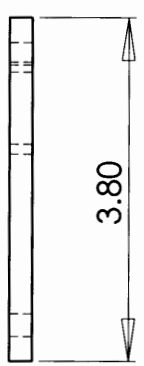

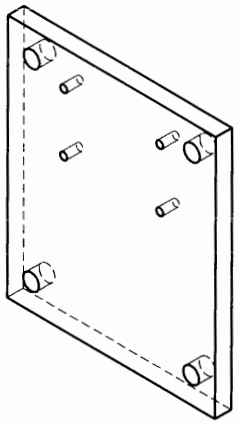

		UNLESS OTHERWISE SPECIFIED:		NAME	DATE
		DIMENSIONS ARE IN INCHES TOLERANCES: FRACTIONAL ± ANGULAR: MACH ± BEND ± TWO PLACE DECIMAL ± THREE PLACE DECIMAL ±	DRAWN	CCC	8/31/05
			CHECKED		
			ENG APPR.		
			MFG APPR.		
		INTERPRET GEOMETRIC TOLERANCING PER:	Q.A.		
		MATERIAL Aluminum	COMMENTS: For questions contact Christina at chestnut@mit.edu or x56355		
NEXT ASSY	USED ON	FINISH None			
APPLICATION		DO NOT SCALE DRAWING			

TITLE:

Sliding fixture

SIZE	DWG. NO.	REV
A		

SCALE: 1:2 | WEIGHT: | SHEET 1 OF 1

5 4 3 2 1

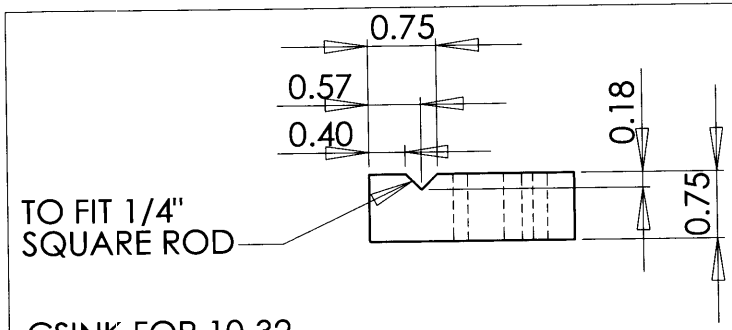

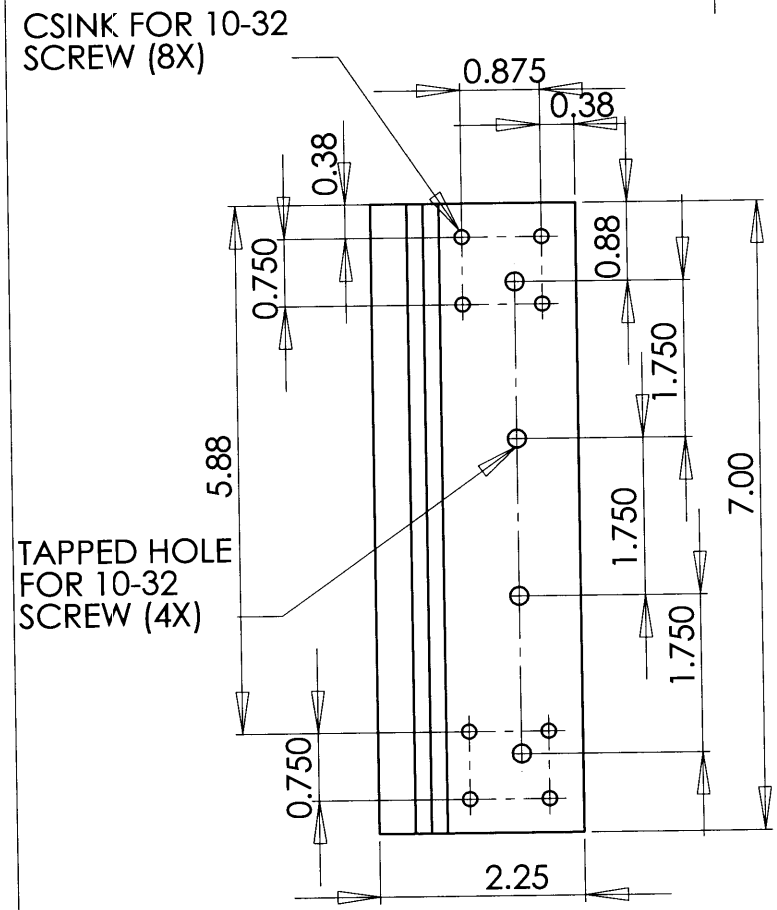

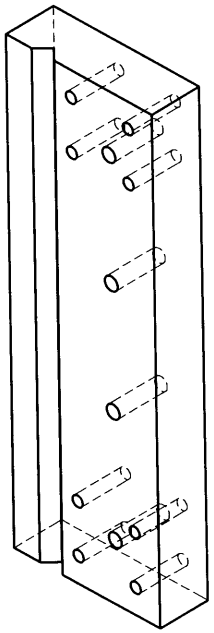

UNLESS OTHERWISE SPECIFIED:		NAME	DATE
DIMENSIONS ARE IN INCHES TOLERANCES: FRACTIONAL ± ANGULAR: MACH ± BEND ± TWO PLACE DECIMAL ± THREE PLACE DECIMAL ±	DRAWN	CCC	8/31/05
	CHECKED		
	ENG APPR.		
	MFG APPR.		
INTERPRET GEOMETRIC TOLERANCING PER:	Q.A.		
MATERIAL Aluminum	COMMENTS: For questions contact Christina at chestnut@mit.edu or x56355		
FINISH None			
DO NOT SCALE DRAWING			

TITLE: **Moving grip bottom**

SIZE	DWG. NO.	REV
A		
SCALE: 1:2	WEIGHT:	SHEET 1 OF 1

NEXT ASSY	USED ON
APPLICATION	

5 4 3 2 1

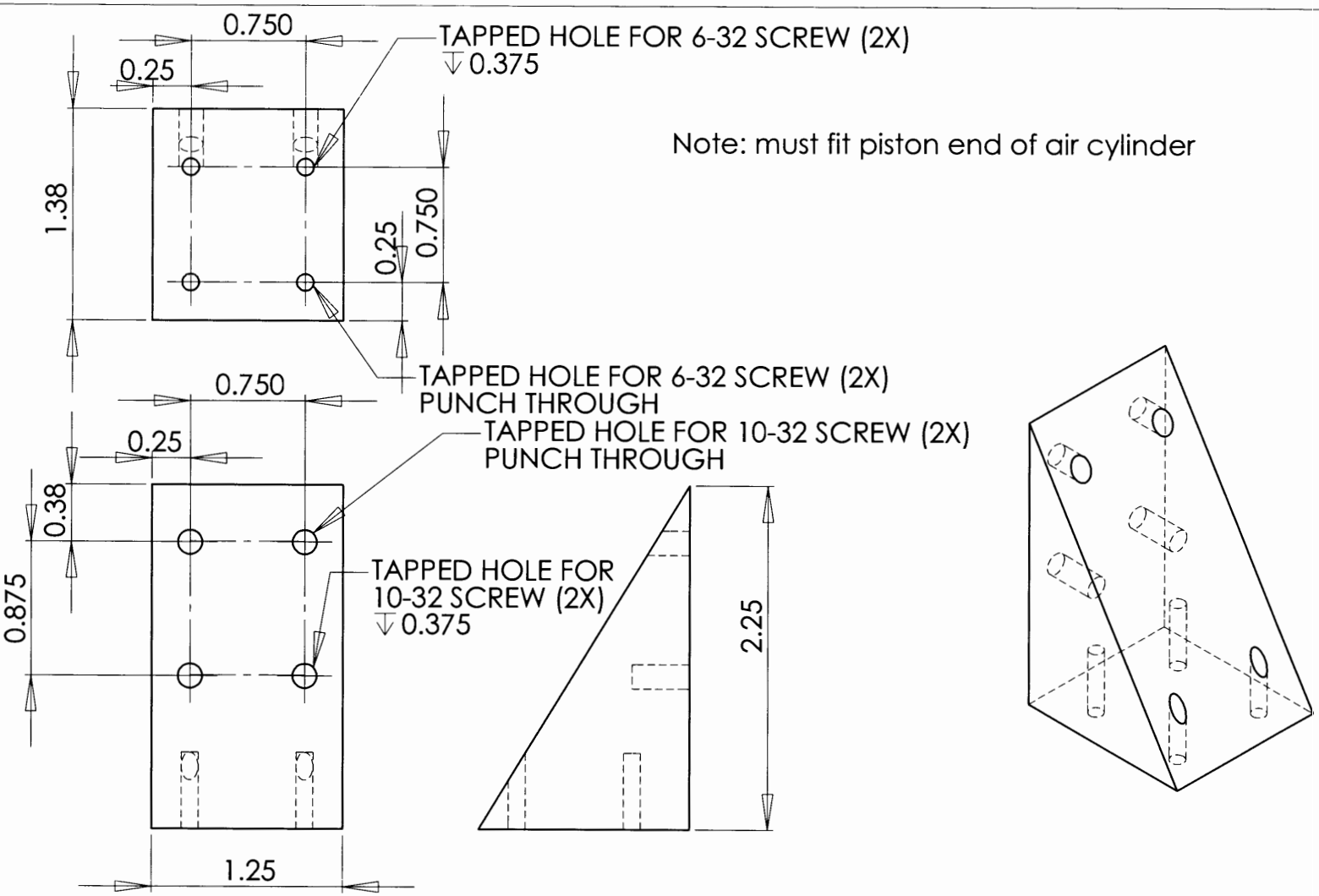

Note: must fit piston end of air cylinder

		UNLESS OTHERWISE SPECIFIED:		NAME	DATE
		DIMENSIONS ARE IN INCHES TOLERANCES: FRACTIONAL ± ANGULAR: MACH ± BEND ± TWO PLACE DECIMAL ± THREE PLACE DECIMAL ±	DRAWN	CCC	8/31/05
			CHECKED		
			ENG APPR.		
			MFG APPR.		
		INTERPRET GEOMETRIC TOLERANCING PER:	Q.A.		
		MATERIAL Aluminum	COMMENTS: For questions contact Christina at chestnut@mit.edu or x56355		
NEXT ASSY	USED ON	FINISH None			
APPLICATION		DO NOT SCALE DRAWING			

TITLE:

Moving block (2X)

SIZE	DWG. NO.	REV
A		

SCALE: 1:1	WEIGHT:	SHEET 1 OF 1

5 4 3 2 1

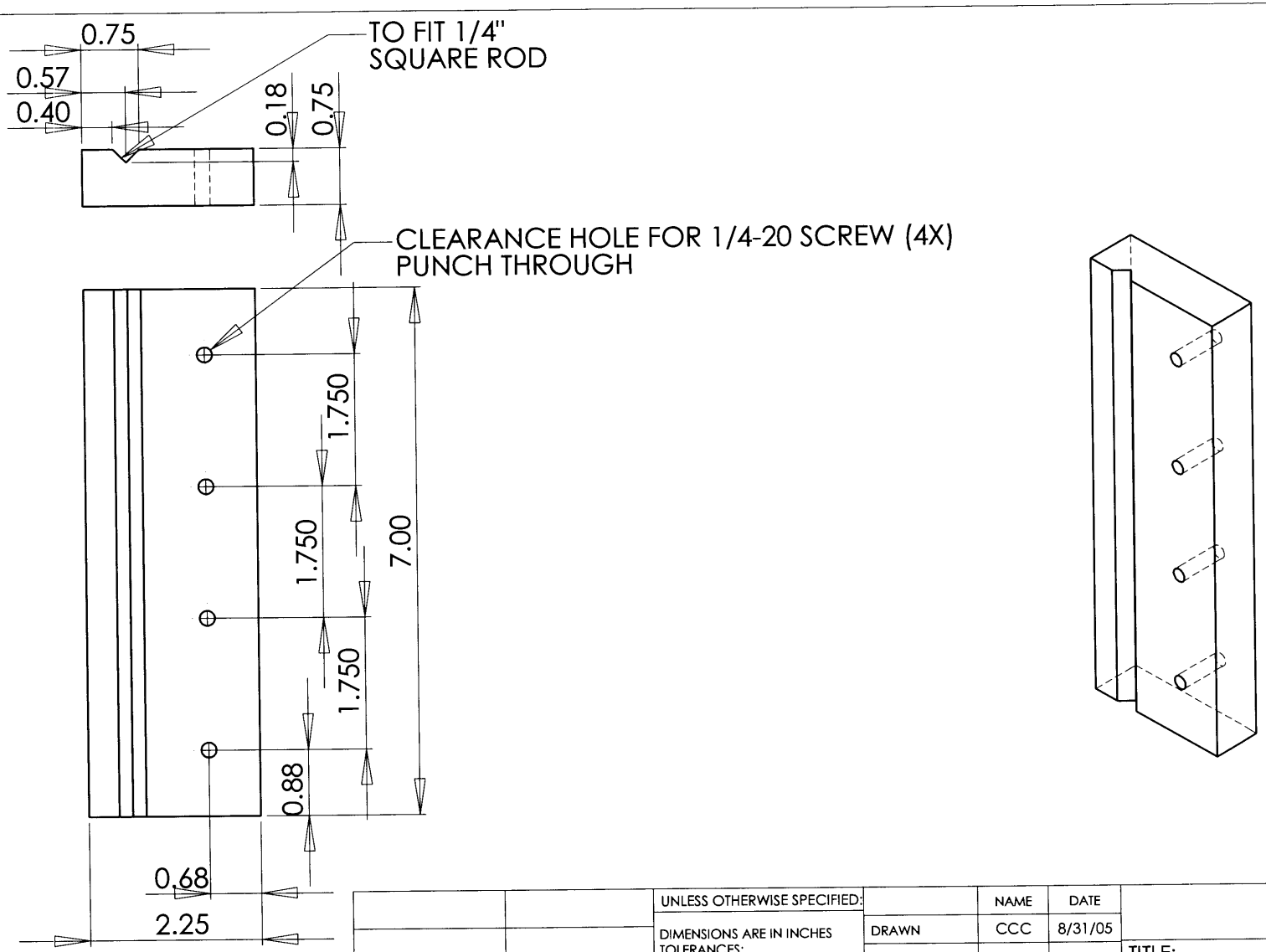

		UNLESS OTHERWISE SPECIFIED:		NAME	DATE
		DIMENSIONS ARE IN INCHES TOLERANCES: FRACTIONAL ± ANGULAR: MACH ± BEND ± TWO PLACE DECIMAL ± THREE PLACE DECIMAL ±	DRAWN	CCC	8/31/05
			CHECKED		
			ENG APPR.		
			MFG APPR.		
			Q.A.		
		INTERPRET GEOMETRIC TOLERANCING PER:	COMMENTS: For questions contact Christina at chestnut@mit.edu or x56355		
		MATERIAL Aluminum			
NEXT ASSY	USED ON	FINISH None			
APPLICATION		DO NOT SCALE DRAWING			

TITLE:

Top grip (2X)

SIZE	DWG. NO.	REV
A		
SCALE: 1:2	WEIGHT:	SHEET 1 OF 1

5 4 3 2 1

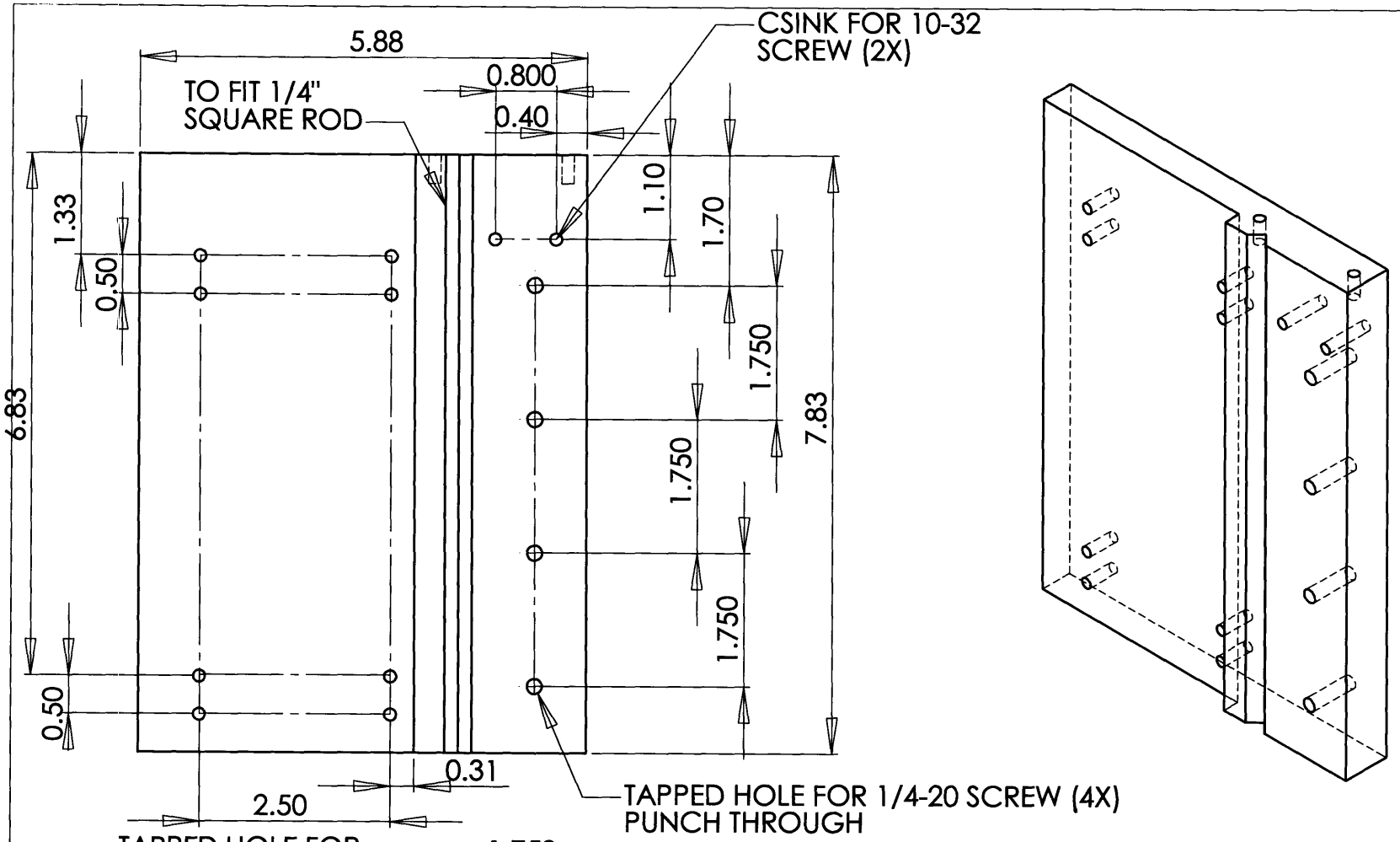

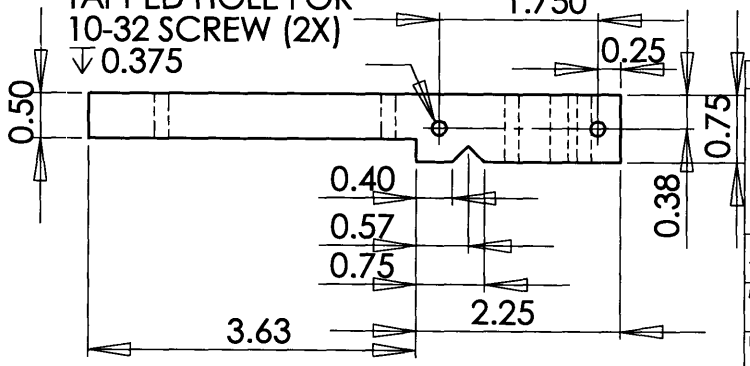

UNLESS OTHERWISE SPECIFIED:		NAME	DATE
DIMENSIONS ARE IN INCHES TOLERANCES: FRACTIONAL ± ANGULAR: MACH ± BEND ± TWO PLACE DECIMAL ± THREE PLACE DECIMAL ±	DRAWN	CCC	8/31/05
	CHECKED		
	ENG APPR.		
	MFG APPR.		
INTERPRET GEOMETRIC TOLERANCING PER:	Q.A.		
MATERIAL: Aluminum	COMMENTS: For questions contact Christina at chestnut@mit.edu or x56355		
FINISH: None			
DO NOT SCALE DRAWING			

TITLE:

Fixed grip bottom

SIZE	DWG. NO.	REV
A		

SCALE: 1:2	WEIGHT:	SHEET 1 OF 1

5 4 3 2 1

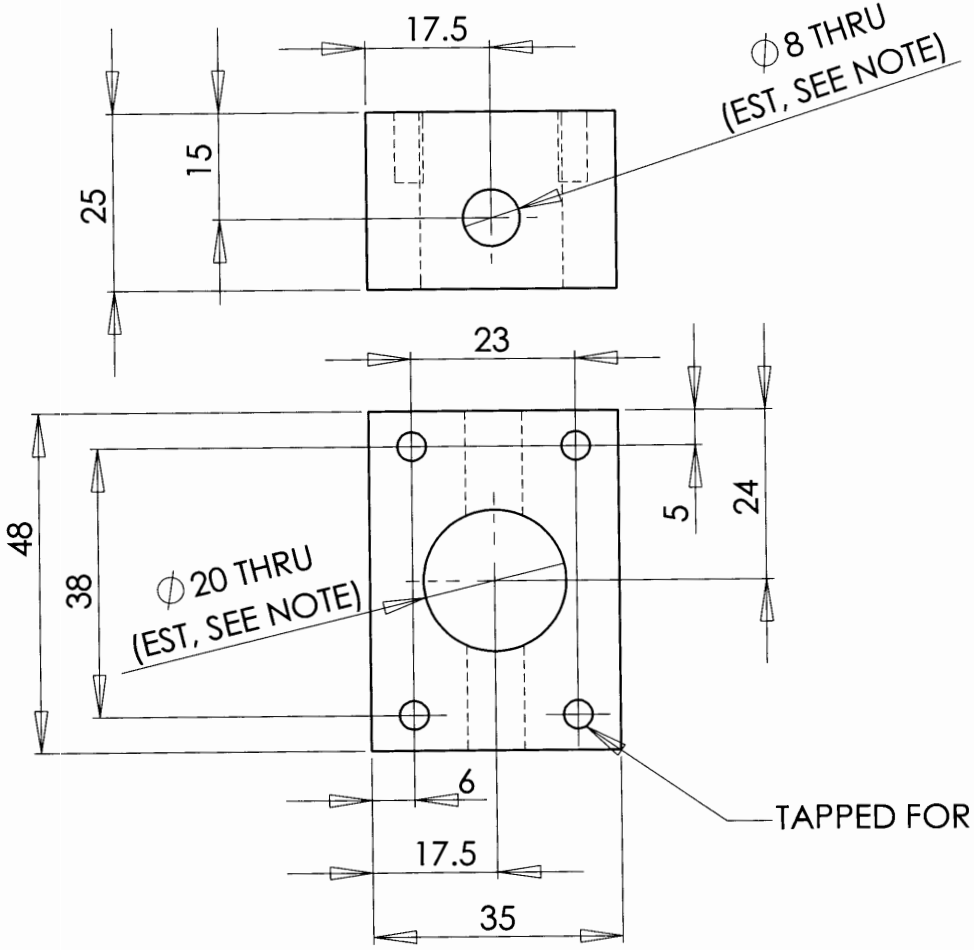

ALL MEASUREMENTS IN MILLIMETERS
UNLESS OTHERWISE SPECIFIED

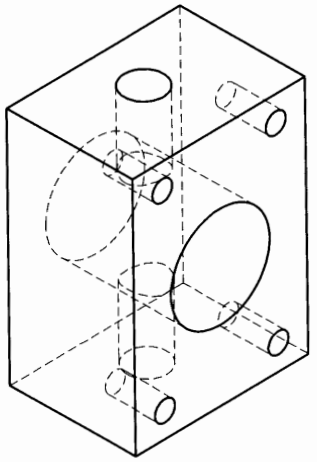

NOTE
THIS PART MUST FIT OVER ZWICK ATTACHMENT STUD (SEE: ATTACHED PRINT FOR DIMENSIONS) ALL FITS SHOULD BE CLEARANCE FITS ONLY WITH MINIMAL PLAY

NEXT ASSY	USED ON
APPLICATION	

UNLESS OTHERWISE SPECIFIED:

DIMENSIONS ARE IN INCHES
TOLERANCES:
FRACTIONAL ±
ANGULAR: MACH ± BEND ±
TWO PLACE DECIMAL ±
THREE PLACE DECIMAL ±

INTERPRET GEOMETRIC TOLERANCING PER:

MATERIAL: Aluminum

FINISH: None

DO NOT SCALE DRAWING

	NAME	DATE
DRAWN	CCC	8/31/05
CHECKED		
ENG APPR.		
MFG APPR.		
Q.A.		

COMMENTS:

For questions contact Christina at chestnut@mit.edu or x56355

TITLE:

Fitting

SIZE	DWG. NO.	REV
A		
SCALE: 1:1	WEIGHT:	SHEET 1 OF 1

5 4 3 2 1

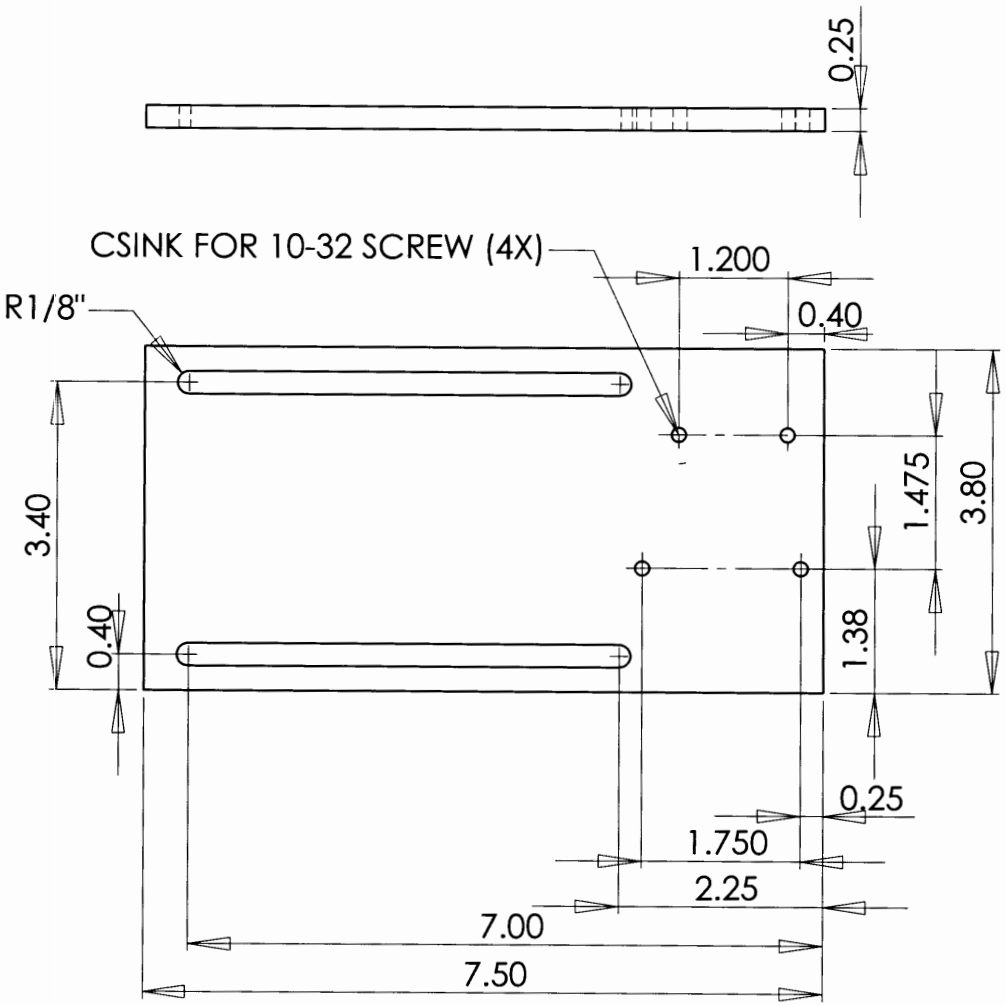

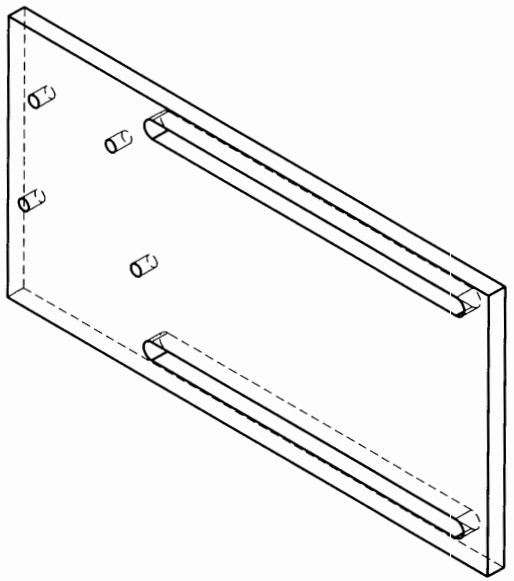

		UNLESS OTHERWISE SPECIFIED:		NAME	DATE
		DIMENSIONS ARE IN INCHES TOLERANCES: FRACTIONAL ± ANGULAR: MACH ± BEND ± TWO PLACE DECIMAL ± THREE PLACE DECIMAL ±	DRAWN	CCC	8/31/05
			CHECKED		
			ENG APPR.		
			MFG APPR.		
		INTERPRET GEOMETRIC TOLERANCING PER:	Q.A.		
		MATERIAL Aluminum	COMMENTS: For questions, contact Christina at chestnut@mit.edu or at x56355		
NEXT ASSY	USED ON	FINISH None			
APPLICATION		DO NOT SCALE DRAWING			

TITLE: **Baseplate**

SIZE	DWG. NO.	REV
A		

SCALE: 1:2 | WEIGHT: | SHEET 1 OF 1

5 4 3 2 1

ZONE	REV.	REVISIONS DESCRIPTION	DATE	APPROVED

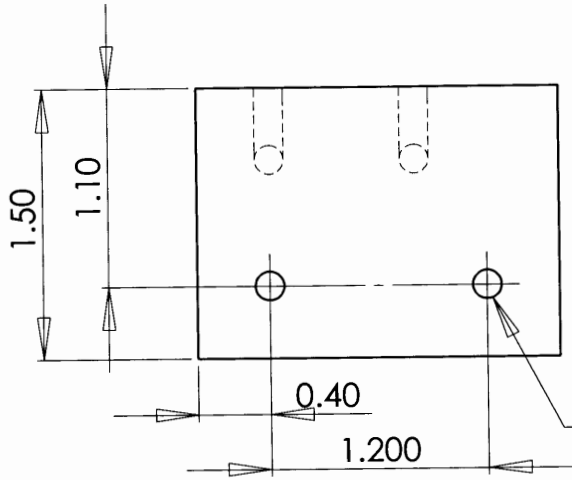

TAPPED HOLE FOR 10-32 SCREW (2X)
PUNCH THROUGH

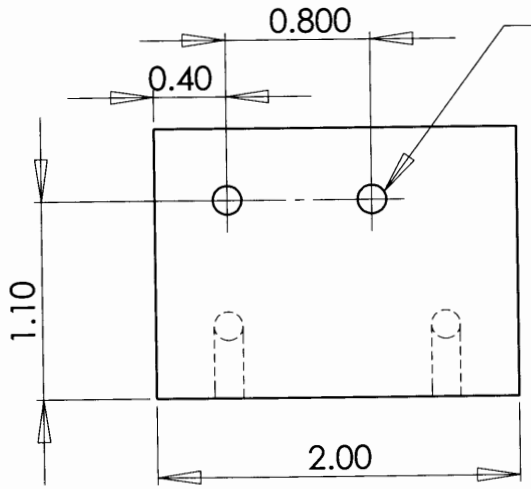

TAPPED HOLE FOR 10-32 SCREW (2X)
PUNCH THROUGH

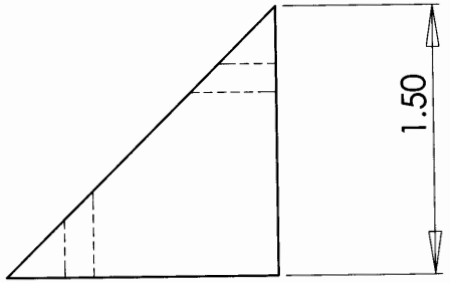

PROPRIETARY AND CONFIDENTIAL

THE INFORMATION CONTAINED IN THIS DRAWING IS THE SOLE PROPERTY OF <INSERT COMPANY NAME HERE>. ANY REPRODUCTION IN PART OR AS A WHOLE WITHOUT THE WRITTEN PERMISSION OF <INSERT COMPANY NAME HERE> IS PROHIBITED.

NEXT ASSY	USED ON
APPLICATION	DO NOT SCALE DRAWING

UNLESS OTHERWISE SPECIFIED:

DIMENSIONS ARE IN INCHES
TOLERANCES:
FRACTIONAL ±
ANGULAR: MACH ± BEND ±
TWO PLACE DECIMAL ±
THREE PLACE DECIMAL ±

INTERPRET GEOMETRIC TOLERANCING PER:

MATERIAL: Aluminum

FINISH: None

	NAME	DATE
DRAWN	CCC	9/7/05
CHECKED		
ENG APPR.		
MFG APPR.		
Q.A.		

COMMENTS:
For questions contact Christina at chestnut@mit.edu or x56355

TITLE:

Grip support

SIZE	DWG. NO.	REV
A		
SCALE: 1:1	WEIGHT:	SHEET 1 OF 1

5 4 3 2 1